Measurement of CP asymmetry in radiative charm decays at LHCb

Aleksei Chernov

Henryk Niewodniczański Institute of Nuclear Physics,
Polish Academy of Sciences,
Kraków, Poland

A Dissertation for a PhD Degree

Kraków, June 2024

Abstract

This thesis presents a measurement of CP asymmetry, A_{CP}, for radiative decays of charm mesons $D^0 \to V\gamma$, and their charge conjugates, where V denotes vector meson $\bar{K}^{*0}$, ϕ or ρ^0. The study is based on the proton-proton collision data collected at a centre-of-mass energy of $\sqrt{s} = 8$ TeV by the LHCb experiment in 2012, during Run-1 of the LHC. This data sample corresponds to an integrated luminosity of 2 fb^{-1}. Reconstructed neutral D mesons originate from strong decays of the $D^{*\pm}$ states, $D^{*+} \to D^0\pi_s^+$ and $D^{*-} \to \bar{D}^0\pi_s^-$, with the soft-pion π_s charge used for tagging of a D flavour at the production. The presented analysis is the first study of radiative charm decays at LHCb.

Large and irreducible background from decays involving π^0 mesons, $D^0 \to V\pi^0$, is suppressed using a multivariate classifier based on distinguished shapes of energy clusters produced by photons and π^0 mesons in the LHCb calorimeter system. The signal decays are separated from residual background with the three-dimensional fit to D^0 invariant mass $M(D^0)$, the difference between invariant masses of D^{*+} and D^0, $\Delta M = M(D^{*+}) - M(D^0)$, and V-meson helicity angle $\cos\theta$, as observables. Correlations observed between $M(D^0)$ and ΔM observables for both signal and background channels, are modelled based on the corresponding simulation samples. The total D^0 and $\bar{D}^0$ signal yields are measured to be: 4263 ± 193 events for $D^0 \to \bar{K}^{*0}\gamma$ decay, and 216 ± 29 events for the $D^0 \to \phi\gamma$ decay; no significant signal is observed for the $D^0 \to \rho\gamma$ decay.

Nuisance asymmetries due to asymmetric charm production and asymmetric detection of positively and negatively charged hadrons, are constrained with high-statistics and high-purity reference channels. The pion-tagged $D^0 \to K^+K^-$ and $D^0 \to \pi^+\pi^-$ decays are chosen as reference channels for $D^0 \to \phi\gamma$ and $D^0 \to \rho^0\gamma$ signal decays, respectively, whereas $D^0 \to K^-\pi^+\pi^0$ is used as a reference channel for $D^0 \to \bar{K}^{*0}\gamma$. The nuisance asymmetries are measured to be about $(-1.0 \pm 0.2)\%$ in $D^0 \to K^+K^-$ and $D^0 \to \pi^+\pi^-$ channels, and $(-1.7 \pm 0.3)\%$ in $D^0 \to K^-\pi^+\pi^0$. They are subtracted from asymmetries measured for the signal channels in order to access A_{CP}.

The asymmetries for the signal channels are measured by performing the three-dimensional fits in $M(D^0)$ vs. ΔM vs. $\cos\theta$ space, simultaneously to the separated D^0 and $\bar{D}^0$ samples. The central values of the asymmetries are still blinded, while their statistical uncertainties are measured to be 5% for $D^0 \to \bar{K}^{*0}\gamma$ and 12% for $D^0 \to \phi\gamma$; the Run-1 analysis is not sensitive to the asymmetry in the $D^0 \to \rho^0\gamma$ decay. The presented measurement is statistically limited. The total systematic uncertainties on the signal A_{CP}'s are expected to be below 1%, and dominated by statistical uncertainties on the asymmetries measured in the reference channels. Unblinding is planned together with the Run-2 measurement, which is currently ongoing.

Streszczenie

Niniejsza rozprawa przedstawia pomiar asymetrii CP, A_{CP}, w radiacyjnych rozpadach mezonów powabnych $D^0 \to V\gamma$, i w rozpadach sprzężonych ładunkowo, gdzie V oznacza mezon wektorowy $\bar{K}^{*0}$, ϕ lub ρ^0. Pomiar jest oparty na danych pochodzących ze zderzeń protonów o energii w środku masy $\sqrt{s} = 8$ TeV, zebranych przez eksperyment LHCb w roku 2012, podczas fazy Run-1 działania LHC. Ta próbka danych odpowiada skumulowanej świetlności wynoszącej 2 fb^{-1}. Rekonstruowane neutralne mezony D pochodzą z silnych rozpadów cząstek $D^{*\pm}$: $D^{*+} \to D^0\pi_s^+$ i $D^{*-} \to \bar{D}^0\pi_s^-$, w których ładunek niskopędowego pionu $\pi_s^\pm$ jest wykorzystywany do oznaczenia zapachu mezonu D podczas jego produkcji. Prezentowana analiza jest pierwszym badaniem radiacyjnych rozpadów powabu w eksperymencie LHCb.

Wysokie i nieredukowalne tło od rozpadów zawierających mezony π^0, $D^0 \to V\pi^0$, jest obniżone przy wykorzystaniu wielowymiarowego klasyfikatora opartego na odmiennych kształtach klastrów energetycznych tworzonych przez fotony i neutralne piony w systemie kalorymetrycznym detektora LHCb. Rozpady sygnałowe są odseparowane od niezredukowanego tła za pomocą trójwymiarowego dopasowania, w którym obserwablami są: masa niezmiennicza mezonu D^0, $M(D^0)$, różnica mas niezmienniczych mezonów D^{*+} i D^0, $\Delta M = M(D^{*+}) - M(D^0)$, oraz kąt helicity mezonu V, $\cos\theta$. Korelacje pomiędzy obserwablami $M(D^0)$ i ΔM, zaobserowane zarówno dla kanałów sygnałowych jak i tła, są modelowane przy użyciu danych z symulacji. Całkowity sygnał zmierzony dla rozpadów D^0 i $\bar{D}^0$ wynosi: 4263 ± 193 przypadków dla rozpadu $D^0 \to \bar{K}^{*0}\gamma$, i 216 ± 29 przypadków dla $D^0 \to \phi\gamma$; nie zaobserwowano znaczącego sygnału dla procesu $D^0 \to \rho\gamma$.

Zaburzające pomiar A_{CP} dodatkowe asymetrie, które pochodzą z asymetrycznej produkcji powabu oraz z różnic w detekcji dodatnio i ujemnie naładowanych hadronów, są oszacowane przy użyciu rozpadów referencyjnych o wysokiej statystyce i czystości. Procesy $D^0 \to K^+K^-$ i $D^0 \to \pi^+\pi^-$ zostały wybrane jako rozpady referencyjne dla $D^0 \to \phi\gamma$ i $D^0 \to \rho^0\gamma$, natomiast $D^0 \to K^-\pi^+\pi^0$ stanowi referencję dla $D^0 \to \bar{K}^{*0}\gamma$. W przypadku procesów referencyjnych, zapach mezonu D jest również oznaczony przez pion $\pi_s^\pm$. Dodatkowe asymetrie wynoszą $(-1.0 \pm 0.2)\%$ dla $D^0 \to K^+K^-$ i $D^0 \to \pi^+\pi^-$, oraz $(-1.7 \pm 0.3)\%$ dla $D^0 \to K^-\pi^+\pi^0$. Asymetrie te są odjęte od asymetrii zmierzonych w rozpadach sygnałowych aby otrzymać A_{CP}.

Asymetrie w rozpadach sygnałowych są mierzone poprzez trójwymiarowe dopasowanie w przestrzeni $M(D^0)$ vs. ΔM vs. $\cos\theta$, przeprowadzone równocześnie dla rozdzielonych próbek D^0 i $\bar{D}^0$. Wartości centralne tych asymetrii nie zostały ujawnione, natomiast ich niepewności statystyczne wynoszą 5% dla $D^0 \to \bar{K}^{*0}\gamma$ i 12% dla $D^0 \to \phi\gamma$; analiza oparta na danych z Run-1 nie jest czuła na asymetrię w rozpadzie $D^0 \to \rho^0\gamma$. Prezentowany pomiar jest zdominowany przez niepewności statystyczne. Całkowite niepewności systematyczne są poniżej 1%, i są zdominowane przez niepewności statystyczne wyżej wspomnianych pomiarów asymetrii w kanałach referencyjnych. Ujawnienie asymetrii zmierzonych dla rozpadów sygnałowych jest planowane równocześnie z ukończeniem trwającej analizy opartej na danych z fazy Run-2.

Acknowledgments

To my PhD supervisor, Jolanta Brodzicka, under whose guidance I participated in this work. To my university professors, especially Adrian Bevan and Marcella Bona, who taught me physics and statistics. To our Head of the Department, Mariusz Witek, who guided that ship through troubled water since 2020 A.D. Last but not the least, to Maciej and Jozef, colleagues on this journey.

This work was supported by the National Science Centre NCN in Poland under the contract no. 2017/26/E/ST2/00934.

Contents

Abstract **3**

Streszczenie **i**

Acknowledgments **iii**

Contents **v**

Preface **3**

Chapter I Introduction **5**

I.1 A brief summary of the Standard Model 5

I.2 Standard Model as an Effective Field Theory 6

I.3 CKM matrix and charm transitions 7

I.3.1 Quark mixing 7

I.3.2 Charm-quark transitions 7

I.3.3 CP-violating phase and unitarity triangles 8

I.4 Basics of CP violation 9

I.4.1 CP violation in decays 9

I.4.2 CP violation related to mixing 9

I.4.3 Conditions for CP-symmetry breaking 11

I.5 Specifics of charm-quark sector 11

I.5.1 Indirect tests of the SM 11

I.5.2 Testing the SM in charm 12

I.5.3 CP violation in charm 12

I.6 Radiative charm decays 14

I.6.1 Quark-level diagrams 14

I.6.2 OPE treatment of charm decays 15

I.6.3 Testing the SM with $D^0 \to V\gamma$ decays 16

I.6.4 Existing measurements 18

Chapter II Experimental environment **19**

II.1 The LHCb experiment at the LHC 19

II.2 Overview of the LHCb detector 19

II.2.1 Vertex Locator (VELO) . . . 21
II.2.2 Tracking detectors and magnet . . . 21
II.2.3 RICH detectors . . . 23
II.2.4 Calorimeter system . . . 24
II.2.5 Muon system . . . 27
II.3 A note on the data flow in the LHCb during Run-1 . . . 27
II.3.1 Level-0 trigger . . . 28
II.3.2 High Level Triggers . . . 28
II.3.3 Stripping . . . 29
II.4 Properties of LHCb charm data . . . 29
II.4.1 Charm production and its asymmetry . . . 29
II.4.2 Detector and detection asymmetries . . . 30
II.4.3 Impact of triggers . . . 31
II.5 Experimental challenges of radiative charm decays . . . 32
II.5.1 Suppressing background from merged π^0 . . . 33
II.5.2 Separating signal and residual π^0 background . . . 34

Chapter III Analysis overview **37**
III.1 Strategy . . . 37
III.2 Data and simulation samples . . . 37
III.2.1 Amplitude models for signal and background decays . . . 38
III.3 Reconstruction and selection of signal decays . . . 40
III.3.1 Stripping preselection . . . 40
III.3.2 Trigger selection . . . 42
III.3.3 Offline selection . . . 43

Chapter IV Simulation studies **49**
IV.1 PID calibration . . . 49
IV.2 Calibration of calorimeter variables . . . 49
IV.3 BDT for γ–π^0 separation . . . 51
IV.4 Optimisation of IsPhoton selection . . . 53
IV.5 Fits to $M(D^0)$, ΔM and $\cos\theta$ observables for K^* channels . . . 57
IV.5.1 Fits for simulated $D^0 \to \bar{K}^{*0}\gamma$ decays . . . 57
IV.5.2 Fits for simulated $D^0 \to \bar{K}^{*0}\pi^0$ background . . . 58
IV.5.3 Fits for simulated $D^0 \to \bar{K}^{*0}\eta$ background . . . 62
IV.6 Describing $M(D^0)$–ΔM correlations in K^* channels . . . 65
IV.6.1 Correlations in $D^0 \to \bar{K}^{*0}\gamma$ signal . . . 65
IV.6.2 Correlations in π^0 background . . . 65
IV.6.3 Correlations in η background . . . 67
IV.7 Validating $M(D^0)$–ΔM correlations in K^* channels . . . 71
IV.7.1 $M(D^0)$–ΔM fit to simulation of $D^0 \to \bar{K}^{*0}\gamma$ signal . . . 71
IV.7.2 $M(D^0)$–ΔM fit to simulation of π^0 background . . . 72

IV.7.3 $M(D^0)$–ΔM fit to simulation of η background . . . 72
IV.8 Fits to $M(D^0)$, ΔM and $\cos\theta$ observables for ϕ channels . . . 77
IV.8.1 Fits for simulated $D^0 \to \phi\gamma$ decays . . . 77
IV.8.2 Fits for simulated $D^0 \to \phi\pi^0$ background . . . 78
IV.8.3 Fits for simulated $D^0 \to \phi\eta$ background . . . 78
IV.9 Describing $M(D^0)$–ΔM correlations in ϕ channels . . . 81
IV.10 Validating $M(D^0)$–ΔM correlations in ϕ channels . . . 86
IV.11 Fits to $M(D^0)$, ΔM and $\cos\theta$ observables for ρ channels . . . 92
IV.11.1 Fits for simulated $D^0 \to \rho^0\gamma$ decays . . . 92
IV.11.2 Fits for simulated $D^0 \to \rho^0\pi^0$ background . . . 93
IV.11.3 Fits for simulated $D^0 \to \rho^0\eta$ background . . . 93
IV.12 Describing $M(D^0)$–ΔM correlations in ρ channels . . . 98
IV.13 Validating $M(D^0)$–ΔM correlations in ρ channels . . . 103

Chapter V Fits to data for combined D^0 and $\bar{D}^0$ **109**
V.1 Best-candidate selection . . . 109
V.2 Two-dimensional $M(D^0)$ vs. $\cos\theta$ fit to $D^0 \to \bar{K}^{*0}\gamma$ sample . . . 110
V.3 Three-dimensional fit to $D^0 \to \bar{K}^{*0}\gamma$ sample . . . 111
V.3.1 Fit to $D^0 \to \bar{K}^{*0}\gamma$ in helicity-edge region . . . 112
V.3.2 Fit to $D^0 \to \bar{K}^{*0}\gamma$ in helicity-center region . . . 118
V.4 Three-dimensional fit to $D^0 \to \phi\gamma$ sample . . . 125
V.4.1 Fit to $D^0 \to \phi\gamma$ in helicity-edge region . . . 125
V.4.2 Fit to $D^0 \to \phi\gamma$ in central helicity region . . . 130
V.5 Three-dimensional fit to $D^0 \to \rho^0\gamma$ sample . . . 136
V.5.1 Fit to $D^0 \to \rho^0\gamma$ in helicity-edge region . . . 136
V.5.2 Fit to $D^0 \to \rho^0\gamma$ in central helicity region . . . 141

Chapter VI Raw asymmetries for signal decays **147**
VI.1 Method for measuring raw asymmetry . . . 147
VI.2 Simultaneous fit to $D^0 \to \bar{K}^{*0}\gamma$ and $\bar{D}^0 \to K^{*0}\gamma$ samples . . . 147
VI.2.1 Fit in helicity-edge region . . . 147
VI.2.2 Fit in helicity-center region . . . 148
VI.3 Simultaneous fit to $D^0 \to \phi\gamma$ and $\bar{D}^0 \to \phi\gamma$ samples . . . 152
VI.3.1 Fit in helicity-edge region . . . 152
VI.3.2 Fit in helicity-center region . . . 152
VI.4 Simultaneous fit to $D^0 \to \rho^0\gamma$ and $\bar{D}^0 \to \rho^0\gamma$ samples . . . 156
VI.4.1 Fit in helicity-edge region . . . 156
VI.4.2 Fit in helicity-center region . . . 156

Chapter VII Analysis of reference channels **161**
VII.1 Method to correct for nuisance asymmetries . . . 161
VII.1.1 Nuisance asymmetries in $D^0 \to \phi\gamma$ and $D^0 \to \rho^0\gamma$ . . . 161
VII.1.2 Nuisance asymmetries in $D^0 \to \bar{K}^{*0}\gamma$ . . . 162

VII.2 Selection of reference channels 162
VII.2.1 Stripping preselection 163
VII.2.2 Trigger selection 163
VII.2.3 Offline selection 163
VII.3 ΔM fits to unweighted reference decays 168
VII.4 Kinematic reweighing of reference decays 171
VII.5 A_{raw} from ΔM fits to reference decays after weighting 176

Chapter VIII Systematic uncertainties **181**

Chapter IX Summary and outlook **183**

Bibliography **185**

List of Figures

I-1 The Standard Model in one picture. Taken from CERN's official website. 5

I-2 Diagrams for charm-quark transitions occurring through (left) tree-level $c \to sW^+$ process, followed by W^+ boson coupling to $u\bar{d}$ pair, and (right) loop-level $c \to u$ process with d, s or b quark entering the loop. This loop process is a QCD penguin, with emitted gluon g coupling to $q\bar{q}$ quark pair. 8

I-3 Charm UT, illustrating the CKM unitarity condition in Eq. **I.7**. Tree-level charm processes are represented by longer triangle sides, while loop-level processes by the shortest side. 9

I-4 A global fit to the beauty UT assuming the SM physics only [7]. The UT defined in Eq. **I.6** with sides rescaled by $|V_{cd}V_{cb}^*|$. It is presented on the plane $(\bar{\rho} + i\bar{\eta}) \simeq (1 - \frac{\lambda^2}{2})(\rho + i\eta)$, with the UT apex located at $(\bar{\rho}, \bar{\eta})$. Coloured bands represent input measurements at 68% confidence level (CL), while tiny red region shows 68% CL contour for the fitted UT apex. 10

I-5 Diagrams for short-distance contributions to $D^0 \to V\gamma$ decays - (left) radiative penguin and (right) tree-level W^+ exchange. To enable hadronization of ϕ, which is mostly an $s\bar{s}$ meson, additional transition $u\bar{u} \to g \to s\bar{s}$ is required. $D^0 \to \bar{K}^{*0}\gamma$ decay does not receive the penguin contribution. 14

I-6 Example of a long-distance process contributing to $D^0 \to V\gamma$ decays at the tree level. 15

II-1 Side view of the LHCb detector in Run-1 and Run-2 data-taking periods, taken from Ref. [45]. The angular coverage of the spectrometer ranges from approximately 10 to 300 mrad in the horizontal direction, and to 250 mrad in the vertical direction. The detector is comprised of the following subsystems, closest to farther from the interaction point: Vertex Locator (VELO), RICH1, Trigger Tracker (TT), Magnet, Tracking Stations (T1-T3), RICH2, Scintillating Pad Detector (SPD) and Preshower Detector (PS), ECAL, HCAL and Muon Stations (M1-M5). 20

II-2 Schematic illustration of various track types reconstructed at the LHCb tracking system [45]. 22

II-3 (Left) Cherenkov angle as a function of momentum for different particle species, and for the three radiators used in RICH1 and RICH2. (Right) Response of the gas radiator in RICH1 to charged particles; the Cherenkov angle is measured with the Run-1 data. Figures are from Ref. [48]. 23

II-4 PID efficiency and mis-identification rate for the discrimination of kaons from pions. PID performance is compared considering two different requirements on $\mathrm{DLL}_{K,\pi}$. Figure is from Ref. [48]. 24

II-5 Scheme for a shower development in the LHCb calorimeter system for different particles. Figure from Ref. [49]. 25

II-6 (Left) Segmentation of the ECAL, as well as SPD/PS detector, and (right) HCAL. Only the top right quadrant is shown. Black squares represent the beam pipe. Figures from Ref. [50]. 26

II-7 A simplified scheme of the data flow from collisions to the offline storage in Run-1. . 27

II-8 Cross-sections of positively and negatively charged pions and kaons interacting with the deuterium target versus their momenta. Figure taken from Ref. [56]. 30

II-9 Asymmetries between detected π_s^+ and π_s^- pions on $p(\pi_s)$ vs. $p_x(\pi_s)$ plane for the Run-1 data collected with the (left) downward and (right) upward magnet-polarity configuration. Soft pions are from reconstructed $D^{*+} \to D^0\pi_s^+$ and $D^{*-} \to \bar{D}^0\pi_s^-$ decays; the related asymmetries are similar regardless of D^0 decay channel. 31

II-10 Distributions of ECAL cluster shape variables (clockwise from top left): $r2$, $r2r4$, $|asym|$, κ, E_{seed}/E_{cl} and $(E_{\text{seed}}+E_{2nd})/E_{cl}$ for photons (blue) and merged π^0 selected as photons (red) in the inner ECAL region. Figure is from Ref. [59]. 34

II-11 Distributions of PS variables (clockwise from top left): $E_{\max}/E_{\text{sum}}$, E_{2nd}/E_{sum}, $r2PS$ and $|asymPS|$, $multi$ and $multi15$ for photons (blue) and merged π^0 reconstructed as photons (red) in the PS inner region. Figure is from Ref. [59]. 35

II-12 (Left) MLP output, IsPhoton, for signal photons (blue) and merged π^0 background (red) samples for the inner calorimeter region. (Right) Efficiencies for signal (red) and background (solid blue) as a function of the MLP output cut. The default cut is selected as IsPhoton> 0.6. Figures are from Ref. [59]. 35

II-13 (Left) Helicity angle θ of the K^+K^- system in $D^0 \to K^+K^-\gamma$ and $D^0 \to K^+K^-\pi^0$ decays. (Right) Expected shapes of the $\cos\theta$ distribution for $D^0 \to \phi\gamma$ (red) and $D^0 \to \phi\pi^0$ (blue) decays, with $\phi \to K^+K^-$. 36

III-1 Effect of vetoing resolved π^0 mesons on (left) $M(D^0)$ and (right) ΔM distributions in simulations of (top) $D^0 \to \bar{K}^{*0}\gamma$ and (bottom) $D^0 \to \bar{K}^{*0}\pi^0$ decays after the full selection except for IsPhoton cut. Distributions before applying π^0 veto are shown in blue, those after π^0 veto in red. 45

III-2 Impact of `DecayTreeFitter` on (left) $M(D^0)$ and (right) ΔM distributions in $D^0 \to \bar{K}^{*0}\gamma$ simulation after the full selection. Distributions before applying DTF are shown in blue, those after applying DTF in red. 46

III-3 Distribution of $\cos\theta$ in $D^0 \to K^-\pi^+\pi^0$ simulation sample passing the $D^0 \to \bar{K}^{*0}\gamma$ signal selection. Edge and central helicity regions are indicated. 47

IV-1 Original (red) and resampled (blue) PID_K responses for (left) kaon-like candidates and (right) pion-like candidates from $D^0 \to \bar{K}^{*0}\gamma$ simulation after the stripping selection. Black line indicates the offline-selection requirement. 50

IV-2 Comparison between cluster-shape variables (clockwise from top left): $r2$ in PS, $E_{\max}/E_{\text{sum}}$ in PS, E_{49} in PS, κ in ECAL and $E_{4\max}$ in PS, for π^0 candidates from $D^0 \to \bar{K}^{*0}\pi^0$ calibration data (blue) and from $D^0 \to \bar{K}^{*0}\pi^0$ simulation (red). The distributions are normalised, and compared before the simulation sample has been matched to the calibration data. 51

IV-3 Comparison between cluster-shape variables (clockwise from top left): $r2$ in PS, $E_{\max}/E_{\text{sum}}$ in PS, E_{49} in PS, κ in ECAL and $E_{4\max}$ in PS, for π^0 candidates from $D^0 \to \bar{K}^{*0}\pi^0$ calibration data (blue) and from $D^0 \to \bar{K}^{*0}\pi^0$ simulation (red). The distributions are normalised and compared after the simulation sample has been matched to the calibration data. 52

IV-4 Comparison between nSPDHits distributions for underlying events in $D^0 \to \bar{K}^{*0}\pi^0$ calibration data (blue) and $D^0 \to \bar{K}^{*0}\pi^0$ simulation (red). On the left normalised distributions are compared before matching the simulation sample to the calibration data, and on the right after the matching. 53

IV-5 Comparison between variables used for training of the MVA classifier for γ–π^0 discrimination. Signal photons (blue) are from calibrated $D^0 \to \bar{K}^{*0}\gamma$ simulation, while background π^0 mesons (red) are from $D^0 \to \bar{K}^{*0}\pi^0$ calibration sample in the helicity-edge region. Discriminating variables are associated with cluster shapes in both sub-detectors, ECAL (top eight plots) and PS (seven bottom plots with x-axis captions starting with *Gamma_PP_CaloPrs*). The variables are defined in the text. 54

IV-6 (Left) ROC curves for various BDT classifiers. (Right) BDT response for γ signal (blue) and π^0 background (red) compared for training and testing samples as indicated in the legend. 55

IV-7 (Left) Normalised distributions of the BDTB response for simulated samples of $D^0 \to \bar{K}^{*0}\gamma$ (orange) and $D^0 \to \bar{K}^{*0}\pi^0$ (blue). (Right) FOM $= \frac{S}{\sqrt{S+B}}$ as a function of BDTB cut, measured for $D^0 \to \bar{K}^{*0}\gamma$ signal and $D^0 \to \bar{K}^{*0}\pi^0$ background, is shown in green. Efficiency dependence on BDTB cut for signal and for π^0 background is shown in blue and red, respectively. 55

IV-8 (Left) Normalised IsPhoton distributions for simulated samples of $D^0 \to \bar{K}^{*0}\gamma$ (green) and $D^0 \to \bar{K}^{*0}\pi^0$ (blue) decays. (Right) FOM $= \frac{S}{\sqrt{S+B}}$ as a function of IsPhoton cut, measured for $D^0 \to \bar{K}^{*0}\gamma$ signal and $D^0 \to \bar{K}^{*0}\pi^0$ background, is shown in green. Efficiency dependence on IsPhoton cut for signal and for π^0 background is shown in red and blue, respectively. Vertical line indicates the optimal selection, IsPhoton> 0.86. 56

IV-9 Distributions of (top left) $M(D^0)$, (top right) ΔM and (bottom) $\cos\theta$ for simulated $D^0 \to \bar{K}^{*0}\gamma$ decays. Results of one-dimensional fits are superimposed. 58

IV-10 Distributions of (top left) $M(D^0)$, (top right) ΔM for simulated $D^0 \to \bar{K}^{*0}\pi^0$ sample passing the full signal selection. Results of one-dimensional fits are superimposed. The threshold asymmetric Gaussian in the $M(D^0)$ fit is constrained to the resolved-π^0 sample in the bottom figure. (Bottom) $M(D^0)$ distribution of the simulated $D^0 \to \bar{K}^{*0}\pi^0$ background involving resolved π^0 with one photon missing. Candidates pass the signal selection with `VetoPi0R` reversed. Result of the fit is superimposed. . . . 59

IV-11 (Top) Efficiency as a function of $\cos\theta$ for $D^0 \to \bar{K}^{*0}\pi^0$ simulation sample in (top left) helicity-edge and (top right) helicity-center regions. (Bottom) Theoretical $\cos\theta$ distribution in (bottom left) helicity-edge and (bottom right) helicity-center regions generated with the BaBar model for the $D^0 \to K^-\pi^+\pi^0$ decay. Results of fits are superimposed. 61

IV-12 Comparison of $\cos\theta$ distributions in (left) helicity-edge and (right) helicity-center regions, generated using the CLEO (blue) and BaBar (red) amplitude model of the $D^0 \to K^-\pi^+\pi^0$ decay. 62

IV-13 Distributions of (left) $M(D^0)$, (right) ΔM for simulated $D^0 \to \bar{K}^{*0}\eta$ background sample passing the full signal selection. Results of one-dimensional fits are superimposed. 63

IV-14 Distributions of $\cos\theta$ for three resonant decays contributing to the simulated η background passing the full signal selection. Contribution from $D^0 \to \bar{K}^{*0}\eta$ decays is plotted in red, from $D^0 \to K^- a_0(980)^+$ in magenta, and from $D^0 \to \bar{K}_0(1430)^0\eta$ in green. 63

IV-15 Distributions of $\cos\theta$ for (top left) $D^0 \to \bar{K}^{*0}\eta$ simulation in the helicity-edge region, (top right) $D^0 \to \bar{K}^{*0}\eta$ simulation in the helicity-center region, (bottom left) $D^0 \to K^- a_0(980)^+$ decays in the helicity-center region and (bottom right) $D^0 \to \bar{K}_0(1430)^0\eta$ decays in the helicity-center region. Fit results are superimposed. 64

IV-16 Results of ΔM fits in $M(D^0)$ bins performed using the $D^0 \to \bar{K}^{*0}\gamma$ simulation sample. Considered $M(D^0)$ regions, as well as fitted λ values are indicated in individual figures. 66

IV-17 Correlation parameter λ for $D^0 \to \bar{K}^{*0}\gamma$ signal, obtained from ΔM fits in $M(D^0)$ bins, plotted against the corresponding $M(D^0)$ range. Result of χ^2 fit using 2^{nd} order polynomial is superimposed, and fit parameters are also given. The lowest- and highest-mass bins are excluded from the fit. 67

IV-18 Results of ΔM fits in $M(D^0)$ bins performed using the $D^0 \to \bar{K}^{*0}\pi^0$ simulation sample. Considered $M(D^0)$ regions, as well as fitted λ values are indicated in individual figures. 68

IV-19 Correlation parameter λ for $D^0 \to \bar{K}^{*0}\pi^0$ background, obtained from ΔM fits in $M(D^0)$ bins, plotted against the corresponding $M(D^0)$ range. Result of χ^2 fit using 2^{nd} order polynomial is superimposed, and fit parameters are also given. Two lowest- and one highest-mass bins are excluded from the fit. 69

IV-20 Results of ΔM fits in $M(D^0)$ bins performed using the simulation sample of $D^0 \to \bar{K}^{*0}\eta$ background. Considered $M(D^0)$ regions, as well as fitted λ values are indicated in individual figures. 69

IV-21 Correlation parameter λ for the $D^0 \to \bar{K}^{*0}\eta$ background, obtained from ΔM fits in $M(D^0)$ bins, plotted against the corresponding $M(D^0)$ range. Result of χ^2 fit using 2^{nd} order polynomial is superimposed, and fit parameters are also given. The highest-mass bin is excluded from the fit. 70

IV-22 Results of two-dimensional $M(D^0)$–ΔM fit performed for $D^0 \to \bar{K}^{*0}\gamma$ simulation. ΔM projections are for $M(D^0)$ regions indicated in individual plots. Red and magenta lines describe G_1 and G_2 signal sub-components, green line is combinatorial background, blue line is total fit function. 71

IV-23 Results of two-dimensional $M(D^0)$–ΔM fit performed for $D^0 \to \bar{K}^{*0}\gamma$ simulation. $M(D^0)$ projections are for ΔM regions indicated in individual plots. Red and magenta lines describe G_1 and G_2 signal sub-components, green line is combinatorial background, blue line is total fit function. 72

IV-24 Results of two-dimensional $M(D^0)$–ΔM fit performed for $D^0 \to \bar{K}^{*0}\pi^0$ simulation. ΔM projections are for $M(D^0)$ regions indicated in individual plots. Red and magenta lines describe G_1 and G_2 π^0 sub-components, brown line is combinatorial background, blue line is total fit function. 73

IV-25 Results of two-dimensional $M(D^0)$–ΔM fit performed for $D^0 \to \bar{K}^{*0}\pi^0$ simulation. $M(D^0)$ projections are for ΔM regions indicated in individual plots. Red and magenta lines describe G_1 and G_2 π^0 sub-components, green line denotes threshold Gaussian, brown line is combinatorial background, blue line is total fit function. . . 74

IV-26 Results of two-dimensional $M(D^0)$–ΔM fit performed for $D^0 \to \bar{K}^{*0}\eta$ simulation. ΔM projections are for $M(D^0)$ regions indicated in individual plots. Red and magenta lines describe G_1 and G_2 η sub-components, green line is combinatorial background, blue line is total fit function. 75

IV-27 Results of two-dimensional $M(D^0)$–ΔM fit performed for $D^0 \to \bar{K}^{*0}\eta$ simulation. $M(D^0)$ projections are for ΔM regions indicated in individual plots. Red line describes η component, green line is combinatorial background, blue line is total fit function. 76

IV-28 Distributions of (top left) $M(D^0)$, (top right) ΔM and (bottom) $\cos\theta$ for simulated $D^0 \to \phi\gamma$ decays. Results of one-dimensional fits are superimposed. 77

IV-29 Distributions of (top left) $M(D^0)$, (top right) ΔM for simulated $D^0 \to \phi\pi^0$ sample and (bottom left) $\cos\theta$ passing the full signal selection. Results of one-dimensional fits are superimposed. The threshold asymmetric Gaussian in the $M(D^0)$ fit is constrained to the resolved-π^0 sample in the bottom right figure. (Bottom right) $M(D^0)$ distribution of the simulated $D^0 \to \phi\pi^0$ background involving resolved π^0 with one photon missing. Candidates pass the signal selection with `VetoPi0R` reversed. Result of the fit is superimposed. 79

IV-30 Distributions of (top left) $M(D^0)$, (top right) ΔM for simulated $D^0 \to \phi\eta$ sample and (bottom) $\cos\theta$ passing the full signal selection. Results of one-dimensional fits are superimposed. 80

IV-31 Results of ΔM fits in $M(D^0)$ bins performed using the $D^0 \to \phi\gamma$ simulation sample. Considered $M(D^0)$ regions, as well as fitted λ values are indicated in individual figures. 81

IV-32 Correlation parameter λ for $D^0 \to \phi\gamma$ signal, obtained from ΔM fits in $M(D^0)$ bins, plotted against the corresponding $M(D^0)$ range. Result of χ^2 fit using 2^{nd} order polynomial is superimposed, and fit parameters are also given. The lowest- and highest-mass bins are excluded from the fit. 82

IV-33 Results of ΔM fits in $M(D^0)$ bins performed using the $D^0 \to \phi\pi^0$ simulation sample. Considered $M(D^0)$ regions, as well as fitted λ values are indicated in individual figures. 83

IV-34 Correlation parameter λ for $D^0 \to \phi\pi^0$ signal, obtained from ΔM fits in $M(D^0)$ bins, plotted against the corresponding $M(D^0)$ range. Result of χ^2 fit using 2^{nd} order polynomial is superimposed, and fit parameters are also given. The lowest- and highest-mass bins are excluded from the fit. 84

IV-35 Results of ΔM fits in $M(D^0)$ bins performed using the $D^0 \to \phi\eta$ simulation sample. Considered $M(D^0)$ regions, as well as fitted λ values are indicated in individual figures. 84

IV-36 Correlation parameter λ for $D^0 \to \phi\eta$ signal, obtained from ΔM fits in $M(D^0)$ bins, plotted against the corresponding $M(D^0)$ bin. Results of χ^2 fit using 2^{nd} order polynomial (blue) and constant (magenta) are superimposed, and fit parameters are also given. The highest-mass bin is excluded from the fit. 85

IV-37 Results of two-dimensional $M(D^0)$–ΔM fit performed for $D^0 \to \phi\gamma$ simulation. ΔM projections are for $M(D^0)$ regions indicated in individual plots. Red and magenta lines describe G_1 and G_2 signal sub-components, green line is combinatorial background, blue line is total fit function. 86

IV-38 Results of two-dimensional $M(D^0)$–ΔM fit performed for $D^0 \to \phi\gamma$ simulation. $M(D^0)$ projections are for ΔM regions indicated in individual plots. Red and magenta lines describe G_1 and G_2 signal sub-components, green line is combinatorial background, blue line is total fit function. 87

IV-39 Results of two-dimensional $M(D^0)$–ΔM fit performed for $D^0 \to \phi\pi^0$ simulation. ΔM projections are for $M(D^0)$ regions indicated in individual plots. Red and magenta lines describe G_1 and G_2 π^0 sub-components, brown line is combinatorial background, blue line is total fit function. 88

IV-40 Results of two-dimensional $M(D^0)$–ΔM fit performed for $D^0 \to \phi\pi^0$ simulation. $M(D^0)$ projections are for ΔM regions indicated in individual plots. Red and magenta lines describe G_1 and G_2 π^0 sub-components, green line denotes threshold Gaussian, brown line is combinatorial background, blue line is total fit function. . . 89

IV-41 Results of two-dimensional $M(D^0)$–ΔM fit performed for $D^0 \to \phi\eta$ simulation. ΔM projections are for $M(D^0)$ regions indicated in individual plots. Red and magenta lines describe G_1 and G_2 sub-components, green line is combinatorial background, blue line is total fit function. 90

IV-42 Results of two-dimensional $M(D^0)$–ΔM fit performed for $D^0 \to \phi\eta$ simulation. $M(D^0)$ projections are for ΔM regions indicated in individual plots. Red line describes η component, green line is combinatorial background, blue line is total fit function. 91

IV-43 Distributions of (top left) $M(D^0)$, (top right) ΔM and (bottom) $\cos\theta$ for simulated $D^0 \to \rho^0\gamma$ decays. Results of one-dimensional fits are superimposed. 92

IV-44 Distributions of (top left) $M(D^0)$, (top right) ΔM for simulated $D^0 \to \rho^0\pi^0$ sample passing the full signal selection. Results of one-dimensional fits are superimposed. The threshold asymmetric Gaussian in the $M(D^0)$ fit is constrained to the resolved-π^0 sample in the bottom figure. (Bottom) $M(D^0)$ distribution of the simulated $D^0 \to \rho^0\pi^0$ background involving resolved π^0 with one photon missing. Candidates pass the signal selection with `VetoPi0R` reversed. Result of the fit is superimposed. 94

IV-45 Distributions of $\cos\theta$ for $D^0 \to \rho^0\pi^0$ simulation sample in (left) helicity-edge and (right) helicity-center regions. Results of fits are superimposed. 95

IV-46 Distributions of (left) $M(D^0)$, (right) ΔM for simulated $D^0 \to \rho^0\eta$ background sample passing the full signal selection. Results of one-dimensional fits are superimposed. 95

IV-47 Distributions of $\cos\theta$ for three decays contributing to the simulated η background passing the full signal selection. Contributions from $D^0 \to \rho^0\eta$ decays are plotted in red, from $D^0 \to a_0(980)^+\pi^-$ in green, and from non-resonant $D^0 \to \pi^+\pi^-\eta$ in magenta. 96

IV-48 Distributions of $\cos\theta$ in the helicity-edge region for (left) $D^0 \to \rho^0\eta$ decays, (middle) $D^0 \to \pi^+\pi^-\eta$ decays, (right) $D^0 \to a_0(980)^+\pi^-$ decays. Fit results are superimposed. 96

IV-49 Distributions of $\cos\theta$ in the helicity-center region for (left) $D^0 \to \rho^0\eta$ decays, (middle) $D^0 \to \pi^+\pi^-\eta$ decays, (right) $D^0 \to a_0(980)^+\pi^-$ decays. Fit results are superimposed. Parameters quoted in the right figure are exponents d_1 and d_2 of two exponential functions, and fraction f of the first function. 97

IV-50 Results of ΔM fits in $M(D^0)$ bins performed using the $D^0 \to \rho^0\gamma$ simulation sample. Considered $M(D^0)$ regions, as well as fitted λ values are indicated in individual figures. 98

IV-51 Correlation parameter λ for $D^0 \to \rho^0\gamma$ signal, obtained from ΔM fits in $M(D^0)$ bins, plotted against the corresponding $M(D^0)$ range. Result of χ^2 fit using 2^{nd} order polynomial is superimposed, and fit parameters are also given. The lowest- and highest-mass bins are excluded from the fit. 99

IV-52 Results of ΔM fits in $M(D^0)$ bins performed using the $D^0 \to \rho^0\pi^0$ simulation sample. Considered $M(D^0)$ regions, as well as fitted λ values are indicated in individual figures. 100

IV-53 Correlation parameter λ for $D^0 \to \rho^0\pi^0$ signal, obtained from ΔM fits in $M(D^0)$ bins, plotted against the corresponding $M(D^0)$ range. Result of χ^2 fit using 2^{nd} order polynomial is superimposed, and fit parameters are also given. The lowest- and highest-mass bins are excluded from the fit. 101

IV-54 Results of ΔM fits in $M(D^0)$ bins performed using the $D^0 \to \rho^0\eta$ simulation sample. Considered $M(D^0)$ regions, as well as fitted λ values are indicated in individual figures. 101

IV-55 Correlation parameter λ for $D^0 \to \rho^0\eta$ signal, obtained from ΔM fits in $M(D^0)$ bins, plotted against the corresponding $M(D^0)$ range. Result of χ^2 fit using 2^{nd} order polynomial is superimposed, and fit parameters are also given. The highest-mass bin is excluded from the fit. 102

IV-56 Results of two-dimensional $M(D^0)$–ΔM fit performed for $D^0 \to \rho^0\gamma$ simulation. ΔM projections are for $M(D^0)$ regions indicated in individual plots. Red and magenta lines describe G_1 and G_2 signal sub-components, green line is combinatorial background, blue line is total fit function. 103

IV-57 Results of two-dimensional $M(D^0)$–ΔM fit performed for $D^0 \to \rho^0\gamma$ simulation. $M(D^0)$ projections are for ΔM regions indicated in individual plots. Red and magenta lines describe G_1 and G_2 signal sub-components, green line is combinatorial background, blue line is total fit function. 104

IV-58 Results of two-dimensional $M(D^0)$–ΔM fit performed for $D^0 \to \rho^0\pi^0$ simulation. ΔM projections are for $M(D^0)$ regions indicated in individual plots. Red and magenta lines describe G_1 and G_2 π^0 sub-components, brown line is combinatorial background, blue line is total fit function. 105

IV-59 Results of two-dimensional $M(D^0)$–ΔM fit performed for $D^0 \to \rho^0\pi^0$ simulation. $M(D^0)$ projections are for ΔM regions indicated in individual plots. Red and magenta lines describe G_1 and G_2 π^0 sub-components, green line denotes threshold Gaussian, brown line is combinatorial background, blue line is total fit function. . . 106

IV-60 Results of two-dimensional $M(D^0)$–ΔM fit performed for $D^0 \to \rho^0\eta$ simulation. ΔM projections are for $M(D^0)$ regions indicated in individual plots. Red and magenta lines describe G_1 and G_2 η sub-components, green line is combinatorial background, blue line is total fit function. 107

IV-61 Results of two-dimensional $M(D^0)$–ΔM fit performed for $D^0 \to \rho^0\eta$ simulation. $M(D^0)$ projections are for ΔM regions indicated in individual plots. Red line describes η component, green line is combinatorial background, blue line is total fit function. 108

V-1 (Left) Multiplicity of D^{*+} signal candidates in the $D^0 \to \bar{K}^{*0}\gamma$ channel reconstructed in the Run-1 data in the full $\cos\theta$ range. (Right) Comparison of DTF χ^2 for multiple D^{*+} candidates before (blue) and after (red) best-candidate selection. 109

V-2 (Left) $M(D^0)$ and (right) $\cos\theta$ projections of two-dimensional $M(D^0)$ vs. $\cos\theta$ fit to $D^0 \to \bar{K}^{*0}\gamma$ candidates reconstructed in the Run-1 data in the helicity edge. The $\cos\theta$ projection is for $1805 < M(D^0) < 1924$ MeV/c^2. No selection on IsPhoton or γ–π^0 BDT classifier is applied. Fit components are indicated in the legend. 110

V-3 (Left) $M(D^0)$ and (right) $\cos\theta$ projections of two-dimensional $M(D^0)$ vs. $\cos\theta$ fit to $D^0 \to \bar{K}^{*0}\gamma$ candidates reconstructed in the Run-1 data in the helicity center. The $\cos\theta$ projection is for $1805 < M(D^0) < 1924$ MeV/c^2. No selection on IsPhoton or γ–π^0 BDT classifier is applied. Fit components are indicated in the legend. 111

V-4 (Top left) $M(D^0)$, (top right) $\cos\theta$ and (bottom) ΔM projections of three-dimensional fit to $D^0 \to \bar{K}^{*0}\gamma$ candidates, with IsPhoton> 0.86, reconstructed in the Run-1 data in the helicity-edge region $-0.97 < \cos\theta < -0.7$. These projections are in the full fit region. Fit components are indicated in the legend. 114

V-5 $M(D^0)$ projections of three-dimensional fit to $D^0 \to \bar{K}^{*0}\gamma$ candidates in the Run-1 data in the helicity edge. $M(D^0)$ projections are for ΔM regions indicated in individual plots. Fit components are indicated with the same colours as in Fig. **V-4**. 115

V-6 ΔM projections of three-dimensional fit to $D^0 \to \bar{K}^{*0}\gamma$ candidates in the Run-1 data in the helicity edge. ΔM projections are for $M(D^0)$ regions indicated in individual plots. Fit components are indicated with the same colours as in Fig. **V-4**. 116

V-7 $\cos\theta$ projections of three-dimensional fit to $D^0 \to \bar{K}^{*0}\gamma$ candidates in the Run-1 data in the helicity edge. Projections of $\cos\theta$ are for $M(D^0)$ regions indicated in individual plots, and in the full ΔM region. Fit components are indicated with the same colours as in Fig. **V-4**. 117

V-8 (Top left) $M(D^0)$, (top right) $\cos\theta$ and (bottom) ΔM projections of three-dimensional fit to $D^0 \to \bar{K}^{*0}\gamma$ candidates, with IsPhoton> 0.86, reconstructed in the Run-1 data in the helicity center $-0.4 < \cos\theta < 0.7$. These projections are in the signal-enhanced region. Fit components are indicated in the legend. 120

V-9 $M(D^0)$ projections of three-dimensional fit to $D^0 \to \bar{K}^{*0}\gamma$ candidates in the Run-1 data in the helicity center. $M(D^0)$ projections are for ΔM regions indicated in individual plots. Fit components are indicated with the same colours as in Fig. **V-8**. 121

V-10 ΔM projections of three-dimensional fit to $D^0 \to \bar{K}^{*0}\gamma$ candidates in the Run-1 data in the helicity center. ΔM projections are for $M(D^0)$ regions indicated in individual plots. Fit components are indicated with the same colours as in Fig. **V-8**. 122

V-11 $\cos\theta$ projections of three-dimensional fit to $D^0 \to \bar{K}^{*0}\gamma$ candidates in the Run-1 data in the helicity center. Projections of $\cos\theta$ are for $M(D^0)$ regions indicated in individual plots, and in the ΔM signal region. Fit components are indicated with the same colours as in Fig. **V-8**. 123

V-12 $M(D^0)$ projections of three-dimensional fit to $D^0 \to \bar{K}^{*0}\gamma$ candidates in the Run-1 data in the helicity center. $M(D^0)$ projections are for $\cos\theta$ regions indicated in individual plots, and in the ΔM signal region. Fit components are indicated with the same colours as in Fig. **V-8**. 124

V-13 (Top left) $M(D^0)$, (top right) $\cos\theta$ and (bottom) ΔM projections of three-dimensional fit to $D^0 \to \phi\gamma$ candidates, with IsPhoton> 0.85, reconstructed in the Run-1 data in the helicity-edge region $|\cos\theta| > 0.8$. These projections are in the full fit region. Fit components are indicated in the legend. 126

V-14 $M(D^0)$ projections of three-dimensional fit to $D^0 \to \phi\gamma$ candidates in the Run-1 data in the helicity edge. $M(D^0)$ projections are for ΔM regions indicated in individual plots. Fit components are indicated with the same colours as in Fig. **V-13**. 127

V-15 ΔM projections of three-dimensional fit to $D^0 \to \phi\gamma$ candidates in the Run-1 data in the helicity edge. ΔM projections are for $M(D^0)$ regions indicated in individual plots. Fit components are indicated with the same colours as in Fig. **V-13**. 128

V-16 $\cos\theta$ projections of three-dimensional fit to $D^0 \to \phi\gamma$ candidates in the Run-1 data in the helicity edge. Projections of $\cos\theta$ are for $M(D^0)$ regions indicated in individual plots, and in the full ΔM region. Fit components are indicated with the same colours as in Fig. **V-13**. 129

V-17 (Top left) $M(D^0)$, (top right) $\cos\theta$ and (bottom) ΔM projections of three-dimensional fit to $D^0 \to \phi\gamma$ candidates, with IsPhoton> 0.85, reconstructed in the Run-1 data in the helicity center $|\cos\theta| < 0.8$. These projections are in the signal-enhanced region. Fit components are indicated in the legend. 131

V-18 $M(D^0)$ projections of three-dimensional fit to $D^0 \to \phi\gamma$ candidates in the Run-1 data in the helicity center. $M(D^0)$ projections are for ΔM regions indicated in individual plots. Fit components are indicated with the same colours as in Fig. **V-17**. 132

V-19 ΔM projections of three-dimensional fit to $D^0 \to \phi\gamma$ candidates in the Run-1 data in the helicity center. ΔM projections are for $M(D^0)$ regions indicated in individual plots. Fit components are indicated with the same colours as in Fig. **V-17**. 133

V-20 $\cos\theta$ projections of three-dimensional fit to $D^0 \to \phi\gamma$ candidates in the Run-1 data in the helicity center. Projections of $\cos\theta$ are for $M(D^0)$ regions indicated in individual plots, and in the ΔM signal region. Fit components are indicated with the same colours as in Fig. **V-17**. 134

V-21 $M(D^0)$ projections of three-dimensional fit to $D^0 \to \phi\gamma$ candidates in the Run-1 data in the helicity center. $M(D^0)$ projections are for $\cos\theta$ regions indicated in individual plots, and in the ΔM signal region. Fit components are indicated with the same colours as in Fig. **V-17**. 135

V-22 (Top left) $M(D^0)$, (top right) $\cos\theta$ and (bottom) ΔM projections of three-dimensional fit to $D^0 \to \rho^0\gamma$ candidates, with IsPhoton> 0.95, reconstructed in the Run-1 data in the helicity-edge region, $\cos\theta > 0.7$. These projections are in the full fit region. Fit components are indicated in the legend. 137

V-23 $M(D^0)$ projections of three-dimensional fit to $D^0 \to \rho^0\gamma$ candidates in the Run-1 data in the helicity edge. $M(D^0)$ projections are for ΔM regions indicated in individual plots. Fit components are indicated with the same colours as in Fig. **V-13**. 138

V-24 ΔM projections of three-dimensional fit to $D^0 \to \rho^0\gamma$ candidates in the Run-1 data in the helicity edge. ΔM projections are for $M(D^0)$ regions indicated in individual plots. Fit components are indicated with the same colours as in Fig. **V-22**. 139

V-25 $\cos\theta$ projections of three-dimensional fit to $D^0 \to \rho^0\gamma$ candidates in the Run-1 data in the helicity edge. Projections of $\cos\theta$ are for $M(D^0)$ regions indicated in individual plots, and in the full ΔM region. Fit components are indicated with the same colours as in Fig. **V-22**. 140

V-26 (Top left) $M(D^0)$, (top right) $\cos\theta$ and (bottom) ΔM projections of three-dimensional fit to $D^0 \to \rho^0\gamma$ candidates, with IsPhoton> 0.95, reconstructed in the Run-1 data in the helicity center $-0.6 < \cos\theta < 0.5$. These projections are in the signal-enhanced region. Fit components are indicated in the legend. 142

V-27 $M(D^0)$ projections of three-dimensional fit to $D^0 \to \rho^0\gamma$ candidates in the Run-1 data in the helicity center. $M(D^0)$ projections are for ΔM regions indicated in individual plots. Fit components are indicated with the same colours as in Fig. **V-26**. 143

V-28 ΔM projections of three-dimensional fit to $D^0 \to \rho^0\gamma$ candidates in the Run-1 data in the helicity center. ΔM projections are for $M(D^0)$ regions indicated in individual plots. Fit components are indicated with the same colours as in Fig. **V-26**. 144

V-29 $\cos\theta$ projections of three-dimensional fit to $D^0 \to \rho^0\gamma$ candidates in the Run-1 data in the helicity center. Projections of $\cos\theta$ are for $M(D^0)$ regions indicated in individual plots, and in the ΔM signal region. Fit components are indicated with the same colours as in Fig. **V-26**. 145

V-30 $M(D^0)$ projections of three-dimensional fit to $D^0 \to \rho^0\gamma$ candidates in the Run-1 data in the helicity center. $M(D^0)$ projections are for $\cos\theta$ regions indicated in individual plots, and in the ΔM signal region. Fit components are indicated with the same colours as in Fig. **V-26**. 145

VI-1 (Top) $M(D^0)$, (middle) $\cos\theta$ and (bottom) ΔM projections of three-dimensional fit performed simultaneously to (left) $D^0 \to \bar{K}^{*0}\gamma$ and (right) $\bar{D}^0 \to K^{*0}\gamma$ candidates reconstructed in the Run-1 data in the helicity-edge region. These projections are in the full fit region. Fit components are indicated in the legend. 150

VI-2 (Top) $M(D^0)$ and (bottom) ΔM projections of three-dimensional fit performed simultaneously to (left) $D^0 \to \bar{K}^{*0}\gamma$ and (right) $\bar{D}^0 \to K^{*0}\gamma$ candidates reconstructed in the Run-1 data in the helicity-center region. These projections are in the signal-enhanced region, and the signal region is currently blinded. Fit components are indicated in the legend. 151

VI-3 (Top) $M(D^0)$, (middle) $\cos\theta$ and (bottom) ΔM projections of three-dimensional fit performed simultaneously to (left) $D^0 \to \phi\gamma$ and (right) $\bar{D}^0 \to \phi\gamma$ candidates reconstructed in the Run-1 data in the helicity-edge region. These projections are in the full fit region. Fit components are indicated in the legend. 154

VI-4 (Top) $M(D^0)$ and (bottom) ΔM projections of three-dimensional fit performed simultaneously to (left) $D^0 \to \phi\gamma$ and (right) $\bar{D}^0 \to \phi\gamma$ candidates reconstructed in the Run-1 data in the helicity-center region. These projections are in the signal-enhanced region, and the signal region is currently blinded. Fit components are indicated with the same colours as in Fig. **VI-3**. 155

VI-5 (Top) $M(D^0)$, (middle) $\cos\theta$ and (bottom) ΔM projections of three-dimensional fit performed simultaneously to (left) $D^0 \to \rho^0\gamma$ and (right) $\bar{D}^0 \to \rho^0\gamma$ candidates reconstructed in the Run-1 data in the helicity-edge region. These projections are in the full fit region. Fit components are indicated in the legend. 158

VI-6 Top) $M(D^0)$, (middle) $\cos\theta$ and (bottom) ΔM projections of three-dimensional fit performed simultaneously to (left) $D^0 \to \rho^0\gamma$ and (right) $\bar{D}^0 \to \rho^0\gamma$ candidates reconstructed in the Run-1 data in the helicity-center region. These projections are in the signal-enhanced region, and, since no significant signal is observed, the signal region is unblinded. Fit components are indicated in the legend. 159

VII-1 ΔM distribution for (left) π_s^+-tagged $D^0 \to K^+K^-$ and (right) π_s^--tagged $\bar{D}^0 \to K^-K^+$ candidates in the Run-1 data before kinematic reweighing. Results of the simultaneous fit are superimposed; black line shows the total fit, dashed magenta line shows combinatorial background. 168

VII-2 ΔM distribution for (left) π_s^+-tagged $D^0 \to \pi^+\pi^-$ and (right) π_s^--tagged $\bar{D}^0 \to \pi^-\pi^+$ candidates in the Run-1 data before kinematic reweighing. Results of the simultaneous fit are superimposed; black line shows the total fit, dashed magenta line shows combinatorial background. 169

VII-3 ΔM distribution for (left) π_s^+-tagged $D^0 \to K^-\pi^+\pi^0$ and (right) π_s^--tagged $\bar{D}^0 \to K^+\pi^-\pi^0$ candidates in the Run-1 data before kinematic reweighing. Results of the simultaneous fit are superimposed; black line shows the total fit, grey dashed lines show two broader Gaussian contributions to the signal, dashed magenta line shows combinatorial background. 170

VII-4 Initial distributions of kinematic variables used in training of the BDT classifier. Green histograms show $D^0 \to K^+K^-$ reference data, while blue histograms show $D^0 \to \phi\gamma$ simulation. The variables are: (top left) $p_T(D^{*+})$, (top right) $p_T(\pi_s^+)$, (bottom left) $\eta(D^{*+})$, (bottom right) $\eta(\pi_s^+)$. 172

VII-5 Weighted distributions of kinematic variables used in training of the BDT classifier. Green histograms show $D^0 \to K^+K^-$ reference data, while blue histograms show $D^0 \to \phi\gamma$ simulation. The variables are: (top left) $p_T(D^{*+})$, (top right) $p_T(\pi_s^+)$, (bottom left) $\eta(D^{*+})$, (bottom right) $\eta(\pi_s^+)$. 172

VII-6 Initial distributions of kinematic variables used in training of the BDT classifier. Green histograms show $D^0 \to K^-\pi^+\pi^0$ reference data, while blue histograms show $D^0 \to \bar{K}^{*0}\gamma$ simulation. The variables are: (top left) $p_T(D^{*+})$, (top middle) $\eta(D^{*+})$, (top right) $p_T(\pi_s^+)$, (bottom left) $p_T(K^-)$, (bottom middle) $p_T(\pi^+)$. 173

VII-7 Weighted distributions of kinematic variables used in training of the BDT classifier. Green histograms show $D^0 \to K^-\pi^+\pi^0$ reference data, while blue histograms show $D^0 \to \bar{K}^{*0}\gamma$ simulation. The variables are: (top left) $p_T(D^{*+})$, (top middle) $\eta(D^{*+})$, (top right) $p_T(\pi_s^+)$, (bottom left) $p_T(K^-)$, (bottom middle) $p_T(\pi^+)$. 173

VII-8 Distributions of control variables before multivariate regression. Green histograms show $D^0 \to K^+K^-$ reference data, while blue histograms show $D^0 \to \phi\gamma$ simulation. The variables are: (top left) $\eta(K^+)$, (top right) ΔM, (middle left) $\eta(D^{*+})$, (middle right) $\ln\chi^2_{IP}(D^0)$, (bottom left) $p_T(K^-)$, (bottom right) $p_T(K^+)$. 174

VII-9 Distributions of control variables after multivariate regression. Green histograms show $D^0 \to K^+K^-$ reference data, while blue histograms show $D^0 \to \phi\gamma$ simulation. The variables are: (top left) $\eta(K^+)$, (top right) ΔM, (middle left) $\eta(D^{*+})$, (middle right) $\ln\chi^2_{IP}(D^0)$, (bottom left) $p_T(K^-)$, (bottom right) $p_T(K^+)$. 174

VII-10 Distributions of control variables before multivariate regression. Green histograms show $D^0 \to K^-\pi^+\pi^0$ reference data, while blue histograms show $D^0 \to \bar{K}^{*0}\gamma$ simulation. The variables are: (top left) $\eta(K^-)$, (top middle) $\eta(\pi^+)$, (top right) $p_T(\pi^0)$, (bottom left) $\ln\chi^2_{IP}(D^0)$, (bottom middle) ΔM. 175

VII-11 Distributions of control variables after multivariate regression. Green histograms show $D^0 \to K^-\pi^+\pi^0$ reference data, while blue histograms show $D^0 \to \bar{K}^{*0}\gamma$ simulation. The variables are: (top left) $\eta(K^-)$, (top middle) $\eta(\pi^+)$, (top right) $p_T(\pi^0)$, (bottom left) $\ln\chi^2_{IP}(D^0)$, (bottom middle) ΔM. 175

VII-12 ΔM distribution for (left) π_s^+-tagged $D^0 \to K^+K^-$ and (right) π_s^--tagged $\bar{D}^0 \to K^-K^+$ candidates in the Run-1 data after kinematic reweighing. Results of the simultaneous fit are superimposed; black line shows the total fit, grey dashed lines show two broader Gaussian contributions to the signal, dashed magenta line shows combinatorial background. 177

VII-13 ΔM distribution for (left) π_s^+-tagged $D^0 \to \pi^+\pi^-$ and (right) π_s^--tagged $\bar{D}^0 \to \pi^-\pi^+$ candidates in the Run-1 data after kinematic reweighing. Results of the simultaneous fit are superimposed; black line shows the total fit, grey dashed lines show two broader Gaussian contributions to the signal, dashed magenta line shows combinatorial background. 178

VII-14 ΔM distribution for (left) π_s^+-tagged $D^0 \to K^-\pi^+\pi^0$ and (right) π_s^--tagged $\bar{D}^0 \to K^+\pi^-\pi^0$ candidates in the Run-1 data after kinematic reweighing. Results of the simultaneous fit are superimposed; black line shows the total fit, grey dashed lines show two broader Gaussian contributions to the signal, dashed magenta line shows combinatorial background. 179

List of Tables

I-1 Current HFLAV averages of A_{CP} measurements for selected charm-meson decays [21]. Experiments with the most precise results contributing into given average, are also mentioned, along with a year of corresponding measurement. 13

I-2 Measurements performed for radiative decays of charm mesons by Belle [40] and BaBar [39]. 18

III-1 Summary of the D^0 decay models used in simulations. Numbers in brackets correspond to fractions of total rate measured or assumed for given resonant or non-resonant (NR) component. 39

III-2 Stripping lines used for signal channels. 40

III-3 Stripping selection for signal channels. DOCA stands for distance of closest approach (Section **II.2**). 41

III-4 Selection for `Hlt1TrackAllL0` line. 42

III-5 Selection requirements in inclusive D^* line `Hlt2CharmHadD02HHXDsthhX`. Requirements on $p_T(D^{*+})$ and ΔM varied during the data taking within the ranges quoted. 43

III-6 Offline selection applied to signal candidates. Requirements on $M(D^0)$ and ΔM are applied to the variables after employing DTF to the full decay chain. The lower ΔM range corresponds to the nominal π^+ mass. 44

III-7 Selection on $\cos\theta$ in signal-enhanced (*central*) region, and π^0 enhanced (*edge*) region. 46

IV-1 Parameter values obtained from one-dimensional fits to $M(D^0)$ and ΔM observables in $D^0 \to \bar{K}^{*0}\gamma$ simulation sample. 58

IV-2 Parameter values obtained from one-dimensional fits to $M(D^0)$ and ΔM observables in $D^0 \to \bar{K}^{*0}\pi^0$ simulation sample passing the full signal selection. Means of Gaussian functions, μ_1 and μ_3, peak offset δ, and Gaussian widths σ_1, σ_L and σ_R, are given in MeV/c^2. 60

IV-3 Parameter values obtained from one-dimensional fits to $M(D^0)$ and ΔM observables in $D^0 \to \bar{K}^{*0}\eta$ simulation sample. Means and widths of Gaussian and CB functions are given in MeV/c^2. 63

IV-4 Parameter values obtained from two-dimensional $M(D^0)$–ΔM fit with correlations for $D^0 \to \bar{K}^{*0}\gamma$ simulation. Parameters given without uncertainties are fixed to those from one-dimensional $M(D^0)$ and ΔM fits in Table **IV-1**. 72

IV-5 Parameter values obtained from two-dimensional $M(D^0)$–ΔM fit with correlations for $D^0 \to \bar{K}^{*0}\pi^0$ simulation. Parameters given without uncertainties are fixed to those from one-dimensional $M(D^0)$ and ΔM fits in Table **IV-2**. Means of Gaussian functions, μ_1 and μ_3, peak offset δ, and Gaussian widths σ_1, σ_L and σ_R, are given in MeV/c^2. 73

IV-6 Parameter values obtained from two-dimensional $M(D^0)$–ΔM fit with correlations for $D^0 \to \bar{K}^{*0}\eta$ simulation. Parameters given without uncertainties are fixed to those from one-dimensional $M(D^0)$ and ΔM fits in Table **IV-3**. Means and widths of Gaussian and CB functions are given in MeV/c^2. 73

IV-7 Parameter values obtained from one-dimensional fits to $M(D^0)$ and ΔM observables in $D^0 \to \phi\gamma$ simulation sample. 78

IV-8 Parameter values obtained from one-dimensional fits to $M(D^0)$ and ΔM observables in $D^0 \to \phi\pi^0$ simulation sample passing the full signal selection. Means of Gaussian functions, μ_1 and μ_3, peak offset δ, and Gaussian widths σ_1, σ_L and σ_R, are given in MeV/c^2. 78

IV-9 Parameter values obtained from one-dimensional fits to $M(D^0)$ and ΔM observables in $D^0 \to \phi\eta$ simulation sample. Means and widths of Gaussian and CB functions are given in MeV/c^2. 78

IV-10 Parameter values obtained from two-dimensional $M(D^0)$–ΔM fit with correlations for the $D^0 \to \phi\gamma$ simulation sample. Parameters given without uncertainties are fixed to those from one-dimensional $M(D^0)$ and ΔM fits in Table **IV-7**. 87

IV-11 Parameter values obtained from two-dimensional $M(D^0)$–ΔM fit with correlations for the $D^0 \to \phi\pi^0$ background sample. Parameters given without uncertainties are fixed to those from one-dimensional $M(D^0)$ and ΔM fits in Table **IV-8**. Means of Gaussian functions, μ_1 and μ_3, peak offset δ, and Gaussian widths σ_1, σ_L and σ_R, are given in MeV/c^2. 87

IV-12 Parameter values obtained from two-dimensional $M(D^0)$–ΔM fit with correlations for the $D^0 \to \phi\eta$ background sample. Parameters given without uncertainties are fixed to those from one-dimensional $M(D^0)$ and ΔM fits in Table **IV-9**. Means and widths of Gaussian and CB functions are given in MeV/c^2. 88

IV-13 Parameter values obtained from one-dimensional fits to $M(D^0)$ and ΔM observables in $D^0 \to \rho^0\gamma$ simulation sample. 93

IV-14 Parameter values obtained from one-dimensional fits to $M(D^0)$ and ΔM observables in $D^0 \to \rho^0\pi^0$ simulation sample passing the full signal selection. Means of Gaussian functions, μ_1 and μ_3, peak offset δ, and Gaussian widths σ_1, σ_L and σ_R, are given in MeV/c^2. 93

IV-15 Parameter values obtained from one-dimensional fits to $M(D^0)$ and ΔM observables in $D^0 \to \rho^0\eta$ simulation sample. Means and widths of Gaussian and CB functions are given in MeV/c^2. 94

IV-16 Parameter values obtained from two-dimensional $M(D^0)$–ΔM fit with correlations for the $D^0 \to \rho^0\gamma$ simulation sample. Parameters given without uncertainties are fixed to those from one-dimensional $M(D^0)$ and ΔM fits in Table **IV-13**. 104

IV-17 Parameter values obtained from two-dimensional $M(D^0)$–ΔM fit with correlations for the $D^0 \to \rho^0\pi^0$ background sample. Parameters given without uncertainties are fixed to those from one-dimensional $M(D^0)$ and ΔM fits in Table **IV-14**. Means of Gaussian functions, μ_1 and μ_3, peak offset δ, and Gaussian widths σ_1, σ_L and σ_R, are given in MeV/c^2. 104

IV-18 Parameter values obtained from two-dimensional $M(D^0)$–ΔM fit with correlations for the $D^0 \to \rho^0\eta$ background sample. Parameters given without uncertainties are fixed to those from one-dimensional $M(D^0)$ and ΔM fits in Table **IV-15**. Means and widths of Gaussian and CB functions are given in MeV/c^2. 105

V-1 Parameter values measured for given component in three-dimensional fit to the combined $D^0 \to \bar{K}^{*0}\gamma$ and $\bar{D}^0 \to K^{*0}\gamma$ candidates from the helicity edge in the Run-1 data. Offsets off^M and off$^{\Delta M}$, and width σ_L are given in MeV/c^2. K_0^0 stands for the $K_0(1430)^0$ meson. 113

V-2 Parameter values measured for given component in three-dimensional fit to the combined $D^0 \to \bar{K}^{*0}\gamma$ and $\bar{D}^0 \to K^{*0}\gamma$ candidates from the helicity center in the Run-1 data. Offsets off^M and off$^{\Delta M}$, and width σ_L are given in MeV/c^2. K_0^0 stands for the $K_0(1430)^0$ meson; a_0^+ stands for the $a_0(980)^+$ meson. 119

V-3 Parameter values measured for given component in three-dimensional fit to the combined $D^0 \to \phi\gamma$ and $\bar{D}^0 \to \phi\gamma$ candidates from the helicity edge in the Run-1 data. Offsets off^M and off$^{\Delta M}$, and width σ_L are given in MeV/c^2. 125

V-4 Parameter values measured for combinatorial component in three-dimensional fit to the combined $D^0 \to \phi\gamma$ and $\bar{D}^0 \to \phi\gamma$ candidates from the helicity edge in the Run-1 data. 125

V-5 Parameter values measured for given component in three-dimensional fit to the combined $D^0 \to \phi\gamma$ and $\bar{D}^0 \to \phi\gamma$ candidates from the helicity center in the Run-1 data. Offsets off^M and off$^{\Delta M}$, and width σ_L are given in MeV/c^2. 130

V-6 Parameter values measured for combinatorial component in three-dimensional fit to the combined $D^0 \to \phi\gamma$ and $\bar{D}^0 \to \phi\gamma$ candidates from the helicity center in the Run-1 data. 131

V-7 Parameter values measured for given component in three-dimensional fit to the combined $D^0 \to \rho^0\gamma$ and $\bar{D}^0 \to \rho^0\gamma$ candidates from the helicity edge in the Run-1 data. Offsets off^M and off$^{\Delta M}$, and width σ_L are given in MeV/c^2. 136

V-8 Parameter values measured for combinatorial component in three-dimensional fit to the combined $D^0 \to \rho^0\gamma$ and $\bar{D}^0 \to \rho^0\gamma$ candidates from the helicity edge in the Run-1 data. 136

V-9 Parameter values measured for given component in three-dimensional fit to the combined $D^0 \to \rho^0\gamma$ and $\bar{D}^0 \to \rho^0\gamma$ candidates from the helicity center in the Run-1 data. Offsets off^M and off$^{\Delta M}$, and width σ_L are given in MeV/c^2. 141

V-10 Parameter values measured for combinatorial component in three-dimensional fit to the combined $D^0 \to \rho^0\gamma$ and $\bar{D}^0 \to \rho^0\gamma$ candidates from the helicity center in the Run-1 data. 141

VI-1 Raw asymmetry and total D^0 and $\bar{D}^0$ yield measured for given component in three-dimensional fit performed simultaneously to $D^0 \to \bar{K}^{*0}\gamma$ and $\bar{D}^0 \to K^{*0}\gamma$ candidates from the helicity edge in the Run-1 data. A_{raw} for the signal is fixed to injected value. 148

VI-2 Raw asymmetry and total D^0 and $\bar{D}^0$ yield measured for given component in three-dimensional fit performed simultaneously to $D^0 \to \bar{K}^{*0}\gamma$ and $\bar{D}^0 \to K^{*0}\gamma$ candidates from the helicity center in the Run-1 data. Central value of A_{raw} for the signal is currently blinded. 149

VI-3 Raw asymmetry and D^0 yield measured for given component in three-dimensional fit performed simultaneously to $D^0 \to \phi\gamma$ and $\bar{D}^0 \to \phi\gamma$ candidates from the helicity edge in the Run-1 data. 152

VI-4 Raw asymmetry and D^0 yield measured for given component in three-dimensional fit performed simultaneously to $D^0 \to \phi\gamma$ and $\bar{D}^0 \to \phi\gamma$ candidates from the helicity center in the Run-1 data. Central value of A_{raw} for the signal is currently blinded. . 153

VI-5 Raw asymmetry and D^0 yield measured for given component in three-dimensional fit performed simultaneously to $D^0 \to \rho^0\gamma$ and $\bar{D}^0 \to \rho^0\gamma$ candidates from the helicity edge in the Run-1 data. 156

VI-6 Raw asymmetry and D^0 yield measured for given component in three-dimensional fit performed simultaneously to $D^0 \to \rho^0\gamma$ and $\bar{D}^0 \to \rho^0\gamma$ candidates from the helicity center in the Run-1 data. 157

VII-1 Stripping lines used for the reference channels. For the $D^0 \to K^-\pi^+\pi^0$ decay, `R_Line` uses resolved π^0 mesons and `M_Line` uses merged π^0 mesons. 163

VII-2 Stripping selection for reference channels $D^0 \to K^+K^-$ and $D^0 \to \pi^+\pi^-$. 164

VII-3 Stripping selection for $D^0 \to K^-\pi^+\pi^0$ reference channel. 165

VII-4 Hlt2 selection used for reference channels. 166

VII-5 Selection requirements in Hlt2 lines dedicated for $D^0 \to K^+K^-$ and $D^0 \to \pi^+\pi^-$ decays. 166

VII-6 Summary of offline selection applied for all reference channels. 167

VII-7 Additional selection imposed on $D^0 \to K^-\pi^+\pi^0$ channel. 167

VII-8 Yields and raw asymmetries of reference channels in the Run-1 data before kinematic reweighing. 169

VII-9 Effective yields and raw asymmetries of reference channels in the Run-1 data after kinematic reweighing. 176

Preface

We were living in trees when they met us.
They showed us each in turn
That Water would certainly wet us, as Fire
would certainly burn:
But we found them lacking in Uplift, Vision
and Breadth of Mind,
So we left them to teach the Gorillas while
we followed the March of Mankind.

Rudyard Kipling, "The Gods of Copybook Headings", London, 1919

Standard Model (SM) of Particle Physics is a theory that describes electromagnetic, weak, and strong interactions between two types of fermions - quarks and leptons - and the force-carriers, bosons. It is a very successful theory, able to describe wide range of phenomena. Despite its' success, there are good reasons to believe the SM is not the end of history for the theory of particle physics.

In 1967, A. Sakharov proposed a set of cosmological conditions necessary for the observable universe to exist. Among those, a violation of CP-symmetry - conjugation of charge and parity symmetries - is necessary in order to explain predominance of baryonic matter over antimatter. At the time, only three quarks were known - u, d and s. Even the charm quark, the main character of this thesis, was not experimentally observed until 1974, with the discovery of J/ψ. After the discovery of the third family of quarks and establishing the CKM matrix, the SM allows for CP violation in the quark sector. However, size of CP violation allowed by the SM is about billion times too small to account for observable baryon-antibaryon asymmetry on the scale of our Universe. This lead physicists to believe there must be some physics not described by the SM that were responsible for generating this large observable asymmetry. The fact that today, in our vast and cold (compared to compact and hot in the aftermath of the Big Bang) Universe those unknown forces do not seem to play a significant role suggests that their intrinsic energy scales are far higher than even masses of top quark, W and Z bosons, and the Higgs boson.

There are two approaches to the quest of Beyond the Standard Model (BSM) physics: direct and indirect. Former is to look for decays of the SM particles into non-SM final states, based on predictions of the SM extensions such as SUSY. Latter is to carry precision measurements of the SM observables with possible BSM contributions. The advantage of the indirect approach that, since unknown particles are off-shell, even processes at the relatively low (compared to masses of BSM particles) energy scale are sensitive. One such observable is the CP violation in the decays that are suppressed within the SM.

Violation of CP symmetry in decays of charmed mesons is a very recent discovery, observed for the first time in 2019 in the $D^0 \to K^+K^-$ and $D^0 \to \pi^+\pi^-$ decays. The observable used was $\Delta A_{CP} \equiv A_{CP}(K^+K^-) - A_{CP}(\pi^+\pi^-)$, and the reported value was $(-15.4 \pm 2.9) \times 10^{-4}$, corresponding to more than 5σ significance. This measurement is at the upper end of the SM predictions, drawing attention to the theoretical side of charm studies.

This thesis focuses on the radiative decays of charm mesons: $D^0 \to V\gamma$, where V stands for vector

meson ϕ, ρ^0, and $\bar{K}^{*0}$. The goal is to measure CP asymmetry for $D^0 \to V\gamma$ decays. In many theoretical aspects these channels are counterparts of the purely hadronic $D^0 \to K^+K^-$ and $D^0 \to \pi^+\pi^-$ decays. In experimental aspects, the radiative channels are much more challenging.

The presented thesis is structured as following. In Chapter **I**, a brief introduction to the SM, quark mixing, CP violation, and phenomenological and theoretical framework of radiative charm decays is given. Chapter is concluded by overview of the earlier results on radiative charm decays from B-factories. In Chapter **II**, the experimental environment of the LHCb and properties of charm data at LHCb are discussed. Experimental challenges of the studies of radiative charm decays in the environment of a proton-proton collider are laid out. In Chapter **III**, a general strategy of the analysis is explained, properties the data from Run-1 of the LHC that is being analyzed are described, and selection requirements that are used in order to increase our ability to separate signal from background are given. Chapter **IV** describes Monte-Carlo simulation of signal and background decays, the models of discriminating observables that we use in the data, and determination of the optimal requirements for the offline selection. Chapters **V** and **VI** describe the study of the experimental data, based on strategy outlined in preceding Chapters. Former deals with the combined sample, in which we do not distinguish between D^0 and $\bar{D}^0$, and the latter directly gives raw decay asymmetry as a fit parameter. Chapter **VII** follows the analysis of reference channels $D^0 \to K^+K^-$, $D^0 \to \pi^+\pi^-$, $D^0 \to K^-\pi^+\pi^0$, that is necessary in order to disentangle the physical CP asymmetry from nuisance asymmetries. Chapter **VIII** gives a brief description of systematic uncertainties affecting the A_{CP} measurement. In Chapter **IX**, a summary of the analysis is given, and prospects for the immediate future are discussed.

Chapter I

Introduction

I.1 A brief summary of the Standard Model

The Standard Model (SM) of particle physics is a theory that aims to describe the building blocks of the Universe, and their interactions. In the SM, as pictured in Fig. **I-1**, there are three generations of elementary spin-$\frac{1}{2}$ fermions, quarks and leptons. Each quark generation contains one up-type quark and one down-type quark, which have an electric charge of, respectively $+\frac{2}{3}$ and $-\frac{1}{3}$. The quarks carry *colour charge*, which allows them to couple to the strong force. Each lepton generation comprises a charged lepton and a neutral lepton (neutrino). Corresponding particles in each lepton generation have different mass and a generation-specific quantum number, *lepton flavour*, but all other properties remain the same. In addition to those, there are four spin-1 boson force carriers - gluons mediating the strong interaction, γ, $W^{\pm}$ and Z^0 carrying the electroweak interaction. And the final element that was the big discovery at the Large Hadron Collider (LHC) in 2012 - the Higgs boson H [1][2], which is responsible for masses of fundamental particles. Charged weak boson $W^{\pm}$ can couple to the quarks of different flavour, and is the only mediator that can change the quarks' flavour.

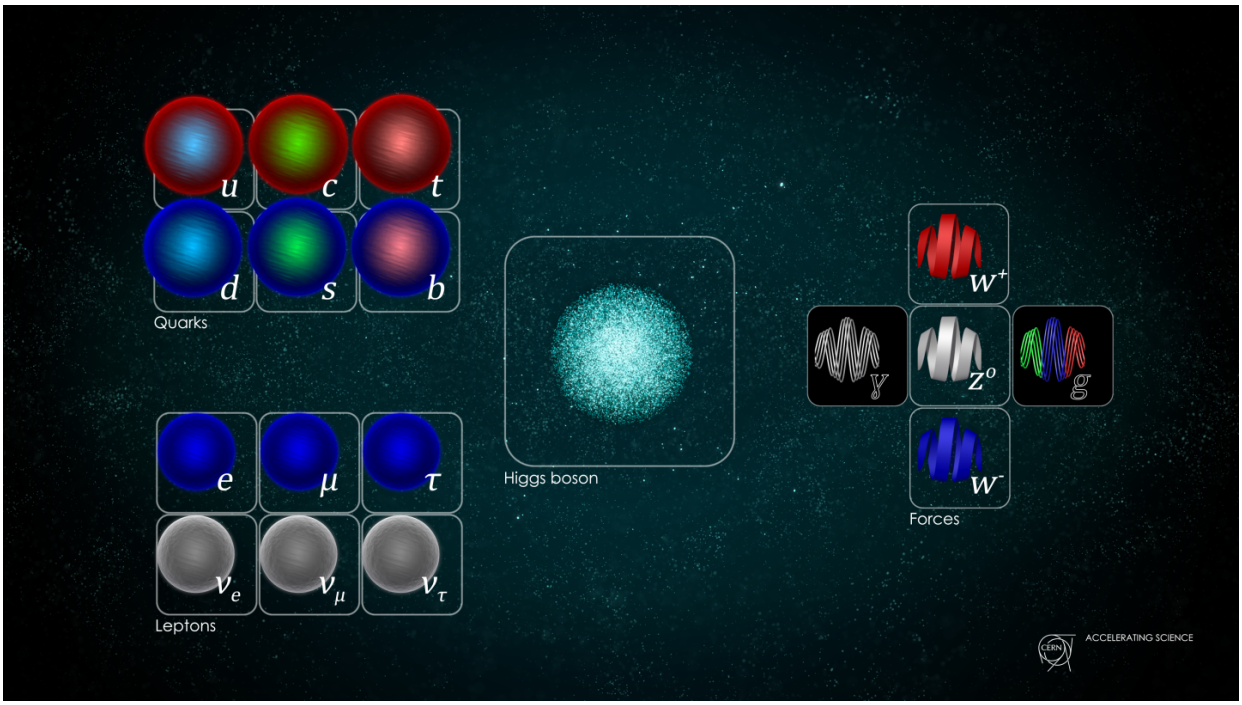

Figure **I-1**: The Standard Model in one picture. Taken from CERN's official website.

Precise predictions provided by the SM for the properties and interactions of fundamental particles, have been tested and confirmed by numerous experiments since the model was established in the 1960's. However, there is a general agreement that the SM cannot be a complete theory. It is unable to explain cosmological observations of the dominance of matter over antimatter (a.k.a baryonic asymmetry), the dark-matter content of the Universe, incorporate the theory of gravitation, or explain the patterns in the interaction strengths. Also, the SM does not accommodate oscillations of neutrinos and their non-zero masses, comprising the only confirmed *failure* of the model. Numerous searches have been carried out to find new particles and interactions from Beyond Standard Model (BSM) physics that could explain these shortcomings of the SM.

The process responsible for producing the baryonic asymmetry during the early Universe is called baryogenesis. There are three cosmological conditions for baryogenesis, named after A. Sakharov [3], that are necessary for the Universe such as the one we observe to exist:

1. Baryon-number violation
2. Violation of charge-parity (CP) symmetry
3. Deviation from thermodynamic equilibrium in the early Universe

The third condition lies firmly in the domain of astrophysics, but the first two are related to particle physics. Baryon number is conserved in the SM, and the benchmark for baryon-number violation - clear BSM physics - is the decay of a proton, searched for in specialized experiments in neutrino laboratories (Gran Sasso, Hyper-Kamiokande). We shall, however, focus on the second condition, since it is the one relevant to the presented work.

CP symmetry implies that physics laws remain the same if a particle is interchanged with its antiparticle (C transformation), and when its spatial coordinates are inverted (P transformation). Breaking a symmetry under such a simultaneous charge-parity CP transformation results in differences between matter and antimatter. The SM allows for CP-symmetry violation (Section **I.3**), but asymmetries observed so far are not sufficient to account for prevalence of matter over antimatter observed in the Universe. Thus, some contribution from BSM physics is expected to significantly enhance observable CP asymmetries.

I.2 Standard Model as an Effective Field Theory

The Lagrangian for the SM can be expressed through products of field operators as:

$$\mathcal{L}_{SM} = -\frac{1}{4}F_{\mu\nu}F^{\mu\nu} + i\bar{\psi}_L\gamma^\mu D_\mu\psi_L + \psi_{L,i}y_{ij}\psi_{L,j}\phi + (D_\mu\phi)^\dagger(D_\mu\phi) - V(\phi) \quad [\text{+h.c.}], \tag{I.1}$$

where $F_{\mu\nu} = -\frac{i}{g}[D_\mu, D_\nu]$ is the field strength tensor describing gauge bosons associated with the fundamental interactions, with g being a gauge coupling; ψ is a fermion field (quark or lepton), D_μ is a covariant derivative, and γ^μ are the Dirac matrices. Particle masses are acquired through Yukawa couplings y to the Higgs field ϕ, and $V(\phi)$ is the Higgs potential, usually taken as $\mu^2\phi^\dagger\phi - \frac{1}{2}\lambda(\phi^\dagger\phi)^2$, where λ and μ are theory parameters setting a vacuum expectation value.

The gauge interactions are associated with the symmetry group factorized into: $SU(3)_C \times SU(2)_W \times U(1)_Y$, where the first term (with index C standing for colour) leads to QCD, and the other two (with W denoting weak isospin and Y denoting hypercharge) combine into electroweak theory. The left-handed (L) quarks and leptons come in doublets of weak isospin, while right-handed (R) quarks and leptons are singlets. The quarks come in triplets of colour. Thus the fermion fields are:

$$\begin{pmatrix} u^\alpha_{L,i} \\ d^\alpha_{L,i} \end{pmatrix} \quad \begin{pmatrix} \nu_{L,i} \\ e_{L,i} \end{pmatrix} \quad u^\alpha_{R,i},\ d^\alpha_{R,i},\ \nu_{R,i},\ e_{R,i} \tag{I.2}$$

Here u is up-type quark, d is down-type quark, ν and e stand for neutral and charged lepton, respectively, i is the family index, while α is the color index. Right- and left-handed fermion fields are eigenstates of the projection operators $\frac{1}{2}(1 \pm \gamma^5)$, e.g. $u_R = \frac{1}{2}(1+\gamma^5)u$ and $u_L = \frac{1}{2}(1-\gamma^5)u$.

In 1972, K. Wilson and W. Zimmermann introduced Operator Product Expansion (OPE) formalism [4]. In order to calculate the OPE expansion for the SM Lagrangian, one needs to first choose a renormalization scale, μ. All effects above that scale are integrated out into effective couplings called Wilson coefficients $C_i(\mu)$, using a perturbation theory. Degrees of freedom involving masses below μ are included in local operators O_i, which involve non-perturbative effects. Effectively, the renormalization scale separates contributions from long-distance dynamics (above $1/\mu$) and short-distance interactions (below $1/\mu$). Within the OPE framework, the SM Lagrangian can be rewritten as:

$$\mathcal{L}_{eff}(\mu;\vec{x}) = \sum_i C_i(\mu) O_i(\mu;\vec{x}). \tag{I.3}$$

An important thing is that the Wilson coefficients are independent of initial/final states of considered processes. However, calculating matrix elements of operators O_i, in particular for hadronic processes, is still challenging, as it requires dealing with non-perturbative effects. The OPE framework is a basic approach broadly used in heavy-flavour physics, including charm decays, as discussed in Section **I.6.2**.

I.3 CKM matrix and charm transitions

I.3.1 Quark mixing

Coupling between up- and down-type quarks is enumerated by a unitary Cabibbo-Kobayashi-Maskawa (CKM) matrix [5]:

$$V_{\text{CKM}} = \begin{pmatrix} V_{ud} & V_{us} & V_{ub} \\ V_{cd} & V_{cs} & V_{cb} \\ V_{td} & V_{ts} & V_{tb} \end{pmatrix}. \tag{I.4}$$

The $V_{qq'}$ element of the CKM matrix describes mixing (coupling) between quarks q and q'.

The most common parametrization of the CKM matrix is the Wolfenstein parametrization, which uses four parameters: $\lambda \simeq 0.22$, $A \simeq 0.84$, $\rho \simeq 0.16$ and $\eta \simeq 0.37$ [6]. Each $V_{qq'}$ element is an expansion in powers of the λ parameter, and up to order $O(\lambda^5)$ the CKM matrix reads [7]:

$$V_{\text{CKM}} \simeq \begin{pmatrix} 1-\frac{\lambda^2}{2}-\frac{\lambda^4}{8} & \lambda & A\lambda^3(\rho-i\eta) \\ -\lambda\left[1+A^2\lambda^4\left(\rho+i\eta-\frac{1}{2}\right)\right] & 1-\frac{\lambda^2}{2}-\frac{\lambda^4}{8}(1+4A^2) & A\lambda^2 \\ A\lambda^3(1-(\rho+i\eta(1-\frac{\lambda^2}{2})) & -A\lambda^2 & 1-\frac{A^2\lambda^4}{2} \end{pmatrix}. \tag{I.5}$$

It clearly exhibits the hierarchy between the CKM matrix elements: the diagonal elements dominate, pointing to the largest mixing between quarks of the same generation.

I.3.2 Charm-quark transitions

The two weak currents that change the charm-quark flavour, $c \to sW^+$ and $c \to dW^+$,[1] have amplitudes governed by the CKM elements $|V_{cs}| \simeq 0.97$ and $|V_{cd}| \simeq 0.22$, respectively. As the former is more frequent than the latter, processes (e.g. decays of charm hadrons) underlain by these two transitions are classified as Cabibbo favoured (CF) and Cabibbo suppressed (CS).

[1] Throughout this thesis, charge conjugation is implied, unless explicitly stated otherwise.

The mentioned $c \to s$ and $c \to d$ transitions are flavour-changing charged currents, with W^+ boson emission occurring at the tree level. Possible is also flavour-changing neutral current (FCNC), e.g. $c \to u$ transition, where a quark changes flavour without altering the electric charge. FCNC corresponds to a higher-order process occurring at the loop level. The diagrams of tree-level and loop-level (a.k.a penguin) transitions are shown in Fig. **I-2**. The properties of FCNC in charm-quark sector, as well as its importance in probing the SM are discussed in Section **I.5**.

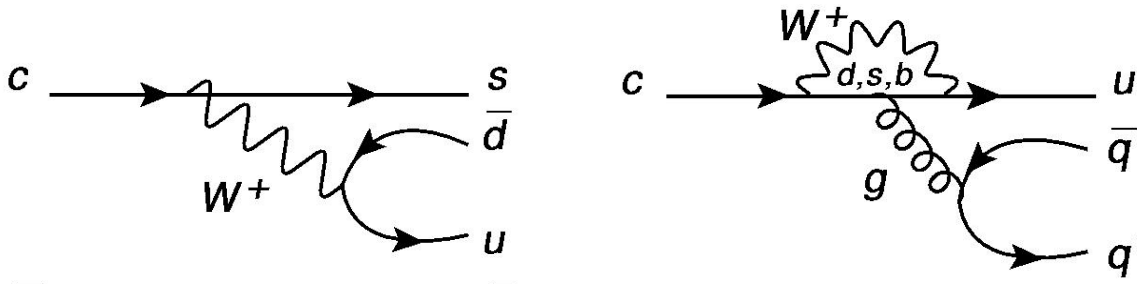

Figure **I-2**: Diagrams for charm-quark transitions occurring through (left) tree-level $c \to sW^+$ process, followed by W^+ boson coupling to $u\bar{d}$ pair, and (right) loop-level $c \to u$ process with d, s or b quark entering the loop. This loop process is a QCD penguin, with emitted gluon g coupling to $q\bar{q}$ quark pair.

I.3.3 CP-violating phase and unitarity triangles

Within the SM, CP violation in the quark sector arises from an irreducible complex phase in the CKM matrix [5]. A presence of this (weak) CP-violating phase, makes some of the CKM elements complex, and processes involving these elements break CP symmetry (Section **I.4**). In the Wolfenstein parametrization, the CP-violating phase corresponds to the single phase η. It enters the charm element V_{cd} only at order λ^5, suggesting that CP violation in charm processes that occur at the tree level is very small. However, the phase η contributes to charm processes at order λ^3 through the element V_{ub}, which underlies a $c \to u$ penguin amplitude (Section **I.5.2**).

An assumption on the unitarity of the CKM matrix, imposes constraints between its elements, forming so called *unitarity triangles* (UT) in the complex unitarity plane ($\rho + i\eta$). For example, the beauty UT, often simply called the Unitarity Triangle, is:

$$V_{ud}V_{ub}^* + V_{cd}V_{cb}^* + V_{td}V_{tb}^* = 0, \tag{I.6}$$

whereas the charm UT is defined through:

$$V_{ud}^*V_{cd} + V_{us}^*V_{cs} + V_{ub}^*V_{cb} = 0. \tag{I.7}$$

The angles of UT can be related to the *amount* of CP violation expected within the SM. While the beauty UT is equilateral, with each side being of $O(\lambda^3)$, the charm UT is of a very *squeezed* shape (Figure **I-3**). Smallness of the angle $\beta_c = \text{Arg}\left(\frac{V_{ud}^*V_{cd}}{V_{us}^*V_{cs}}\right)$ indicates that very little CP asymmetry is expected in preferred charm processes underlain with V_{cd}. Rare charm decays with amplitudes involving $|V_{ub}| \simeq 0.004$, can have larger asymmetries, but being loop-level processes, they are very suppressed (Section **I.5.2**).

BSM physics can introduce a new CP-violating phase, and violate the unitarity condition of the CKM matrix. The unitarity can be tested by over-constraining UTs through measuring their sides and angles. The beauty UT has been thoroughly tested using numerous measurements from, mainly, the B-factory experiments and LHCb, analysed together through a global fit. The fit performed assuming

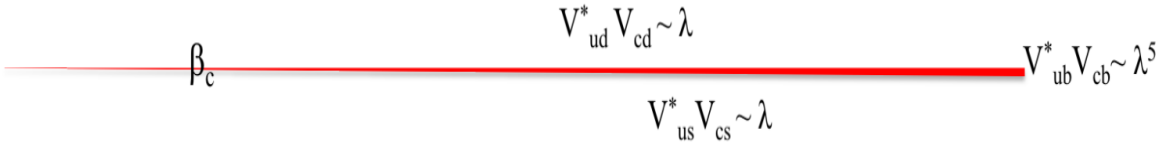

Figure **I-3**: Charm UT, illustrating the CKM unitarity condition in Eq. **I.7**. Tree-level charm processes are represented by longer triangle sides, while loop-level processes by the shortest side.

the SM physics only, presented in Fig. **I.3.3**, gives a good agreement between the input measurements, leaving insignificant room for BSM effects at the current level of the measurements' precision.

Charm-quark sector is complementary to beauty, and can be affected by different BSM effects (Section **I.5.2**). Testing the charm UT in a similar *global* manner would be very valuable, though not yet possible due to limited precision of CP asymmetry measurements in charm (Section **I.5.3**).

I.4 Basics of CP violation

There are two types of CP-symmetry breaking. It can arise in relation to oscillations between neutral mesons and antimesons, or occur in particle decays.

I.4.1 CP violation in decays

CP violation occurring in decays, a.k.a *direct* CP violation, results in different rates (or amplitudes) for decays of particles and corresponding CP-conjugate decays of antiparticles. For a particle D decay to a final state f, having an amplitude A_f, and antiparticle $\bar{D}$ decay to a CP-conjugate final state $\bar{f}$, with an amplitude $\bar{A}_{\bar{f}}$, the CP-violating condition is:

$$\frac{|\bar{A}_{\bar{f}}|}{|A_f|} \neq 1 \quad \text{and/or} \quad Arg\left(\frac{\bar{A}_{\bar{f}}}{A_f}\right) \neq 0. \tag{I.8}$$

Direct CP violation can differ for different decays, and is allowed for all charm hadron types. The direct CP asymmetry is most often measured as an asymmetry between a decay rate and its CP conjugate:

$$A_{CP} = \frac{\Gamma(D \to f) - \Gamma(\bar{D} \to \bar{f})}{\Gamma(D \to f) + \Gamma(\bar{D} \to \bar{f})} = \frac{|\mathcal{A}_f|^2 - |\bar{\mathcal{A}}_{\bar{f}}|^2}{|\mathcal{A}_f|^2 + |\bar{\mathcal{A}}_{\bar{f}}|^2}, \tag{I.9}$$

where D stands for any charm hadron species. For decays to multibody final states, A_{CP} corresponds to a *global* asymmetry, i.e. an asymmetry integrated over decay phase space. *Local* asymmetries can be measured, for instance, for individual amplitudes contributing into multibody decays, in particular amplitudes of intermediate resonances.

I.4.2 CP violation related to mixing

Neutral mesons, like D^0, can oscillate into their antiparticles $\bar{D}^0$ and back, which is often called $D^0 - \bar{D}^0$ mixing. Oscillations occur for neutral mesons as their mass eigenstates do not coincide with their flavour eigenstates. Mass eigenstates, D_1 and D_2, are *physical* particles having defined masses and widths ($m_{1,2}$ and $\Gamma_{1,2}$), while flavour eigenstates, D^0 and $\bar{D}^0$, have specified quark content ($c\bar{u}$ and $\bar{c}u$). These two are related as:

$$|D_{1,2}\rangle = p|D^0\rangle \pm q|\bar{D}^0\rangle, \tag{I.10}$$

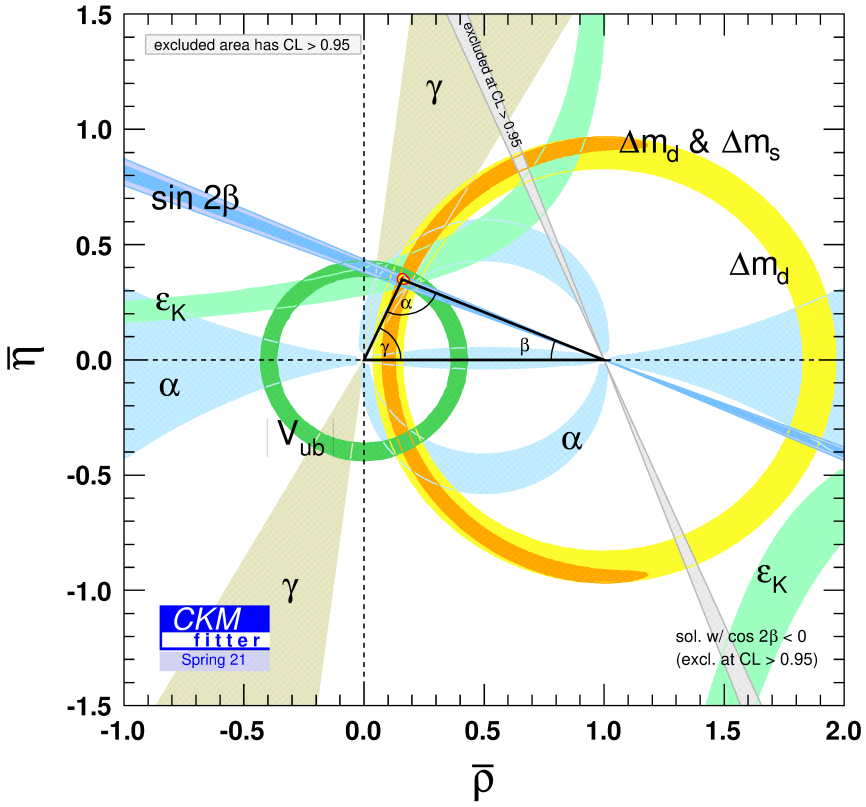

Figure **I-4**: A global fit to the beauty UT assuming the SM physics only [7]. The UT defined in Eq. **I.6** with sides rescaled by $|V_{cd}V_{cb}^*|$. It is presented on the plane $(\bar{\rho} + i\bar{\eta}) \simeq (1 - \frac{\lambda^2}{2})(\rho + i\eta)$, with the UT apex located at $(\bar{\rho}, \bar{\eta})$. Coloured bands represent input measurements at 68% confidence level (CL), while tiny red region shows 68% CL contour for the fitted UT apex.

with complex p and q coefficients satisfying $|p|^2 + |q|^2 = 1$. As oscillations occur periodically in time, they modulate a distribution of D^0 decay time, with the two mixing frequencies, corresponding to differences of masses and widths of physical states:

$$x = \frac{m_2 - m_1}{\Gamma} \quad y = \frac{\Gamma_2 - \Gamma_1}{2\Gamma}, \tag{I.11}$$

where $\Gamma = (\Gamma_1 + \Gamma_2)/2$.

CP violation in the mixing occurs if probability for $D^0 \to \bar{D}^0$ oscillations is not equal to the one for $\bar{D}^0 \to D^0$. It implies:

$$\left|\frac{q}{p}\right| \neq 1. \tag{I.12}$$

If D^0 and $\bar{D}^0$ can both decay into the same final state f, it is impossible to separate decays occurring directly $D^0 \to f$, from those via oscillations $D^0 \to \bar{D}^0 \to f$. In such a case, taking place in majority of D^0 studies, both *paths* contribute and interfere. CP violation in the interference between decay and mixing occurs if:

$$\phi = Arg\left(\frac{q}{p}\right) \neq 0, \tag{I.13}$$

i.e. the mixing amplitude introduces an additional phase with respect to decays.

CP-symmetry breaking related to the mixing, called *indirect* CP violation, is possible only for D^0 mesons, and is universal within the SM, i.e. independent of D^0 decay channels. Both, the $D^0-\bar{D}^0$ mixing and the related CP violation are accessed in a time-dependent manner, by measuring, respectively, rates for combined D^0 and $\bar{D}^0$ decays and their asymmetries as a function of D^0 decay time.

I.4.3 Conditions for CP-symmetry breaking

In general, two amplitudes contributing with different weak phases are necessary for CP violation to occur. These can be mixing and decay amplitudes (for indirect CP asymmetry), or two different decay *paths* leading to the same final state (for direct CP asymmetries). In majority of cases, these amplitudes are also required to carry different strong phases. Strong amplitudes can be related to, for instance, intermediate resonances contributing into multi-body final state, or amplitudes of different isospin in two-body decays.

Let us therefore consider two amplitudes A_1 and A_2, which contribute into $D \to f$ decay with weak phases ψ_{w1} and ψ_{w2}, and strong phases ψ_{s1} and ψ_{s2}. The total amplitudes for a decay $D \to f$ and for the CP-conjugate process $\bar{D} \to \bar{f}$, become respectively:

$$\begin{aligned} A_f =& |A_1| e^{i\psi_{s1}} e^{i\psi_{w1}} + |A_2| e^{i\psi_{s2}} e^{i\psi_{w2}} \\ \bar{A}_{\bar{f}} =& |A_1| e^{i\psi_{s1}} e^{-i\psi_{w1}} + |A_2| e^{i\psi_{s2}} e^{-i\psi_{w2}}. \end{aligned} \tag{I.14}$$

Thus, unlike weak phases, strong phases do not change sign under CP conjugation; they are CP-conserving. The decay rates for the considered processes correspond to amplitude squared, $|A_f^2|$ and $|\bar{A}_{\bar{f}}|^2$, respectively, whereas their difference is:

$$|A_f|^2 - |\bar{A}_{\bar{f}}|^2 \propto |A_1||\bar{A}_2| \sin(\psi_{s1} - \psi_{s2}) \sin(\psi_{w1} - \psi_{w2}). \tag{I.15}$$

It leads to a non-zero CP asymmetry (Eq. **I.9**) if $\psi_{w1} \neq \psi_{w2}$ and $\psi_{s1} \neq \psi_{s2}$. Therefore, although CP violation is a weak phenomenon, strong-decay effects also play a role and affect sensitivity to measuring CP asymmetry. If a single amplitude contributes into $D \to f$ process, i.e. $A_f = |A_1| e^{i\psi_{s1}} e^{i\psi_{w1}}$, there is no phase impact on the decay rates as $|A_f|^2 = |\bar{A}_{\bar{f}}|^2 = |A_1|^2$, and no CP violation occurs.

I.5 Specifics of charm-quark sector

I.5.1 Indirect tests of the SM

A heavy BSM particle that cannot be produced *directly* at the energy frontier, i.e LHC, can still contribute virtually to an SM process at much lower energies through quantum loops present in FCNC transitions. As a result, properties of the FCNC processes could become significantly deviant from the SM predictions. Such deviations could be observed through precision studies of various flavour observables.

This approach, taken by the LHCb experiment, and earlier at the B-factories, corresponds to searching for the SM extensions *indirectly*. BSM particles could be from models like, for instance, supersymmetry or dark matter, whereas flavour observables sensitive to BSM effects could be decay rates, CP asymmetries, angular observables, etc. While the choice of observables depends on studied processes, SM predictions for these observables should be calculated with precision better than expected experimental sensitivity.[2]

[2] Experimental sensitivity typically refers to a total uncertainty that includes statistical and systematic contributions.

I.5.2 Testing the SM in charm

Indirect BSM searches performed in charm sector are complementary to those for beauty and strangeness. Charmed hadrons are the only ones with penguin transitions featuring down-type quarks running in the loops (Fig. **I-2**); FCNCs for b- and s-hadrons involve up-type quarks. Penguins are crucial for indirect probing of BSM physics, and penguins with up-type and down-type quarks can be sensitive to different BSM particles. This makes charm an important counterpart to beauty and strangeness decays. In addition, charm quark is unique as it is the only up-type quark that both forms (meta-)stable hadrons and decays to other quarks via weak transition; top quark decays before it can hadronize. Some phenomena, like meson-antimeson mixing, can be probed in up-type sector only in charm.

On the other hand, charm sector is very challenging for BSM searches. One reason for that is significant suppression of penguin amplitudes in charm decays, another lies in the difficulties in theoretical calculation of penguin contributions due to significant long-distance (i.e. low-energy) hadronic effects.

For the $c \to u$ transition, shown in Fig. **I-2** (right), CKM factor is $V_{cq}^* V_{uq}$, where q is down-type quark. Thus loops involving b-quarks are CKM-suppressed down to $O(10^{-5})$ through $(m_b/m_W)^2 V_{cb}^* V_{ub}$, where m_b and m_W denote the b-quark mass and the W-boson mass.

Loops with d- and s-quark are suppressed by the GIM (Glashow-Iliopoulos-Maiani) mechanism [8].[3] The corresponding suppression factor is $(m_s^2 - m_d^2)/m_W^2$, where m_d and m_s denote d- and s-quark mass, respectively. In the limit of the flavour $SU(3)_F$ symmetry ($m_d = m_s$), the d-loop and s-loop amplitudes cancel out exactly. In contrast, penguin amplitudes in beauty sector are significantly enlarged by a contribution from top quark.

Heavily suppressed loop diagrams are not the only possibility for $c \to u$ transition. Owing to strong GIM suppression of light-quark loops and CKM suppression of b-quark loops, FCNCs in charm are usually dominated by long-distance effects. A typical example is *rescattering* from a tree-level process (Section **I.6.1**). Calculation of long-distance hadronic effects is challenging, since now one is not only dealing with the electroweak theory, but with the QCD as well.

For beauty decays, heavy-quark approximation in the Heavy-Quark Effective Theory (HQET) is used for calculating hadronic effects. A basic idea of the HQET is to treat the mass of the heavy quark Q as infinitely larger than light ones ($u,\ d,\ s$), and the condition for applicability of HQET is that $m_Q \gg \Lambda_{QCD}$, where $\Lambda_{QCD} \simeq 200\,\mathrm{MeV/c^2}$ denotes the QCD scale. However, as quark masses are not infinite, HQET leaves a correction term of the order of $\frac{\Lambda_{QCD}}{m_Q} + O(\frac{\Lambda_{QCD}}{m_Q})^2$. Since charm quark is relatively light compared to beauty, correction is comparatively large and non-perturbative.

Imprecise calculations of hadronic effects lead to limited precision of the SM expectations for some penguin-based observables. Testing the SM with such observables becomes infeasible. A typical example here are the $D^0 - \bar{D}^0$ mixing frequencies (Section **I.4.2**). On the other hand, CP asymmetries in charm become calculated with steadily increasing precision, triggered by improved experimental sensitivity.

I.5.3 CP violation in charm

As shown in Eq. **I.15**, two different weak phases are necessary in order to induce CP asymmetry. In charm, this condition means final states accessible to both tree-level and penguin amplitudes, and penguin contribution needs to be significant. This is satisfied only for Cabibbo-suppressed charm decays, and $D^0 \to K^+K^-$, $D^0 \to \pi^+\pi^-$, $D^0 \to K_S^0 K_S^0$, $D^+ \to K_S^0 K^+$, $D^+ \to \eta\pi^+$, $D_s^+ \to K_S^0\pi^+$ are common choice for direct CP-violation searches. For indirect CP violation, one can compare the $D^0 - \bar{D}^0$ mixing measured separately for D^0 and $\bar{D}^0$ decays to common final states, such as K^+K^- or $\pi^+\pi^-$.

The SM prediction for the direct CP asymmetries in Cabibbo-suppressed charm decays is $10^{-4} \div 10^{-3}$ [9][10][11][12]. Such a small CP violation (CPV) in charm is due to the suppressed penguin

[3] GIM mechanism was developed in order to explain apparent anomalies in the known FCNC - suppression in the $K^0 \to \mu^-\mu^+$ decays and rate of $K^0 - \bar{K}^0$ mixing. In fact, it predates the experimental observation of charm, as the fourth quark is necessary for GIM suppression in kaon sector.

Decay	A_{CP} $[10^{-3}]$	Experiment(year)
$D^0 \to \pi^+\pi^-$	$+2.30 \pm 0.59$	LHCb(2023), CDF(2012), Belle(2008), BaBar(2008)
$D^0 \to \pi^0\pi^0$	-0.3 ± 6.4	Belle(2014)
$D^0 \to K^+K^-$	$+0.44 \pm 0.54$	LHCb(2023), CDF(2012), Belle(2008), BaBar(2008)
$D^0 \to K^0_S K^0_S$	-19 ± 10	LHCb(2021), Belle(2017)
$D^+ \to \pi^+\pi^0$	$+4 \pm 8$	LHCb(2021), Belle(2018)
$D^+ \to \eta\pi^+$	$+3.1 \pm 4.7$	LHCb(2023), Belle(2011)
$D^+ \to K^0_S K^+$	-1.2 ± 2.5	Belle(2013), BaBar(2013)
$D^+_s \to K^+\pi^0$	$+20 \pm 30$	LHCb(2021), Belle(2021)
$D^+_s \to K^+\eta$	$+19 \pm 19$	Belle(2021), LHCb(2021)

Table **I-1**: Current HFLAV averages of A_{CP} measurements for selected charm-meson decays [21]. Experiments with the most precise results contributing into given average, are also mentioned, along with a year of corresponding measurement.

contributions.[4] CP asymmetry related to the charm mixing is within the SM even smaller, of the order of 10^{-5} or less [13][14], owing to the small mixing parameters (x, $y \simeq 10^{-3}$). However, BSM processes can introduce additional CP-violating phases and affect these SM expectations.

Direct CP violation in charm was discovered only recently, in 2019, by the LHCb collaboration [15]. It is achieved through measuring:

$$\Delta A_{CP} \equiv A_{CP}(D^0 \to K^+K^-) - A_{CP}(D^0 \to \pi^+\pi^-) = (-15.4 \pm 2.9) \times 10^{-4}, \qquad \textbf{(I.16)}$$

where uncertainty combines both statistical and systematic contributions. Experimentally, this observable is very sensitive, as nuisance asymmetries, due to the charge-asymmetric charm production and detection (Sections **II.4.1** and **II.4.2**), cancel out in the difference. Measuring A_{CP} for individual decay channels, one needs to correct for these additional contributions (Section **VII.1**). This usually introduces a significant systematic uncertainty. Theoretically, in the $SU(3)_F$-symmetry limit, $A_{CP}(D^0 \to K^+K^-) = -A_{CP}(D^0 \to \pi^+\pi^-)$, thus CPV effects are not *diluted* in the difference. The ΔA_{CP} result in Eq. **I.16** shows some tension with the SM [16], although not strong enough to claim that only BSM interpretation can explain it - previously underestimated non-perturbative effect can give enough enhancement to explain the experimental observation [17].

So far, the ΔA_{CP} remains the only charm CPV measurement that has the significance above 5 standard deviations (σ). Sensitivities of the A_{CP} measured for some individual Cabibbo-suppressed charm decays reach $O(10^{-4})$ [18]. Table **I-1** summarizes current HFLAV averages of the A_{CP} results for a few charm-meson decays. None of them reaches 5σ significance. However, $A_{CP}(D^0 \to \pi^+\pi^-)$ comprises (more than 3σ) evidence for CP violation owing to the recent LHCb measurement, which gives: $A_{CP}(D^0 \to \pi^+\pi^-) = (23.2 \pm 5.1) \times 10^{-4}$ and $A_{CP}(D^0 \to K^+K^-) = (7.7 \pm 5.4) \times 10^{-4}$ [19]. Interestingly, the sum of these two A_{CP}'s is non-zero at about 3σ, which indicates breaking of the flavour $SU(3)_F$ symmetry. This suggests that the GIM cancellation is weakened, which leads to the increased $c \to u$ penguin contributions.

On the indirect CP violation, the easiest way to access it is through measuring the A_Γ observable[5] for $D^0 \to h^+h^-$, where $h = K$ or π. It is defined as the asymmetry of the effective widths between

[4] In some B-meson decays, CP asymmetries reach $O(10\%)$.

[5] In terms of the basic mixing and mixing-related CPV parameters (Section **I.4.2**), A_Γ is defined as: $A_\Gamma = \frac{1}{2}(|q/p| - |p/q|)\, y \cos\phi + \frac{1}{2}(|q/p| + |p/q|)\, x \sin\phi$.

$D^0 \to h^+h^-$ and $\bar{D}^0 \to h^-h^+$ decays:

$$A_\Gamma = \frac{\hat{\Gamma}(D^0 \to h^+h^-) - \hat{\Gamma}(\bar{D}^0 \to h^-h^-)}{\hat{\Gamma}(D^0 \to h^+h^-) + \hat{\Gamma}(\bar{D}^0 \to h^-h^+)}. \tag{I.17}$$

An effective decay width $\hat{\Gamma}$ is the decay width *modified* by the $D^0 - \bar{D}^0$ mixing. Thus, through A_Γ one measures if the mixing modifies given decay width differently for D^0 and $\bar{D}^0$ decays. In the recent time-dependent analysis, LHCb measured $\Delta Y \simeq -A_\Gamma$ for $D^0 \to K^+K^-$ and $D^0 \to \pi^+\pi^-$ decays [20]. The measurement combined for both channels is: $\Delta Y(D^0 \to h^+h^-) = (-2.7 \pm 1.3 \pm 0.3) \times 10^{-4}$, where the first error is statistical and second systematic. Being consistent with zero, it has an unprecedented precision. However, the sensitivity of 10^{-4} is still below the SM expectation.

It is worth mentioning that $D^0 \to \phi\gamma$ and $D^0 \to \rho^0\gamma$ decays are radiative counterparts of hadronic $D^0 \to K^+K^-$ and $D^0 \to \pi^+\pi^-$ decays. While the former proceed through the radiative penguin amplitude (Section **I.6.1**), the latter contain the gluonic penguin (Fig. **I-2**). Thus, whatever process, SM-like or clearly BSM, is responsible for the tension of the ΔA_{CP} with the SM predictions in purely hadronic decays will also affect the radiative counterparts.

I.6 Radiative charm decays

I.6.1 Quark-level diagrams

This thesis concerns primarily radiative decays $D^0 \to V\gamma$, and their charge-conjugate decays, where V stands for vector meson $\phi \to K^+K^-$, $\rho^0 \to \pi^+\pi^-$ and $\bar{K}^{*0} \to K^-\pi^+$. Figure **I-5** shows diagrams of two short-distance contributions to radiative decays - a tree-level $c \to s(d)\,\gamma$ with W^+ exchange, and a loop-level $c \to u\gamma$ radiative penguin. The penguin is a FCNC, which in the SM is suppressed by the GIM mechanism and the underlying CKM factor (Section **I.5.2**). It is worth noting that $D^0 \to \bar{K}^{*0}\gamma$ proceeds via flavour-changing charged current $c \to s\gamma$, where penguin does not contribute, and thus we do not expect SM-like CP asymmetry for that decay.

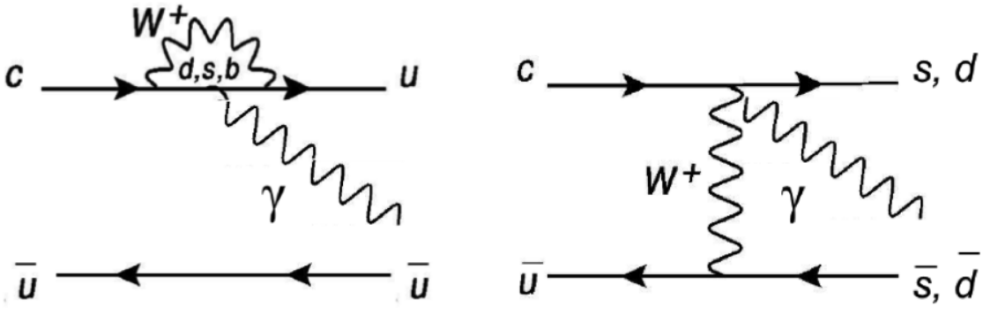

Figure **I-5**: Diagrams for short-distance contributions to $D^0 \to V\gamma$ decays - (left) radiative penguin and (right) tree-level W^+ exchange. To enable hadronization of ϕ, which is mostly an $s\bar{s}$ meson, additional transition $u\bar{u} \to g \to s\bar{s}$ is required. $D^0 \to \bar{K}^{*0}\gamma$ decay does not receive the penguin contribution.

In Section **I.6.4**, discoveries of the $D^0 \to V\gamma$ decays at the B-factories are discussed; $D^0 \to \phi\gamma$ and $D^0 \to \rho^0\gamma$ have their branching fractions ($\mathcal{BF}$s) measured to be of $\mathcal{BF} \simeq 10^{-5}$, whereas $\mathcal{BF}(D^0 \to \bar{K}^{*0}\gamma) \simeq 10^{-4}$. Theoretical estimations of the short-distance contributions give $\mathcal{BF} \simeq 10^{-8}$ (Section **I.6.2**). So why is an experimentally measured $\mathcal{BF}$ several orders of magnitude higher? The answer lies in long-distance contributions, but, in contrast to $D^0 \to K^+K^-$ and $D^0 \to \pi^+\pi^-$, they must also produce a photon in the final state, $q\bar{q} \to \gamma$. An examples of such a contribution originating from a tree-level transition is presented in Fig. **I-6**. $D^0 \to V\gamma$ decays are dominated by long-distance hadronic effects, which may dilute some observables used for testing the SM (Section **I.6.3**). Precise theoretical

calculations for long-distance effects are difficult, as mentioned in Section **I.5.2** and discussed more in Section **I.6.2**.

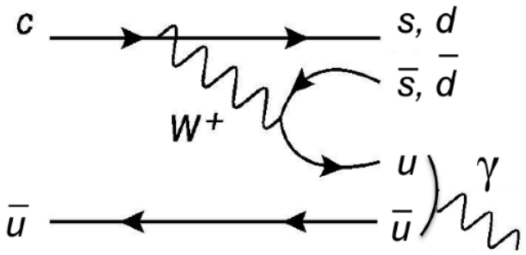

Figure **I-6**: Example of a long-distance process contributing to $D^0 \to V\gamma$ decays at the tree level.

I.6.2 OPE treatment of charm decays

Moving from general considerations introduced in Section **I.2** to particular decays of interest, one usually considers effective Hamiltonian rather than the Lagrangian, describing the $D \to f$ interaction in the OPE approach as:

$$\langle f\,|\mathcal{H}_{eff}|\,D\rangle = -\frac{G_F}{\sqrt{2}} V_{CKM} \langle f| \sum_i C_i(\mu) O_i(\mu) |D\rangle, \tag{I.18}$$

where G_F is the Fermi constant, V_{CKM} is a CKM factor, and $\mu = m_c$ is typically taken.

The weak effective Hamiltonian for a charm-changing decay is [22]:

$$\mathcal{H}_{eff} = -\frac{G_F}{\sqrt{2}} \left[\sum_{q=d,s} V_{uq} V_{cq}^* \sum_{i=1}^{2} C_i O_i^{(q)} + \sum_{i=3}^{6} C_i O_i + C_7 O_7 + C_8 O_8 \right] + \text{h.c.}, \tag{I.19}$$

where $V_{qq'}$ are CKM matrix elements, C_k are Wilson coefficients at m_c, and O_k are effective four-fermion operators.

$O_1^{(q)}$ and $O_2^{(q)}$ are the tree-level operators, expressed (for $q = d$ quark) as products of the currents:

$$\begin{aligned} O_1^{(d)} &= (\bar{u}_L^\alpha \gamma_\mu d_L^\beta)(\bar{d}_L^\beta \gamma^\mu c_L^\alpha), \\ O_2^{(d)} &= (\bar{u}_L^\alpha \gamma_\mu d_L^\alpha)(\bar{d}^\beta \gamma^\mu c_L^\beta), \end{aligned} \tag{I.20}$$

with α and β denoting contracted colour indices.[6] The difference between these operator is that charged currents in $O_1^{(q)}$ are in $O_2^{(q)}$ changed into the product of effective neutral currents due to QCD effects (e.g. gluon exchange). Both $O_1^{(q)}$ and $O_2^{(q)}$ contribute to tree-level hadronic charm decays, and are relevant for radiative decays as they are a source of the long-distance contribution (Fig. **I-6**).

O_3 through O_6 correspond to QCD-penguin amplitudes, as evinced by presence of summing over

[6] Operators $O_1^{(s)}$ and $O_2^{(s)}$ can be obtained by substitution of d for s in Eq. **I.20**.

quarks q (with $m_q < m_c$) in the loop:

$$\begin{aligned} O_3 =&(\bar{u}_L^\alpha \gamma_\mu c_L^\alpha) \sum_{q=u,d,s} (\bar{q}_L^\beta \gamma^\mu q_L^\beta), \\ O_4 =&(\bar{u}_L^\alpha \gamma_\mu c_L^\beta) \sum_{q=u,d,s} (\bar{q}_L^\beta \gamma^\mu q_L^\alpha), \\ O_5 =&(\bar{u}_L^\alpha \gamma_\mu c_L^\alpha) \sum_{q=u,d,s} (\bar{q}_R^\beta \gamma^\mu q_R^\beta), \\ O_6 =&(\bar{u}_L^\alpha \gamma_\mu c_L^\beta) \sum_{q=u,d,s} (\bar{q}_R^\beta \gamma^\mu q_R^\alpha), \end{aligned} \tag{I.21}$$

O_8 is the chromomagnetic dipole operator describing a gluon emission. It is defined as:

$$O_8 = \frac{g_s}{8\pi^2} m_c \, (\bar{u}_L \sigma_{\mu\nu} c_R) \, G^{\mu\nu}, \tag{I.22}$$

where g_s is the strong decay constant, $\sigma_{\mu\nu} = i[\gamma_\mu, \gamma_\nu]$, and $G^{\mu\nu}$ is the gluonic-field strength tensor. This gluonic penguin contributes to Cabibbo-suppressed decays, such as $D^0 \to K^+K^-$ and $D^0 \to \pi^+\pi^-$. For radiative decays, we consider the electromagnetic dipole operator O_7, which describes a photon emission as:

$$O_7 = \frac{e}{16\pi^2} m_c \, (\bar{u}_L \sigma_{\mu\nu} c_R) \, F^{\mu\nu}, \tag{I.23}$$

where $F^{\mu\nu}$ denotes the electromagnetic-field strength tensor. It is important to note that many BSM models exploit similarities between O_7 and O_8, which make radiative $D^0 \to h^+h^-\gamma$ decays important counterparts of $D^0 \to h^+h^-$ hadronic channels (Section **I.6.3**).

At the m_c scale, Wilson coefficients calculated to the next-to-leading order (NLO) corrections (i.e. including one-loop QCD diagrams) are: $C_1 = 1.21, C_2 = -0.41, C_3 = 0.02, C_4 = -0.04, C_5 = 0.01, C_6 = -0.05$ and $C_8 = -0.06$ [22]. C_7 is much smaller, and is estimated including perturbative contributions from two-loop QCD diagrams (NNLO), which requires considering contributions from O_1 and O_2. This gives $C_7 \simeq 10^{-3}$ [23][24].

Calculating the hadronic matrix elements for $D \to f$ process, $\langle f \left| \sum_i C_i(\mu) O_i(\mu) \right| D \rangle$, is very challenging as it involves non-perturbative effects. The problem is in applicability of the HQET (Section **I.5.2**), where one performs an expansion in powers of $\frac{\Lambda_{QCD}}{m_c}$, and, for each power, also an expansion in the strong coupling α_s to account for non-perturbative corrections. While the HQET is successfully exploited in beauty sector, it is still unclear whether it works in charm sector [14][25].

BSM operators

Staying within the OPE framework, one can naturally assume that BSM physics will result in modified operators and/or Wilson coefficients. In fact, SM extensions can be constructed starting from adding extra terms to the effective Hamiltonian in Eq. **I.19**. For radiative charm decays, relevant ones are *primed* operators O_7' and O_8' having opposite chirality compared to O_7 and O_8:

$$\begin{aligned} O_7' &= \frac{e}{16\pi^2} m_c \, (\bar{u}_R \sigma_{\mu\nu} c_L) \, F^{\mu\nu}, \\ O_8' &= \frac{g_s}{8\pi^2} m_c \, (\bar{u}_R \sigma_{\mu\nu} c_L) \, G^{\mu\nu}, \end{aligned} \tag{I.24}$$

Within the SM, both C_7' and C_8' are negligible [29]. Measurement of branching fractions and CP asymmetries of radiative decays can be used to constrain C_7'.

I.6.3 Testing the SM with $D^0 \to V\gamma$ decays

The Standard Model is the most successful physical theory up to date, however, as discussed in Section **I.1**, there are compelling arguments for BSM physics. In order to test possible contributions from BSM particles, the SM predictions for a given observable must be precise.

$\mathcal{BF}$s

Experimentally, one cannot distinguish between short-distance FCNCs and long-distance hadronic effects, and for latter, significant non-perturbative contributions are difficult to compute. Short-distance contributions account only for $\mathcal{BF}(D^0 \to \rho\gamma)$ of the order of 10^{-8} [26][27], which is about $3 \div 4$ orders of magnitude below the actually measured rates (Section **I.6.4**); the difference is due to long-distance dynamics. Theoretical estimations of the long-distance contributions serve more as a validation of methods employed. The calculations, which either exploit HQET to some extent, or are based on more phenomenological models give $\mathcal{BF}(D^0 \to \rho^0\gamma)$ of $10^{-6} \div 10^{-5}$, at the lower end of the experimental value, though with large uncertainties [28][29]. Given this, rates of the radiative charm decays are not useful for testing the SM.

CP asymmetry

Compared to decay rates, estimates of CP asymmetries are less affected by uncertainties on long-distance effects, which largely cancel in differences between decay widths of charm particles and antiparticles. Within the SM, $A_{CP} \lesssim O(10^{-3})$ is predicted for $D^0 \to \phi\gamma$ and $D^0 \to \rho^0\gamma$ decays [30][29].[7] This asymmetry is driven by $c \to u$ penguin amplitude. The penguin size depends primarily on breaking of the flavour $SU(3)_F$ symmetry, which eliminates GIM cancellation between d-loop and s-loop (Section **I.5.2**). The $SU(3)_F$ symmetry is known to be significantly broken in charm sector, as suggested by the ratio $\mathcal{BF}(D^0 \to K^+K^-)/\mathcal{BF}(D^0 \to \pi^+\pi^-) \simeq 3$.[8] As discussed in Section **I.5.3**, CP asymmetries measured for $D^0 \to K^+K^-$ and $D^0 \to \pi^+\pi^-$ also point towards the $SU(3)_F$ violation.

The size of the $SU(3)_F$ breaking can be estimated using, so called, topological diagram approach, by performing a global fit to measured $\mathcal{BF}$s of the decays belonging to the same $SU(3)_F$ multiplet, for instance $D^{0,+}$ and D_s^+ decays to two pseudoscalar mesons [11][31]. Such a data-driven phenomenological approach allows to constrain the penguin-to-tree amplitude ratio, and give predictions for CP asymmetries. Some of these analyses [32] managed to obtain the penguin amplitude enhanced enough to reproduce the measured ΔA_{CP}.

Recently an increased interest on radiative charm decays has been triggered by the charm CPV discovery. Various scenarios proposed to explain somewhat large ΔA_{CP} value (Section **I.5.3**), are expected also to increase CP asymmetry in the radiative decays. This includes SM extensions which generate CPV in $D^0 \to h^+h^-$ decays through the chromomagnetic penguin operator O_8, and should also have impact on the electromagnetic operator O_7 [30][33][34]; both operators are of similar origins in these models. As the O_7 contribution in $D^0 \to h^+h^-\gamma$ is substantially larger than the O_8 in $D^0 \to h^+h^-$, one can expect sizeable, up to a few percent, CP asymmetries in $D^0 \to \phi\gamma$ and $D^0 \to \rho^0\gamma$ decays.

It is worth mentioning also other popular BSM models. Contributions from leptoquarks into $c \to u\gamma$ can increase CP asymmetry in $D^0 \to \rho\gamma$ decays to $A_{CP} \lesssim 10\%$, while keeping the SM-like decay rate [29]. In supersymmetric (SUSY) extensions of the SM, both A_{CP} and $\mathcal{BF}$ can be even larger [29]. In general, an impact of these models on $D^0 \to \phi\gamma$ is expected to be smaller compared to $D^0 \to \rho^0\gamma$.

Given that non-perturbative enhancement of the penguin amplitude cannot be excluded [35], SM-like contribution up to a few % cannot be excluded either. So measured $A_{CP}(D^0 \to V\gamma) \geq 3\%$, would be considered a clear sign of BSM contribution to $c \to u\gamma$.

Photon polarization

A complementary observable accessible in radiative charm decays is a photon polarization. In the SM, fermions are left-handed and anti-fermions are right-handed, thus, in $c \to u\gamma$ one would expect the emitted photon to be left-handed, and in $\bar{c} \to \bar{u}\gamma$, to be right-handed. Therefore, within the SM, P-symmetry is also expected to be maximally violated, up to a small correction of $O(\frac{m_u}{m_c})$, which

[7] $D^0 \to \bar{K}^{*0}\gamma$ is expected to be CP-symmetric in the SM (Section **I.6.1**).

[8] It would be close to unity in the $SU(3)_F$-symmetry limit.

gives an opposite-parity contribution. Some BSM particles can significantly enhance deviation from maximal parity violation [36]. Measurement of photon polarisation in radiative charm decays can serve to constrain BSM models in a way complementary to CPV measurements.

A direct access to the photon polarization would require four-body final states, for instance $D^+_{(s)} \to K^-\pi^+\pi^+\gamma$ decays [37]. In $D^0 \to V\gamma$ decays the photon polarization can be accessed indirectly through the $D^0 - \bar{D}^0$ mixing; vanishing of the opposite-parity contribution should result in vanishing of the $D^0-\bar{D}^0$ oscillation pattern [36]. Measurement of photon polarization in charm decays remains a prospect for the future.

I.6.4 Existing measurements

Radiative decays $D^0 \to V\gamma$ were first observed at the B-factories - Belle observed $D^0 \to \phi\gamma$ in 2004 [38], BaBar observed $D^0 \to \bar{K}^{*0}$ in 2008 [39]. $D^0 \to \rho^0\gamma$ was observed by Belle only in 2017 [40], owing to the fact that, despite having $\mathcal{BF}$ similar to $D^0 \to \phi\gamma$, $D^0 \to \rho^0\gamma$ is affected by much higher background, as the final state involves pions and the ρ^0 state is quite broad.

Measurements of the $\mathcal{BF}$s and CP asymmetries performed so far for $D^0 \to V\gamma$ decays are summarised in Table **I-2**. For $D^0 \to \bar{K}^{*0}\gamma$, there is some tension between Belle and BaBar measurements of the $\mathcal{BF}$. Sensitivities of the A_{CP}'s for $D^0 \to \phi\gamma$ and $D^0 \to \rho^0\gamma$ channels are of the magnitude of $O(10\%)$, meaning that this measurement is not sensitive to even most optimistic predicted values (Section **I.6.3**). For comparison, A_{CP}'s for their purely hadronic counterparts, $D^0 \to K^+K^-$ and $D^0 \to \pi^+\pi^-$ reach sensitivities of $O(10^{-4})$ (Table **I-1**).

Charmed mesons are not the only possible species to study; charmed baryons also attract interest. Recently, Belle published a search for $\Lambda_c^+ \to \Sigma^+\gamma$ and $\Xi_c^0 \to \Xi^0\gamma$, with subsequent hyperons decaying into hadronic final states: $\Sigma^+ \to p\pi^0$, $\Xi^0 \to \Lambda\pi^0$ and $\Lambda \to p\pi^-$ [41]. These radiative decays involve flavour-changing charged current $c \to s\gamma$, rather than FCNC $c \to u\gamma$. No signal had been observed, and upper limits at 90% CL were set: $\mathcal{BF}(\Lambda_c^+ \to \Sigma^+\gamma) < 2.6 \times 10^{-4}$ and $\mathcal{BF}(\Xi_c^0 \to \Xi^0\gamma) < 1.8 \times 10^{-4}$. They are at the level of the measured $\mathcal{BF}(D^0 \to \bar{K}^{*0}\gamma)$, although the final states of baryonic decays are more complex than mesonic ones.

Experimental environments of the B-factories, which are e^+e^- machines, and LHC are quite different, and experimental challenges that need to be overcome when analysing radiative charm decays at LHCb, are described in detail in Chapter **II.1**.

Mode	$D^0 \to \bar{K}^{*0}\gamma$	$D^0 \to \phi\gamma$	$D^0 \to \rho^0\gamma$
$\mathcal{BF}$ [39]	$(3.22 \pm 0.20 \pm 0.27) \times 10^{-4}$	$(2.73 \pm 0.30 \pm 0.26) \times 10^{-5}$	—
$\mathcal{BF}$ [40]	$(4.66 \pm 0.21 \pm 0.18) \times 10^{-4}$	$(2.76 \pm 0.20 \pm 0.08) \times 10^{-5}$	$(1.77 \pm 0.30 \pm 0.08) \times 10^{-5}$
$A_{\rm CP}$ [40]	$(-0.3 \pm 2.0 \pm 0.0)\%$	$(9.4 \pm 6.6 \pm 0.1)\%$	$(5.6 \pm 15.1 \pm 0.6)\%$

Table **I-2**: Measurements performed for radiative decays of charm mesons by Belle [40] and BaBar [39].

Chapter II

Experimental environment

II.1 The LHCb experiment at the LHC

The LHCb is an experiment at the Large Hadron Collider (LHC), dedicated to studying heavy-flavour physics. It exploits large cross-sections for the production of heavy quarks in the proton-proton (pp) collisions at centre-of-mass (cms) energies of $\sqrt{s} = 7$, 8 and 13 TeV reached at the LHC during Run-1 and Run-2 data-taking periods. While the production cross-section for $b\bar{b}$ pairs is at the level of 100 μb [42], the cross-section for $c\bar{c}$ pairs is by one order of magnitude higher. The $c\bar{c}$ cross-section for producing a charm hadron within the LHCb detector acceptance is measured to be $\sigma(pp \to c\bar{c}X) \simeq 1400$ μb at $\sqrt{s} = 7$ TeV [43], and about 2400 μb at $\sqrt{s} = 13$ TeV [44]. The world's largest collected sample of charm hadrons, makes the LHCb experiment an excellent *charm factory*.

The typical instantaneous luminosity of the LHC, $\mathcal{L} \simeq 10^{34}$ cm^{-2}s^{-1}, is designed for the ATLAS and CMS detectors. However the LHCb design luminosity is limited by the maximum occupancy and radiation hardness of sub-detectors. LHCb has operated with an average luminosity reduced to $\mathcal{L} \simeq 2 \div 4 \times 10^{32}$ cm^{-2}s^{-1} by tuning the beam focus at the LHCb collision point. This lower instantaneous luminosity facilitates collecting and processing data from decays of heavy hadrons. In particular, pile-up events, arising due to several inelastic pp collisions occurring within the same bunch crossing, are reduced to minimum.

II.2 Overview of the LHCb detector

The LHCb detector is a single-arm forward spectrometer covering pseudorapidity range of $2 < \eta < 5$. It is optimized for studying beauty and charm hadron decays. The limited angle means smaller acceptance compared to nearly full solid-angle detectors (e.g. ATLAS and CMS). There is a good reason for this - most of $c\bar{c}$ and $b\bar{b}$ pairs are produced in pp collisions at fairly small angle from the beam direction, either in *forward* or in *backward* region. Unfortunately, covering both forward and backward regions would require every detector subsystem, except the vertexing, in duplicate. With the forward setup, the LHCb detector assures that about 25% of produced heavy-quark pairs can be accessed.

The layout of the LHCb detector is shown in Fig. **II-1**. The coordinate system used by LHCb has the origin located at the pp interaction point, associated with primary vertex (PV), the z axis is aligned with the beam direction, the y axis points vertically upwards, while the x axis points horizontally towards the centre of the LHC ring. The detector subsystems are designed to be symmetric around the vertical axis, with two halves mounted on rails, allowing access for maintenance, repair or replacement of sub-detectors.

In order to perform high-precision measurements of heavy-hadron decays, including charm decays, the LHCb detector is required to provide:

– excellent vertex and impact-parameter (IP) resolutions. The former is crucial for identifying decays

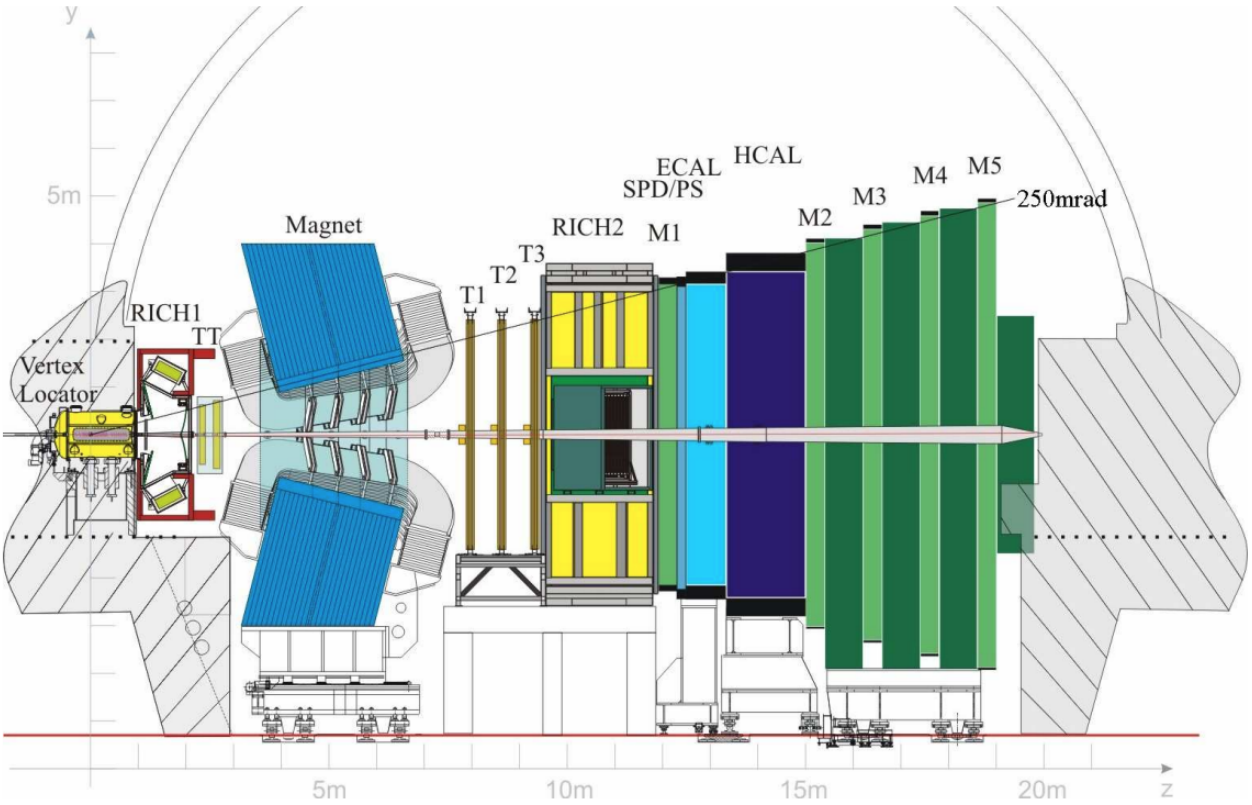

Figure **II-1**: Side view of the LHCb detector in Run-1 and Run-2 data-taking periods, taken from Ref. [45]. The angular coverage of the spectrometer ranges from approximately 10 to 300 mrad in the horizontal direction, and to 250 mrad in the vertical direction. The detector is comprised of the following subsystems, closest to farther from the interaction point: Vertex Locator (VELO), RICH1, Trigger Tracker (TT), Magnet, Tracking Stations (T1-T3), RICH2, Scintillating Pad Detector (SPD) and Preshower Detector (PS), ECAL, HCAL and Muon Stations (M1-M5).

of heavy hadrons, which are relatively long-lived particles, and their decay vertex, a.k.a. secondary vertex (SV), is significantly displaced from PV. In particular, due to the large relativistic boost at the LHC, D^0 mesons travel a few millimetres before decaying. A precise measurement of this flight distance helps to reduce background from processes occurring directly at PV, or from decays of particles having different lifetimes. Obviously, it also facilitates any time-dependent measurement, e.g. related to the $D^0 - \bar{D}^0$ oscillations. IP is defined as a distance of the closest approach (DOCA) of a particle trajectory to PV. It is particularly useful to discriminate between tracks from decays of heavy particles and combinatorial background; the former have larger IP values than tracks coming from PV.

– very good momentum resolution, which is necessary for precise reconstruction of the invariant mass of decay products. Invariant mass can be then used to identify signal decays and reject a background due to random combinations of tracks.

– precise particle identification (PID), which is needed to distinguish between decays of similar topologies, e.g. involving the same number of final-state tracks or neutral objects.

These requirements are assured by the sub-detectors categorized according to their purpose into two groups: tracking system and particle-identification system. The tracking system reconstructs trajectories (tracks) of charged particles, measures their momenta (p) and identifies interaction vertices. The PID system combines the momentum information with velocity or energy measurements in order to separate different species of charged particle, as well as identifies neutral particles, such as π^0 mesons or photons.

The tracking detectors comprise VELO surrounding the pp interaction region, Trigger Tracker (TT)

located upstream the magnet, and three Tracking Stations (T1-T3) installed downstream the magnet. The particle-identification detectors comprise two Ring Imaging Cherenkov detectors (RICH1 and RICH2), the calorimeter system composed of the preshower (PS), the scintillating pad detector (SPD), the electromagnetic and hadronic calorimeters (ECAL and HCAL), and five Muon Stations (M1-M5). More details on these subsystems are given in the following sections.

II.2.1 Vertex Locator (VELO)

VELO is located about 7 mm from the interaction point and is composed of 21 circular silicon stations, installed in the transverse plane to the beam pipe. Each station is divided into two semi-circular sensors, which move away from the interaction point during a beam injection. VELO sensors are about 220 μm thin micro-strip silicon wafers, each housing approximately two thousand diode strips. There are two types of sensors - radial R-sensors, and azimuthal ϕ-sensors. Each station has an R-sensor and ϕ-sensor mounted back to back, and stations are located a couple centimeters apart along the beam pipe. These sensors enable measuring the radial distance from the beam and the azimuthal angle of hits generated by ionizing particles that traverse the VELO modules; the z coordinate is given by the module position.

Resolution of the PV position measured with VELO tracks varies between 9 and 35 μm for the x and y coordinates, and between 50 and 280 μm for the z, depending on multiplicity of tracks used for the PV reconstruction. The IP resolution varies between 10 and 80 μm, depending on the transverse momentum (p_T) of the considered track. The IP resolution is worsen due to the multiple scattering of the particles crossing VELO, which is more likely to occur for the low-p_T tracks.

II.2.2 Tracking detectors and magnet

Charged particles traversing the LHCb detector are bent by the magnetic field. Their momenta are measured from a deflection of the trajectories, as the momentum is inversely proportional to the bending. The track deflection is obtained from the difference between the track slopes in VELO and Tracking Stations.

Magnet

The spectrometer magnet is a warm (i.e. non-superconducting) dipole magnet providing the maximum magnetic field strength above 1 T and the bending power of 4 Tm. The main component of the magnetic field is along the y axis, and thus the x-z plane is, to a good approximation, the bending plane. The polarity of the magnetic field is periodically reversed, giving downward and upward magnet-polarity configurations, called *MagDown* and *MagUp* configurations, respectively. This enables controlling any left-right asymmetries introduced by the detector (Section **II.4.2**).

Trigger Tracker (TT)

Trigger Tracker is located immediately upstream the magnet, and provides reference segments for particle trajectories before they are deflected. They are used to combine tracks reconstructed in Tracking Stations with those reconstructed in VELO. This improves precision of the momentum measurement, reduces fraction of tracks reconstructed with spurious hits, and allows reconstruction of decay vertices for particles that decay outside of VELO, such as K^0_S mesons.

TT is composed of two double-layer stations located about 30 cm apart, with each station covering a rectangular region of about 130 cm by 150 cm. Each layer is composed of 512 micro-strip silicon sensors and covers the full acceptance. The first and last layer measure the x track coordinate, the remaining two are inclined by ± 5 degrees. Combining information from all the sensors, removes ambiguities in the track reconstruction.

Tracking Stations

Three Tracking Stations (T1-T3) are located downstream the magnet. Each station is divided, according to the distance from the beam pipe, into Inner Tracker (IT) and Outer Tracker (OT). While IT is composed of silicon micro-strip sensors, OT employs drift tubes. Using the different technologies is motivated primarily by different occupancy of the detector across its acceptance. The geometrical coverage of IT is about 2% of the LHCb acceptance, but it corresponds to 20% of the particle flux.

Each IT station is arranged in a cross-shaped geometry, and its silicon sensors are grouped into four independent boxes having one or two micro-strip layers. OT is composed of straw tubes, 2.4 m long and with an inner diameter of 4.9 mm, and filled with a gas mixture which guarantees a drift time below 50 ns. Each OT station comprises four planes of the straw tubes, oriented in the same way as TT and IT layers. The spatial hit resolution of the IT and OT detectors are about 50 μm and 200 μm, respectively.

Tracking algorithm

Tracks reconstructed at LHCb are categorised depending on the hit information used in the reconstruction, as shown in Fig. **II-2**. A category exploited in the majority of analyses is long tracks made out of hits in both, VELO and the tracking stations. They have accurately measured momenta; the momentum resolution is $\sigma(p)/p \simeq 0.5\%$ for particles with $p < 10$ GeV/c, and about 2% at 200 GeV/c.

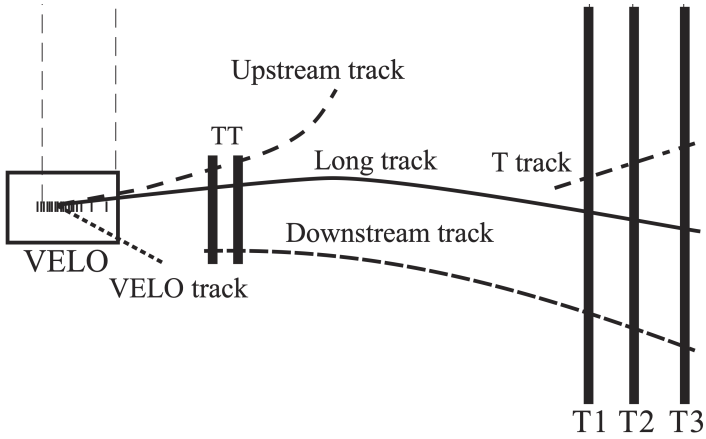

Figure **II-2**: Schematic illustration of various track types reconstructed at the LHCb tracking system [45].

The track reconstruction starts from pattern recognition, which aims at associating energy deposits left by a particle traversing the detector. It is performed through either forward tracking or track matching. In the former, a starting track seed is reconstructed within VELO and then extrapolated forward to Tracking Stations, where corresponding energy deposits are associated. In the latter, track seeds are reconstructed in both VELO and Tracking Stations, and extrapolated to the magnet plane, where their compatibility (i.e. matching) is checked. In the next step, the tracks are fitted to determine their parameters and momenta; the resulting χ^2 is used to asses the track quality. The Kalman filter [46] is employed to account for the multiple scattering. A clone-killer algorithm is run to remove tracks which are largely duplicated, i.e. share significant number of hits. Finally, a dedicated neural-network classifier is employed to measure the probability that tracks are *ghosts*, meaning that they are reconstructed using unrelated hits.

The tracking efficiency is defined as the probability that the trajectory of a charged particle that passed through the entire tracking system is reconstructed. The efficiency is measured with $J/\psi \to \mu^+\mu^-$ decays using a *tag-and-probe* technique, in which one of the muons (tag) is fully reconstructed, while the other (probe) is only partially reconstructed, such that the J/ψ invariant mass is measured

with a sufficient resolution. Matching the probe muon to a fully reconstructed long track enables evaluating the tracking efficiency. The average efficiency is above 95% in the momentum range $5 < p < 200$ GeV/c, and slightly below 95% for events with high track multiplicity (above 200 tracks) [47].

II.2.3 RICH detectors

Having measured the momentum of a charge particle, its mass can be derived if either velocity or energy is determined; knowing the mass enables particle identification. Ring Imaging Cherenkov detector (RICH) exploits Cherenkov photons emitted by a charged particle traversing a dielectric medium with the velocity (v) larger than the speed of light in the same medium, i.e. when $v > \frac{c}{n}$, where n is the refractive index of the radiator. The Cherenkov angle (θ_C) at which these photons are emitted is $\cos\theta_C = \frac{c}{nv}$, and thus depends on a particle momentum and mass. For particles approaching the speed of light, θ_C saturates to its maximal value of $\arccos\frac{1}{n}$. Therefore different radiators are necessary in order to discriminate between particle species in a wide momentum range relevant to LHCb, $1 < p < 150$ GeV/c.

There are two RICH detectors at LHCb, RICH1 and RICH2, located upstream and downstream the spectrometer magnet, respectively. In both, the Cherenkov light is focused through a system of spherical and plane mirrors onto a lattice of photo-detectors, Hybrid Photon Detectors (HPDs). HPDs are located outside the LHCb acceptance and magnetically shielded by large iron boxes to protect photo-electrons created in the photo-multipliers from being deflected.

RICH1 covers the full LHCb acceptance, and is optimized to identify particles in the momentum range of $1 < p < 60$ GeV/c. During Run-1, RICH1 volume was filled with 5 cm thick aerogel layer ($n = 1.03$) and C_4F_{10} gas ($n = 1.0014$); in Run-2 the aerogel was removed. RICH2 is filled with CF_4 gas ($n = 1.0005$) optimal for the higher momenta, $15 < p < 100$ GeV/c, in the acceptance region between 15 and 120 mrad. As can be seen in Fig. **II-3** (left), this RICH setup is expected to discriminate well between various mass hypotheses for a given particle. This is confirmed with the RICH2 performance presented in Fig. **II-3** (right).

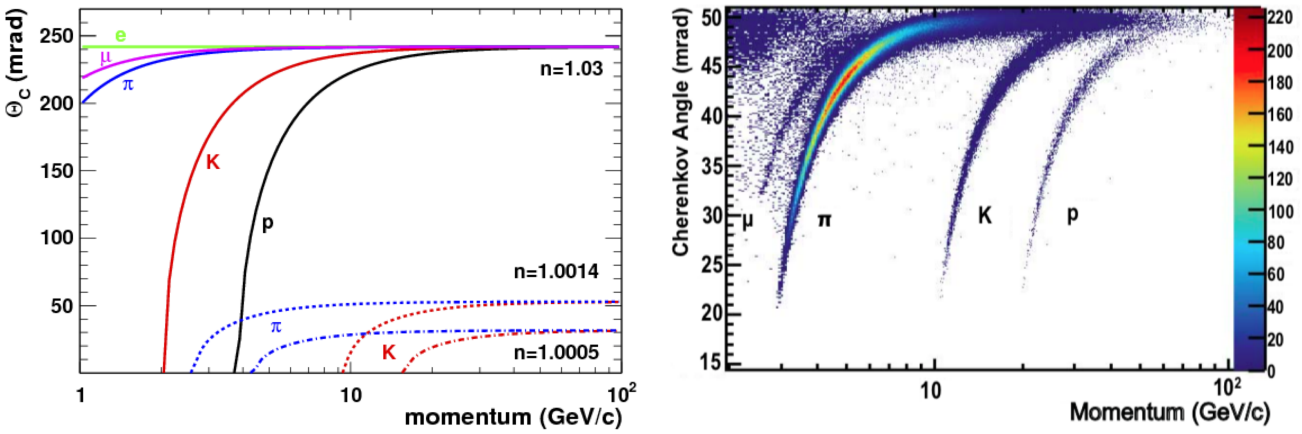

Figure **II-3**: (Left) Cherenkov angle as a function of momentum for different particle species, and for the three radiators used in RICH1 and RICH2. (Right) Response of the gas radiator in RICH1 to charged particles; the Cherenkov angle is measured with the Run-1 data. Figures are from Ref. [48].

PID algorithm

Photons emitted by a charged particle in the RICH radiators form a ring on the HPD plane, with the ring radius proportional to θ_C. The ring is measured from positions of the activated photo-detectors, and compared against a reference ring for each particle species, depending on the momentum and assuming given mass hypothesis. Five hypotheses are considered: electron, muon, pion, kaon and proton.

In the first step, pion mass hypothesis is used for detected tracks, and the corresponding likelihood is calculated. Then the hypothesis is changed to other species and the change in the likelihood is computed. The chosen, best mass hypothesis is the one giving the largest improvement in the likelihood.

A likelihood function is evaluated and associated with detected tracks in order to define a PID classifier, which is then used in physics analyses. The classifier is a variable discriminating between various mass hypotheses, and typically is expressed as the log-likelihood difference between two particle hypotheses, h_1 and h_2:

$$\mathrm{DLL}_{h_1,h_2} = \log(\mathcal{L}_{h_1}) - \log(\mathcal{L}_{h_2}). \qquad \textbf{(II.1)}$$

DLL classifiers combine the information from RICH, the calorimeter system and the muon system.

PID performance is described with the PID efficiency, defined as the fraction of correctly identified particles, and the mis-identification rate corresponding to the number of wrongly identified particles. They are studied using control decays from experimental data, in particular $K^0_S \to \pi^+\pi^-$, $\Lambda^0 \to p\pi^-$ and $D^{*+} \to D^0\pi^+$, with $D^0 \to K^-\pi^+$. These decays have large statistics and purity, and can be reconstructed independent of any PID information, based on kinematical and topological requirements only. This data-based PID evaluation is also used for calibration of the PID simulation in Monte Carlo (MC) samples (Section **IV.1**).

As can be seen in Fig. **II-4**, the kaon PID efficiency, integrated over the full momentum range, is between 85% and 95%, depending on the $\mathrm{DLL}_{K,\pi}$ requirement, while the corresponding pion mis-identification rate ranges between 3% and 10% [48].

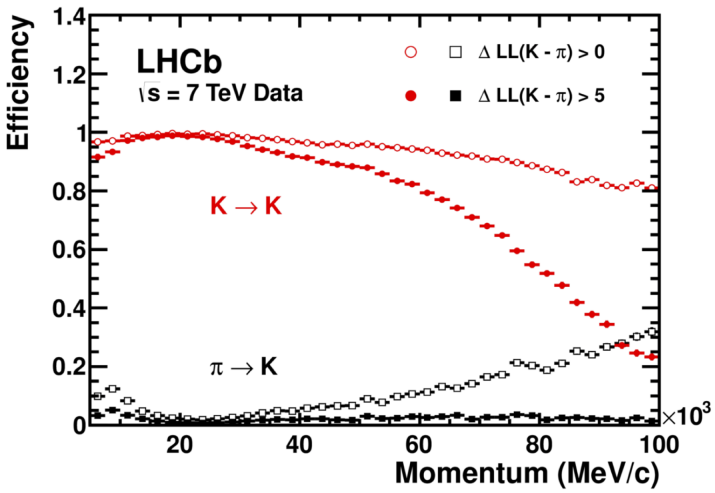

Figure **II-4**: PID efficiency and mis-identification rate for the discrimination of kaons from pions. PID performance is compared considering two different requirements on $\mathrm{DLL}_{K,\pi}$. Figure is from Ref. [48].

II.2.4 Calorimeter system

Calorimeter measures the energy which a particle loses as it passes through detector. A basic idea is to put a thin plate of material with a small radiation length (X_0)[9], usually heavy metal, such as lead, iron or tungsten, in the way of impinging particle, followed by a block of scintillating material with an optical fiber running through it. Incident particles interact with a calorimeter material and produce a cascade of secondary particles. They excite atoms in scintillators that emit light when returning to ground states. The light is transmitted to Photomultiplier Tubes (PMTs) by optical fibres, and

[9]Radiation length in a material is defined as a distance at which the energy of an electron traversing the material decreases due to radiation loss by a factor of $1/e$. Radiation length in a pure material depends on the atomic number and nucleus charge.

amplified signal is then passed to the readout. Total amount of the measured light is proportional to the energy deposit of the particle shower in calorimeter.

The calorimeter system at LHCb is composed of Scintillating Pad Detector (SPD), PreShower (PS), a electromagnetic calorimeter (ECAL) and a hadronic calorimeter (HCAL). It provides the identification of electrons, photons and hadrons, as well as the measurement of their energies and positions, and selects candidates with high transverse energy (E_T) for the Level-0 (L0) hardware trigger.

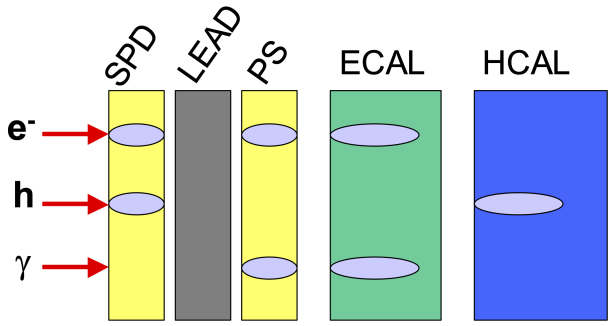

Figure **II-5**: Scheme for a shower development in the LHCb calorimeter system for different particles. Figure from Ref. [49].

SPD/PS

SPD/PS detector is a thin lead wafer (of $2.5X_0$) sandwiched between two rectangular scintillator pads; one located before the absorber is SPD, and the one after is PS. PS and SPD are divided into inner (closest to the beam pipe), middle and outer layers (Figure **II-6**), with dimensions of cells being approximately 4×4 cm^2, 6×6 cm^2 and 12×12 cm^2. SPD identifies charged particles, and allows electrons to be separated from photons, whereas PS identifies electromagnetic particles (Fig. **II-5**).

ECAL

ECAL is a sampling calorimeter of a shashlik type, and instrumented with independent modules. An individual ECAL module is made of alternating layers of lead (2mm thick) and scintillating tile (4mm thick). 66 alternating lead-scintillator layers form a stack, approximately 42 cm long that corresponds to about $25X_0$. Size of the module and number of readout channels increase with the distance from the beam pipe. As a result, each calorimeter layer is segmented in the transverse direction (Fig. **II-6**). The segmentation into three different sections has been chosen to ensure a constant occupancy over the whole ECAL layer. Moliere radius[10] of modules is 3.5 cm, thus smaller than the size of the ECAL cells.

ECAL measures the energy of electromagnetic showers. Design energy resolution for the LHCb ECAL is $\sigma(E)/E = 10\%/\sqrt{E} \oplus 1\%$, where E is expressed in GeV, and $\oplus$ indicates the sum in quadrature. A trivial observation, that is nevertheless important for the presented analysis, is that the ECAL resolution gets better with higher energies, and worse with lower, so for low-E_T photons energy resolution is low. The calibration of ECAL is done using $\pi^0 \to \gamma\gamma$ decays, with a photon that hits a cell to be calibrated being combined with another reconstructed photon. A fit to the $\gamma\gamma$ invariant-mass distribution is then performed for each individual ECL cell.

HCAL

Main task of HCAL is to measure an energy of hadronic showers, which is fundamental for the L0 hadron trigger (Section **II.3.1**). Whereas in ECAL and PS scintillating tiles are normal to the beam axis, in

[10]Radius of a cylinder within which 90% of the energy deposited by a particle shower in the material is contained.

HCAL they are parallel to improve the angular resolution. Iron is used as the absorber. Scintillating tiles and iron absorbers alternate longitudinally and laterally, resembling a folded chessboard. The inner section has square cells the size of 13×13 cm^2, and the outer 26×26 cm^2 (Fig. **II-6**). Overall HCAL structure is a wall, located about 13 m away from the interaction point, and symmetrical around the vertical axis. There is 52 modules in total. The total HCAL thickness is only $5.6X_0$, limited by the space in the LHCb cavern. Consequently, the HCAL energy resolution is limited to $\sigma(E)/E = 69\%/\sqrt{E} \oplus 9\%$.

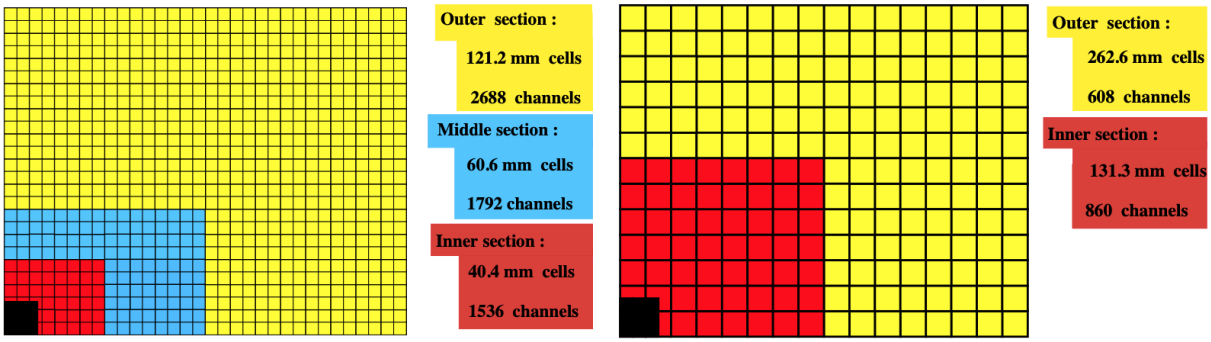

Figure **II-6**: (Left) Segmentation of the ECAL, as well as SPD/PS detector, and (right) HCAL. Only the top right quadrant is shown. Black squares represent the beam pipe. Figures from Ref. [50].

Photon and π^0 reconstruction

ECAL cells having energy deposits are grouped to form clusters. A single ECAL cluster comprises 3×3 cells around the maximum of a local energy deposition. Any cell shared between different clusters, has its energy redistributed between these clusters according to their total energies. Each cluster is characterised by its total energy, the energy-weighted position, and the two-dimensional energy-spread matrix describing a transverse (x-y) profile of a cluster. The z barycentre of a cluster is estimated as the energy-weighted position of clusters in z, corrected for the penetration depth of a photon assuming the logarithmic energy dependence.

Clusters without associated (i.e. matched) charged tracks are identified as energy deposits of neutral particles, such as photons. The photon energy is determined from the total cluster energy in ECAL and reconstructed energy deposit in PS, and corrected for energy leakages outside of the 3×3 cluster. The direction of a photon is derived from an assumed origin of the photon, and its energy-weighted position. Typically PV is assumed as a photon origin. However, if SV is fitted for particles which decay into final states involving photon, then the SV is taken as the photon production vertex, and the photon four momentum is recalculated accordingly.

Neutral pions with low transverse momenta, $p_T < 2$ GeV/c, are reconstructed as *resolved* π^0 mesons i.e. from pairs of well separated photons. Photon pairs from decays of higher-p_T π^0 mesons often cannot be resolved as individual clusters due to their small opening angle compared to the finite ECAL granularity. These are *merged* π^0 mesons, and their overlapping clusters are identified using an algorithm which splits an ECAL cluster into two 3×3 sub-clusters around the two highest energy deposits [51]. The energy of the shared cells is then distributed between the two sub-clusters. Neutral pions having $p_T > 5$ GeV/c are reconstructed primarily as merged π^0 mesons. The invariant-mass resolution is about 8 MeV/c^2 for the resolved pions and above 15 MeV/c^2 for merged pions [51]. The cluster shape is used to distinguish between photons and merged π^0 mesons (Section **II.5.1**).

Particle identification with the calorimeter system

Calorimetric (i.e. non-converted) photons[11] are identified by evaluating a photon-hypothesis likelihood based on several variables and their distributions for the signal photon and electron or hadron background. The discriminating variables are: the PS energy, χ^2 for the matching between the cluster and any charged track ($\chi^2_{\text{cl-tr}}$), and the ratio between the energy of the central cell of the ECAL cluster and the total ECAL energy. Photon clusters tend to be isolated, so they have small $\chi^2_{\text{cl-tr}}$ values. Typically photon candidates are selected by requiring $\chi^2_{\text{cl-tr}} < 4$ to suppress clusters from charged particles. The log-likelihood difference $\text{DLL}_{\gamma,e+h}$ is constructed to distinguish between photon and electron or hadron background.

Electrons are identified using information derived from ECAL, PS and HCAL. The log-likelihood difference for electron and hadron hypotheses, $\text{DLL}_{e,h}$, is evaluated based on energy deposits in PS and HCAL, cluster-track matching $\chi^2_{\text{cl-tr}}$, as well as E/pc distribution which compares an energy measured in ECAL with a momentum measured in the tracking system. The E/pc ratio is close to unity for electrons, and significantly below unity for hadrons, as most of their energies are deposited in HCAL. The electron energy is further corrected by including any bremsstrahlung photons measured in ECAL.

II.2.5 Muon system

The first muon station (M1) is located before the calorimeter system, to minimize effects from multiple scattering. The other four (M2 to M5) are placed behind HCAL, where muons are predominant species of charged particles. Each muon station is divided into four regions around the beam pipe, with the dimension and segmentation increasing with the distance from the beam. Technology used for muon stations is Multi-Wire Proprotional Chamber (MWPC), except for the innermost part of M1, where Gas Electron Multipliers (GEMs) are used. Between M2 through M5 station, 80 cm thick iron plates are inserted. MWPCs of each station give x and y coordinates of hits, and z coordinate is taken from known position of each station along the beam axis.

The momentum threshold for muons to penetrate through all the muon stations is 6 GeV/c. The muon system plays a significant role in the L0 trigger (Section **II.3.1**), being capable of rough track reconstruction and measuring p_T, albeit with a resolution of about 20%. Matching energy deposits in the muon stations with long and downstream tracks reconstructed in the tracking stations enables calculating muon DLL classifiers comparing muon and non-muon hypotheses. Combined with RICH and calorimeter classifiers, they assure the muon identification efficiency of about 93%, with hadron mis-identification rate below 0.6% [52].

II.3 A note on the data flow in the LHCb during Run-1

Busy environment of a hadron collider necessitates multiple steps of data processing between the crossing of the proton bunches and the final data saved into *n-tuples* ready for statistical analysis. Figure **II-7** shows the path of data from collisions to the offline storage.

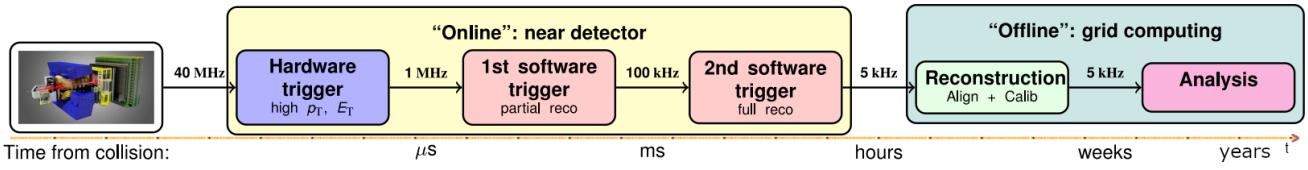

Figure **II-7**: A simplified scheme of the data flow from collisions to the offline storage in Run-1.

[11] Photons that converted before the magnet are reconstructed from pairs of electron-positron tracks. Efficiency of detecting converted photons is a few percent of that for calorimetric photons.

A trigger system is necessary to accept interesting events, in particular those which include b- or c-hadron decays, and reject most of background events. The LHCb trigger is designed to operate at the LHC bunch-crossing frequency (40 MHz). In order to reach an expected performance, it is divided into three levels (one hardware and two software triggers), each processing output of the preceding level. The raw data are processed with algorithms implemented in the software triggers, where simplified reconstruction and necessary calibrations are performed.[12] Raw events accepted by the triggers are saved and then fully reconstructed. The full reconstruction provides useful quantities, such as tracks, momenta, energies, PID information, saved into Data Summary Tapes (DSTs). Between the offline data storage and the final analysis, there is also *stripping* - a centrally-managed offline selection. In general, the end-user (analyst) deals only with already stripped data. Simulated data, obtained using the full simulation of the LHCb detector and its responses, undergo the same procedures as real data.

II.3.1 Level-0 trigger

Level-0 (L0) trigger is a hardware trigger based on dedicated custom electronics. It operates at the input rate of bunch crossings (40 MHz) and output rate of about 1 MHz. L0 trigger has to be extremely fast, so it is simple - typically, a threshold response on E_T or p_T of particles within given event. Calorimeter and muon stations provide the information for the L0 decisions used in the data taking. Calorimeter trigger selects for high-E_T particles by forming 2×2 cells into clusters, then selecting clusters with largest E_T. Clusters are identified as electrons, photons or hadrons based on the information from all calorimeter subsystems, and hits in SPD allow for estimating track multiplicity independent of VELO or tracking system. Muon trigger is based on information from muon stations and fast reconstruction, selecting high-p_T tracks.

The L0 trigger has three independent systems running in parallel: `L0Muon` accepts events containing at least one muon candidate with p_T exceeding 1.8 GeV/c. `L0Photon` and `L0Electron` accept events having at least one cluster with E_T above 3.0 GeV; `L0Electron` also requires at least one SPD cell hit in front of the PS cells. `L0Hadron` accepts events with at least one cluster with $E_T > 3.7$ GeV. These thresholds were used during data taking in 2012. In addition, events with large number of SPD hits (above 600) are rejected, as they would take too much time to be processed by software triggers.

II.3.2 High Level Triggers

Both High Level Triggers, Hlt1 and Hlt2 are software-based, and thus more flexible than L0. The aim of Hlt1 is to filter events in an inclusive way, and to reduce the rate of accepted events from the L0 trigger to 110 kHz. Hlt1 is typically simple, involving only partial particle reconstruction (tracks, momenta, vertices, calorimeter hits, muon PID). Inclusive Hlt1 lines rely on one or two-body signatures rather than specific decay channels. In particular, in order to distinguish beauty or charm hadrons from light-quark particles, Hlt1 exploits the displacement of their decay vertex and large p_T of decay products.

Hlt2 can be as complex as needed if it satisfies timing requirements. Typically, Hlt2 lines apply an exclusive selection of beauty or charm decays, performing a full reconstruction of processes of interest. However, there are also inclusive Hlt2 lines designed to trigger on partially reconstructed processes, and dedicated to, for instance, decays of similar topologies. During Run-1 data taking, Hlt2 operated with an output rate up to about 5 kHz, with the 2 kHz rate for charm.

The exact values of the L0 thresholds as well as Hlt1 and Hlt2 requirements varied slightly during the data taking. Combinations of trigger lines for Hlt1, Hlt2 and L0 with given selection requirements form a unique Trigger Configuration Key (TCK).

[12] In Run-2, the full event reconstruction has been performed already at the trigger level.

II.3.3 Stripping

Raw data of events accepted by the trigger system undergo the full reconstruction. The produced output, *full stream*, contains all reconstructed objects describing the events. Rather than processing the full stream, each analysis provides selection for central production. At this stripping stage, candidates for given decay of interest are built. A selection algorithm is encapsulated into a *Stripping line*, and lines dedicated to similar processes e.g. charm decays, are grouped into a *Stream*. While stripping is ran centrally, each analysis is responsible for writing their own stripping lines; modifications can be submitted during restripping campaigns. The output of the stripping is finally available to analysts, and is processed with the DaVinci application to produce n-tuples that can be easily analysed.

II.4 Properties of LHCb charm data

Properties of charm data at the LHCb experiment largely depend on a production mechanism (cross-section, production asymmetry), an experimental environment (charm boost, trigger selection, backgrounds), as well as the detector properties (particle identification, momentum resolution, photon-energy resolution, D^0 decay-time resolution, detection asymmetries). These aspects determine feasibility and sensitivity of charm measurements performed at LHCb, especially for studies which involve processes of difficult topologies or challenging final states, and deal with irreducible background. While the resolutions and particle identification have been already mentioned in Section **II.2**, the following sections discuss an impact of nuisance asymmetries, triggers and backgrounds on radiative decays of charm hadrons in particular.

II.4.1 Charm production and its asymmetry

The main mechanism by which charmed hadrons are produced in the LHC is prompt (or direct) production from pp collisions. As mentioned in Section **II.1**, the total charm cross-section at $\sqrt{s} = 7$ TeV measured within the LHCb acceptance, i.e. for charm hadrons with $p_T < 8$ GeV/c and $2.0 < \eta < 4.5$, is as high as 1.4 mb, whereas the cross-section for $D^{*\pm}$ mesons is about 0.7 mb [43]. It is relevant here, as the presented analysis exploits D^0 and $\bar{D}^0$ mesons originating from strong decays of excited $D^{*\pm}$ mesons, namely $D^{*+} \to D^0\pi^+$ and $D^{*-} \to \bar{D}^0\pi^-$. The electric charge of the accompanying pion provides *flavour tagging* of a neutral D meson, i.e. specifies whether it has been produced as D^0 or $\bar{D}^0$.[13] Obviously, the flavour tagging is crucial for studying CP asymmetries between and D^0 and $\bar{D}^0$ decays.

The prompt charm production is known to be asymmetric - cross-sections of charge-conjugate charmed particles in pp collisions are different by about a percent. There are more charmed baryons than anti-baryons produced, and the situation is opposite for mesons, with asymmetries assumed to cancel out since constituent charm of a pp system is naught. The production asymmetry (A_{prod}) has been measured for charmed D^+ and charmed-strange D_s^+ mesons [53] [54]. Although it has not been yet experimentally confirmed, A_{prod} is expected to be dependent on kinematics of produced charm hadrons [55]. A presence of the A_{prod} can bias a measurement of CP asymmetry in charmed-hadron decays, especially if it is at the level of an expected sensitivity for A_{CP}. Therefore it is treated as a nuisance asymmetry, and subtracted using reference channels (Chapter **VII**).

Another production mechanism exploited at LHCb is secondary production, i.e charm hadrons originating from decays of beauty hadrons. These are in particular semi-muonic channels, for instance $\bar{B} \to D^{*+}X\mu^-\bar{\nu}_\mu$, with X denoting any additional particles, as semi-leptonic decays have significantly larger rates than hadronic decays. As the cross-section for beauty production in the pp collisions is about one order of magnitude smaller than the charm cross-section, the secondary charm sample is smaller. In addition, it is affected by the production asymmetry of beauty hadrons produced in the

[13] Flavour of a produced neutral D meson can then be changed through the $D^0 - \bar{D}^0$ oscillations.

pp collisions. Therefore, in CPV studies of the prompt charm sample, any secondary contribution is treated as a background, and suppressed. The separation of the two charm samples is usually based on variables related to the IP of a charm hadron. Due to the large lifetime of B mesons, secondary charm hadrons are in average more displaced from PV than promptly produced ones. This significantly different topology is another reason of treating a secondary contribution as a background in prompt analyses. Some topological constraints improving momentum and decay-time resolution in the prompt sample may result in distortions for the secondary contamination (Section **III.3.3**).

II.4.2 Detector and detection asymmetries

Charged-hadron detection asymmetry

The LHCb detector is made out of ordinary matter - nucleons and electrons. The cross-sections of interactions of positively and negatively charged hadrons with the detector material, h^+ and h^-, are not equal, even with the same mass and momentum (Fig. **II-8**). This results in detection asymmetry (A_{det}) because of slightly different detection efficiencies between h^+ and h^- particles. A_{det} is dependent on the particle momentum - highly boosted particles behave like minimum ionizing particles (MIPs), and thus A_{det} is minimal, and for low momentum particles A_{det} is most significant. In particular, the cross-sections significantly differ between K^+ and K^-; the cross-section for K^-p interactions is for low-momentum kaons about twice as large as the one for K^+p [6]. This makes a detection efficiency for K^- mesons up to a few percent lower than for K^+ mesons.

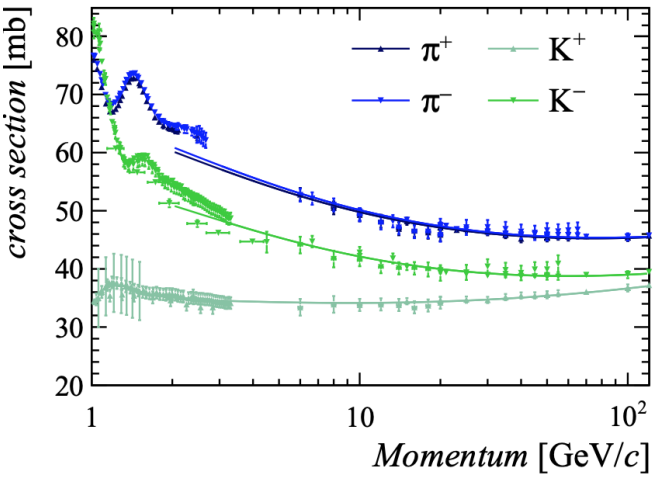

Figure **II-8**: Cross-sections of positively and negatively charged pions and kaons interacting with the deuterium target versus their momenta. Figure taken from Ref. [56].

In measurements of CP asymmetry in charm decays, a common approach to dealing with detection asymmetry is to subtract it using reference channels involving in their final state the same charged particles as a given signal channel.

Detector asymmetry and fiducial volume cuts

Some residual detector asymmetries can arise if the detector geometry is not ideally symmetric and a particle-detection efficiency differs in different parts of the detector. The LHCb detector layout also results in significant asymmetries for low-momentum tracks close to the detector-acceptance boundaries. This is particularly the case for soft pions $\pi_s^\pm$ from the $D^{*\pm}$ decays,[14] which are bent more by the magnetic field than the D^0 daughters due to their lower momentum. There are regions in the LHCb

[14]The pion from $D^{*+} \to D^0\pi_s^+$ decay is called *soft* as it has low momentum due to the small energy release in this decay.

detector where detection asymmetry for the soft pion gets anomalously high, up to 100%. Essentially, some regions of the soft-pion phase space are only accessible for a π_s^+ or a π_s^-. This is visible in Fig. **II-9**, where the large asymmetries at the edges of the $p(\pi_s)$ vs. $p_x(\pi_s)$ distribution are induced when soft pions of one charge are bent outside the LHCb detector acceptance, while ones of the opposite charge into the acceptance. Soft pions bent back into the beam pipe are also lost, resulting in the *beam shadow* effect visible in Fig. **II-9** as horizontal regions of large asymmetries at $p_x(\pi_s) \simeq \pm 300$ MeV/c.

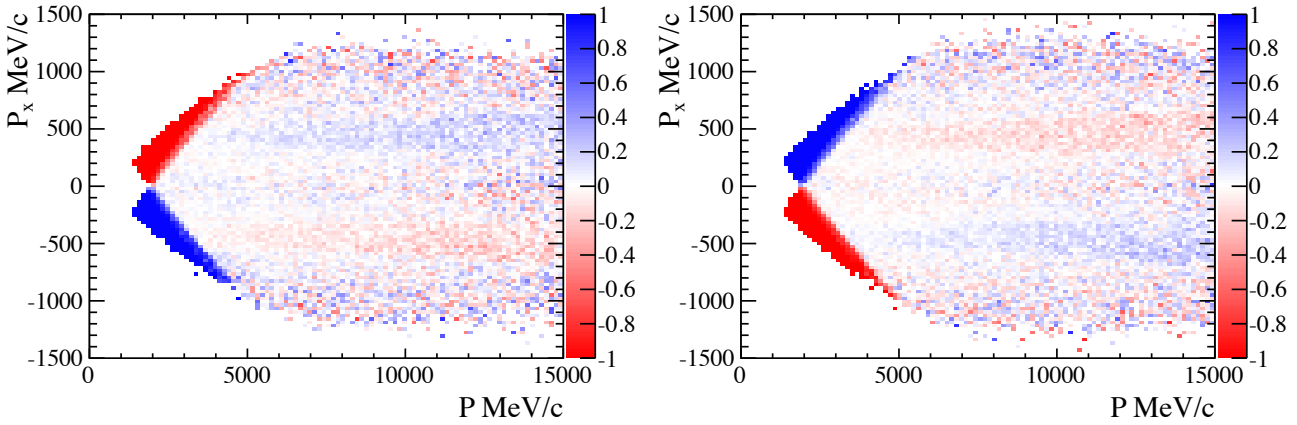

Figure **II-9**: Asymmetries between detected π_s^+ and π_s^- pions on $p(\pi_s)$ vs. $p_x(\pi_s)$ plane for the Run-1 data collected with the (left) downward and (right) upward magnet-polarity configuration. Soft pions are from reconstructed $D^{*+} \to D^0\pi_s^+$ and $D^{*-} \to \bar{D}^0\pi_s^-$ decays; the related asymmetries are similar regardless of D^0 decay channel.

These soft-pion asymmetries are reduced to first order when averaging data collected with the opposite magnet polarities. Such a cancellation has a limited precision of about 1%, which is not sufficient for most charm CP-asymmetry studies at LHCb. Unfortunately, there is no widely known solution to this problem better than simply excluding regions with large asymmetries. This procedure is known as fiducial volume cuts, and applied in majority of charm CPV measurements. The detector-acceptance asymmetry and beam-shadow asymmetry are respectively reduced by excluding the following two regions in the π_s phase space:

$$\begin{aligned} &|p_x| > \alpha(p_z - p_0), \\ &p_y/p_z < 0.02 \ \wedge (p_2 - \beta_2 p_z > |p_x| > p_1 - \beta_1 p_z), \end{aligned} \tag{**II.2**}$$

where the constants are defined as: $\alpha = 0.317$, $p_0 = 2.4$ GeV/c, $\beta_1 = 0.01397$, $\beta_2 = 0.01605$, $p_1 = 418$ MeV/c, $p_2 = 497$ MeV/c. These fiducial volume requirements reject typically about 20% of reconstructed D^0 decays.

In the presented analysis, there are two possible sources for detection and detector asymmetries, $A_{det}(h^+h^-)$ between the charged products of the $D^0 \to h^+h^-\gamma$ and $\bar{D}^0 \to h^-h^+\gamma$ decays, and $A_{det}(\pi_s^+)$ between soft pions from $D^{*+} \to D^0\pi_s^+$ and $D^{*-} \to \bar{D}^0\pi_s^-$ decays. The method of correcting for these nuisance asymmetries is discussed in Section **VII.1**.

II.4.3 Impact of triggers

As discussed in Section **II.3**, not all the charm produced at LHCb can be reconstructed online or stored for offline studies, and quite tight trigger selections are employed, followed by stripping requirements. Those selections often contain topological cuts (measured D^0 decay time, SV displacement), and kinematical cuts on p_T of a charm hadron and its decay products. The reason for this is twofold - abundant

background in low-momentum regions, and limited rate of data to storage. Unfortunately, those requirements distort the phase space of charmed-hadron decays, as well as decay-time distribution, and produce correlations between observables used to identify signal decays. The exact impact of distortions is hard to model with simulation, so it is one of the reasons why it is popular to employ a calibration channel with selection matched as closely as possible to the channel of interest.

A combined trigger and stripping efficiency at LHCb varies between the 10^{-2} level for charm decays involving a muon pair, owing to efficient muon-based triggers, and the 10^{-5} level for charm decays involving photons, where very tight selection is required on photon kinematics. In particular, although photons with $p_T(\gamma) > 200$ MeV/c are reconstructed at LHCb, $p_T(\gamma) > 1.7$ GeV/c cut is necessary in the trigger and/or striping selection for radiative charm decays to suppress large background resulting from high multiplicity of soft photons. Such an efficiency reduction is absent at the Belle experiment, where practically all the produced charm was saved.

The selection requirements of the trigger lines employed in the presented analysis, as well as the stripping requirements are demonstrated in Section **III.3**.

II.5 Experimental challenges of radiative charm decays

LHCb studies of radiative decays of beauty hadrons, in particular $B^0 \to K^{*0}\gamma$ and $B_s^0 \to \phi\gamma$, have shown that photons can be successfully handled at the proton collider [57][58]. Radiative decays of charm hadrons are more challenging, as they involve photons of significantly lower energies than their beauty counterparts. As mentioned in Section **II.4.3**, due to the trigger and background limitations, one can afford saving and analysing candidates for radiative charm decays involving photons with $p_T(\gamma) > 1.7$ GeV/c only, which significantly reduces the reconstruction efficiency of $D^0 \to V\gamma$ decays. However, the main challenge for the presented analysis is a large peaking background from $D^0 \to V\pi^0$ decays. $\mathcal{BF}$s of $D^0 \to V\pi^0$ decays exceed those for the radiative $D^0 \to V\gamma$ channels by up to two orders of magnitude,[15] and π^0 meson predominantly, in about 99%, decays into two photons.

The π^0 background arises when one photon from a resolved $\pi^0 \to \gamma\gamma$ is missing or a merged π^0 is mis-identified as a photon. The resolved π^0 background can be suppressed by applying π^0 veto using `VetoPi0R`. In this method, the photon from a signal $D^0 \to V\gamma$ candidate is combined with another photon from the underlying event, and a π^0 candidate is built. If the $M(\gamma\gamma)$ invariant mass of a π^0 candidate is close to the nominal π^0 mass, the signal candidate is rejected. Suppressing the background from merged π^0 relies on a multivariate classifier trained to distinguish between energy clusters for π^0 and γ. This method is discussed in Section **II.5.1**.

Both methods have limited efficiencies, whereas a remaining π^0 background cannot be separated from radiative decays using the invariant mass of a D^0 candidate, corresponding to the invariant mass of its decay products, $M(D^0) = M(V\gamma)$. This is due to the limited energy resolution of photons, which drives the $M(D^0)$ resolution (Sections **IV.5.1** and **IV.5.2**). Instead, separation of the residual π^0 background exploits a distinct helicity structure in the signal and background D^0 decays, as discussed in Section **II.5.2**.

Non-negligible background is also expected to arise from decays involving η meson, namely $D^0 \to V\eta$, followed by $\eta \to \gamma\gamma$. $\mathcal{BF}$s of such decays exceed those for radiative channels similarly to the channels involving π^0, in particular $\mathcal{BF}(D^0 \to \phi\eta) = (1.8 \pm 0.1) \times 10^{-4}$ [6]. Origin of the η background is similar to that of the π^0 background, however it is easier to distinguish from radiative decays. As the nominal η mass, $m_\eta = 548$ MeV/c^2, is significantly larger than the π^0 mass, the opening angle between photons is larger, while ECAL clusters of η are also larger. As a result, photons from η decays are more likely to be resolved. On the other hand, any missing photon from η decays has larger momentum, therefore $M(D^0)$ distribution for $D^0 \to V\eta$ decays reconstructed as radiative D^0 decays is expected

[15] In particular, $\mathcal{BF}(D^0 \to \phi\pi^0) = (6.6 \pm 0.4) \times 10^{-4}$, compared to $\mathcal{BF}(D^0 \to \phi\gamma) = (2.8 \pm 0.2) \times 10^{-5}$ [6]. Similar comparison between modes involving $\bar{K}^{*0}$ or ρ^0 is not straightforward, as it would require comparing against $\mathcal{BF}(D^0 \to K^-\pi^+\pi^0)$ for $M(K^-\pi^+)$ in the $\bar{K}^{*0}$ region, and $\mathcal{BF}(D^0 \to \pi^+\pi^-\pi^0)$ for $M(\pi^+\pi^-)$ in the ρ^0 region.

to be significantly shifted with respect to the signal $M(D^0)$ distribution, and thus relatively easy to separate (Section **IV.5.3**).

II.5.1 Suppressing background from merged π^0

The default tool to distinguish between reconstructed π^0 and γ candidates is IsPhoton [59]. It was created and optimised for radiative B-meson decays, but applicable to charm nevertheless. The separation is performed using a multivariate classifier and based on distinguished shapes of electromagnetic clusters; ECAL clusters for merged π^0's are usually broader than single-photon clusters of the comparable energy. The following energy-spread variables are defined for an ECAL cluster of 3×3 calorimeter cells:

$$\begin{aligned} S_{XX} &= \frac{\sum_j e_j (x - x_c)^2}{\sum_j e_j}, \; S_{YY} = \frac{\sum_j e_j (y - y_c)^2}{\sum_j e_j}, \\ S_{XY} &= S_{YX} = \frac{\sum_j e_j (x - x_c)(y - y_c)}{\sum_j e_j}, \end{aligned} \qquad \textbf{(II.3)}$$

where x_j and y_j are the transverse position of the individual j^{th} cell, and e_j is measured energy in this cell. The barycentre positions of the cluster, x_c and y_c, are calculated as energy-weighted positions, $x_c = \frac{\sum_j x_j e_j}{\sum_j e_j}$, $y_c = \frac{\sum_j y_j e_j}{\sum_j e_j}$. Those form a diagonal energy-spread matrix $S = \begin{pmatrix} S_{XX} & S_{XY} \\ S_{YX} & S_{YY} \end{pmatrix}$.

Four statistical moments are used to distinguish between cluster shapes:

- $r2 =< r^2 >= S_{XX} + S_{YY}$
  is related to the size of the cluster, and referred to as shower shape;
- $r2r4 = 1 - \frac{<r^2>^2}{<r^4>}$
  describes importance of the cluster tails;
- $\kappa = \sqrt{1 - 4\frac{\det S}{\mathrm{Tr}^2 S}}$
  is related to the major and minor semi-axes of an ellipse;
- $asym = \frac{S_{XY}}{\sqrt{S_{XX} S_{YY}}}$
  provides information about correlation between x and y coordinates i.e. the ellipse orientation.

The most energetic cell of an ECAL cluster (i.e. j with the highest e_j) is called a *seed* cell, and its energy is E_{seed}, while the total energy of a j^{th} cluster is $E_{cl} = \sum_j e_j$. Among the feature variables, there are also E_{seed}/E_{cl}, and similarly ratio including the second most energetic cell $(E_{\mathrm{seed}} + E_{2nd})/E_{cl}$.

Other variables underlying the γ–π^0 separation tool are constructed using information from PS. Multiplicity of hits in the PS part of the calorimeter is used by considering 3×3 clusters in front of the seed cell in ECAL. Four multiplicity variables are defined, *multi*, *multi*15, *multi*30 and *multi*45, where numbers are the minimal energy (in MeV) required per cell. In addition, PS cluster shape variables are constructed similar to the above ECAL variables: $E_{\max}/E_{\mathrm{sum}}$, E_{2nd}/E_{sum}, $r2PS$ and $asymPS$, with E_{sum} being the total energy deposited in the PS cluster, $E_{\max}$ and E_{2nd} the energy of the most and the second most energetic PS cell.

The actual multivariate classifier is a Multi-Layered Perceptron (MLP) implemented using the TMVA tool [60]. Photons from simulated events of $B^0 \to K^{*0}\gamma$ decays are used as the signal, while π^0 mesons from a simulated cocktail of B decays, in particular $B^0 \to K^+K^-\pi^0$ and $B_s^0 \to K^+K^-\pi^0$, and reconstructed as photons, serve as the background. Only photons with $p_T(\gamma) > 2$ GeV/c are considered, as this is the minimal p_T for π^0 to be reconstructed as merged. The three regions of the calorimeter are

considered separately. Signal and background distributions of the input ECAL variables for the inner region are compared in Fig. **II-10**, while for some of the PS variables in Fig. **II-11**. The distribution of the MLP output, corresponding to IsPhoton, obtained in the inner calorimeter region is shown in Fig. **II-12** (left). Efficiencies for signal and background as a function of a cut on the MLP output is presented in Fig. **II-12** (right). The performance of the method is slightly worse in the middle and outer calorimeter regions. Overall, for the default requirement of IsPhoton>0.6, the photon efficiency is around 98%, with the merged π^0 rejection[16] of about 45%.

A dedicated multivariate classifier has been developed for the presented analysis, and trained on simulated data for charm decays. Its performance compared to IsPhoton is discussed in Section **IV.3**.

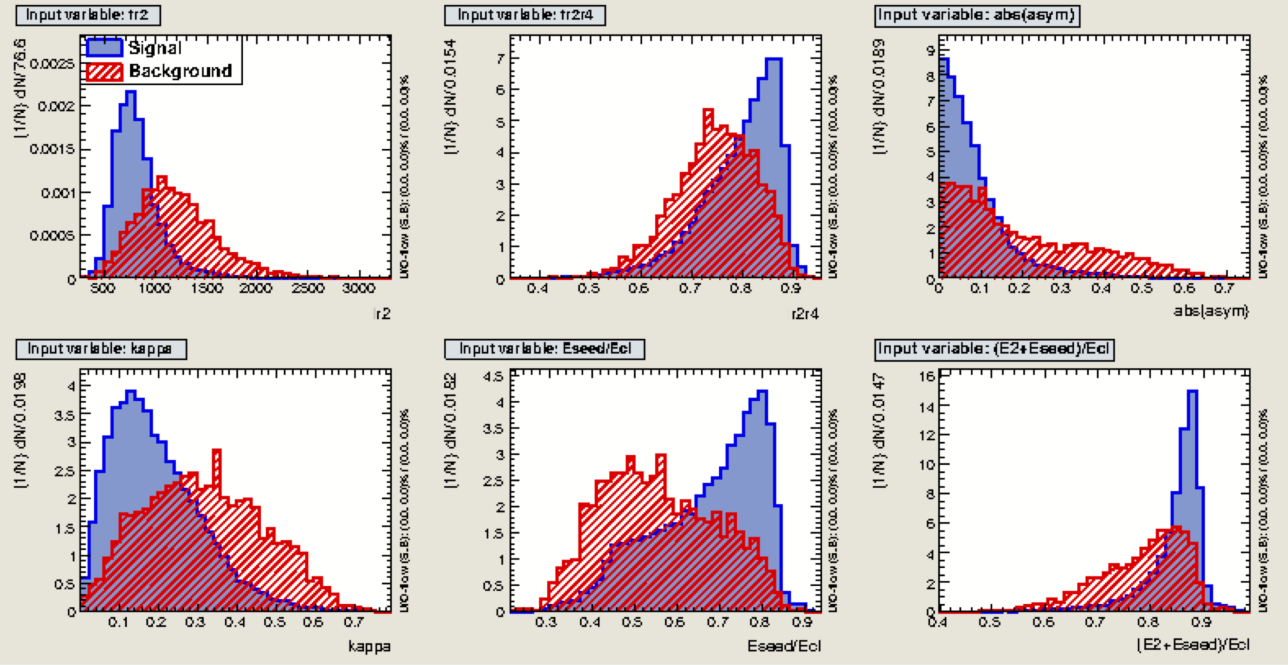

Figure **II-10**: Distributions of ECAL cluster shape variables (clockwise from top left): $r2$, $r2r4$, $|asym|$, κ, E_{seed}/E_{cl} and $(E_{\text{seed}}+E_{2nd})/E_{cl}$ for photons (blue) and merged π^0 selected as photons (red) in the inner ECAL region. Figure is from Ref. [59].

II.5.2 Separating signal and residual π^0 background

Irreducible π^0 background is separated from the radiative signal by exploiting different polarization of the vector meson V in $D^0 \to V\gamma$ and $D^0 \to V\pi^0$ decays. In $D^0 \to V\gamma$, the V meson is accompanied with a transversely polarised photon, and thus V is also transversely polarised (has helicity of ± 1). Whereas in $D^0 \to V\pi^0$, the pseudo-scalar π^0 meson accompanying the V meson implies that V is longitudinally polarised (has helicity of 0). The helicity angle θ of the V meson (Fig. **II-13**) is defined as the angle between the momentum of one of the final-state hadrons[17] and the D^0 momentum, both in the rest frame of the $V \to h^+h^-$ system. The θ distribution is expected to have $(1-\cos^2\theta)$ shape for $D^0 \to V\gamma$ decays, and $\cos^2\theta$ shape for $D^0 \to V\pi^0$ decays (Fig. **II-13**).

However, the V meson is typically selected by taking the h^+h^- system (where $h = K, \pi$) having the invariant mass within the V mass region (Section **III.3.3**). Thus, the π^0 background includes not only $D^0 \to V\pi^0$ decays, but also other resonances decaying to $h^\pm\pi^0$ final states, as well as resonances in the h^+h^- system contributing into the considered V mass region. These contributions are expected

[16] Background-rejection factor is defined as $(1-\epsilon_{bkg})$, where ϵ_{bkg} corresponds to the background efficiency.
[17] By convention, K^- is chosen in $K^-\pi^+$ final state, while K^+ for K^+K^- and π^+ for $\pi^+\pi^-$.

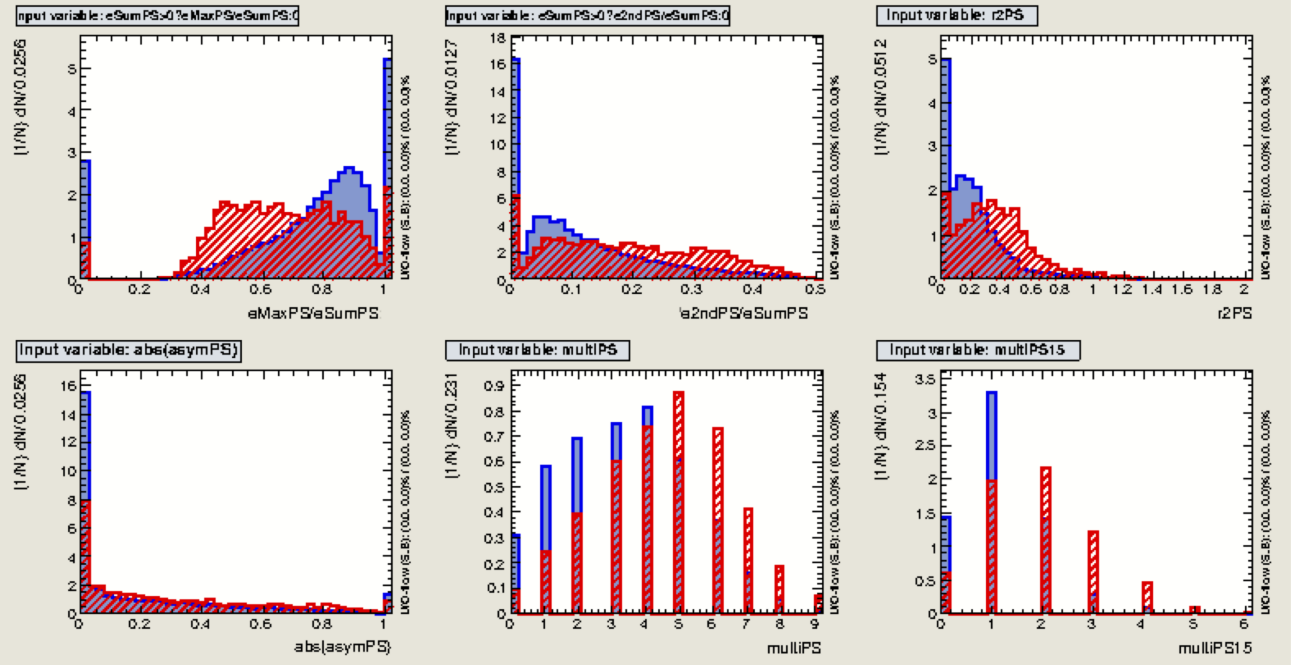

Figure **II-11**: Distributions of PS variables (clockwise from top left): $E_{\max}/E_{\rm sum}$, $E_{2nd}/E_{\rm sum}$, $r2PS$ and $|asymPS|$, $multi$ and $multi15$ for photons (blue) and merged π^0 reconstructed as photons (red) in the PS inner region. Figure is from Ref. [59].

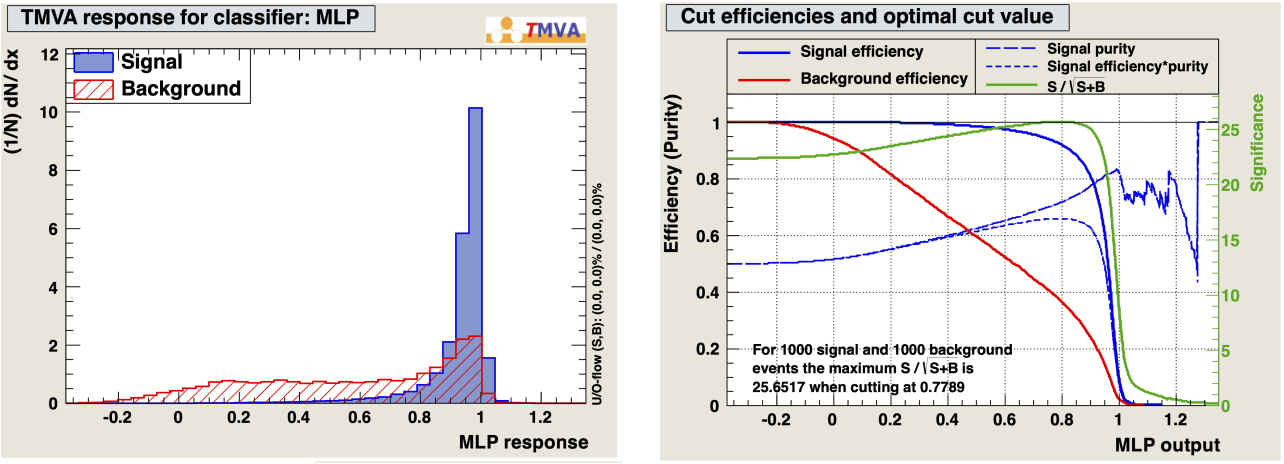

Figure **II-12**: (Left) MLP output, IsPhoton, for signal photons (blue) and merged π^0 background (red) samples for the inner calorimeter region. (Right) Efficiencies for signal (red) and background (solid blue) as a function of the MLP output cut. The default cut is selected as IsPhoton>0.6. Figures are from Ref. [59].

to modify the simple $\cos^2\theta$ shape for the π^0 background, typically making it less distinct from the signal. This is the case for the K^{*0} and ρ^0 regions, which are broad due to the relatively large widths of these states. Therefore, helicity-angle shapes of the π^0 background for the channels involving $\bar{K}^{*0}$ and ρ^0 are extracted according to the amplitude models measured for $D^0\to K^-\pi^+\pi^0$ and $D^0\to\pi^+\pi^-\pi^0$ processes (Section **III.2.1**). The $\cos^2\theta$ shape should be a good approximation for $D^0\to\phi\pi^0$, as ϕ meson is relatively narrow and very close to the $M(K^+K^-)$ threshold, which make any non-ϕ contribution very suppressed.

All the above considerations for $D^0\to V\pi^0$ apply also to $D^0\to V\eta$ background, as both π^0 and η

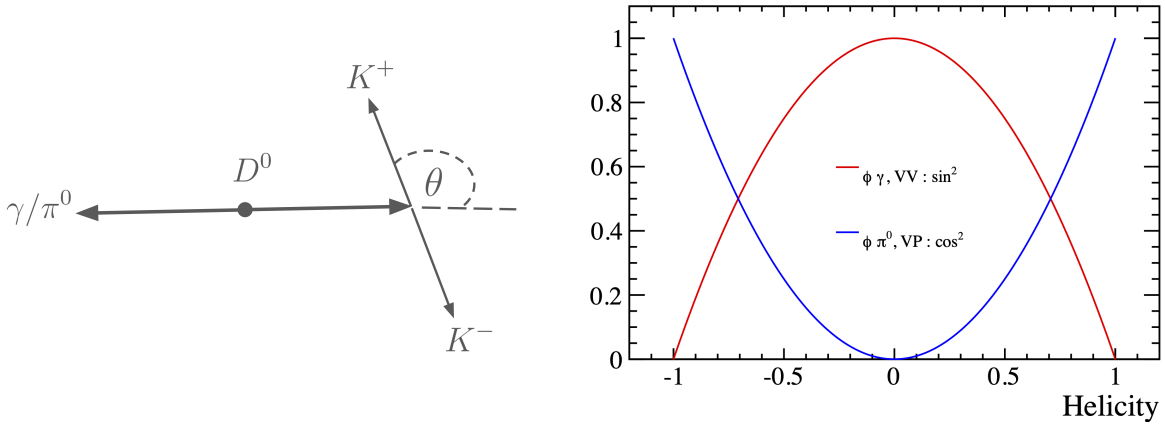

Figure **II-13**: (Left) Helicity angle θ of the K^+K^- system in $D^0 \to K^+K^-\gamma$ and $D^0 \to K^+K^-\pi^0$ decays. (Right) Expected shapes of the $\cos\theta$ distribution for $D^0 \to \phi\gamma$ (red) and $D^0 \to \phi\pi^0$ (blue) decays, with $\phi \to K^+K^-$.

are pseudo-scalar mesons. Therefore, any residual η background can be distinguished from the signal decays using helicity angle, in addition to the $M(D^0)$ distribution. Contrary to the hadronic $h^+h^-\pi^0$ or $h^+h^-\eta$ final states, $D^0 \to h^+h^-\gamma$ is expected to be dominated by the contribution from $V \to h^+h^-$, so the helicity-angle shape should follow $(1 - \cos^2\theta)$ for the considered radiative decays.

Chapter III

Analysis overview

III.1 Strategy

The aim of the analysis is to measure CP asymmetries of the $D^0 \to \phi\gamma$ and $D^0 \to \rho^0\gamma$ and $D^0 \to \bar{K}^{*0}\gamma$ decays. Those had previously been measured at Belle [40], but not at LHCb.

The full decay chains studied are: $D^{*+} \to D^0\pi_s^+$, with $D^0 \to V\gamma$, where vector meson V is reconstructed as $\phi \to K^+K^-$, $\rho^0 \to \pi^+\pi^-$ and $\bar{K}^{*0} \to K^-\pi^+$. Obviously, the charge-conjugate decays are also considered: $D^{*-} \to \bar{D}^0\pi_s^-$, with $\bar{D}^0 \to \bar{V}\gamma$, where $\bar{V}$ stands for $\phi \to K^+K^-$, $\rho^0 \to \pi^+\pi^-$[18], and $K^{*0} \to K^+\pi^-$. The electric charge of the soft pion $\pi_s^\pm$ provides a flavour of the neutral D meson at its production. In the correctly reconstructed $D^{*\pm}$ decays, π_s^+ is associated with D^0 and π_s^- with $\bar{D}^0$.

Candidates for the D^0 and D^{*+} decays are constructed by combining two charged hadron candidates, a neutral object in the calorimeter, and a soft pion. Offline selection is applied to increase signal significance; it includes optimisation of the γ–π^0 separation. Yields for π_s^+ and π_s^--tagged samples and their *raw* asymmetries, are obtained from multidimensional fits to D^0 invariant mass $M(D^0)$, the difference between invariant masses of D^{*+} and D^0, $\Delta M = M(D^{*+}) - M(D^0)$, and V meson helicity angle $\cos\theta$ as observables.

Simulation samples used to optimise the offline selection, and to model shapes of the fit observables, are calibrated using the $D^0 \to \bar{K}^{*0}\pi^0$ decays selected in the helicity *edge* region with negligible $D^0 \to \bar{K}^{*0}\gamma$ signal contribution. These helicity-edge regions are also exploited for data-based calibration of $M(D^0)$ and ΔM shapes of $D^0 \to V\pi^0$ background decays.

In order to correct for charged-hadron detection asymmetries and D^{*+} production asymmetry, a reference channel is chosen for each signal mode: $D^0 \to K^+K^-$ for $D^0 \to \phi\gamma$, $D^0 \to \pi^+\pi^-$ for $D^0 \to \rho^0\gamma$ and $D^0 \to K^-\pi^+\pi^0$ for $D^0 \to \bar{K}^{*0}\gamma$ mode. Similar to the signal channels, D^0 mesons originating from D^{*+} decays are considered for the reference channels. An offline selection closely matched to the signal modes is applied to reference modes. Kinematics of the D^{*+}, π_s^+ and $K^-\pi^+$ in the reference modes are reweighed in order to match those of corresponding signal channel, as nuisance asymmetries are known to be kinematic dependent. Raw asymmetries measured for yields of the reference channels are then subtracted from raw asymmetries of the corresponding signal channels to extract CP asymmetries.

III.2 Data and simulation samples

The presented analysis is based on samples of $D^0 \to V\gamma$ decays reconstructed from the pp collisions collected at a centre-of-mass energy of $\sqrt{s} = 8$ TeV by the LHCb experiment in 2012 during Run-1 of the LHC.[19] This data sample corresponds to an integrated luminosity of 2 fb^{-1}. The data considered

[18] As ϕ and ρ^0 mesons decay to self-conjugated final states.

[19] The reason for using 2012 data, and excluding the data collected in 2011, is that the Hlt2 trigger line exploited in this work was introduced only starting from 2012.

are taken from the `CharmCompleteEvent` stream, which includes charm data stored as full DSTs rather than micro-DSTs. Standard ntuples have been produced using DaVinci v39r1p6,[20] and based on signal candidates from the stripping version `Stripping21r0p2`.

In the MC simulations, *pp* collisions are generated using Pythia8 [61] with a specific LHCb configuration, Gauss [62]. Decays underlying signal and background channels are described with models implemented in EvtGen [63], with final-state radiation generated using Photos [64]. Interactions of generated particles with the detector, and its response, are implemented using the Geant4 toolkit [65]. Simulation samples contain the standard mixture of the prompt D^{*+} production and the secondary D^{*+} production from b-hadron decays. Their respective contributions are determined by the charm and beauty production cross-sections assumed in Pythia8.

All the simulation samples are produced as *filtered* samples, meaning that only decays which fulfill the stripping selection[21] are saved for further analysis. This allows for saving disk space, though impedes estimating any absolute efficiency of signal selection; such efficiency is not necessary for measuring CP asymmetry. The stripping version used for simulated samples is the same as for the experimental data.

III.2.1 Amplitude models for signal and background decays

Decays of $D^{*+} \to D^0\pi^+$ are generated with `VSS` model [62], describing vector meson V decaying to two (pseudo-)scalar particles SS. Some details of the amplitude models used for generating signal and background D^0 decays are summarized in Table **III-1**. $D^0 \to V\gamma$ signal decays are generated with `SVP_HELAMP` model, intended for a decay of a pseudo-)scalar particle to a vector meson V and a photon P. Helicity amplitudes in this model are set to produce transversely polarised V meson and photon. As for background channels, there are two physical backgrounds that are considered significant for the signal decays, $D^0 \to V\pi^0$ and $D^0 \to V\eta$. Among those, $D^0 \to \phi\pi^0$ and $D^0 \to \phi\eta$ are generated with `SVS` model describing a (pseudo-)scalar particle decaying into a vector and a (pseudo-)scalar, while $\phi \to K^+K^-$ is produced with `VSS` model.

As discussed in Section **II.5.2**, for background modes involving ρ^0 and K^{*0}, one needs to generate $D^0 \to h^+h^-\pi^0$ and $D^0 \to h^+h^-\eta$ decays including intermediate resonances through which these processes proceed. Such resonances will contribute into the $M(h^+h^-)$ ranges selected as the ρ^0 and K^{*0} regions, and affect $\cos\theta$ shapes expected for background channels. Therefore, $D^0 \to \pi^+\pi^-\pi^0$ and $D^0 \to K^-\pi^+\pi^0$ decays are generated with the dedicated `D_DALITZ` models implemented in EvtGen. The amplitude model for $D^0 \to K^-\pi^+\pi^0$ decays is based on the analysis performed by the CLEO collaboration [69]. According to this measurement, the $D^0 \to K^-\pi^+\pi^0$ decay is dominated by the contributions from vector mesons, ρ^+, K^{*-} and $\bar{K}^{*0}$, with only subleading contributions from scalar $\bar{K}_0(1430)^0$ and non-resonant (NR) component. The decay model of $D^0 \to \pi^+\pi^-\pi^0$ is also measured by CLEO [70] and is fairly simple. The decay is dominated with vector mesons ρ^+, ρ^- and ρ^0, with only a small NR component.[22]

The amplitude model of the $D^0 \to K^-\pi^+\eta$ decay has been recently measured by Belle [71], but not yet implemented into EvtGen. Therefore, it is approximated with a *cocktail* of resonance contributions, $\bar{K}^{*0}$, $a_0(980)^+$ and $\bar{K}_0(1430)^0$, motivated by the Belle measurement. These contributions are added incoherently, i.e. neglecting any interference effects between resonances. Similarly, an incoherent cocktail describing the $D^0 \to \pi^+\pi^-\eta$ decay comprises contributions from ρ^0, $a_0(980)^+$ and NR component. It is based on the Belle analysis [72], which is not an amplitude analysis but presents the Dalitz distribution for the $D^0 \to \pi^+\pi^-\eta$ decay, $M^2(\pi^+\pi^-)$ vs. $M^2(\pi^-\eta)$, as well as its projections. As the models used to describe the η background are rough, the experimental data are fitted also with the contributing

[20] The same DaVinci version has been used for most of the simulation samples; DaVinci v45r8 has been used for the last of a few productions of the π^0 background and for all the η-background samples.

[21] With an exception of requirements on the particle identification, which are known to be poorly modelled in simulations.

[22] The three ρ states contributing into $D^0 \to \pi^+\pi^-\pi^0$ interfere destructively, hence the sum of their decay fractions in Table **III-1** exceeds 100%.

Channel	Model	Details
$D^0 \to \phi\gamma$		
$D^0 \to \rho^0\gamma$	SVP_HELAMP	V meson and γ with helicities of ± 1
$D^0 \to \bar{K}^{*0}\gamma$		
$D^0 \to K^+K^-\pi^0$	SVS	$D^0 \to \phi\pi^0$ (100%), ϕ helicity = 0
$D^0 \to \pi^+\pi^-\pi^0$	D_DALITZ	$D^0 \to \rho^+[\to \pi^+\pi^0]\pi^-$ (76%) $D^0 \to \pi^+\rho^-[\to \pi^-\pi^0]$ (32%) $D^0 \to \rho^0[\to \pi^+\pi^-]\pi^0$ (24%) $D^0 \to [\pi^+\pi^-\pi^0]_{NR}$ (3%)
$D^0 \to K^-\pi^+\pi^0$	D_DALITZ	$D^0 \to K^-\rho^+[\to \pi^+\pi^0]$ (78%) $D^0 \to K^{*-}[\to K^-\pi^0]\pi^+$ (16%) $D^0 \to \bar{K}^{*0}[\to K^-\pi^+]\pi^0$ (13%) $D^0 \to [K^-\pi^+\pi^0]_{NR}$ (7%) $D^0 \to \bar{K}_0(1430)^0[\to K^-\pi^+]\pi^0$ (4%)
$D^0 \to K^+K^-\eta$	SVS	$D^0 \to \phi\eta$ (100%), ϕ helicity = 0
$D^0 \to \pi^+\pi^-\eta$	incoherent cocktail	$D^0 \to \rho^0[\to \pi^+\pi^-]\eta$ (33%) $D^0 \to a_0(980)^+[\to \pi^+\eta]\pi^-$ (33%) $D^0 \to [\pi^+\pi^-\eta]_{NR}$ (33%)
$D^0 \to K^-\pi^+\eta$	incoherent cocktail	$D^0 \to \bar{K}^{*0}[\to K^-\pi^+]\eta$ (48%) $D^0 \to K^-a_0(980)^+[\to \pi^+\eta]$ (39%) $D^0 \to \bar{K}_0(1430)^0[\to K^-\pi^+]\eta$ (32%)

Table **III-1**: Summary of the D^0 decay models used in simulations. Numbers in brackets correspond to fractions of total rate measured or assumed for given resonant or non-resonant (NR) component.

components allowed to have free and independent yields (Section **V**), rather than relative rates fixed as in the cocktail samples (Table **III-1**).

The full detector simulation is performed for all the above mentioned samples. In addition, the analysis exploits a sample of the $D^0 \to K^-\pi^+\pi^0$ decays generated according to the resonance model measured by the BaBar collaboration [73], for which the detector effects have not been simulated. The fully simulated $D^0 \to K^-\pi^+\pi^0$ sample based on the CLEO model is used to measure an acceptance (i.e. reconstruction and selection efficiency) as a function of $\cos\theta$ (Section **IV.5.2**); in this estimation an impact of the decay model cancels out. The theoretical shape of $\cos\theta$ is obtained using the sample generated with the BaBar model. The BaBar model is based on the larger data sample, of about 660×10^3 events, and thus more reliable compared to the CLEO model, which was measured using a limited signal statistics of 7×10^3 events only.

Hereafter, background denoted as $D^0 \to V\pi^0$ corresponds to the background originating from $D^0 \to h^+h^-\pi^0$ decays with the $M(h^+h^-)$ selected within V mass region. Similar applies to $D^0 \to V\eta$ background.

III.3 Reconstruction and selection of signal decays

The decay chain considered as the signal decays is: $D^{*+} \to D^0\pi_s^+$, with $D^0 \to V\gamma$, where V meson is reconstructed as $\phi \to K^+K^-$, $\rho^0 \to \pi^+\pi^-$ and $\bar{K}^{*0} \to K^-\pi^+$; the charge-conjugate decays are also included. Candidates for the D^0 decays are constructed by combining two oppositely-charged charged hadrons (kaons, pions, or both) with a neutral object in the calorimeter; D^{*+} candidates are formed by adding a soft tagging pion to a D^0 candidate. The D^{*+} candidates are constructed within the stripping, where they are selected based on kinematic, particle-identification and topological criteria, described in Section **III.3.1**. The stripping selection includes also some trigger requirements, which then are tightened to obtain the final trigger selection discussed in Section **III.3.2**. The offline selection, presented in Section **III.3.3**, is applied to further suppress background contributions and increase the signal significance.

III.3.1 Stripping preselection

Table **III-2** shows the stripping lines used for the signal, and Table **III.3.1** presents the stripping requirements. There is a dedicated line for each $D^0 \to V\gamma$ signal channel, but their selections are identical except for the PID requirements placed for hadron D^0 daughters; they differ between kaons and pions.

Signal channel	Stripping line
$D^0 \to \phi\gamma$	`StrippingDstarD2XGammaDstarD2KKGammaLine`
$D^0 \to \bar{K}^*0\gamma$	`StrippingDstarD2XGammaDstarD2KPiGammaLine`
$D^0 \to \rho^0\gamma$	`StrippingDstarD2XGammaDstarD2PiPiGammaLine`

Table **III-2**: Stripping lines used for signal channels.

The p_T requirements on the D^0 daughters and D^0 candidates help to suppress combinatorial background from random combinations of tracks and photons. PID selection requiring that charged tracks are identified as pions or kaons, significantly reduce background originating from (primarily hadronic) charm decays due to kaon wrongly identified as pion, or vice versa. In particular, this selection will suppress the $K \to \pi$ mis-identification (misID) background from $D^0 \to K^-\pi^+\pi^0$ CF decays in the reconstructed sample of $D^0 \to \rho^0\gamma$ candidates. The PID_K variable discriminates between kaon and pion hypotheses in terms of the likelihood-based classifier $DLL_{K,\pi}$, discussed in Section **II.2.3** and defined in Eq. **II.1**. The corresponding variable discriminating between pion and kaon is $PID_\pi = DLL_{\pi,K}$, and thus $PID_\pi = -PID_K$. Hence, an upper threshold on PID_K is set to identify pions.

Track-related variables comprise χ^2_{track} corresponding to the track fit χ^2, which describes track quality, as well as the ghost probability *GhostProb*. Both are discussed along with the tracking algorithm in Section **II.2.2**. Requirements on the quality of decay vertex χ^2_{VTX}[23] placed for V, D^0 and D^{*+} candidates remove those formed using random tracks.

Topological variables are calculated with respect to the associated PV, a.k.a best PV (BPV), defined as a reconstructed PV with respect to which a signal candidate has the smallest IP. The stripping selection exploits an important feature of charm-hadron decays, namely the displaced decay vertex with respect to the BPV. Hence the requirement on the significance of such a displacement, χ^2_{VD}. Decay time of a D^0 candidate is reconstructed from its flight distance (FD) between BPV and SV. Cutting off the low decay-time region also helps to suppress combinatorial background. A very useful topological

[23]Vertex fitter used for SV fitting in offline analysis takes as an input vector of particles, forms a common vertex, in which particle momenta intersect, by adding particles one by one, and changing their position and four-momentum vectors. After the fit converges, the mother particle is updated with new four-momentum, mass, SV position and the vertex-fit χ^2.

Variable	Cut	Variable description
		Photon
p_T	> 1.7 GeV/c	Transverse momentum
		Charged track $h^{\pm}$
p_T	> 250 MeV/c	Transverse momentum
$PID_K(K)$	> 5	Kaon-like PID applied for kaons
$PID_K(\pi)$	< 0	Kaon-like PID applied for pions
$GhostProb$	< 0.5	Probability that track is a ghost
χ^2_{IP}	> 3	Significance of IP
χ^2_{track}	< 4	Track quality
		$V \to h^+h^-$
χ^2_{DOCA}	< 10	Significance of DOCA between h^+ and h^- tracks
χ^2_{VTX}	< 16	Vertex quality
χ^2_{VD}	> 100	Significance of decay vertex displacement from BPV
$M(V)$	$(0, 1865)$ MeV/c^2	h^+h^- invariant mass
		$D^0 \to V\gamma$
p_T	> 2 GeV/c	Transverse momentum
χ^2_{VTX}	< 12	Vertex quality
$t(D^0)$	> 0.1 ps	Decay time with respect to BPV
χ^2_{IP}	< 35	Significance of IP
$DIRA$	> 0.9995	Cosine of direction angle
$M(D^0)$	$(1610, 2100)$ MeV/c^2	$V\gamma$ invariant mass
		Soft pion
χ^2_{track}	< 3	Track quality
		$D^{*+} \to D^0\pi^+_s$
χ^2_{VTX}	< 15	Vertex quality
ΔM	< 163 MeV/c^2	$M(D^{*+}) - M(D^0)$

Table **III-3**: Stripping selection for signal channels. DOCA stands for distance of closest approach (Section **II.2**).

variable is χ^2_{IP}, defined as the difference between the vertex-fit χ^2 of a given PV reconstructed with and without considered particle. Selecting the relatively small values of χ^2_{IP} for D^0 candidates reduces contamination from the secondary charm sample, while requiring the significant χ^2_{IP} for $h^{\pm}$ removes tracks originating from given PV. Direction angle (DIRA), defined as an angle between the particle momentum and the direction vector between SV and the BPV, suppresses contamination from partially-

reconstructed decays; for properly reconstructed decays the direction angle is close to zero.

III.3.2 Trigger selection

Trigger selection at the L0 level requires:

$$\texttt{D\_L0HadronDecision\_TOS==1 OR Dst\_L0GlobalDecision\_TIS==1}, \qquad \textbf{(III.1)}$$

where `TOS` (Trigger On Signal) means that given particle has fired the specified trigger; in this case, `L0Hadron` has been fired by any of hadron daughters of a D^0 candidate. Whereas `TIS` (Trigger Independent of Signal) means that `L0Global` has been fired by any particle from the underlying event, except for those forming given D^{*+} candidate. `L0Global` indicates any of the L0 trigger lines, namely `L0Hadron`, `L0Muon`, `L0Electron` or `L0Photon` (Section **II.3.1**).

Hlt1 selection, applied to signal candidates that have fulfilled the L0 selection, is:

$$\texttt{D\_Hlt1TrackAllL0Decision\_TOS==1}. \qquad \textbf{(III.2)}$$

It requires that at least one of D^0 daughter tracks, h^+ or h^-, satisfies criteria listed in Table **III.3.2**. Basically, a track firing `Hlt1TrackAllL0` must be of a very good quality, have large p_T and be significantly displaced from PV.

Variable	Cut
VELO hits	> 9
VELO missing hits	< 3
Tracker hits	> 16
χ^2_{track}	< 2
p_T	> 1.6 GeV/c
p	> 3 GeV/c
IP	> 0.1 mm
χ^2_{IP}	> 16

Table **III-4**: Selection for `Hlt1TrackAllL0` line.

Hlt2 selection, applied to signal candidates that have fulfilled the L0 and Hlt1 requirements, is:

$$\texttt{Dst\_Hlt2CharmHadD02HHXDsthhXDecision\_TOS==1}. \qquad \textbf{(III.3)}$$

This Hlt2 line is an *inclusive* D^* line, very broad in scope - the final state of reconstructed decays has two oppositely-charged hadrons, soft pion and some other unreconstructed particle(s). The inclusive line has been employed, as no exclusive trigger dedicated to radiative charm decays existed in Run-1. Basically, this D^* inclusive line requires two charged particles h^+h^- to be combined with a soft pion to form a partially reconstructed D^{*+} candidate. To allow for missing particles, only a very loose selection is applied on $M(h^+h^-)$. The detailed selection is summarised in Table **III.3.2**. In addition to those selections, it is required that two tracks are associated to the same PV, and that π_s^+ and h^+h^- system originate from the same PV.

Variable	Cut	Brief description
	Global Event Cuts	
N_{tracks}	< 180	Number of long tracks
Trigger	`D_Hlt1TrackAllL0`	Track firing Hlt1
	Charged track $h^{\pm}$	
p_T	> 300 MeV/c	Transverse momentum
p	> 3 GeV/c	Momentum
χ^2_{track}	< 3	Track quality
χ^2_{IP}	> 6	Significance of IP
	h^+h^-	
$p_T(h^+) + p_T(h^-)$	> 0	Vector sum of p_T
$min[\chi^2_{track}(h^+), \chi^2_{track}(h^-)]$	< 2.25	Smallest χ^2_{track}
$DOCA$	< 0.1 mm	DOCA between h^+ and h^-
χ^2_{VTX}	< 10	Vertex quality
χ^2_{FD}	> 100	Significance of flight distance
$max[\chi^2_{IP}(h^+), \chi^2_{IP}(h^-)]$	> 36	Largest χ^2_{IP}
$DIRA$	> 0.99	Cosine of direction angle
$M(h^+h^-)$	< 2100 MeV/c^2	h^+h^- invariant mass
	Soft pion	
p_T	> 300 MeV/c	Transverse momentum
p	> 3 GeV/c	Momentum
χ^2_{track}	< 2.25	Track quality
χ^2_{IP}	< 9	Significance of IP
	$D^{*+} \to (h^+h^-)\pi^+_s$	
$DOCA$	< 100 mm	DOCA between h^+h^- and π_s
p_T	$> 3500 \div 3850$ MeV/c	Transverse momentum
ΔM	$< 250 \div 285$ MeV/c^2	$M(h^+h^-\pi_s) - M(h^+h^-)$

Table **III-5**: Selection requirements in inclusive D^* line `Hlt2CharmHadD02HHXDsthhX`. Requirements on $p_T(D^{*+})$ and ΔM varied during the data taking within the ranges quoted.

III.3.3 Offline selection

At this stage only the D^{*+} candidates that have passed the stripping selection and the trigger requirements are considered. Within the offline selection some of the stripping cuts are tightened, additional requirements are applied for γ candidates, and $M(h^+h^-)$ is selected within mass ranges of the considered

Variable	Cut	Variable description
	Photon	
p_T	> 2 GeV/c	Transverse momentum
γ_{CL}	> 0.25 and $\neq 0.5$	PID of γ
`VetoPi0R`	$== 0$	Resolved π^0 veto
IsPhoton	> 0.86 (0.95 for $D^0 \to \rho^0\gamma$)	γ–π^0 separation
	Hadron daugthers $h^\pm$	
$PID_K(K)$	> 10	Kaon-like PID applied for kaons
$PID_K(\pi)$	< -10	Kaon-like PID applied for pions
p_T	> 800 MeV/c	Transverse momentum
	$V \to h^+h^-$	
$M(K^{*0})$	(892 ± 60) MeV/c^2	
$M(\phi)$	(1020 ± 10) MeV/c^2	h^+h^- invariant mass
$M(\rho^0)$	(770 ± 150) MeV/c^2	
	$D^0 \to V\gamma$	
$M(D^0)$	$(1680, 2080)$ MeV/c^2	$V\gamma$ invariant mass
$\ln \chi^2_{IP}$	< 3	Significance of IP
$\arccos(DIRA)$	< 0.02 rad	Direction angle
	Soft pion	
$GhostProb$	< 0.8	Probability that track is a ghost
	$D^{*+} \to D^0\pi^+_s$	
ΔM	$(139.5, 161.0)$ MeV/c^2	$M(D^{*+}) - M(D^0)$

Table **III-6**: Offline selection applied to signal candidates. Requirements on $M(D^0)$ and ΔM are applied to the variables after employing DTF to the full decay chain. The lower ΔM range corresponds to the nominal π^+ mass.

V mesons taking into account their natural widths.

Tighter requirements on PID of the $h^\pm$ tracks and their p_T are needed primarily to align the signal selection with the stripping selection of $D^0 \to h^+h^-$ reference channels (Section **VII.2**). Tighter cut on $\chi^2_{IP}(D^0)$ suppresses further a secondary-charm contamination, which is important for employing a kinematic fit discussed below.

The offline selection includes also the standard requirements on the photon confidence level, γ_{CL}.[24] This is a photon PID variable discriminating between photons and electrons or charged hadrons. The γ_{CL} is related to $\mathrm{DLL}_{\gamma,e+h}$ (Section **II.2.4**) through $\gamma_{CL} = \frac{1}{2}(\tanh \mathrm{DLL}_{\gamma,e+h} + 1)$. Vetoing resolved π^0 mesons using `VetoPi0R` method (Section **II.5**) allows to suppress a large fraction of background from photons originating from π^0 decays. A D^0 candidate is rejected if its daughter photon combined

[24] Note that $\gamma_{CL} \neq 0.5$ removes calorimeter objects that cannot be identified.

with any other photon from given event has the $M(\gamma\gamma)$ value within ± 30 MeV/c^2 of the nominal π^0 mass, $m_{\pi^0} = 135$ MeV/c^2. Effects of vetoing resolved π^0 mesons on $M(D^0)$ and ΔM distributions in simulations of $D^0 \to \bar{K}^{*0}\gamma$ and $D^0 \to \bar{K}^{*0}\pi^0$ decays, are illustrated in Fig. **III-1**. While the impact on $D^0 \to \bar{K}^{*0}\gamma$ decays is minor, the $M(D^0)$ shape in $D^0 \to \bar{K}^{*0}\pi^0$ decays is significantly affected in the low-mass region, where a contribution from $\pi^0 \to \gamma\gamma$ with one missing photon is expected.

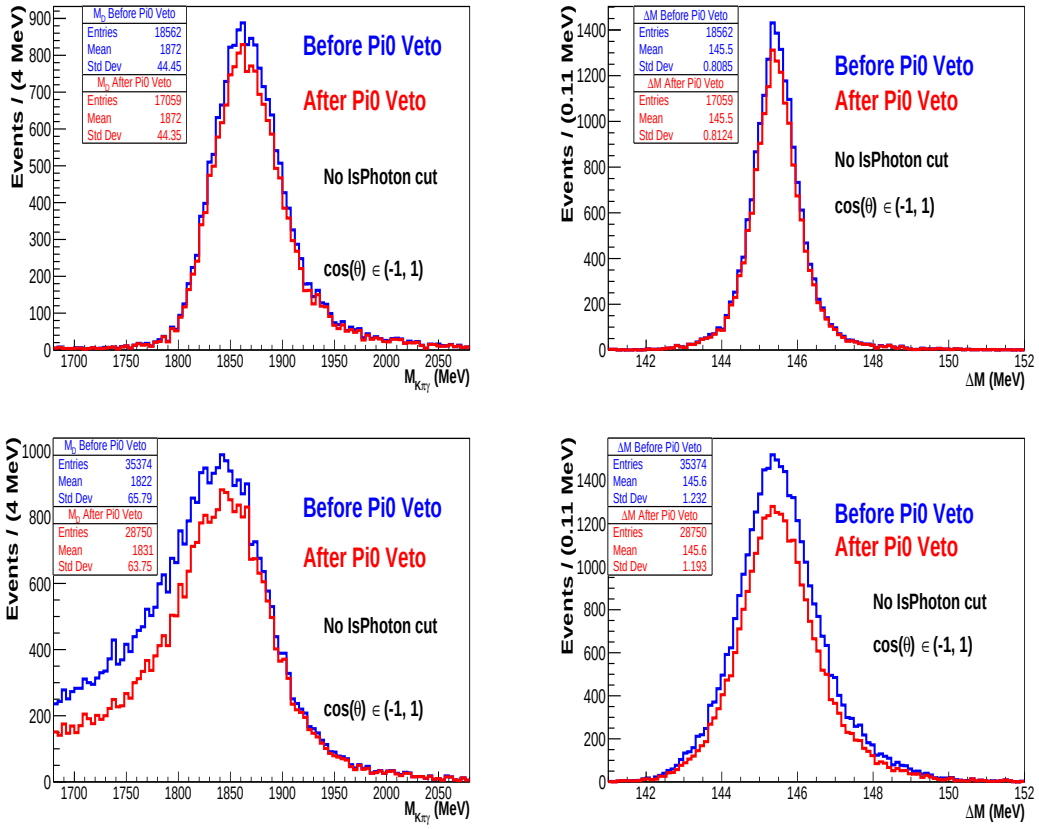

Figure **III-1**: Effect of vetoing resolved π^0 mesons on (left) $M(D^0)$ and (right) ΔM distributions in simulations of (top) $D^0 \to \bar{K}^{*0}\gamma$ and (bottom) $D^0 \to \bar{K}^{*0}\pi^0$ decays after the full selection except for IsPhoton cut. Distributions before applying π^0 veto are shown in blue, those after π^0 veto in red.

Increasing the photon p_T cut value facilitates using the IsPhoton classifier to distinguish between γ and merged π^0 candidates (Section **II.5.1**). This tool is designed for neutral objects having $p_T > 2$ GeV/c, which is the threshold for neutral pions to be reconstructed as merged. In any case, signal candidates reconstructed in the range $1.7 < p_T < 2.0$ GeV/c are largely dominated by combinatorial background. The standard γ_{CL} selection, as in Table **III.3.3**, is also applied for samples used in training/testing the IsPhoton classifier. IsPhoton> 0.86 is already the optimal requirement; the optimisation is presented in Section **IV.4**.

The requirements on $M(D^0)$ and ΔM in Table **III.3.3** are applied to the variables recalculated after employing a kinematic fit using `DecayTreeFitter` (DTF) [74]. DTF is applied to the full signal decay chain, with the constraint that D^{*+} candidates originate from the associated PV. After the DTF converges, the position and four-momentum vectors of all the particles in the decay chain are recalculated. Applying DTF improves resolution of the signal observables, in particular of ΔM (Fig. **III-2**). Obviously, the DTF condition is not satisfied for secondary D^{*+} candidates, and any significant secondary contribution would result in distorted ΔM after DTF. To avoid this, a secondary contamination is suppressed with the tightened χ^2_{IP} requirement to a few percent level. In the presented analysis only refitted $M(D^0)$ and ΔM are used.

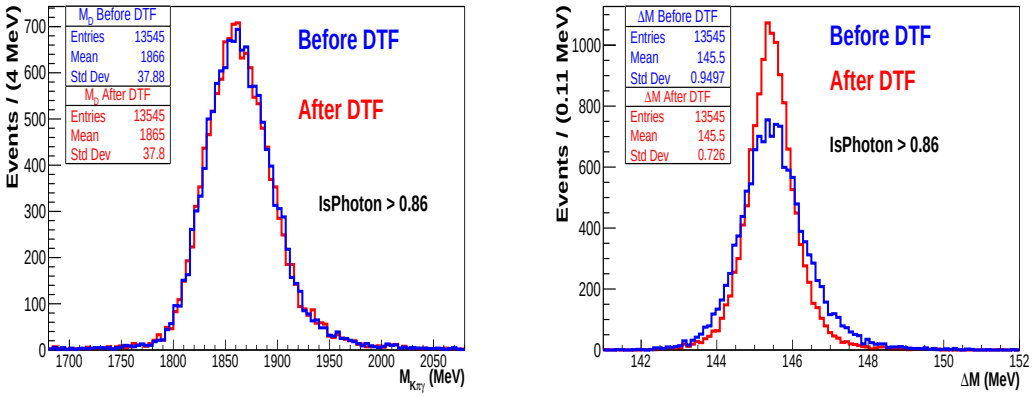

Figure **III-2**: Impact of `DecayTreeFitter` on (left) $M(D^0)$ and (right) ΔM distributions in $D^0 \to \bar{K}^{*0}\gamma$ simulation after the full selection. Distributions before applying DTF are shown in blue, those after applying DTF in red.

Helicity-angle selection

As discussed in Section **II.5.2**, distinct $\cos\theta$ shapes are expected for radiative signal decays and for π^0 or η background channels. In order to take advantage of this feature, $\cos\theta$ in a central region (with $\cos\theta \simeq 0$) is chosen for the signal selection. In addition, an edge region (with $\cos\theta \simeq \pm 1$) is also considered for π^0 enhanced selection; any signal contribution to this region is negligible or very small. Samples of $D^0 \to V\pi^0$ background decays, obtained from the helicity-edge regions in the experimental data, are used for calibrating calorimeter variables in simulation samples (Section **IV.2**), as well as for data-based calibration of $M(D^0)$ and ΔM shapes of $D^0 \to V\pi^0$ background (Sections **V.3** - **V.5**). As $\cos\theta$ is based on kinematics of hadron D^0 daughters, it is largely independent of neutral D^0 daughter. Therefore, shape/resolution of variables, which are driven by properties of γ candidates, are to a good approximation the same between both helicity regions. The two helicity regions are specified independently for each $D^0 \to V\gamma$ decay, as reported in Table **III.3.3**.

Channel	Central region	Edge region
$D^0 \to \bar{K}^{*0}\gamma$	$-0.4 < \cos\theta < 0.7$	$-0.95 < \cos\theta < -0.7$
$D^0 \to \phi\gamma$	$-0.8 < \cos\theta < 0.8$	$\cos\theta < -0.8$ or $\cos\theta > 0.8$
$D^0 \to \rho^0\gamma$	$-0.6 < \cos\theta < 0.5$	$\cos\theta > 0.7$

Table **III-7**: Selection on $\cos\theta$ in signal-enhanced (*central*) region, and π^0 enhanced (*edge*) region.

Helicity-center regions for channels involving $\bar{K}^{*0}$ and ρ^0 states is decided mostly taking into account how intermediate resonances in $D^0 \to K^-\pi^+\pi^0$ and $D^0 \to \pi^+\pi^-\pi^0$ decays are expected to contribute to the $\cos\theta$ distributions. Regions of $\cos\theta$ with sharp features are avoided, as their exact shapes would be largely dependent on amplitude models of $D^0 \to K^-\pi^+\pi^0$ and $D^0 \to \pi^+\pi^-\pi^0$ decays, in particular on interference of narrow resonances. Helicity-edge regions are also chosen to avoid any $\cos\theta$ features that would be strongly dependent on $D^0 \to K^-\pi^+\pi^0$ and $D^0 \to \pi^+\pi^-\pi^0$ resonance models. An impact of imperfect modelling of η background is also minimised as much as possible, given that assumed $D^0 \to K^-\pi^+\eta$ and $D^0 \to \pi^+\pi^-\eta$ models assumed are rough (Section **III.2.1**). In addition, avoiding such regions facilitates parametric description of $\cos\theta$ distributions for π^0 or η background. Selecting a positive helicity edge for the $D^0 \to \rho^0\gamma$ channel allows to avoid residual $K \to \pi$ misID background from the $D^0 \to K^-\pi^+\pi^0$ channel.

On the other hand, helicity-edge regions should be broad enough to assure π^0 background yields large enough for the calibration purpose. An illustration of the $\cos\theta$ selection for the $D^0 \to K^-\pi^+\pi^0$ decay is shown in Fig. **III-3**. It presents the $\cos\theta$ distribution in the simulation sample based on the CLEO model (Section **III.2.1**), and passing the full selection of the $D^0 \to \bar{K}^{*0}\gamma$ signal.

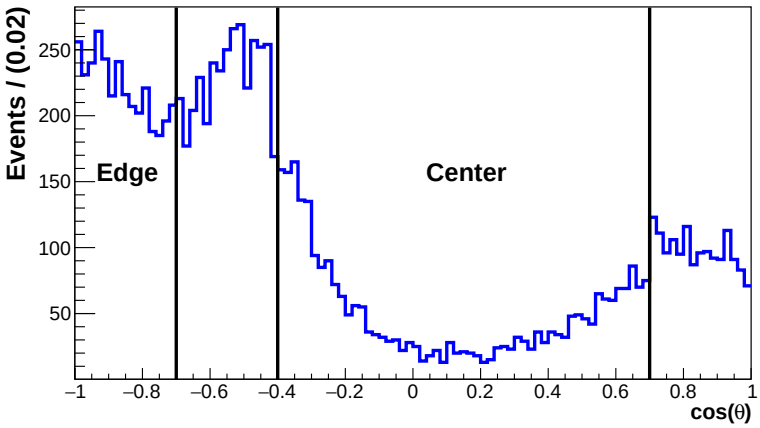

Figure **III-3**: Distribution of $\cos\theta$ in $D^0 \to K^-\pi^+\pi^0$ simulation sample passing the $D^0 \to \bar{K}^{*0}\gamma$ signal selection. Edge and central helicity regions are indicated.

For the $D^0 \to \phi\gamma$ channel, where no significant non-ϕ contribution is expected in either π^0 or η background, the central and edge helicity regions are selected taking into account the signal efficiency, and expected yield of the π^0 background.

Chapter IV

Simulation studies

Simulation samples for the signal and background decays have been produced using procedures described in Section **III.2**, and with the decay models discussed in Section **III.2.1**. Reconstructed D^{*+} candidates are selected using the same stripping, trigger and offline requirements as for the experimental data; they are detailed in Sections **III.3.1**, **III.3.2** and **III.3.3**, respectively. In addition, `TruthMatching`[25] is employed to accept only correctly reconstructed signal candidates, and to select background candidates mis-reconstructed in the way that is expected for given background decays, i.e. with one neutral particle missing or wrongly reconstructed.

IV.1 PID calibration

The PID response, for example the PID_K variable that is employed in the selection, is known to be poorly simulated in MC samples. This leads to different efficiencies of the PID requirements in the selection, and can distort signal shapes, in particular, the helicity angle which is based on $h^{\pm}$ momenta. Therefore, it is necessary to calibrate simulation samples, using data-driven techniques and abundant control channels, as mentioned in Section **II.2.3**. $D^0 \to K^-\pi^+$ decays originating from $D^{*+} \to D^0\pi_s^+$, are usually exploited for calibrating PID of charged kaons and pions. There is a suit of tools for PID calibration, `PIDCalib`, that provides several solutions for recalibrating simulated data [75]. In the presented analysis, the so-called PID resampling is employed. Resampling uses probability density functions (PDFs) of the PID response of the calibration data to generate random PID variables in bins of momentum, pseudorapidity, and number of tracks in the underlying event. Figure **IV-1** shows the effect of the resampling on the PID_K for the $D^0 \to \bar{K}^{*0}\gamma$ simulation sample after the stripping selection.

IV.2 Calibration of calorimeter variables

Simulation of the calorimeter response is also imperfect, as already demonstrated in the LHCb studies of radiative decays of B mesons. This may lead to data-MC differences in particular in $M(D^0)$ shapes of both, $D^0 \to V\gamma$ signal and $D^0 \to V\pi^0$ background; these shapes are driven primarily by a neutral-object energy resolution. In addition, a simulation-based classifier for the γ–π^0 separation (Section **IV.3**) might be suboptimal if constructed with calorimeter variables having distributions significantly different from the experimental data.

The $D^0 \to \bar{K}^{*0}\pi^0$ sample, obtained from the experimental data in the helicity-edge region, is used for calibrating calorimeter variables. It is required to pass the full selection of the $D^0 \to \bar{K}^{*0}\gamma$ signal, except for the requirement on IsPhoton, as it is a calorimeter-based classifier. The $D^0 \to \bar{K}^{*0}\pi^0$ events

[25] `TruthMatching` is a tool available for simulations, which allows to associate reconstructed particles with generated (true) ones, and to track back their mother and grandmother particles.

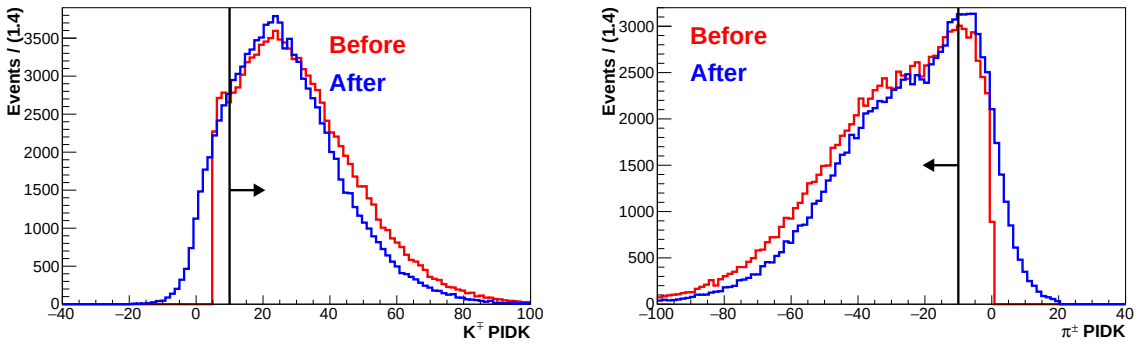

Figure **IV-1**: Original (red) and resampled (blue) PID_K responses for (left) kaon-like candidates and (right) pion-like candidates from $D^0 \to \bar{K}^{*0}\gamma$ simulation after the stripping selection. Black line indicates the offline-selection requirement.

are extracted statistically using the *sPlot* technique [76], with *sWeights* based on the two-dimensional fit to the $M(D^0)$ and $\cos\theta$ distributions. The fit is described in Section **V.2**. The total yield of the $D^0 \to \bar{K}^{*0}\pi^0$ calibration sample is about 65×10^3 events.

Simulation samples of both, signal and π^0 background are calibrated using the $D^0 \to \bar{K}^{*0}\pi^0$ sample. There are a few reasons justifying this approach. The π^0 mesons within the calibration sample are reconstructed as photons, so their calorimeter clusters are photon-like. At LHCb, similar techniques are employed for the photon and π^0 reconstruction (Section **II.2.4**). Therefore, similar biases can be expected in the simulation of ECAL and PS cluster characteristics for photons and π^0 mesons. This is indeed visible in data-MC comparison of the ECAL and PS variables underlying IsPhoton [59]; the data-MC differences are similar for γ and π^0 candidates.

Calibration of calorimeter variables is performed in two steps. First, the distributions in the $D^0 \to \bar{K}^{*0}\pi^0$ simulation are matched to those in the calibration data sample using multivariate reweighing in the `Folding Reweighter` tool. The obtained weights are applied to the distributions in simulation samples of $D^0 \to \phi\pi^0$, $D^0 \to \rho^0\pi^0$, and all the signal samples, on candidate-by-candidate basis.

The variables which show the largest discrepancy between the simulated $D^0 \to \bar{K}^{*0}\pi^0$ sample and the calibration sample are: κ in ECAL, $r2$, $E_{\max}/E_{\text{sum}}$, $E_{4\max}$, and E_{49} in PS, as well as nSPDHits. Here E_{49} denotes the ratio of the energy deposit between the 2×2 and 3×3 clusters, $E_{4\max}$ refers to the energy of the most energetic cell in 2×2 cluster, the remaining variables describing cluster shapes are defined in Section **II.5.1**. nSPDHits is the number of hits left in SPD in a given event. This *minimal* set of variables in the simulation has been matched to the $D^0 \to \bar{K}^{*0}\pi^0$ calibration data. Comparison of the cluster-shape variables before the reweighing is shown in Fig. **IV-2**, and after the reweighing in Fig. **IV-3**. Distributions of nSPDHits are compared in Fig. **IV-4**.

After the reweighing, some disagreement initially present in the π^0 related variables, such as γ_{CL} and IsPhoton, have been reduced. The reweighing based on the minimal set of variables also improved the data-MC agreement for other cluster-shape observables through correlations between them. Topological variables ($\chi^2_{IP}(D^0)$, D^0 direction angle), and kinematic variables ($p_T(D^{*+})$, $p_T(D^0)$, $p_T(\pi_s^+)$) have shown a good agreement between the calibration data and the simulation to begin with.[26]

The calibrated simulation samples are used for constructing a dedicated classifier for γ–π^0 separation, described in Section **IV.3**. The calibration is found to have very little impact on the shapes of the variables used for the signal extraction, $M(D^0)$, $\cos\theta$ and ΔM. Fits to these variables for the simulated signal and background samples are introduced in Sections **IV.5** - **IV.11**.

[26] Some discrepancy is observed in p_T of the charged D^0 daughters, but this is expected as the calibration sample originates from the helicity-edge region while the simulation is considered in the full $\cos\theta$ range.

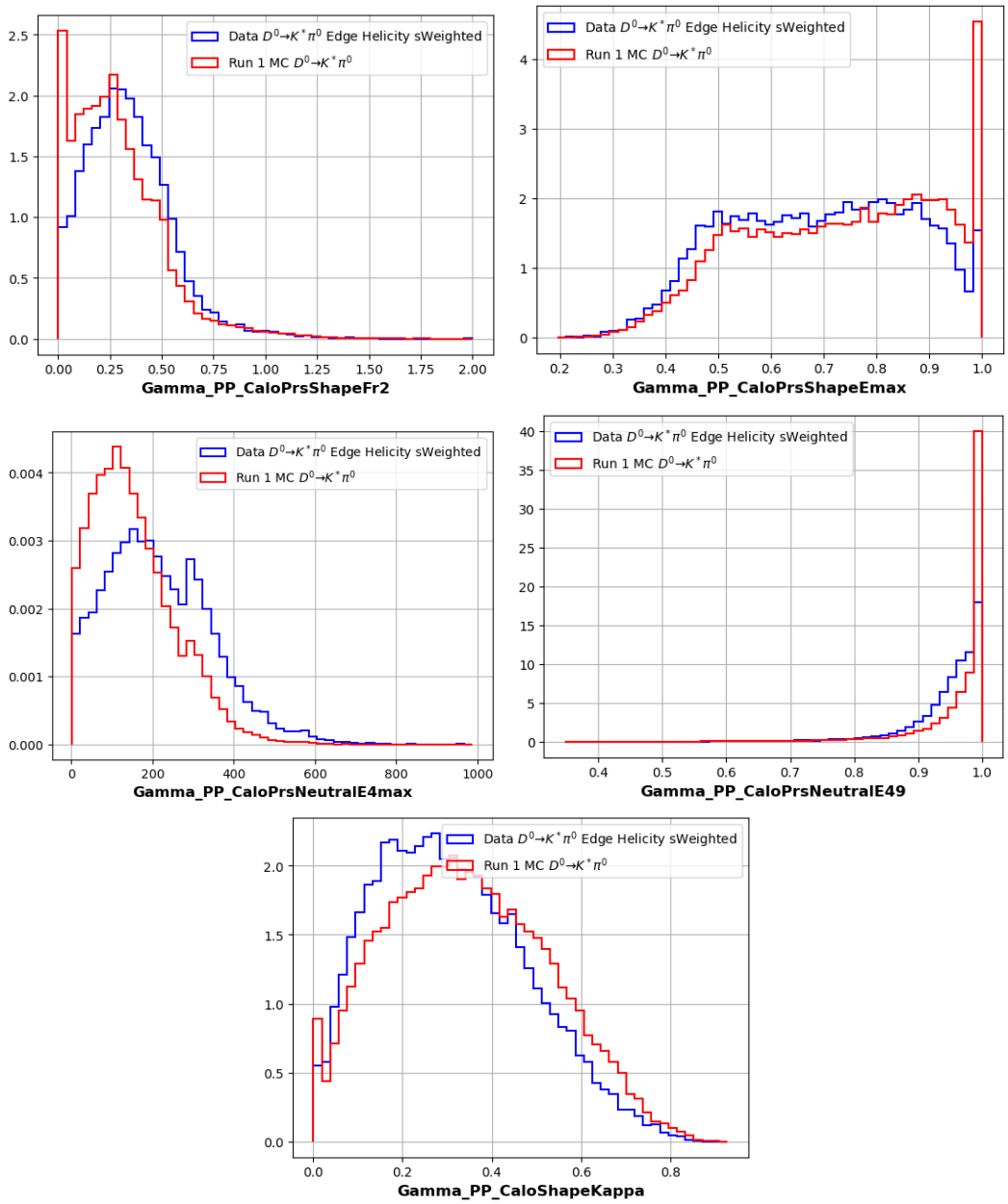

Figure **IV-2**: Comparison between cluster-shape variables (clockwise from top left): $r2$ in PS, $E_{\max}/E_{\text{sum}}$ in PS, E_{49} in PS, κ in ECAL and $E_{4\max}$ in PS, for π^0 candidates from $D^0 \to \bar{K}^{*0}\pi^0$ calibration data (blue) and from $D^0 \to \bar{K}^{*0}\pi^0$ simulation (red). The distributions are normalised, and compared before the simulation sample has been matched to the calibration data.

IV.3 BDT for γ–π^0 separation

Multivariate analysis (MVA) is performed to discriminate between signal photons and π^0 background. Discriminating variables employed to train the MVA classifier are associated with cluster shapes measured in ECAL: $r2$, $r2r4$, κ, $asym$, $E_1 = E_{\text{seed}}/E_{cl}$, $E_2 = (E_{\text{seed}} + E_{2nd})/E_{cl}$, E_{19} and E_{49}. The corresponding variables in PS are also employed. E_{49} denotes the ratio of the energy deposits between the 2×2 and 3×3 clusters, whereas E_{19} the ratio of the energy deposits between the 1×1 and 3×3 clusters; the remaining variables are defined in Section **II.5.1**. No variable describing kinematics or topology of the studied decays is used in the MVA training to avoid constructing a classifier that affects

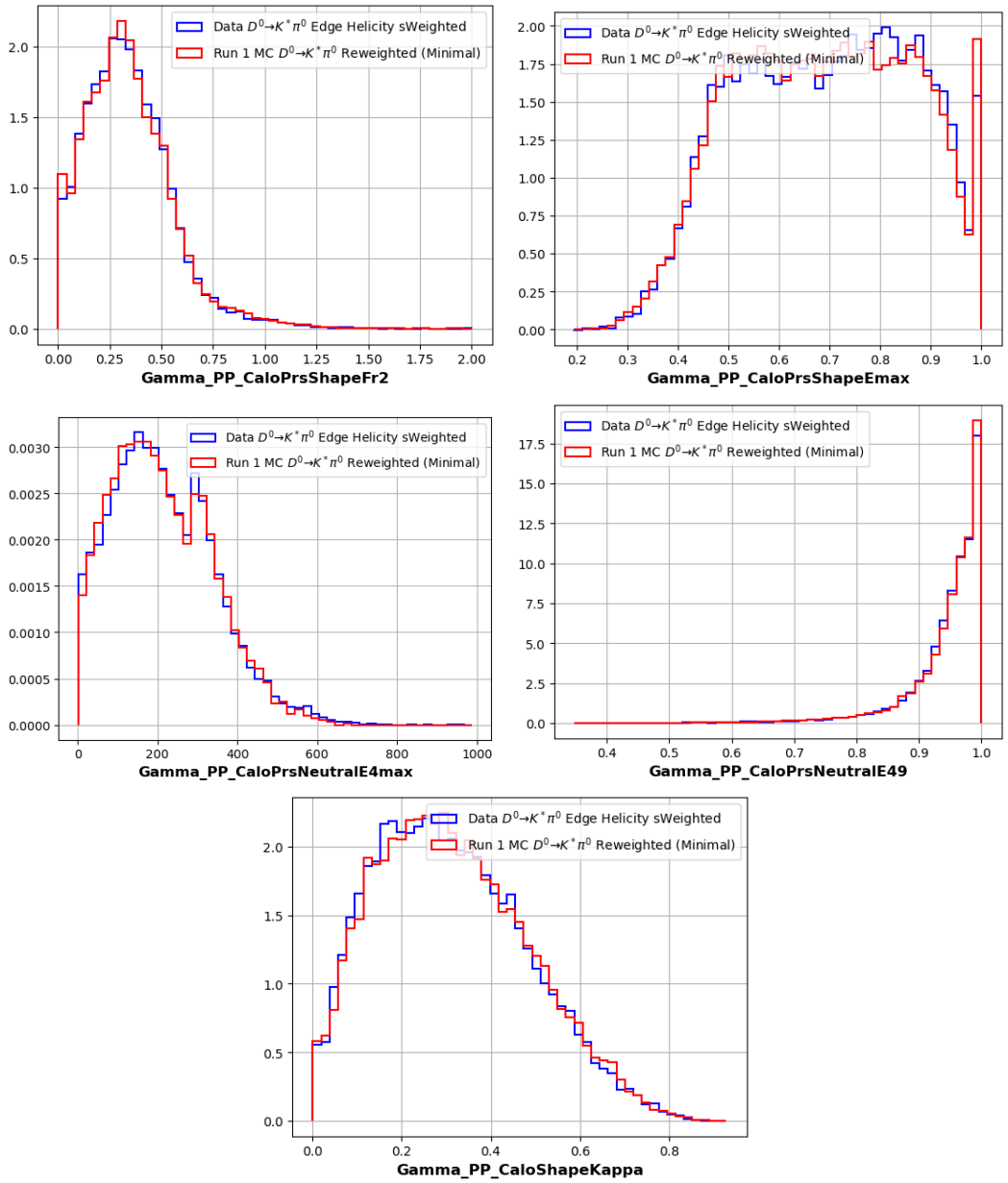

Figure **IV-3**: Comparison between cluster-shape variables (clockwise from top left): $r2$ in PS, $E_{\max}/E_{\text{sum}}$ in PS, E_{49} in PS, κ in ECAL and $E_{4\max}$ in PS, for π^0 candidates from $D^0 \to \bar{K}^{*0}\pi^0$ calibration data (blue) and from $D^0 \to \bar{K}^{*0}\pi^0$ simulation (red). The distributions are normalised and compared after the simulation sample has been matched to the calibration data.

differently candidates in the edge and central helicity regions.[27]

Comparison between the cluster-shape variables used for training of the MVA classifier is shown in Fig. **IV-5**. Signal photons are modelled using the $D^0 \to \bar{K}^{*0}\gamma$ simulation sample, with calorimeter variables calibrated as described in Section **IV.2**. Background π^0 mesons are taken from the $D^0 \to \bar{K}^{*0}\pi^0$ calibration sample, obtained from the data in the helicity-edge region with sWeights applied, as introduced in Section **IV.2**.

Several Boosted Decision Tree (BDT) classifiers have been considered, and the area under their receiver-operator characteristic (ROC) curve is used to select the optimal one. The ROC curves, showing

[27] Helicity-dependent classifier would impede data-driven calibration of $M(D^0)$ and ΔM distributions of π^0 background in the helicity center with their shapes from the helicity edge.

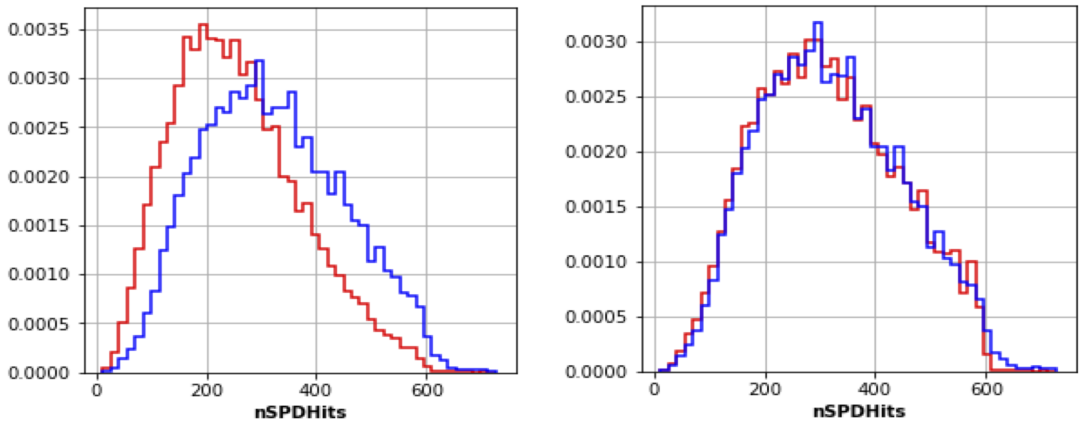

Figure **IV-4**: Comparison between nSPDHits distributions for underlying events in $D^0 \to \bar{K}^{*0}\pi^0$ calibration data (blue) and $D^0 \to \bar{K}^{*0}\pi^0$ simulation (red). On the left normalised distributions are compared before matching the simulation sample to the calibration data, and on the right after the matching.

signal efficiency as a function of background rejection for a range of cuts on a classifier response, are presented in Fig. **IV-6** (left). BDTB method is chosen as it has the largest area under the ROC curve. Distributions of the BDT response for the signal and background are shown in Fig. **IV-6** (right). Comparison between training and testing samples indicates some over-training, which is due to the limited statistics of the samples.

In the optimization of the BDT selection, the signal significance is used as a Figure of Merit, FOM $= \frac{S}{\sqrt{S+B}}$, where S and B are expected yields of the $D^0 \to \bar{K}^{*0}\gamma$ signal and $D^0 \to \bar{K}^{*0}\pi^0$ background, respectively. They are estimated based on the yields obtained from the data without any BDT selection, S_0 and B_0, and MC-based efficiencies for a given BDT requirement. S_0 and B_0 yields are measured in the helicity-center region from the two-dimensional fit to the $M(D^0)$ and $\cos\theta$ distributions. This fit is presented in Section **V.2**. The yields are measured for both D^0 and $\bar{D}^0$ samples combined, in order not to introduce any bias on the CP asymmetry measurement. The yields are $S_0 \simeq 5 \times 10^3$ and $B_0 \simeq 72 \times 10^3$. They are taken from the extended mass range, $1807 < M(D^0) < 1925$ MeV/c^2, to allow for enhanced π^0 contribution, and thus to assure better suppression of the π^0 background. Signal and background efficiencies for the FOM calculation are also considered in this extended mass range. The FOM measured as a function of the BDT selection is shown in Fig. **IV-7**. The optimal requirement, BDT> 0.33, is chosen for the maximal FOM value of about 22.8.

IV.4 Optimisation of IsPhoton selection

Performance of the dedicated classifier for the γ–π^0 separation described in Section **IV.3** is compared against the IsPhoton classifier. The default selection applied in radiative B-decay measurements, IsPhoton> 0.6 (Section **II.5.1**), might not be optimal for the charm decays due to significantly larger π^0 background. The IsPhoton selection is optimised for $D^0 \to \bar{K}^{*0}\gamma$ decays using the same FOM as for the BDT optimisation is Section **IV.3**.

The IsPhoton distributions for the simulated samples of $D^0 \to \bar{K}^{*0}\gamma$ and $D^0 \to \bar{K}^{*0}\pi^0$ decays, and the FOM measured as a function of IsPhoton cut are presented in Fig. **IV-8**. The optimal selection is chosen for the maximal FOM value, at IsPhoton> 0.86. The largest FOM value, of about 27.5, is larger than the one obtained for the BDT selection. It means that IsPhoton gives better performance, and is exploited throughout the next analysis steps.

Similar IsPhoton selection, IsPhoton> 0.85, is also obtained from the optimisation performed independently for the $D^0 \to \phi\gamma$ decays. Tighter selection, IsPhoton> 0.95 is used for $D^0 \to \rho^0\gamma$ decays, in

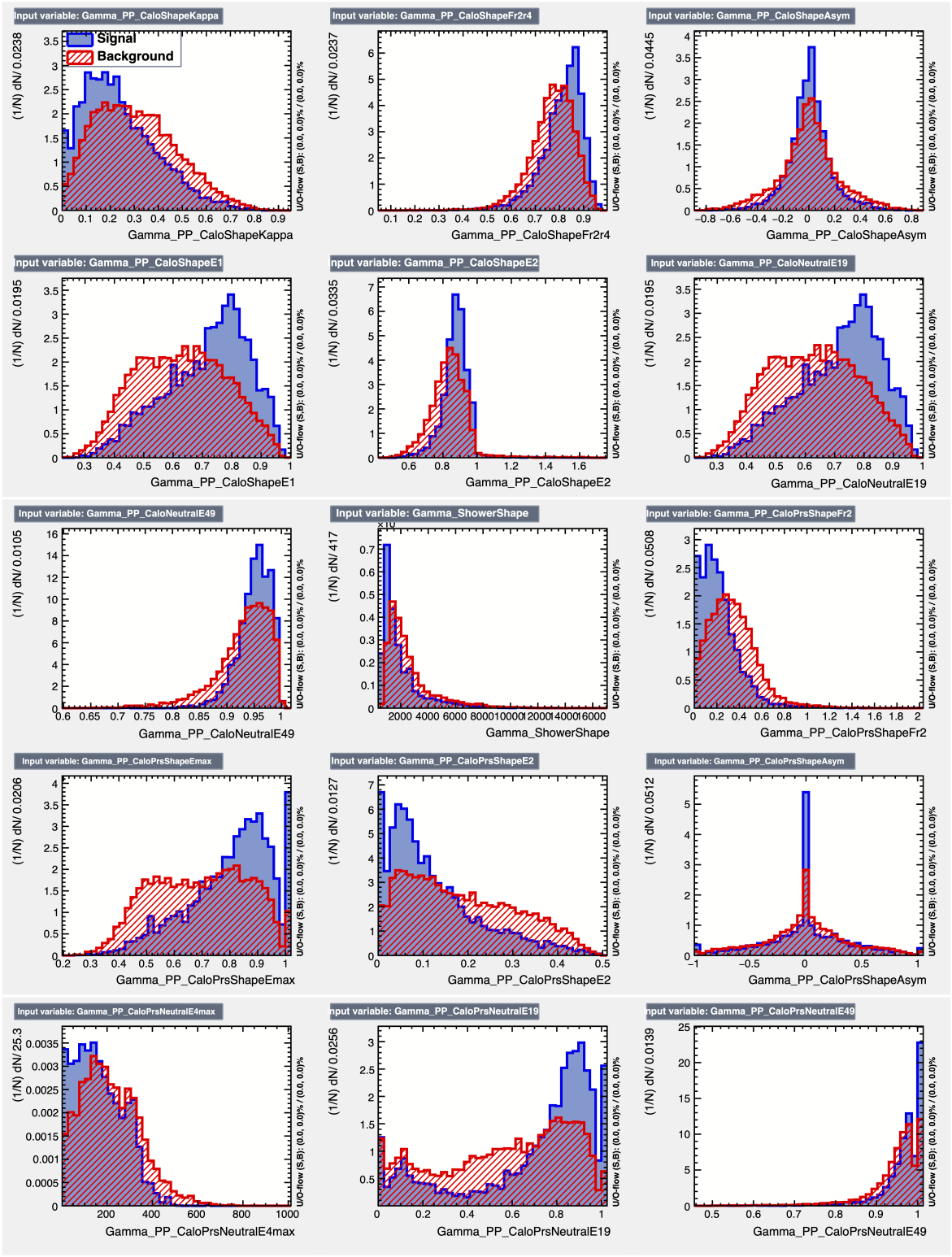

Figure **IV-5**: Comparison between variables used for training of the MVA classifier for γ–π^0 discrimination. Signal photons (blue) are from calibrated $D^0 \to \bar{K}^{*0}\gamma$ simulation, while background π^0 mesons (red) are from $D^0 \to \bar{K}^{*0}\pi^0$ calibration sample in the helicity-edge region. Discriminating variables are associated with cluster shapes in both sub-detectors, ECAL (top eight plots) and PS (seven bottom plots with x-axis captions starting with *Gamma_PP_CaloPrs*). The variables are defined in the text.

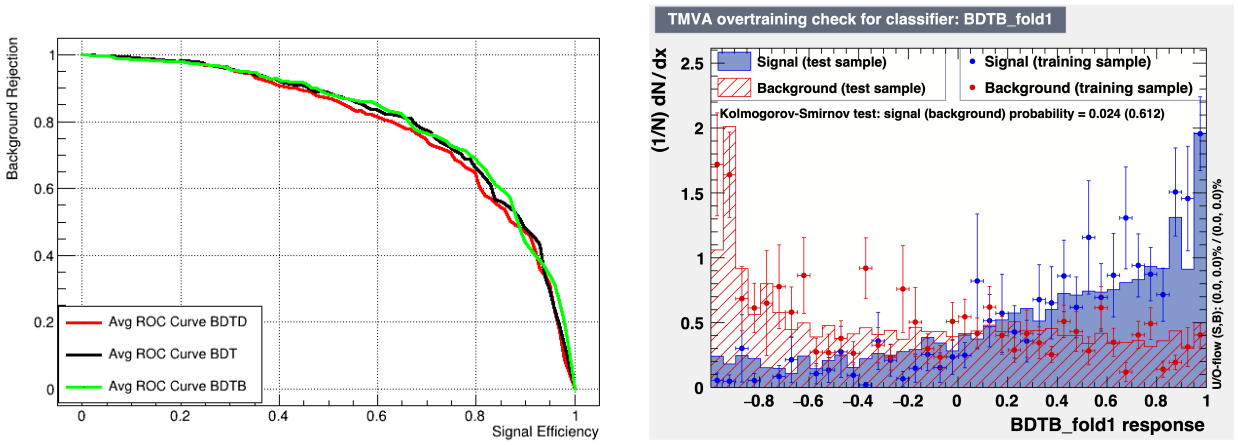

Figure **IV-6**: (Left) ROC curves for various BDT classifiers. (Right) BDT response for γ signal (blue) and π^0 background (red) compared for training and testing samples as indicated in the legend.

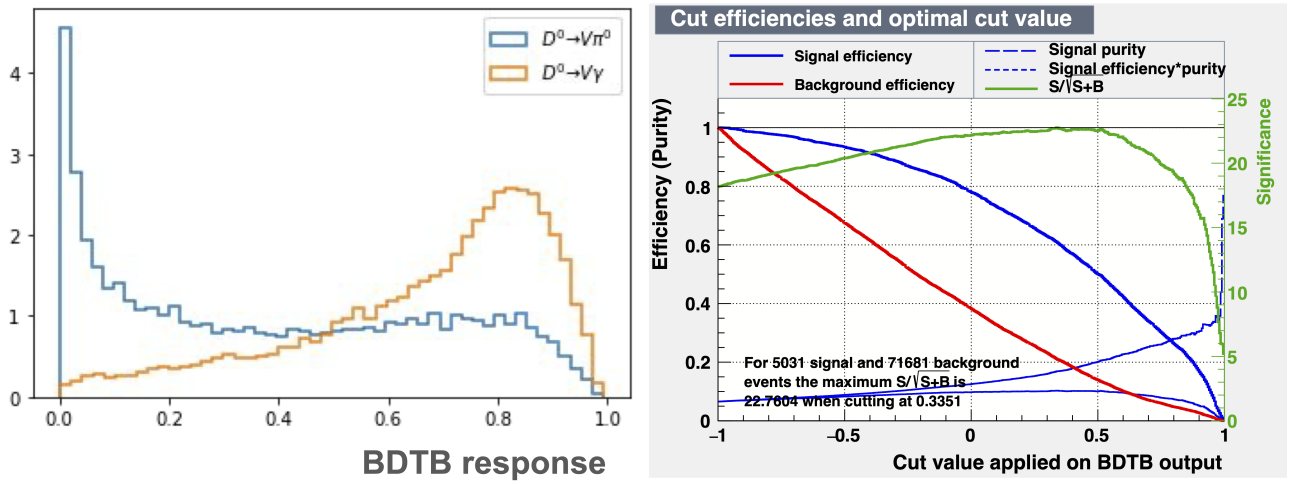

Figure **IV-7**: (Left) Normalised distributions of the BDTB response for simulated samples of $D^0 \to \bar{K}^{*0}\gamma$ (orange) and $D^0 \to \bar{K}^{*0}\pi^0$ (blue). (Right) FOM $= \frac{S}{\sqrt{S+B}}$ as a function of BDTB cut, measured for $D^0 \to \bar{K}^{*0}\gamma$ signal and $D^0 \to \bar{K}^{*0}\pi^0$ background, is shown in green. Efficiency dependence on BDTB cut for signal and for π^0 background is shown in blue and red, respectively.

order to reduce also combinatorial background being large in this sample (Section **V.5**).

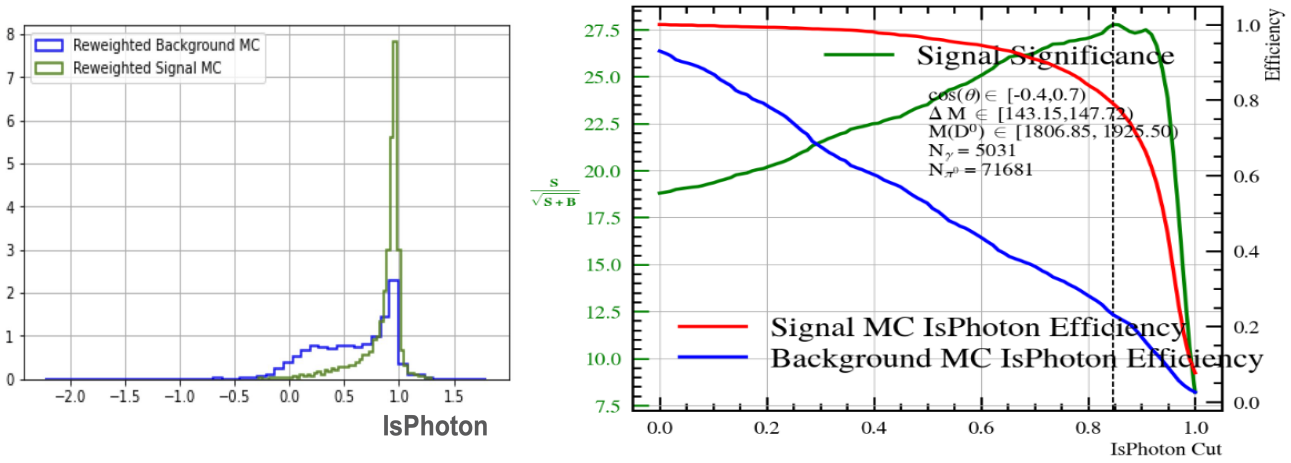

Figure **IV-8**: (Left) Normalised IsPhoton distributions for simulated samples of $D^0 \to \bar{K}^{*0}\gamma$ (green) and $D^0 \to \bar{K}^{*0}\pi^0$ (blue) decays. (Right) FOM = $\frac{S}{\sqrt{S+B}}$ as a function of IsPhoton cut, measured for $D^0 \to \bar{K}^{*0}\gamma$ signal and $D^0 \to \bar{K}^{*0}\pi^0$ background, is shown in green. Efficiency dependence on IsPhoton cut for signal and for π^0 background is shown in red and blue, respectively. Vertical line indicates the optimal selection, IsPhoton$>$ 0.86.

IV.5 Fits to $M(D^0)$, ΔM and $\cos\theta$ observables for K^* channels

In addition to the most common observables for π_s^+-tagged D^0 decays - the invariant mass of D^0 candidate, $M(D^0) = M(V\gamma)$, and the difference between the invariant mass of the D^{*+} and D^0 candidates $\Delta M = M(D^{*+}) - M(D^0)$, the cosine of the V helicity angle, $\cos\theta$, is also employed to identify the signal decays. For the usage of $\cos\theta$ as discriminating variable, it is important that its distribution is expected to be quite distinct between $D^0 \to V\gamma$ signal decays and $D^0 \to V\pi^0$ or $D^0 \to V\eta$ background decays (Section **II.5.2**). Employing $\cos\theta$ is particularly helpful in separating the signal decays from residual π^0 background. Such a separation cannot be done with $M(D^0)$ only, due to its limited resolution; D^0 mass distributions for the signal and π^0 background largely overlap.

Using ΔM allows for discriminating the *random soft-pion background* - combination of a properly reconstructed D^0 candidate with a π_s^+ that did not come from the D^{*+} decay. Removing this background assures correct tagging of the flavour of neutral D mesons. This is crucial for CP asymmetry measurements, as discussed in Section **II.4.1**. ΔM observable has some sensitivity to distinguishing between the signal and π^0 background. Different ΔM resolutions between these two processes come mostly from the fact that presence of a neutral object in the D^0 final state is not removed in ΔM. Another consequence is that $M(D^0)$ and ΔM observables are largely correlated. Such correlations need to be accounted for in three-dimensional fits in the phase space of $M(D^0)$ vs. ΔM vs. $\cos\theta$, employed to extract signal yields and their asymmetries.

IV.5.1 Fits for simulated $D^0 \to \bar{K}^{*0}\gamma$ decays

Distributions of discriminating variables for the $D^0 \to \bar{K}^{*0}\gamma$ simulation sample are shown in Fig. **IV-9**; given variable is selected in the full ranges of the other two. The distributions are fitted using the extended maximum-likelihood method,[28] with the following PDFs describing the $D^0 \to \bar{K}^{*0}\gamma$ signal:

$$\begin{aligned}
&\mathrm{PDF}_\gamma(M) = f_1 G_1(M;\mu_1,\sigma_1) + (1-f_1)G_2(M;\mu_1+\delta, r\sigma_1),\\
&\mathrm{PDF}_\gamma(\Delta M) = f_1^{\Delta m} G_1(\Delta M;\mu_1^{\Delta M},\sigma_1^{\Delta M}) + (1-f_1^{\Delta M})G_2(\Delta M;\mu_1^{\Delta M}, r^{\Delta M}\sigma_1^{\Delta M}),\\
&\mathrm{PDF}_\gamma(\cos\theta) = (1-\cos^2\theta)\times(1+a_1\cos\theta+a_2\cos^2\theta).
\end{aligned} \qquad \textbf{(IV.1)}$$

Both ΔM and $M(D^0)$ observables are modelled with a double Gaussian function, in the case of ΔM it has a common mean, and in the case of $M(D^0)$ it has an offset between mean of two subcomponents, making the overall shape slightly asymmetric. Those components have an interpretation - narrow one, denoted as G_1, contains the candidates reconstructed with better resolution, and the broader component G_2 describes the candidates with poorer reconstruction quality. The broader $M(D^0)$ component describes, so called, *radiative tail*. It accounts for the fact that reconstructed photon energy is slightly overestimated at LHCb.[29] The fits to ΔM and $M(D^0)$ also include a small background contribution, modelled with a first-order polynomial, taking care of spurious outliers far away from signal peaks. Parameter values obtained from one-dimensional fits to $M(D^0)$ and ΔM are summarised in Table **IV-1**.

PDF for the helicity angle is the *theoretical* shape multiplied by a second-order polynomial accounting for the reconstruction and selection efficiency. This efficiency shape, often referred to as acceptance, is slightly asymmetric with respect to $\cos\theta = 0$, as the V system comprises kaon and pion. For $\cos\theta \simeq -1$, the pions have low momenta (measured in the laboratory system), and the selection efficiency, in particular for the p_T cut, is smaller than for $\cos\theta \simeq +1$ where the low-momentum kaons contribute. The acceptance parameters are: $a_1 = 0.154 \pm 0.017$ and $a_2 = -0.300 \pm 0.034$.

Before moving on to a multi-dimensional fit, it is necessary to take correlations between $M(D^0)$ and ΔM into account, and that procedure is described in Section **IV.6.1**.

[28] This is the default fit method used in the analysis, unless explicitly stated otherwise.

[29] In majority of experiments photon energy is underestimated due to energy leakage outside of calorimeter clusters. In that case a radiative tail contributes below a signal peak.

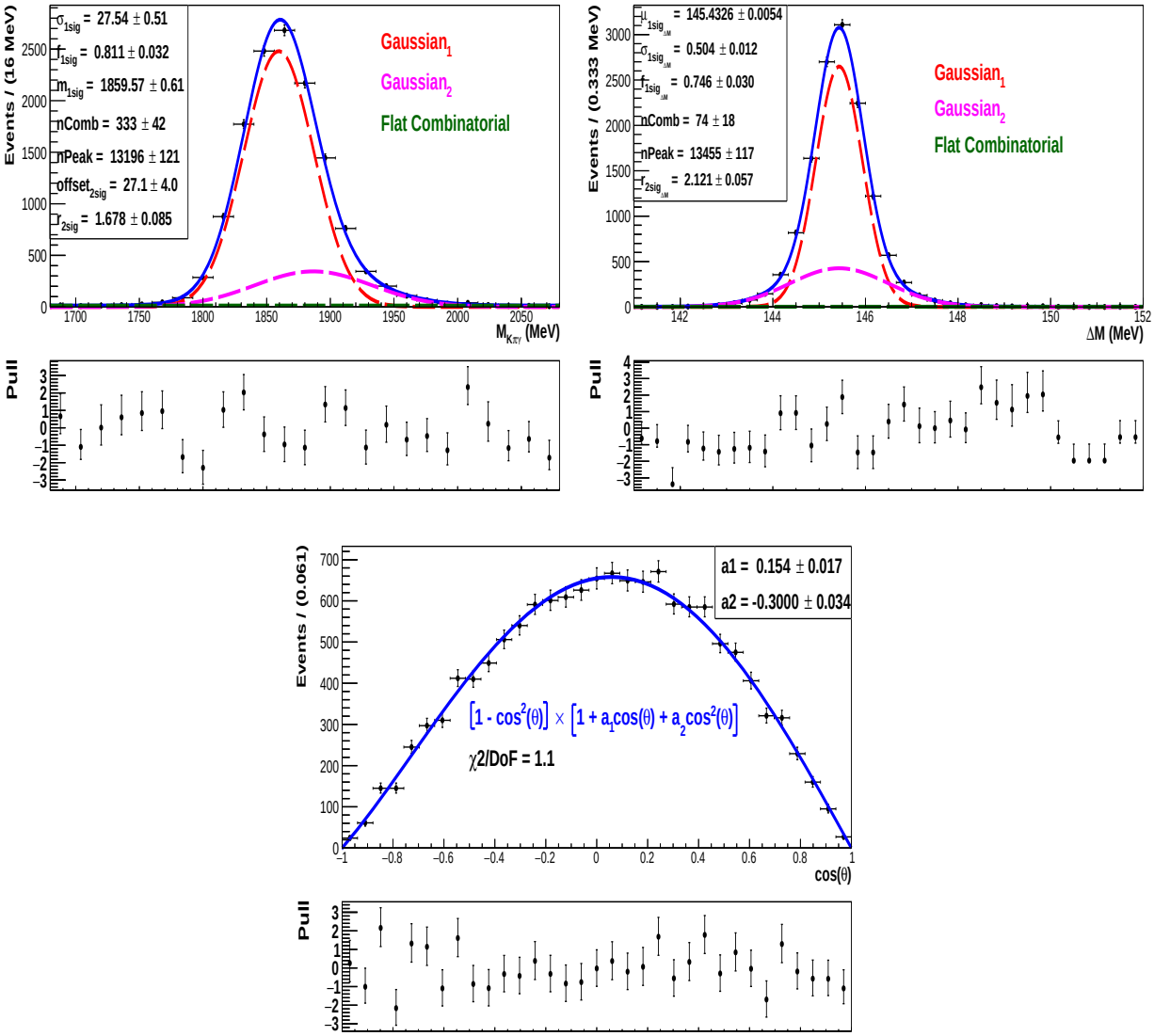

Figure **IV-9**: Distributions of (top left) $M(D^0)$, (top right) ΔM and (bottom) $\cos\theta$ for simulated $D^0 \to \bar{K}^{*0}\gamma$ decays. Results of one-dimensional fits are superimposed.

Par/Obs	f_1 [%]	μ_1 [MeV/c^2]	σ_1 [MeV/c^2]	δ [MeV/c^2]	r
$M(D^0)$	81.1 ± 3.2	1859.57 ± 0.61	27.54 ± 0.51	27.1 ± 4.0	1.68 ± 0.08
ΔM	74.6 ± 3.0	145.433 ± 0.005	0.504 ± 0.012	0.0	2.12 ± 0.06

Table **IV-1**: Parameter values obtained from one-dimensional fits to $M(D^0)$ and ΔM observables in $D^0 \to \bar{K}^{*0}\gamma$ simulation sample.

IV.5.2 Fits for simulated $D^0 \to \bar{K}^{*0}\pi^0$ background

In the experimental data, even after the selection designed to maximise the signal significance, there is still significant contribution from the $D^0 \to \bar{K}^{*0}\pi^0$ background. Therefore, it is necessary to model this π^0 background accurately using simulation data, and validate the model with calibration data - a subset of data in the helicity-edge region where signal is insignificant but π^0 background is enhanced.

Fits to $M(D^0)$ and ΔM

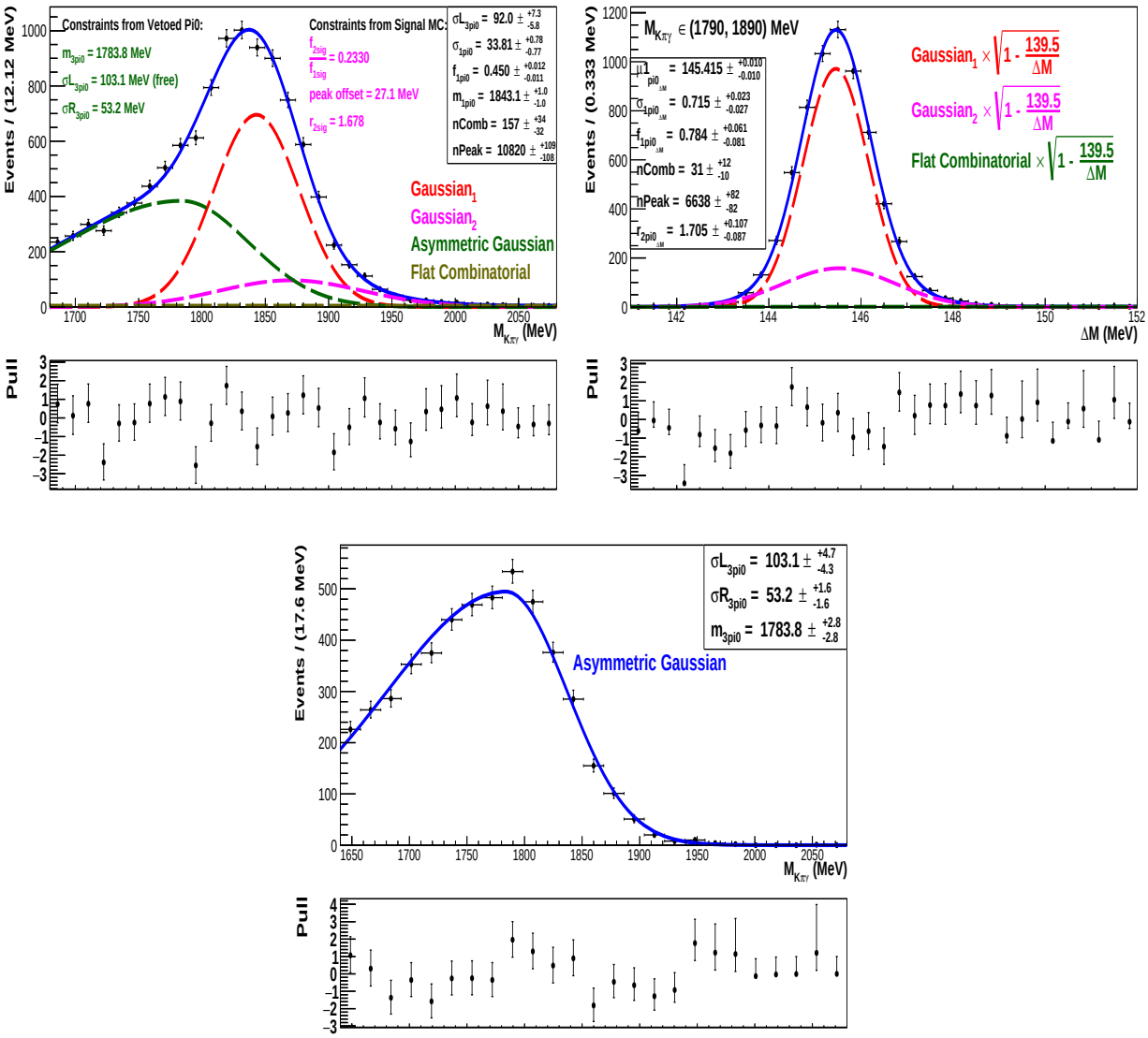

Figure **IV-10**: Distributions of (top left) $M(D^0)$, (top right) ΔM for simulated $D^0 \to \bar{K}^{*0}\pi^0$ sample passing the full signal selection. Results of one-dimensional fits are superimposed. The threshold asymmetric Gaussian in the $M(D^0)$ fit is constrained to the resolved-π^0 sample in the bottom figure. (Bottom) $M(D^0)$ distribution of the simulated $D^0 \to \bar{K}^{*0}\pi^0$ background involving resolved π^0 with one photon missing. Candidates pass the signal selection with `VetoPi0R` reversed. Result of the fit is superimposed.

The $M(D^0)$ and ΔM distributions for the $D^0 \to \bar{K}^{*0}\pi^0$ simulation sample, passing the full signal selection, are shown in Fig. **IV-10**; they are selected in the full $\cos\theta$ range. The broad peak in $M(D^0)$ at 1850 MeV/c^2 originates mostly from merged π^0's, whereas the low-mass tail can be associated with resolved π^0's with one photon missing. The latter is only partially suppressed with `VetoPi0R`, as presented in Figure **III-1**. The ΔM distribution, plotted for $M(D^0)$ in a signal-enhanced region, $1790 < M(D^0) < 1890$ MeV/c^2,[30] is similar to that of the signal but has worse resolution. Thus, the

[30] Effects from $M(D^0)$ tails are considered along with $M(D^0)$-ΔM correlations.

$M(D^0)$ and ΔM PDFs for the π^0 background are chosen as:

$$\begin{aligned}\mathrm{PDF}_{\pi^0}(M) &= f_1 G_1(M;\mu_1,\sigma_1) + f_2 G_2(M;\mu_1+\delta, r\sigma_1) + (1-f_1-f_2)G_3(M;\mu_3,\sigma_L,\sigma_R),\\ \mathrm{PDF}_{\pi^0}(\Delta M) &= \sqrt{1-\frac{m_\pi}{\Delta M}}\left[f_1^{\Delta M} G_1(\Delta M;\mu_1^{\Delta M},\sigma_1^{\Delta M}) + (1-f_1^{\Delta M})G_2(\Delta M;\mu_1^{\Delta M}, r^{\Delta M}\sigma_1^{\Delta M})\right].\end{aligned} \quad \textbf{(IV.2)}$$

The double Gaussian function, G_1 and G_2, resembles that in the signal PDFs in Eq. **IV.1**. An additional term in the $M(D^0)$ model - an asymmetric (a.k.a bifurcated) Gaussian function G_3, describes the low-mass region. The double Gaussian function that is centered around the mass peak is further referred to as a *core* of the $M(D^0)$ distribution, while the bifurcated Gaussian as a *threshold*.

In the $\mathrm{PDF}_{\pi^0}(M)$, the parameters of the threshold component are constrained using a sample with the requirement on the `VetoPi0R` reversed, i.e a sample consisting purely of rejected resolved π^0 candidates. This sample is fitted with the bifurcated Gaussian as shown in Fig. **IV.2** (bottom). The position μ_3 of the threshold Gaussian and its right width σ_R are fixed to those in the vetoed sample, whereas the left width σ_L is Gaussian-constrained.[31] Within the core part of the $\mathrm{PDF}_{\pi^0}(M)$, the parameters of G_2, namely its fraction f_2 relative to f_1, as well as width ratio r and peak offset δ, are fixed to those of the $D^0 \to \bar{K}^{*0}\gamma$ signal (Table **IV-1**). Overall, the $M(D^0)$ fit in Fig. **IV-10** has a good quality.

Using the sample comprising vetoed π^0's to model photons from π^0's which have not been vetoed, assumes that an efficiency to reconstruct another photon in the underlying event is independent of efficiency to reconstruct a signal photon. If this assumption is not fully satisfied, separating out resolved and merged π^0 background is not exact, but modelling of the $M(D^0)$ shape remains valid.

The $\mathrm{PDF}_{\pi^0}(\Delta M)$ includes the multiplicative factor to describe a phase-space suppression for ΔM approaching the soft-pion mass $m_\pi = 139.5$ MeV/c^2. Similar to the signal fits in Fig. **IV-9**, the fits to $M(D^0)$ and ΔM distributions in Fig. **IV-10** also include a small combinatorial background component. Parameter values obtained from one-dimensional fits to $M(D^0)$ and ΔM are summarised in Table **IV-2**.

Although the two helicity regions are analysed separately (see below), $M(D^0)$ and ΔM variables in Fig. **IV-10** are selected and fitted in the full $\cos\theta$ range. This is facilitated by the fact that $M(D^0)$ and ΔM are independent of the helicity observable.

Par/Obs	f_1 [%]	μ_1	σ_1	f_2/f_1	δ	r	μ_3	σ_L	σ_R
$M(D^0)$	45 ± 1	1843 ± 1	33.8 ± 0.8	0.233	27.1	1.678	1783.8	92^{+7}_{-6}	53.2
ΔM	$78.4^{+0.6}_{-0.8}$	145.41 ± 0.01	0.71 ± 0.02	–	0.0	1.7 ± 0.1	–	–	–

Table **IV-2**: Parameter values obtained from one-dimensional fits to $M(D^0)$ and ΔM observables in $D^0 \to \bar{K}^{*0}\pi^0$ simulation sample passing the full signal selection. Means of Gaussian functions, μ_1 and μ_3, peak offset δ, and Gaussian widths σ_1, σ_L and σ_R, are given in MeV/c^2.

Fits to $\cos\theta$

As discussed in Section **III.2.1**, the $D^0 \to \bar{K}^{*0}\pi^0$ simulation sample based on the CLEO amplitude model for $D^0 \to K^-\pi^+\pi^0$ decays is used to measure an acceptance as a function of the $\cos\theta$. It is obtained by dividing the $\cos\theta$ distribution of the selected candidates in the simulation sample by the *theoretical* $\cos\theta$ distribution for the candidates generated with EvtGen according to the CLEO amplitude model (Section **III.2.1**). Both, the simulated and generated distributions are normalised,

[31] It means that a fit likelihood is multiplied by a Gaussian term with mean set to the nominal value of given parameter and width to the standard deviation.

so only relative efficiency variations are measured. The resulting $\cos\theta$ acceptance in the helicity-edge and helicity-center regions are shown in Fig. **IV-11** (top). They are fitted with a first-order polynomial using the minimum-χ^2 method. The $\cos\theta$ acceptance is flat in the helicity-center region, and slightly decreases in the helicity-edge region for $\cos\theta$ approaching -1.

In the acceptance calculation an impact of the decay model has been removed. The theoretical helicity shape is generated with EvtGen based on the BaBar model (Section **III.2.1**). The corresponding $\cos\theta$ distributions for the helicity-edge and helicity-center regions are presented in Fig. **IV-11** (bottom), together with fit results. In these fits, a second-order polynomial is used for the edge region, and a fourth-order polynomial for the central region. In fits to the experimental data (Section **V.3**), the $\cos\theta$ variable for the $D^0 \to \bar{K}^{*0}\pi^0$ background is parameterised as the product of the acceptance and the theoretical shape based on the BaBar model.

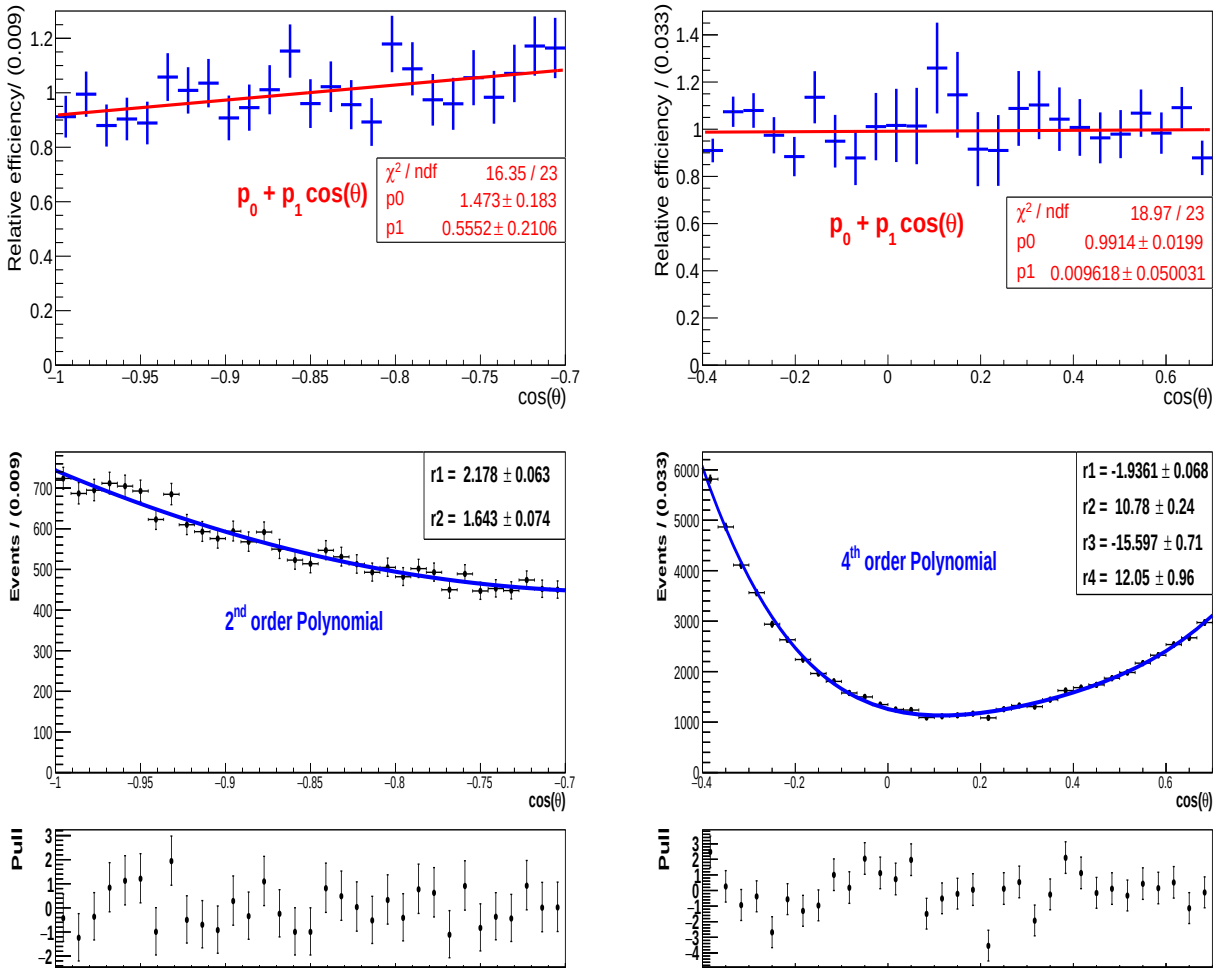

Figure **IV-11**: (Top) Efficiency as a function of $\cos\theta$ for $D^0 \to \bar{K}^{*0}\pi^0$ simulation sample in (top left) helicity-edge and (top right) helicity-center regions. (Bottom) Theoretical $\cos\theta$ distribution in (bottom left) helicity-edge and (bottom right) helicity-center regions generated with the BaBar model for the $D^0 \to K^-\pi^+\pi^0$ decay. Results of fits are superimposed.

Comparison of $\cos\theta$ distributions generated with the CLEO and BaBar models is shown in Fig. **IV-12**. Both generated $D^0 \to K^-\pi^+\pi^0$ samples have the $M(K^-\pi^+)$ selected in the K^{*0} mass region considered in the analysis. Both models give very similar $\cos\theta$ shapes in the helicity-edge region, but somewhat different shapes in the helicity-center region where subdominant scalar resonances contribute.

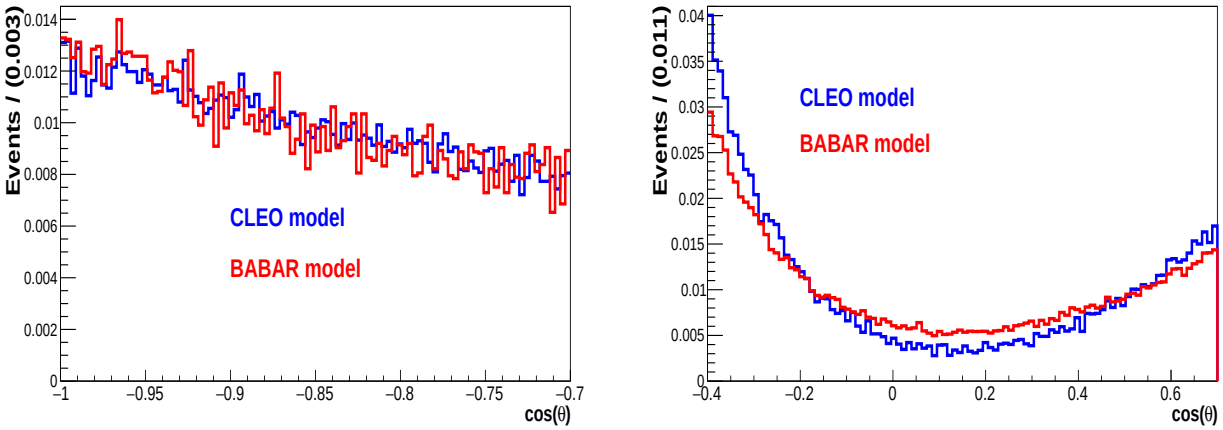

Figure **IV-12**: Comparison of $\cos\theta$ distributions in (left) helicity-edge and (right) helicity-center regions, generated using the CLEO (blue) and BaBar (red) amplitude model of the $D^0 \to K^-\pi^+\pi^0$ decay.

IV.5.3 Fits for simulated $D^0 \to \bar{K}^{*0}\eta$ background

The simulation sample of $D^0 \to \bar{K}^{*0}\eta$ background has been generated as an incoherent mixture of the following resonant decays: $D^0 \to \bar{K}^{*0}\eta$, $D^0 \to K^- a_0(980)^+$ and $D^0 \to \bar{K}_0(1430)^0\eta$ (Section **III.2.1**). As relative fractions assumed in the simulation are uncertain, these three sub-components of the η background are considered independently (i.e. with independent yields and asymmetries) in fits to the experimental data. Their $M(D^0)$ and ΔM distributions have indistinguishable shapes, but their $\cos\theta$ distributions differ significantly.

Fits to $M(D^0)$ *and* ΔM

The $M(D^0)$ and ΔM distributions, for the three sub-components of the η background combined, are shown in Fig. **IV-13**. Given variable is selected in the full range of the other. Only upper part of the invariant-mass distribution is within the analysed $M(D^0)$ range, the ΔM shape resembles a top-hat function due to poor resolution. The $M(D^0)$ and ΔM are modelled with a Crystal-Ball (CB) function and a double-Gaussian function, respectively:

$$\begin{aligned}
\mathrm{PDF}_\eta(M) &= CB(M;\mu_1,\sigma_1,\alpha,n) = \begin{cases} \exp\left(-\frac{1}{2}\left[\frac{M-\mu_1}{\sigma_1}\right]^2\right), & \text{for } \frac{M-\mu_1}{\sigma_1} > -\alpha \\ A(B-\frac{M-\mu_1}{\sigma_1})^{-n}, & \text{for } \frac{M-\mu_1}{\sigma_1} \le -\alpha, \end{cases} \\
\mathrm{PDF}_\eta(\Delta M) &= \sqrt{1-\frac{m_\pi}{\Delta M}}\left[f_1^{\Delta M} G_1(\Delta M;\mu_1^{\Delta M},\sigma_1^{\Delta M}) + (1-f_1^{\Delta M}) G_2(\Delta M;\mu_2,\sigma_2^{\Delta M})\right],
\end{aligned} \tag{IV.3}$$

where $A = (\frac{n}{|\alpha|})^n \exp(-\frac{|\alpha|^2}{2})$ and $B = \frac{n}{|\alpha|} - |\alpha|$. CB function comprises a Gaussian core and a power-law tail, with exponent n, for $M(D^0)$ values above the threshold given by α. The two Gaussian sub-components in the $\mathrm{PDF}_\eta(\Delta M)$ give effective description of the ΔM shape, they do not have any reconstruction-related interpretation. The fit results are superimposed on the distributions in Fig. **IV-13**. Parameter values obtained from one-dimensional fits to $M(D^0)$ and ΔM are summarised in Table **IV-3**.

Fits to $\cos\theta$

Distributions of $\cos\theta$ for the three resonant decays contributing to the simulated η background are compared in Fig. **IV-14**. The contribution from $D^0 \to \bar{K}_0(1430)^0\eta$ decays is significantly suppressed

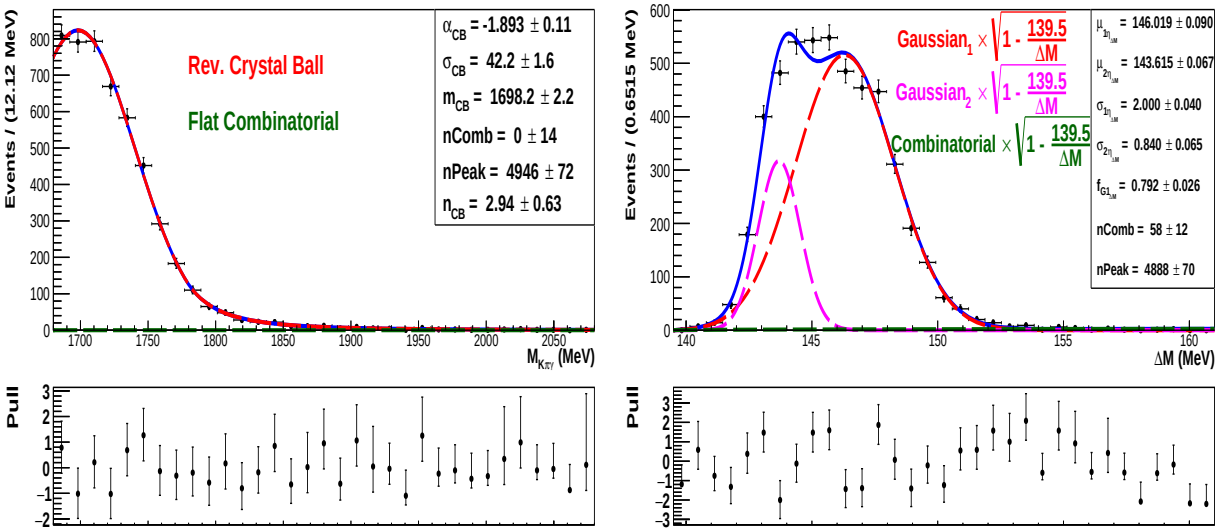

Figure **IV-13**: Distributions of (left) $M(D^0)$, (right) ΔM for simulated $D^0 \to \bar{K}^{*0}\eta$ background sample passing the full signal selection. Results of one-dimensional fits are superimposed.

Par/Obs	f_1 [%]	μ_1	σ_1	μ_2	σ_2	α	n
$M(D^0)$	–	1698.2 ± 2.2	42.2 ± 1.6	–	–	-1.9 ± 0.1	2.9 ± 0.6
ΔM	79 ± 3	146.02 ± 0.09	2.00 ± 0.04	143.61 ± 0.07	0.84 ± 0.06	–	–

Table **IV-3**: Parameter values obtained from one-dimensional fits to $M(D^0)$ and ΔM observables in $D^0 \to \bar{K}^{*0}\eta$ simulation sample. Means and widths of Gaussian and CB functions are given in MeV/c^2.

after selecting $M(K^-\pi^+)$ in the K^{*0} mass region. Only $D^0 \to \bar{K}^{*0}\eta$ decays are expected to contribute significantly into the η background in the helicity-edge region, $\cos\theta < -0.7$.

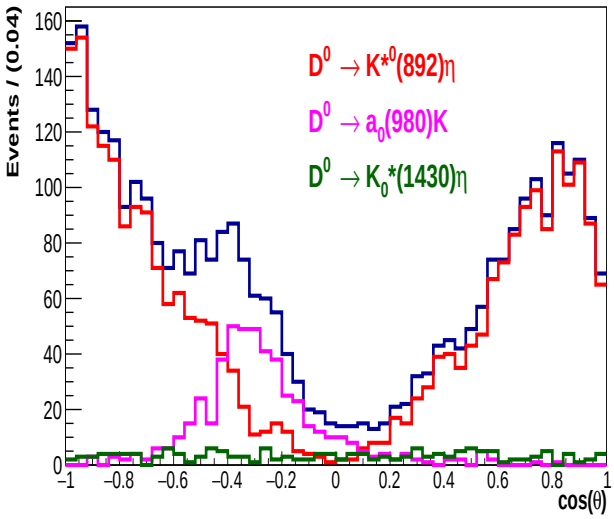

Figure **IV-14**: Distributions of $\cos\theta$ for three resonant decays contributing to the simulated η background passing the full signal selection. Contribution from $D^0 \to \bar{K}^{*0}\eta$ decays is plotted in red, from $D^0 \to K^- a_0(980)^+$ in magenta, and from $D^0 \to \bar{K}_0(1430)^0\eta$ in green.

Fits to $\cos\theta$ distributions are shown in Fig. **IV-15**. The helicity shape for $D^0 \to \bar{K}^{*0}\eta$ decays is consistent with the theoretical function $\cos^2\theta$ in both, the helicity-edge and helicity-center regions; no significant acceptance effects are observed. Similarly for $D^0 \to \bar{K}_0(1430)^0\eta$ decays, whose $\cos\theta$ distribution is consistent with being flat in the helicity-center region, as expected for $K^-\pi^+$ system originating from a scalar resonance. Statistics for this channel is very limited, but the conclusion about negligible acceptance effects can be drawn already from the fits to the $D^0 \to \bar{K}^{*0}\eta$ sample. The $\cos\theta$ distribution for $D^0 \to K^- a_0(980)^+$ decays is non-trivial as $K^-\pi^+$ system does not originate from the same particle. Its shape is fitted with a single exponential function, and the exponential parameter is -4.64 ± 0.27.

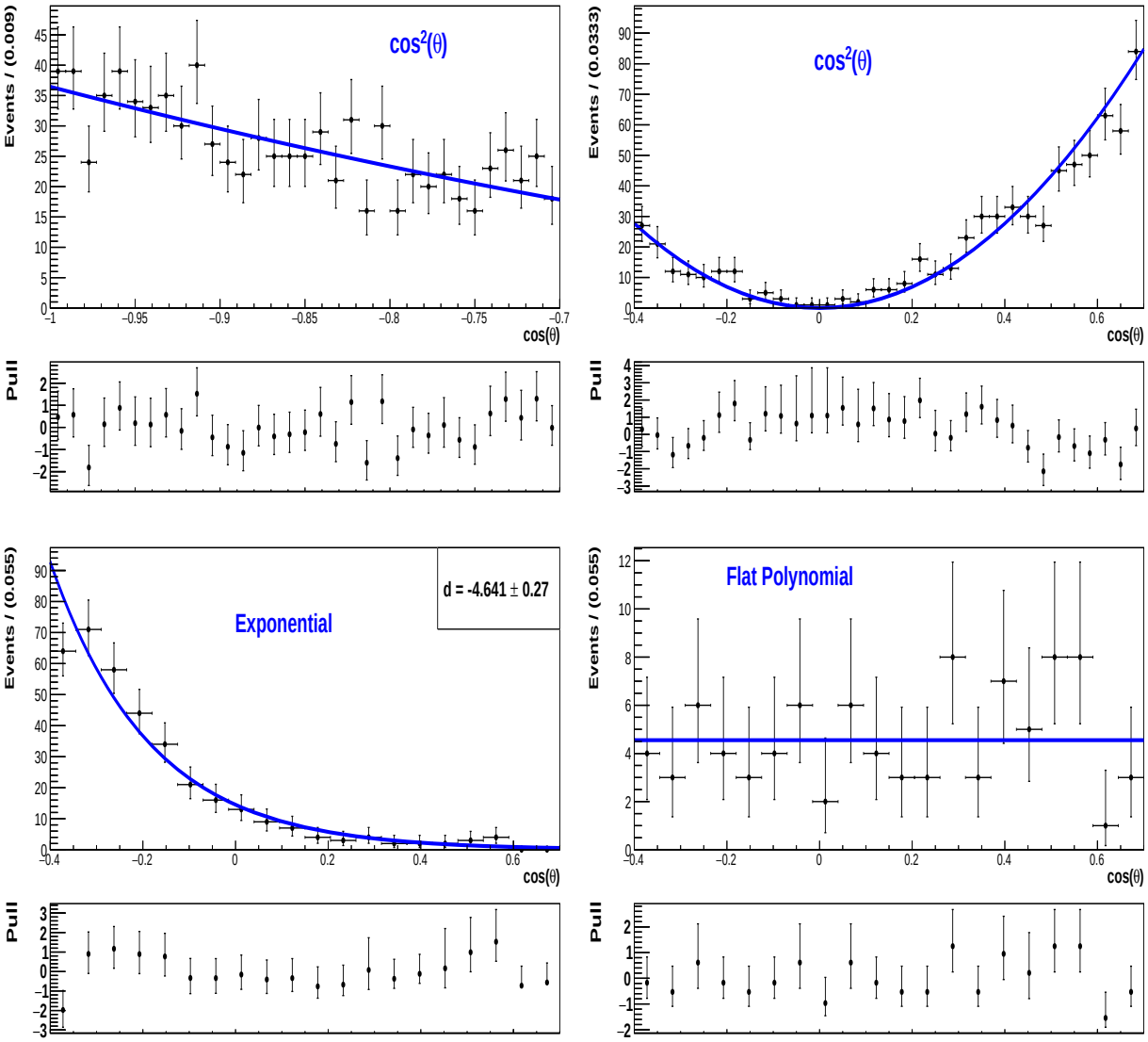

Figure **IV-15**: Distributions of $\cos\theta$ for (top left) $D^0 \to \bar{K}^{*0}\eta$ simulation in the helicity-edge region, (top right) $D^0 \to \bar{K}^{*0}\eta$ simulation in the helicity-center region, (bottom left) $D^0 \to K^- a_0(980)^+$ decays in the helicity-center region and (bottom right) $D^0 \to \bar{K}_0(1430)^0\eta$ decays in the helicity-center region. Fit results are superimposed.

IV.6 Describing $M(D^0)$–ΔM correlations in K^* channels

One complication in the chosen set of observables is that while $\cos\theta$ can be treated as independent of $M(D^0)$ and ΔM variables, $M(D^0)$ and ΔM are manifestly not so, as they are correlated. There are broadly two techniques that can be employed to resolve this difficulty. First is to perform fits with two-dimensional $M(D^0)$–ΔM templates, second is to parameterize ΔM with a functional dependence on $M(D^0)$ (or vice versa). A variant of the second technique is employed, where simulation samples are used to model effects of $M(D^0)$–ΔM correlations on $M(D^0)$ and ΔM resolutions.

IV.6.1 Correlations in $D^0 \to \bar{K}^{*0}\gamma$ signal

To account for $M(D^0)$–ΔM correlations, the $\mathrm{PDF}_\gamma(\Delta M)$ in Eq. **IV.1** is modified as:

$$\mathrm{PDF}_\gamma(\Delta M|M) = f_1^{\Delta m} G_1(\Delta M; \mu_1^{\Delta M}, \lambda(M)\sigma_1^{\Delta M}) + (1 - f_1^{\Delta M}) G_2(\Delta M; \mu_1^{\Delta M}, \lambda(M) r^{\Delta M} \sigma_1^{\Delta M}). \quad \textbf{(IV.4)}$$

In this conditional PDF, the mass-dependent ΔM resolution is introduced through $\lambda(M)$ function. It is more feasible to introduce correlations into the ΔM PDF rather than the $M(D^0)$ PDF, because the ΔM observable has better resolution, so is more sensitive to the correlations, and it has simpler shape, in particular for the π^0 background.

In order to measure $\lambda(M)$ dependence, the $M(D^0)$ range in the $D^0 \to \bar{K}^{*0}\gamma$ simulation sample is divided into several bins, and ΔM distribution is fitted in each of them separately. The bin width varies between 10 MeV/c^2 around the $M(D^0)$ peak, where the resolution is highest, and $80 \div 120$ MeV/c^2 in the tail regions where statistics is small. All the parameters in $\mathrm{PDF}_\gamma(\Delta M|M)$ are fixed to those from the one-dimensional ΔM fit in Section **IV.5.1**, except for λ, which is kept free. Yields of combinatorial background are fixed to zero, as they are negligible after splitting the sample.

Results of these ΔM fits in $M(D^0)$ bins are presented in Fig. **IV-16**. The fitted values of the λ parameter are plotted against the corresponding $M(D^0)$ regions in Fig. **IV-17**. The resulting distribution is fitted in order to obtain the desired functional dependence of $\lambda(M)$. The fit is performed using the minimum-χ^2 method, and the fit function is a second-order polynomial. The extreme $M(D^0)$ sidebands (the lowest and highest $M(D^0)$ bins in Fig. **IV-17**) are excluded from the fit, as the simple quadratic model does not describe correlations that far away from the $M(D^0)$ peak. Effectively, the $\lambda(M)$ function measured in the mass range of $1800 < M(D^0) < 1950$ MeV/c^2, is extrapolated to these sidebands. These regions have anyway small statistics, thus, overall such an extrapolation works well (Section **IV.7**).

IV.6.2 Correlations in π^0 background

Everything said about $M(D^0)$–ΔM correlations for the $D^0 \to \bar{K}^{*0}\gamma$ signal applies to the π^0 background. The procedure to measure $\lambda(M)$ function is similar, except the ΔM parameters for fits in $M(D^0)$ bins are taken from the reduced mass range of $1790 < M(D^0) < 1890$ MeV/c^2, as presented in Section **IV.5.2**. Reducing a contribution from $M(D^0)$ tails, in particular from the low-mass region, facilitates modelling of the $M(D^0)$–ΔM correlations in signal-enhanced mass region. The λ factor is applied to both Gaussian components of the ΔM PDF, as in Eq. **IV.4**.

ΔM fits in $M(D^0)$ bins for the $D^0 \to \bar{K}^{*0}\pi^0$ simulation sample are presented in Fig. **IV-18**, whereas the fitted values of the λ parameter as a function of $M(D^0)$ in Fig. **IV-19**. The $\lambda(M)$ distribution is fitted in the mass range of $1800 < M(D^0) < 1950$ MeV/c^2 (i.e. excluding two lowest- and one highest-mass bins) with a second-order polynomial. Compared to the correlation curve for the $D^0 \to \bar{K}^{*0}\gamma$ signal in Fig. **IV-17**, one can clearly see that $\lambda(M)$ dependence is weaker for the π^0 background, but still significant.

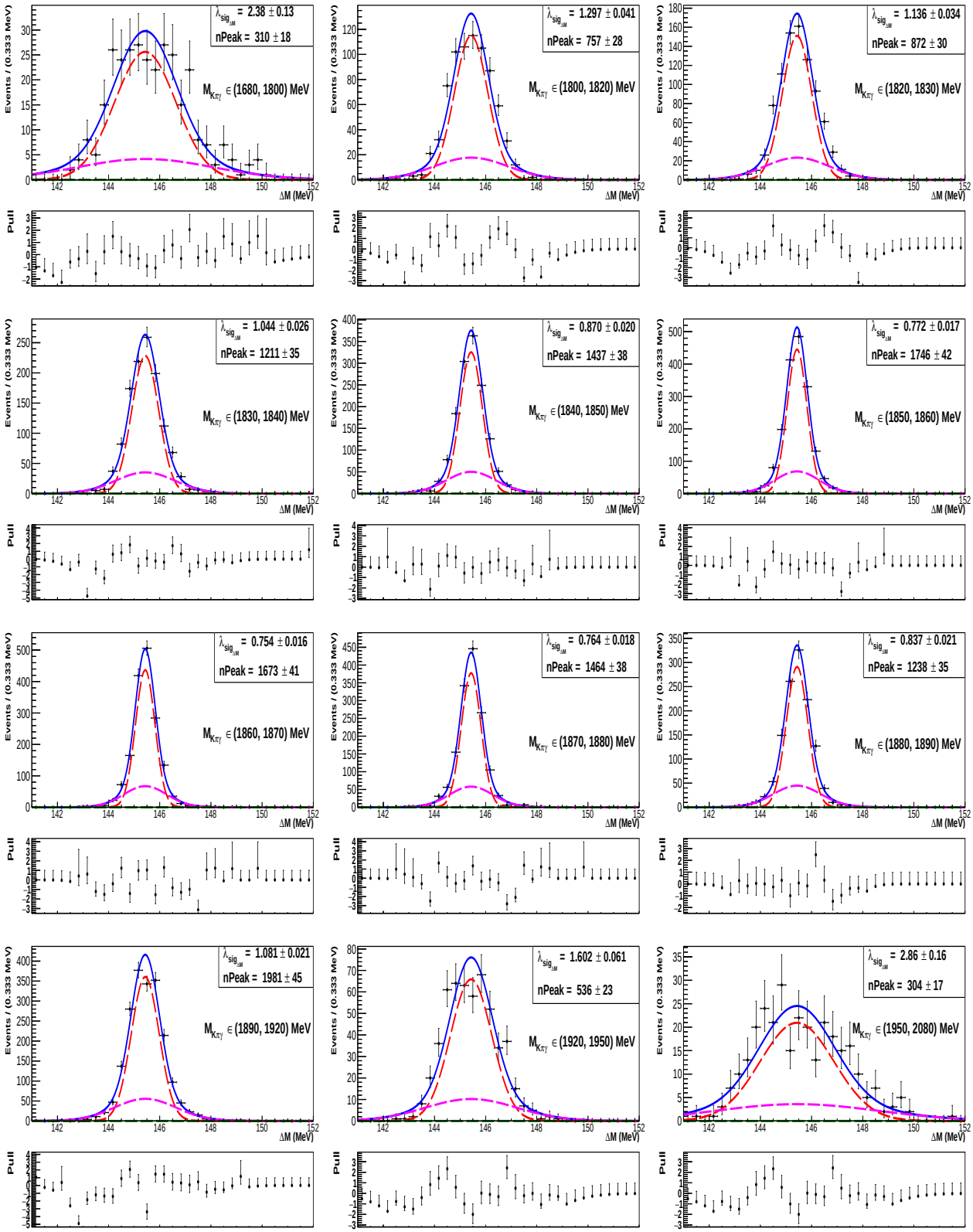

Figure **IV-16**: Results of ΔM fits in $M(D^0)$ bins performed using the $D^0 \to \bar{K}^{*0}\gamma$ simulation sample. Considered $M(D^0)$ regions, as well as fitted λ values are indicated in individual figures.

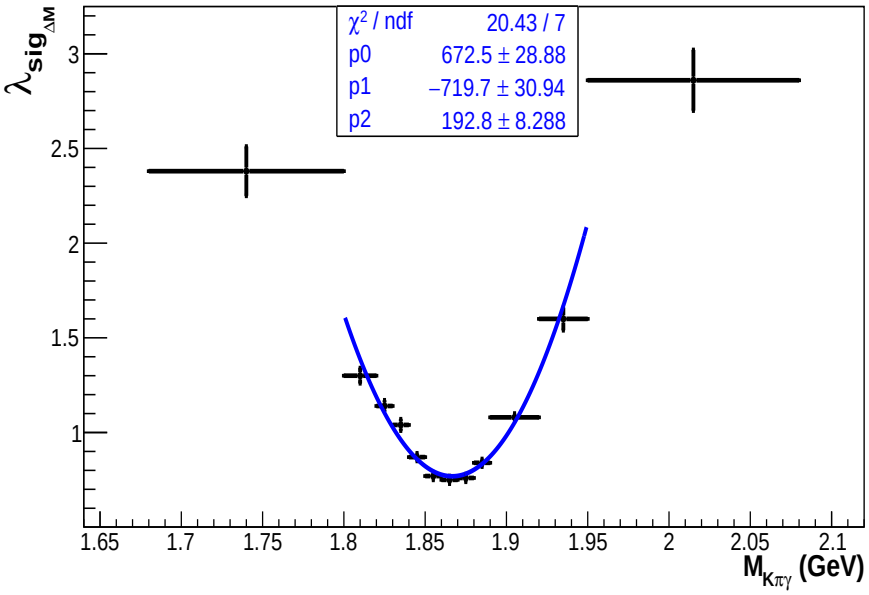

Figure **IV-17**: Correlation parameter λ for $D^0 \to \bar{K}^{*0}\gamma$ signal, obtained from ΔM fits in $M(D^0)$ bins, plotted against the corresponding $M(D^0)$ range. Result of χ^2 fit using 2^{nd} order polynomial is superimposed, and fit parameters are also given. The lowest- and highest-mass bins are excluded from the fit.

IV.6.3 Correlations in η background

Measurement of $\lambda(M)$ function for the η background starts from ΔM fits in $M(D^0)$ bins, shown in Fig. **IV-20**. In these fits, simulation samples of the three resonant decays of the η background are combined. The λ factor is applied to both Gaussian components of the ΔM PDF, as in Eq. **IV.4**. The ΔM parameters are fixed to those from the one-dimensional ΔM fit in Section **IV.5.3**. The fitted values of the λ parameter as a function of $M(D^0)$ are shown in Fig. **IV-21**. This $\lambda(M)$ distribution is fitted in the mass range of $1680 < M(D^0) < 1800$ MeV/c^2 (i.e. excluding the highest-mass bin) with a second-order polynomial.

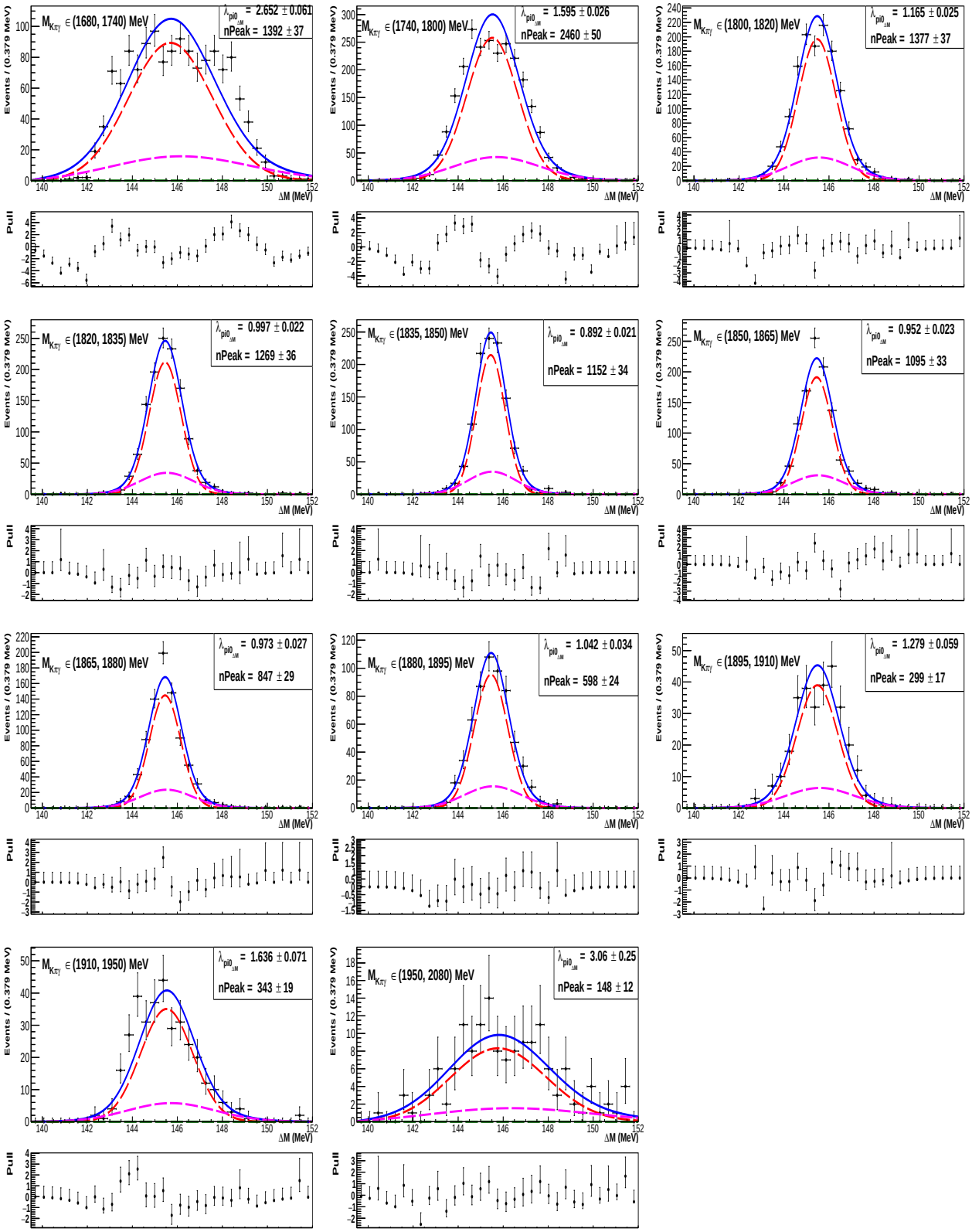

Figure **IV-18**: Results of ΔM fits in $M(D^0)$ bins performed using the $D^0 \to \bar{K}^{*0}\pi^0$ simulation sample. Considered $M(D^0)$ regions, as well as fitted λ values are indicated in individual figures.

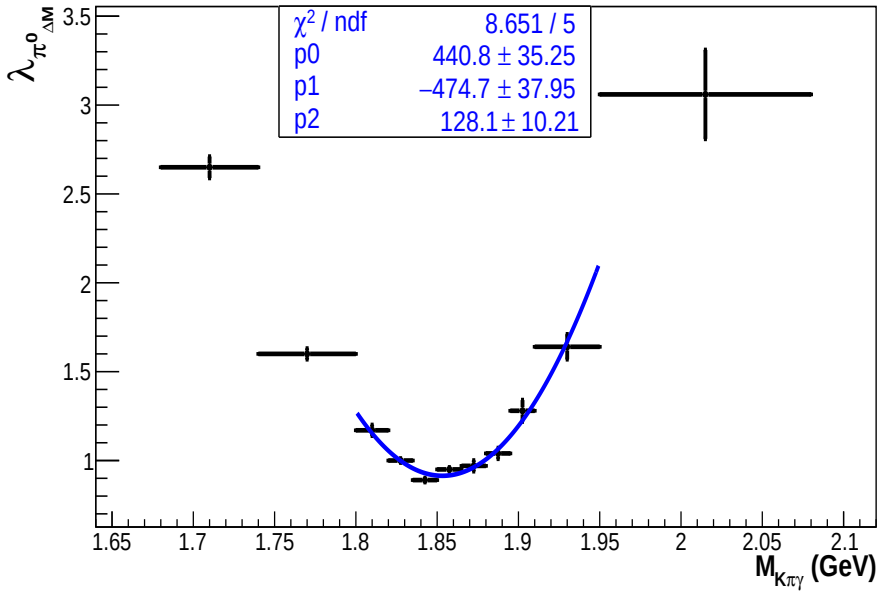

Figure **IV-19**: Correlation parameter λ for $D^0 \to \bar{K}^{*0}\pi^0$ background, obtained from ΔM fits in $M(D^0)$ bins, plotted against the corresponding $M(D^0)$ range. Result of χ^2 fit using 2$^{\text{nd}}$ order polynomial is superimposed, and fit parameters are also given. Two lowest- and one highest-mass bins are excluded from the fit.

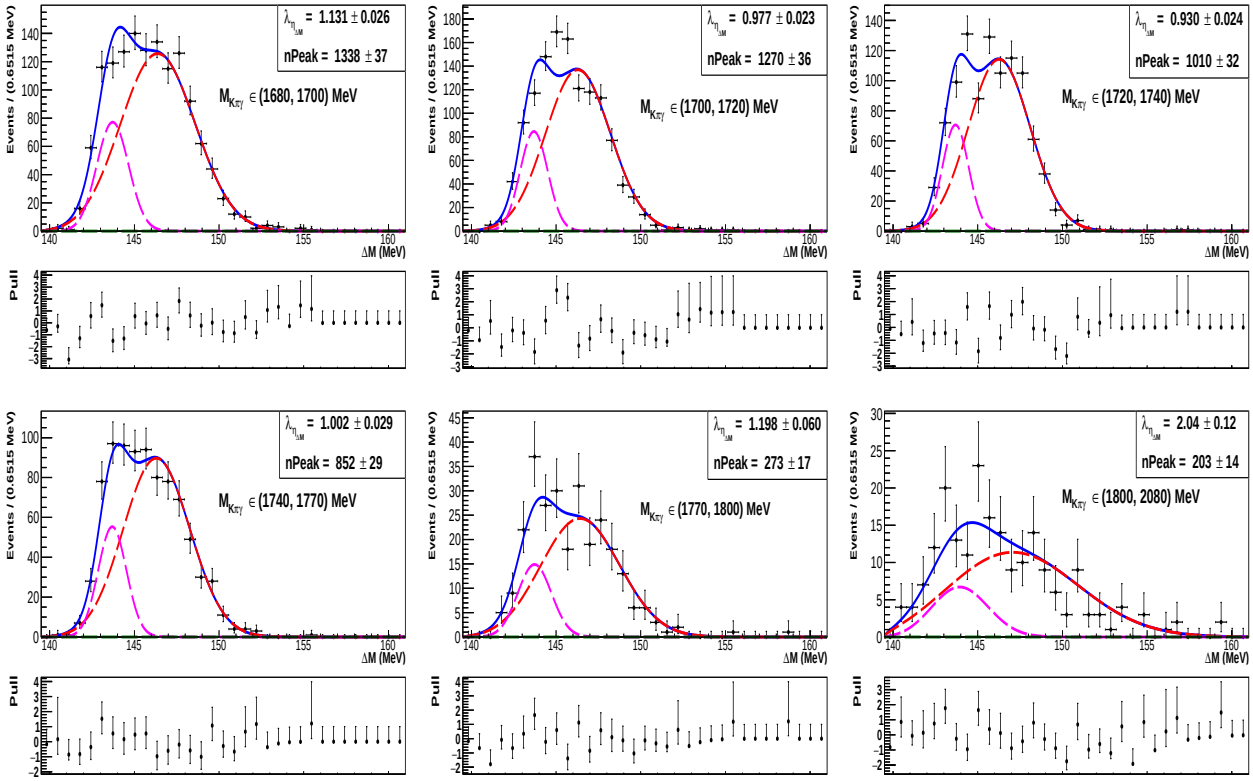

Figure **IV-20**: Results of ΔM fits in $M(D^0)$ bins performed using the simulation sample of $D^0 \to \bar{K}^{*0}\eta$ background. Considered $M(D^0)$ regions, as well as fitted λ values are indicated in individual figures.

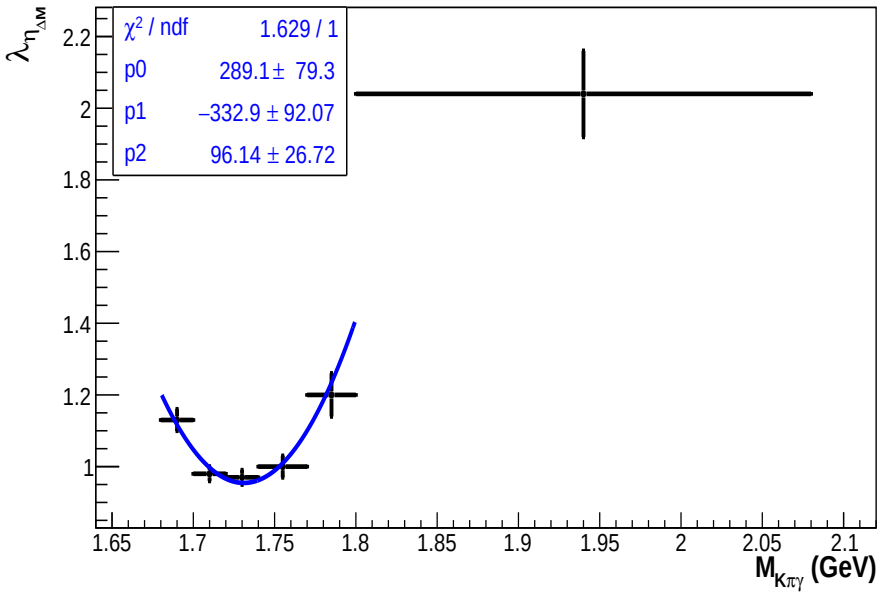

Figure **IV-21**: Correlation parameter λ for the $D^0 \to \bar{K}^{*0}\eta$ background, obtained from ΔM fits in $M(D^0)$ bins, plotted against the corresponding $M(D^0)$ range. Result of χ^2 fit using 2^{nd} order polynomial is superimposed, and fit parameters are also given. The highest-mass bin is excluded from the fit.

IV.7 Validating $M(D^0)$–ΔM correlations in K^* channels

Having parameterized the $M(D^0)$–ΔM correlations, one can return to the $M(D^0)$ and ΔM observables and perform a two-dimensional fit for each considered K^* channel, the $D^0 \to \bar{K}^{*0}\gamma$ signal, as well as π^0 and η background. PDFs for $M(D^0)$ variable are as introduced in Sections **IV.5.1- IV.5.3**, whereas PDFs for ΔM are conditional functions with correlations included according to Eq. **IV.4**. In this fit $\lambda(M)$ correlation function is fixed to that obtained from ΔM fits in $M(D^0)$ bins, whereas ΔM parameters $\sigma_1^{\Delta M}$ and $\mu_1^{\Delta M}$ are kept free. This way ΔM resolutions can get *adjusted* with respect to that from one-dimensional ΔM fit, to account for the fact that $\lambda(M)$ dependence is measured excluding $M(D^0)$ tails. $M(D^0)$ parameters, f_1, σ_1, μ_1, and also σ_L for the π^0 background and α for the η background are free parameters of fits. Remaining shape parameters of $M(D^0)$ and ΔM are fixed to those from one-dimensional fits presented in Sections **IV.5.1- IV.5.3**.

Parameters obtained from these two-dimensional fits, quoted in Tables **IV-4-IV-6**, are used to model signal and peaking-background components in fits to the $D^0 \to \bar{K}^{*0}\gamma$ candidates from the experimental data in Section **V.3**.

IV.7.1 $M(D^0)$–ΔM fit to simulation of $D^0 \to \bar{K}^{*0}\gamma$ signal

Results of the two-dimensional $M(D^0)$–ΔM fit performed for the $D^0 \to \bar{K}^{*0}\gamma$ simulation sample are presented in Fig. **IV-22** showing ΔM projections in $M(D^0)$ regions, and in Fig. **IV-23** showing $M(D^0)$ projections in ΔM regions. The projections show good fit quality also in tail regions of $M(D^0)$ and ΔM. Figure **IV-23** shows that further from the ΔM peak correlations modify the $M(D^0)$ shape in non-trivial way. This is the reason why describing correlations through modelling ΔM dependence on $M(D^0)$ is easier than other way around. Fit parameters are given in Table **IV-4**.

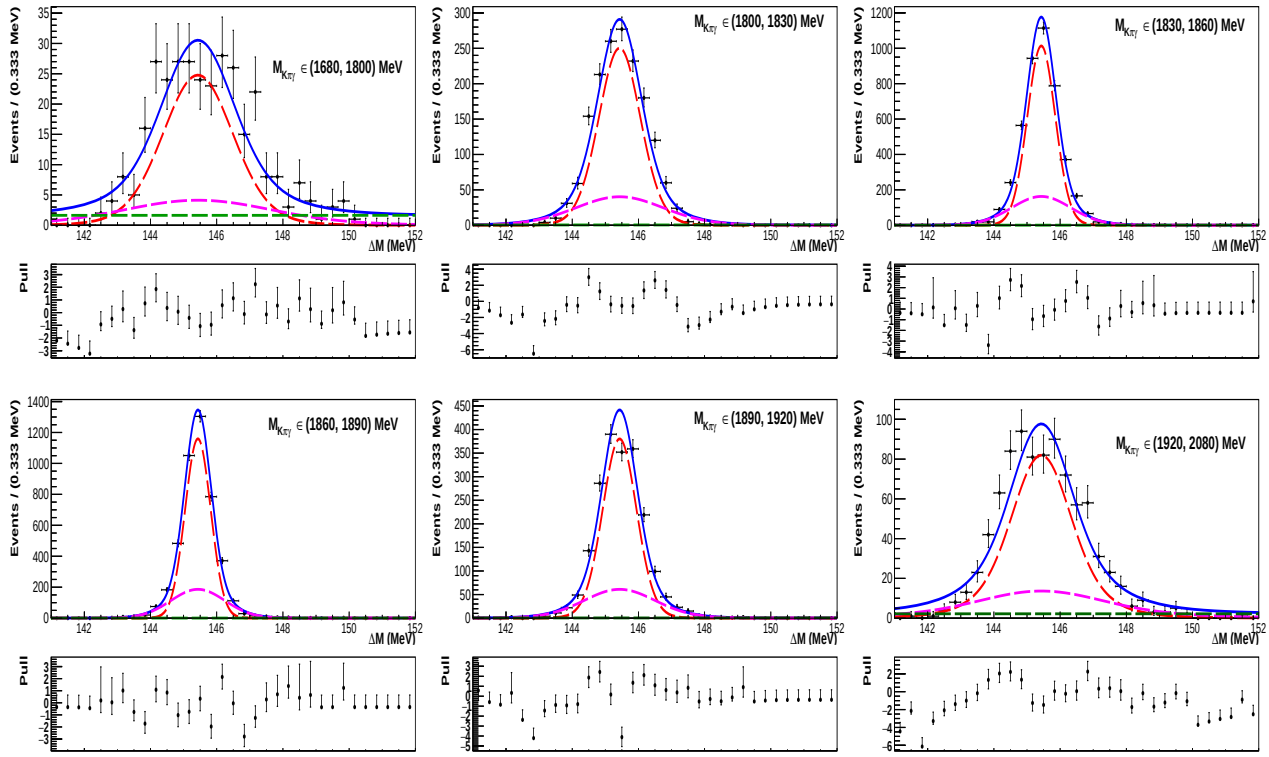

Figure **IV-22**: Results of two-dimensional $M(D^0)$–ΔM fit performed for $D^0 \to \bar{K}^{*0}\gamma$ simulation. ΔM projections are for $M(D^0)$ regions indicated in individual plots. Red and magenta lines describe G_1 and G_2 signal sub-components, green line is combinatorial background, blue line is total fit function.

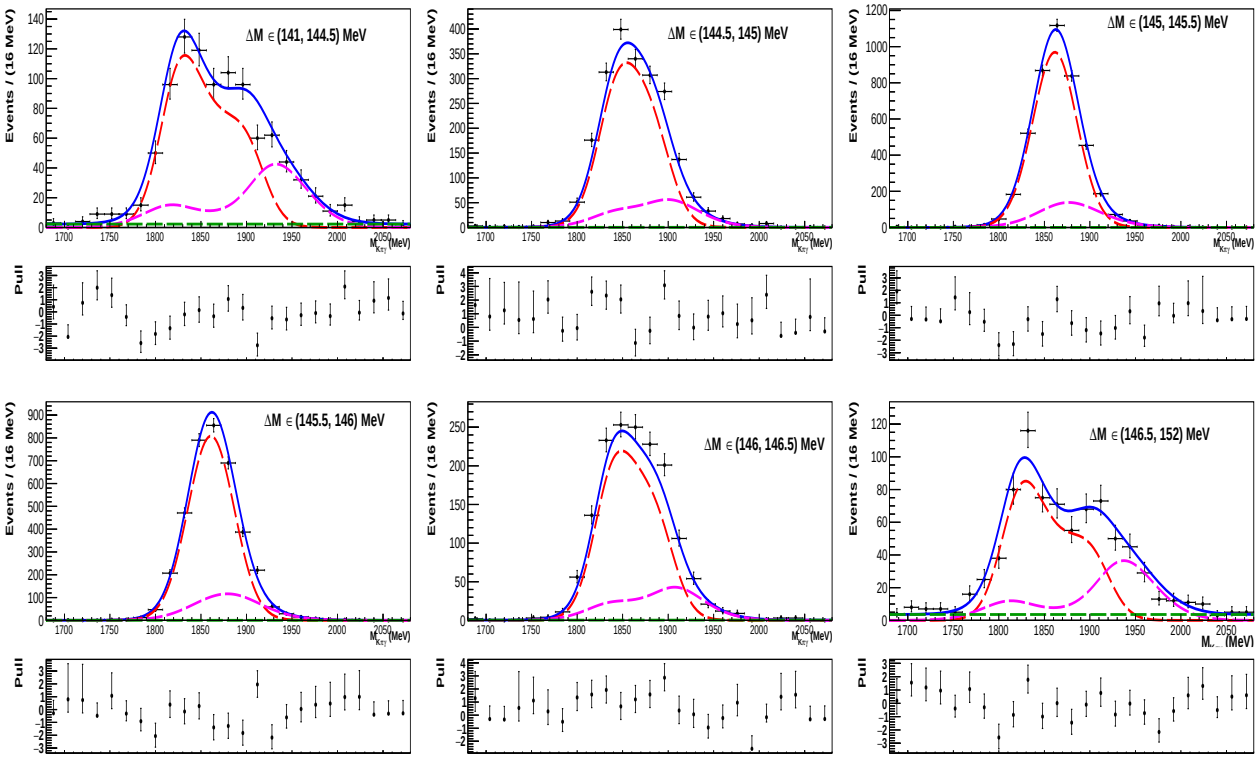

Figure **IV-23**: Results of two-dimensional $M(D^0)$–ΔM fit performed for $D^0 \to \bar{K}^{*0}\gamma$ simulation. $M(D^0)$ projections are for ΔM regions indicated in individual plots. Red and magenta lines describe G_1 and G_2 signal sub-components, green line is combinatorial background, blue line is total fit function.

Par/Obs	f_1 [%]	μ_1 [MeV/c^2]	σ_1 [MeV/c^2]	δ [MeV/c^2]	r
$M(D^0)$	$80.1^{+1.4}_{-1.5}$	$1859.78^{+0.42}_{-0.43}$	28.17 ± 0.35	27.1	1.68
ΔM	74.6	145.432 ± 0.005	0.575 ± 0.004	0.0	2.12

Table **IV-4**: Parameter values obtained from two-dimensional $M(D^0)$–ΔM fit with correlations for $D^0 \to \bar{K}^{*0}\gamma$ simulation. Parameters given without uncertainties are fixed to those from one-dimensional $M(D^0)$ and ΔM fits in Table **IV-1**.

IV.7.2 $M(D^0)$–ΔM fit to simulation of π^0 background

Results of the two-dimensional $M(D^0)$–ΔM fit performed for the simulated $D^0 \to \bar{K}^{*0}\pi^0$ background are presented in Fig. **IV-24** showing ΔM projections in $M(D^0)$ regions, and in Fig. **IV-25** showing $M(D^0)$ projections in ΔM regions. The fit quality is somewhat worse in the region of low values of both, $M(D^0)$ and ΔM. Improving this region would require more complicated correlation model. On the other hand, the signal does not contribute to this region, thus its mis-modelling will result in cross-feed between the threshold Gaussian of the π^0 background and the η background. This can be limited by modelling of correlations in the η background.

IV.7.3 $M(D^0)$–ΔM fit to simulation of η background

Results of the two-dimensional $M(D^0)$–ΔM fit performed for the simulated $D^0 \to \bar{K}^{*0}\eta$ background are presented in Fig. **IV-26** showing ΔM projections in $M(D^0)$ regions, and in Fig. **IV-27** showing $M(D^0)$ projections in ΔM regions. $M(D^0)$–ΔM correlations are not as strong for the η background, but

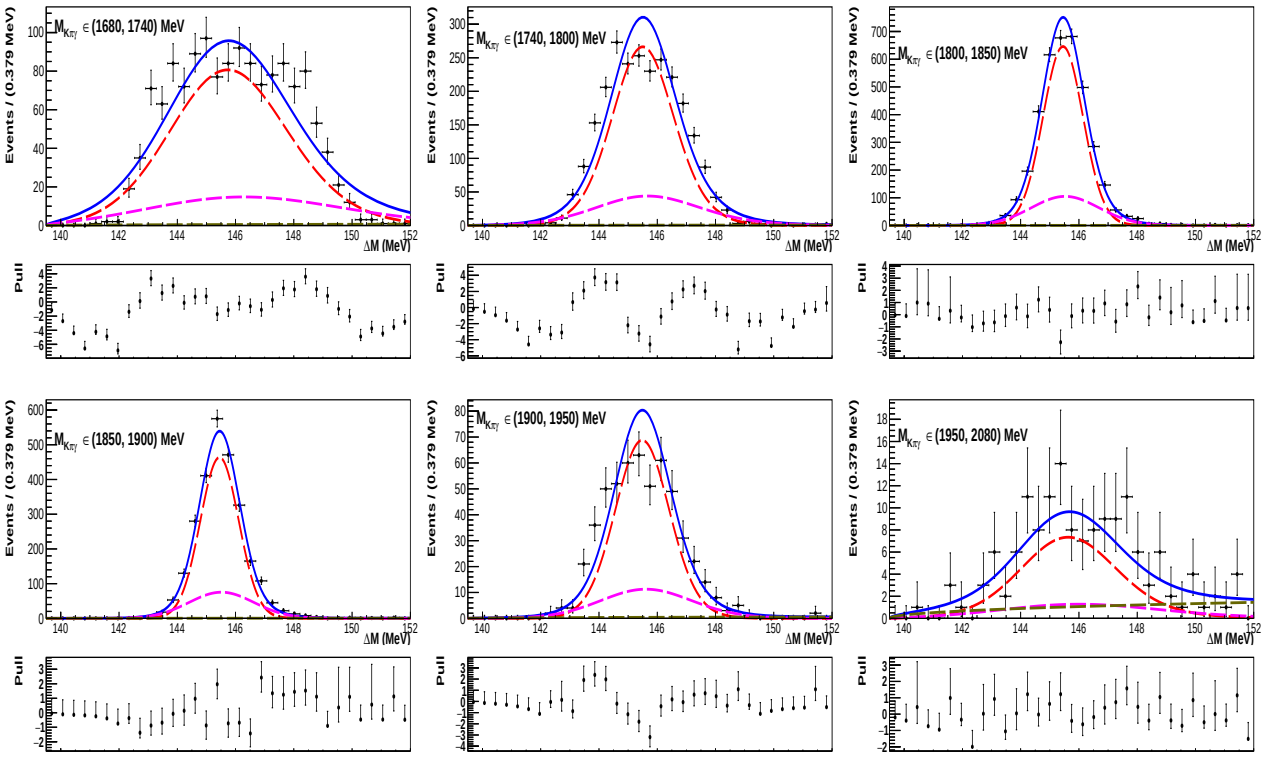

Figure **IV-24**: Results of two-dimensional $M(D^0)$–ΔM fit performed for $D^0 \to \bar{K}^{*0}\pi^0$ simulation. ΔM projections are for $M(D^0)$ regions indicated in individual plots. Red and magenta lines describe G_1 and G_2 π^0 sub-components, brown line is combinatorial background, blue line is total fit function.

Par/Obs	f_1 [%]	μ_1	σ_1	f_2/f_1	δ	r	μ_3	σ_L	σ_R
$M(D^0)$	46 ± 1	1843 ± 1	34.6 ± 0.7	0.233	27.1	1.678	1783.8	95^{+8}_{-6}	53.2
ΔM	78.4	145.41	0.613 ± 0.005	–	0.0	1.7	–	–	–

Table **IV-5**: Parameter values obtained from two-dimensional $M(D^0)$–ΔM fit with correlations for $D^0 \to \bar{K}^{*0}\pi^0$ simulation. Parameters given without uncertainties are fixed to those from one-dimensional $M(D^0)$ and ΔM fits in Table **IV-2**. Means of Gaussian functions, μ_1 and μ_3, peak offset δ, and Gaussian widths σ_1, σ_L and σ_R, are given in MeV/c^2.

including them is important for describing of low $M(D^0)$ region, where modelling of the π^0 background is difficult. To some extent it also helps to control a possible cross-feed between the η background and the signal through the high-mass tail of the former.

Par/Obs	f_1 [%]	μ_1	σ_1	μ_2	σ_2	α	n
$M(D^0)$	–	1697.7 ± 2.3	42.7 ± 1.6	–	–	-1.99 ± 0.07	2.9
ΔM	79	146.02	2.09 ± 0.02	143.61	0.84	–	–

Table **IV-6**: Parameter values obtained from two-dimensional $M(D^0)$–ΔM fit with correlations for $D^0 \to \bar{K}^{*0}\eta$ simulation. Parameters given without uncertainties are fixed to those from one-dimensional $M(D^0)$ and ΔM fits in Table **IV-3**. Means and widths of Gaussian and CB functions are given in MeV/c^2.

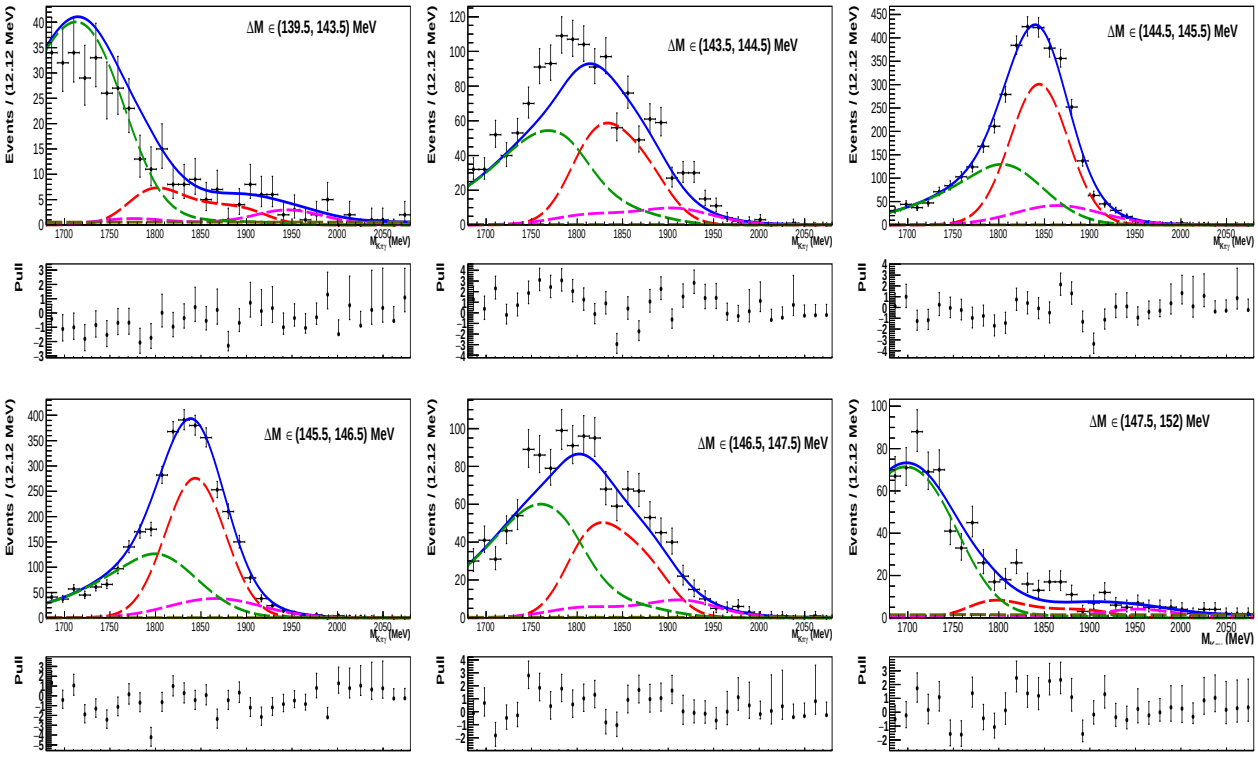

Figure **IV-25**: Results of two-dimensional $M(D^0)$–ΔM fit performed for $D^0 \to \bar{K}^{*0}\pi^0$ simulation. $M(D^0)$ projections are for ΔM regions indicated in individual plots. Red and magenta lines describe G_1 and G_2 π^0 sub-components, green line denotes threshold Gaussian, brown line is combinatorial background, blue line is total fit function.

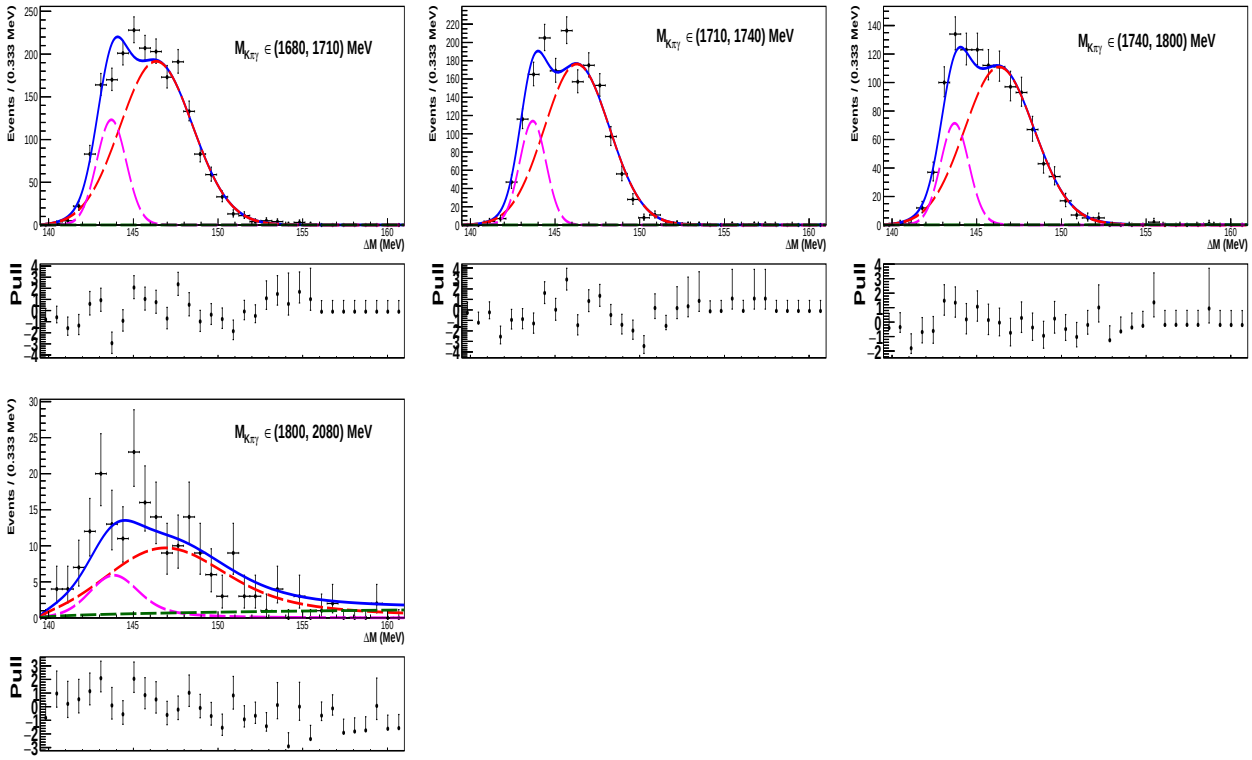

Figure **IV-26**: Results of two-dimensional $M(D^0)$–ΔM fit performed for $D^0 \to \bar{K}^{*0}\eta$ simulation. ΔM projections are for $M(D^0)$ regions indicated in individual plots. Red and magenta lines describe G_1 and G_2 η sub-components, green line is combinatorial background, blue line is total fit function.

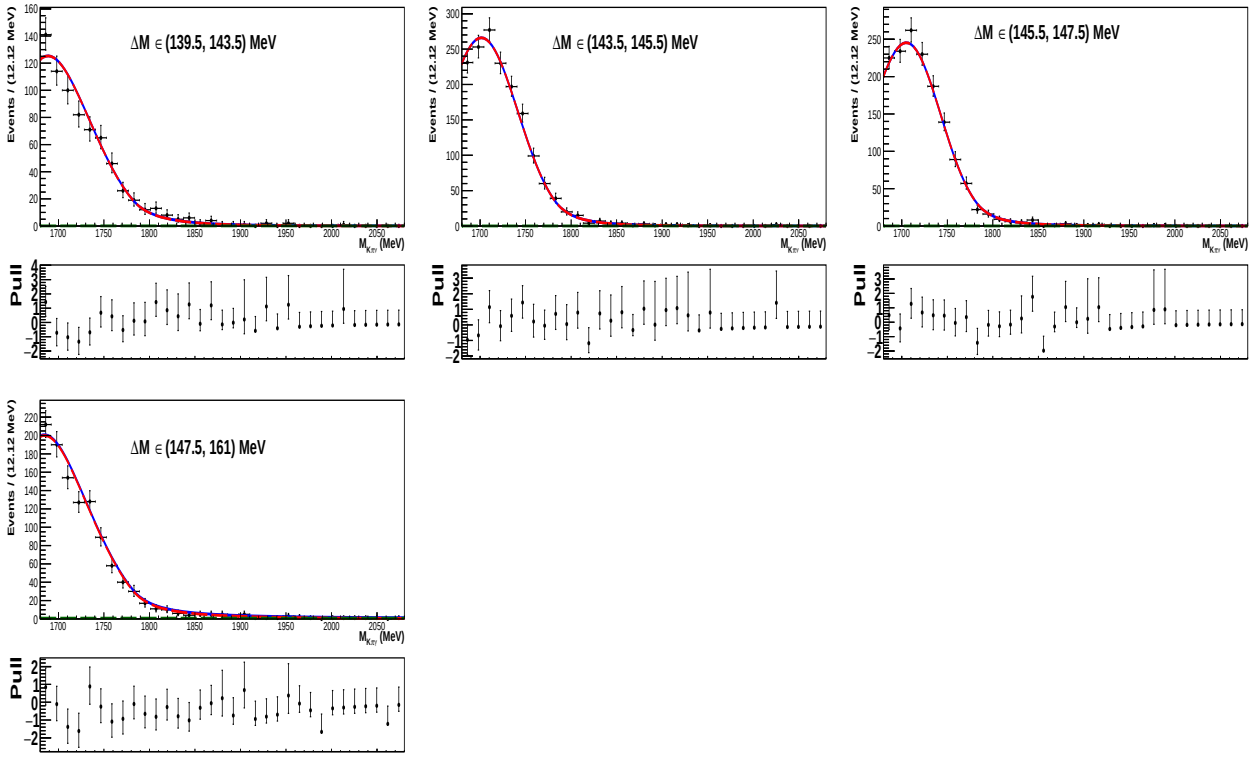

Figure **IV-27**: Results of two-dimensional $M(D^0)$–ΔM fit performed for $D^0 \to \bar{K}^{*0}\eta$ simulation. $M(D^0)$ projections are for ΔM regions indicated in individual plots. Red line describes η component, green line is combinatorial background, blue line is total fit function.

IV.8 Fits to $M(D^0)$, ΔM and $\cos\theta$ observables for ϕ channels

IV.8.1 Fits for simulated $D^0 \to \phi\gamma$ decays

Distributions of discriminating variables for the $D^0 \to \phi\gamma$ simulation sample with fit results superimposed, are presented in Fig. **IV-28**; given variable is selected in the full ranges of the other two. The distributions are fitted using PDFs as for the $D^0 \to \bar{K}^{*0}\gamma$ signal in Eq. **IV.1**. Parameter values obtained from one-dimensional fits to $M(D^0)$ and ΔM are summarised in Table **IV-7**. Overall, $M(D^0)$ and ΔM shapes are very similar between $D^0 \to \phi\gamma$ and $D^0 \to \bar{K}^{*0}\gamma$ signal channels. In the $\cos\theta$ PDF, the a_1 parameter is fixed to zero, as an acceptance is symmetric with respect to $\cos\theta = 0$ for the charge-symmetric final state. The parameter $a_2 = 0.047 \pm 0.080$ is consistent with zero, implying that any acceptance effects in $\cos\theta$ are negligible for this channel.

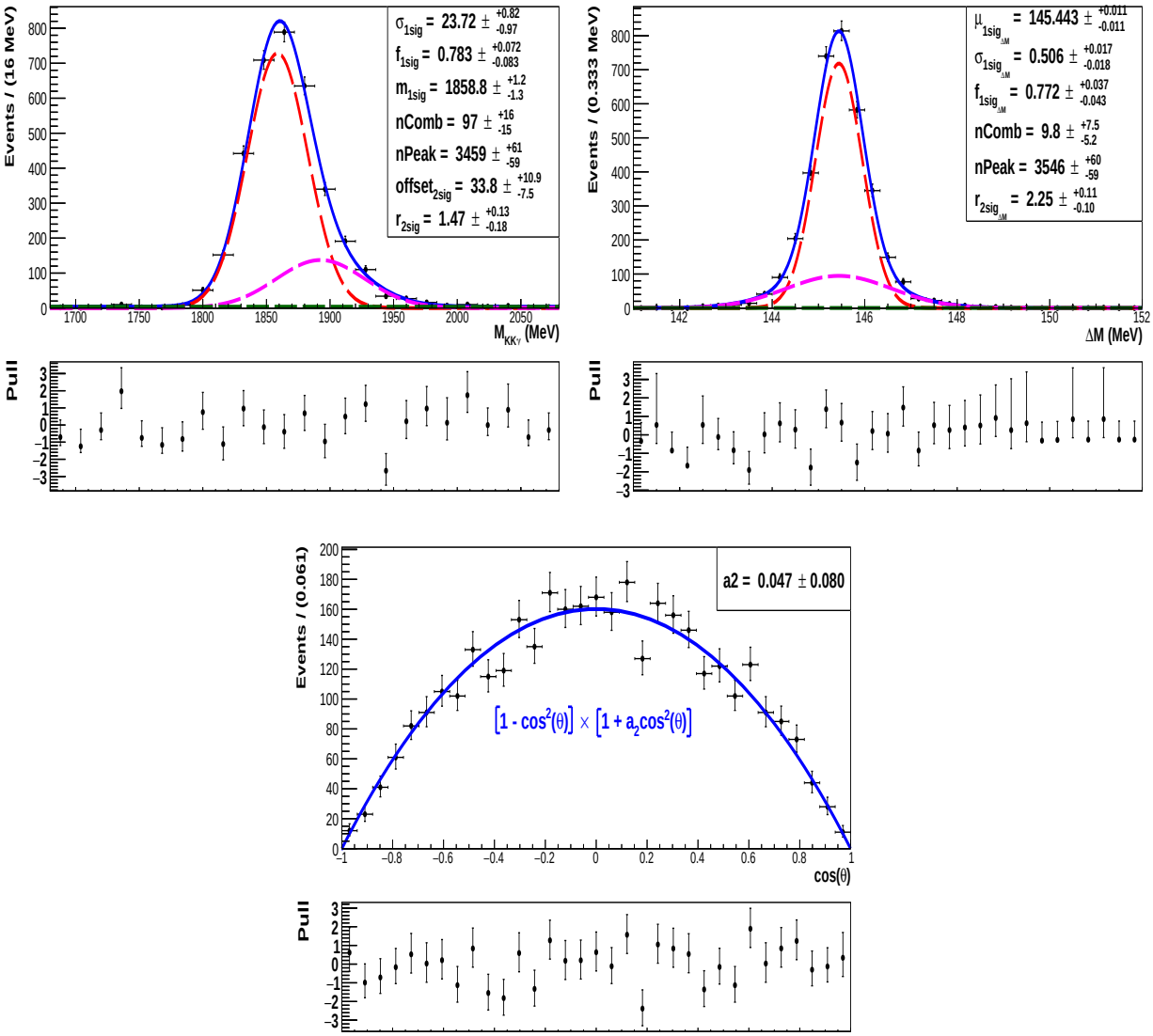

Figure **IV-28**: Distributions of (top left) $M(D^0)$, (top right) ΔM and (bottom) $\cos\theta$ for simulated $D^0 \to \phi\gamma$ decays. Results of one-dimensional fits are superimposed.

Par/Obs	f_1 [%]	μ_1 [MeV/c^2]	σ_1 [MeV/c^2]	δ [MeV/c^2]	r
$M(D^0)$	$78.3^{+7.2}_{-8.3}$	$1858.8^{+1.2}_{-1.3}$	$23.7^{+0.8}_{-1.0}$	$33.8^{+10.9}_{-7.5}$	$1.47^{+0.13}_{-0.18}$
ΔM	$77.2^{+3.7}_{-4.3}$	145.443 ± 0.011	$0.506^{+0.017}_{-0.018}$	0.0	$2.25^{+0.11}_{-0.10}$

Table **IV-7**: Parameter values obtained from one-dimensional fits to $M(D^0)$ and ΔM observables in $D^0 \to \phi\gamma$ simulation sample.

IV.8.2 Fits for simulated $D^0 \to \phi\pi^0$ background

The $M(D^0)$, ΔM and $\cos\theta$ distributions for the $D^0 \to \phi\pi^0$ simulation sample, passing the full signal selection, are shown in Fig. **IV-29**. They are selected in the full range of the other observables, except for ΔM considered in the restricted $M(D^0)$ range, $1750 < M(D^0) < 1890$ MeV/c^2, to facilitate modelling of $M(D^0)$–ΔM correlations.

PDFs for the $M(D^0)$ and ΔM shapes are the same as for $D^0 \to \bar{K}^{*0}\pi^0$ background, given in Eq. **IV.2**. Parameters of the asymmetric *threshold* Gaussian in the $M(D^0)$ PDF are constrained using the sample involving background from resolved π^0's. It is selected with the reversed `VetoPi0`, and shown in Fig. **IV-29** (bottom right) together with results of the fit performed with an asymmetric Gaussian function. The parameters of G_2 in the $M(D^0)$ PDF, namely its fraction f_2 relative to f_1, as well as width ratio r and peak offset δ, are fixed to those of the $D^0 \to \phi\gamma$ signal (Table **IV-7**). Parameter values obtained from one-dimensional fits to $M(D^0)$ and ΔM are summarised in Table **IV-8**.

The $\cos\theta$ distribution is described with PDF$(\cos\theta) = \cos^2\theta \times (1 + b_2 \cos^2\theta)$, corresponding to the theoretical function multiplied by an acceptance term, with $b_2 = -0.094 \pm 0.090$ being insignificant.

Par/Obs	f_1 [%]	μ_1	σ_1	f_2/f_1	δ	r	μ_3	σ_L	σ_R
$M(D^0)$	46^{+4}_{-3}	1833 ± 3	$36.1^{+2.4}_{-2.3}$	0.277	33.8	1.47	1771.8	108 ± 39	58.5
ΔM	82^{+9}_{-15}	145.42 ± 0.03	$0.80^{+0.05}_{-0.06}$	–	0.0	$1.8^{+0.3}_{-0.2}$	–	–	–

Table **IV-8**: Parameter values obtained from one-dimensional fits to $M(D^0)$ and ΔM observables in $D^0 \to \phi\pi^0$ simulation sample passing the full signal selection. Means of Gaussian functions, μ_1 and μ_3, peak offset δ, and Gaussian widths σ_1, σ_L and σ_R, are given in MeV/c^2.

IV.8.3 Fits for simulated $D^0 \to \phi\eta$ background

The $M(D^0)$, ΔM and $\cos\theta$ distributions for the $D^0 \to \phi\eta$ simulation sample, passing the full signal selection, are shown in Fig. **IV-30**. They are selected in the full range of the other observables. PDFs for the $M(D^0)$ and ΔM shapes are the same as for $D^0 \to \bar{K}^{*0}\eta$ background, given in Eq. **IV.3**. Parameter values obtained from one-dimensional fits to $M(D^0)$ and ΔM are summarised in Table **IV-9**. The $\cos\theta$ distribution is described with the theoretical function of $\cos^2\theta$; no acceptance corrections are necessary.

Par/Obs	f_1 [%]	μ_1	σ_1	μ_2	σ_2	α	n
$M(D^0)$	–	1700.3 ± 2.9	31.6 ± 2.5	–	–	-1.5 ± 0.2	3.5 ± 1.0
ΔM	72 ± 3	145.98 ± 0.01	2.09 ± 0.03	143.44 ± 0.12	1.09 ± 0.10	–	–

Table **IV-9**: Parameter values obtained from one-dimensional fits to $M(D^0)$ and ΔM observables in $D^0 \to \phi\eta$ simulation sample. Means and widths of Gaussian and CB functions are given in MeV/c^2.

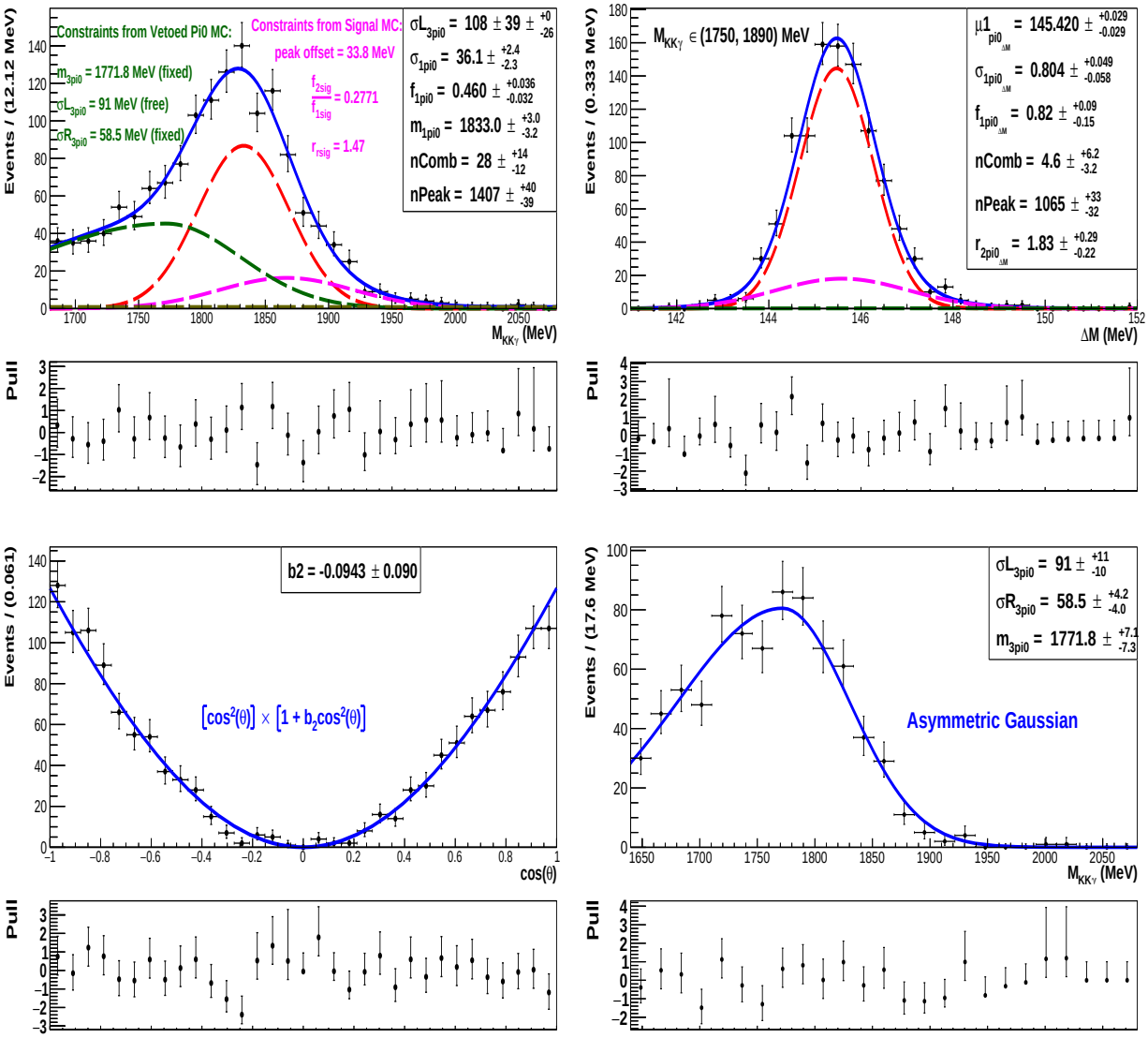

Figure **IV-29**: Distributions of (top left) $M(D^0)$, (top right) ΔM for simulated $D^0 \to \phi\pi^0$ sample and (bottom left) $\cos\theta$ passing the full signal selection. Results of one-dimensional fits are superimposed. The threshold asymmetric Gaussian in the $M(D^0)$ fit is constrained to the resolved-π^0 sample in the bottom right figure. (Bottom right) $M(D^0)$ distribution of the simulated $D^0 \to \phi\pi^0$ background involving resolved π^0 with one photon missing. Candidates pass the signal selection with `VetoPi0R` reversed. Result of the fit is superimposed.

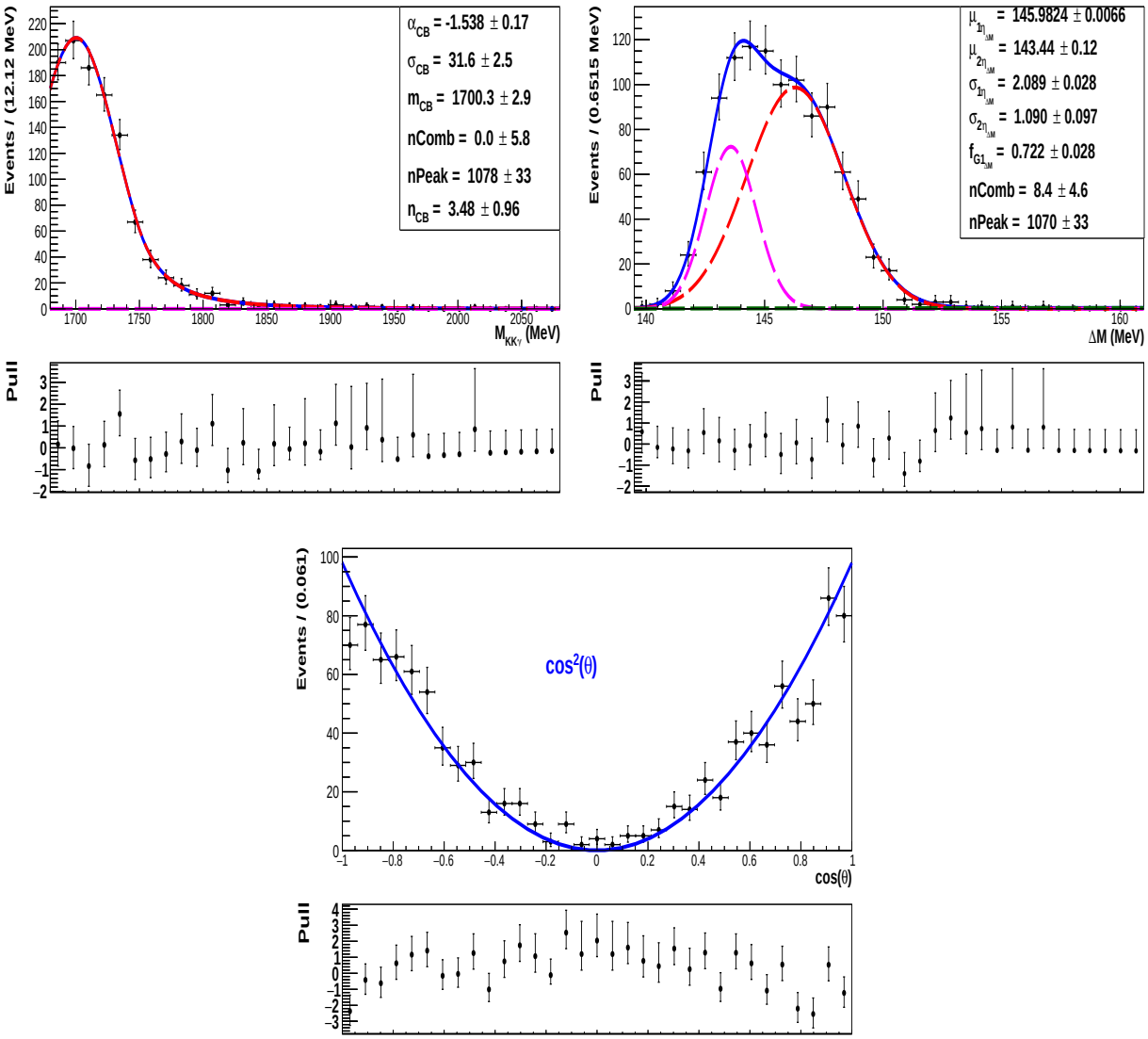

Figure **IV-30**: Distributions of (top left) $M(D^0)$, (top right) ΔM for simulated $D^0 \to \phi\eta$ sample and (bottom) $\cos\theta$ passing the full signal selection. Results of one-dimensional fits are superimposed.

IV.9 Describing $M(D^0)$–ΔM correlations in ϕ channels

Method to measure a dependence of the ΔM resolution on $M(D^0)$, described by $\lambda(M)$ function, is the same as for the K^* channels in Section **IV.6**. This measurement starts from ΔM fits in $M(D^0)$ bins, performed for each signal and background ϕ channel. A λ factor is applied to both Gaussian components of a ΔM PDF, as in Eq. **IV.4**. ΔM parameters are fixed to those from the one-dimensional ΔM fits in Section **IV.8**. The fitted values of the λ parameter as a function of $M(D^0)$ are then parameterised with a second-order polynomial function. For the $D^0 \to \phi\eta$ background, where correlations are not significant, $\lambda(M)$ dependence is also described with a constant, and this parameterization is used as a default one.

The above steps are illustrated for the $D^0 \to \phi\gamma$ signal in Figs. **IV-31** and **IV-32**, for the $D^0 \to \phi\pi^0$ background in Figs. **IV-33** and **IV-34**, and for the $D^0 \to \phi\eta$ background in Figs. **IV-35** and **IV-36**.

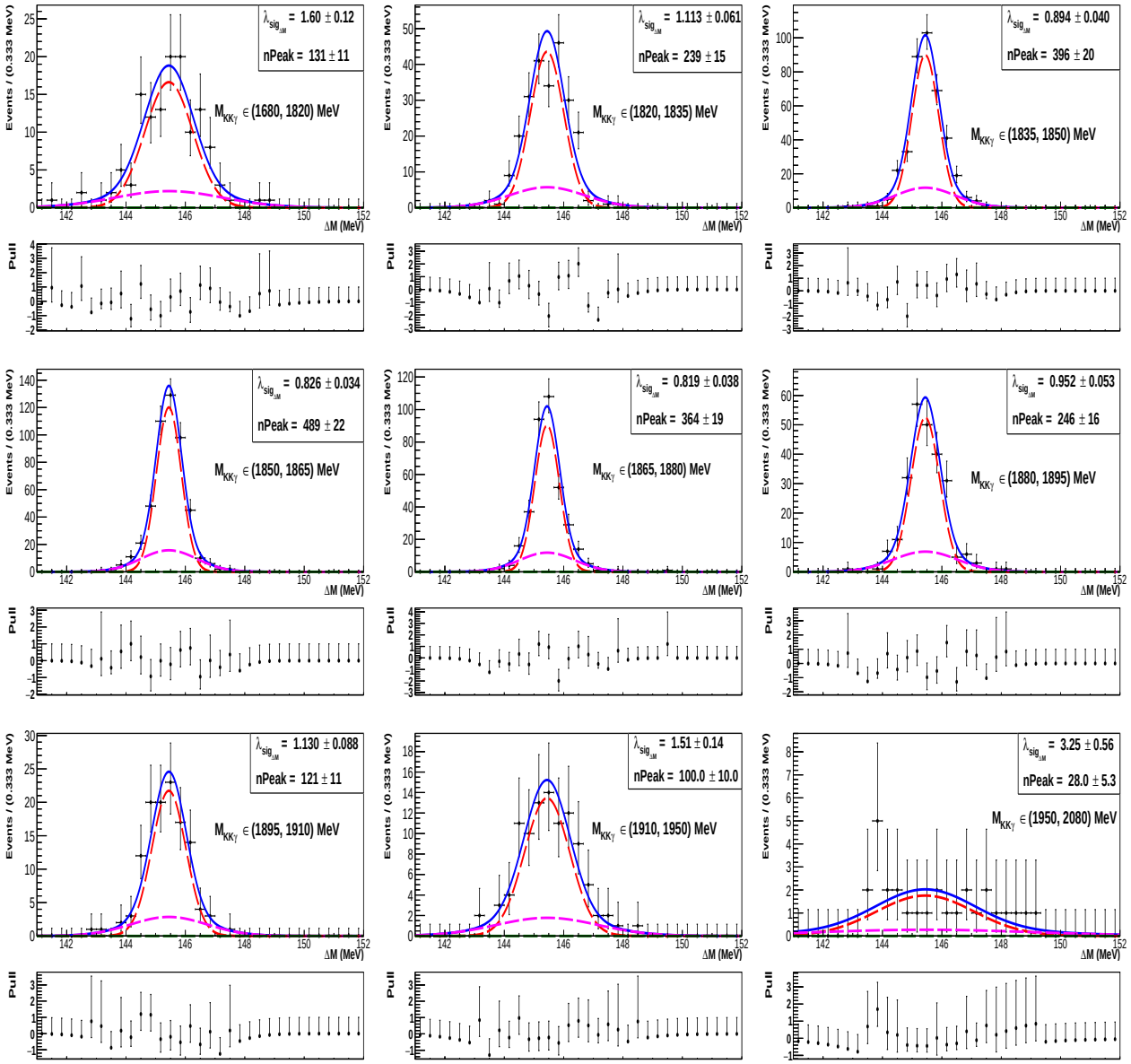

Figure **IV-31**: Results of ΔM fits in $M(D^0)$ bins performed using the $D^0 \to \phi\gamma$ simulation sample. Considered $M(D^0)$ regions, as well as fitted λ values are indicated in individual figures.

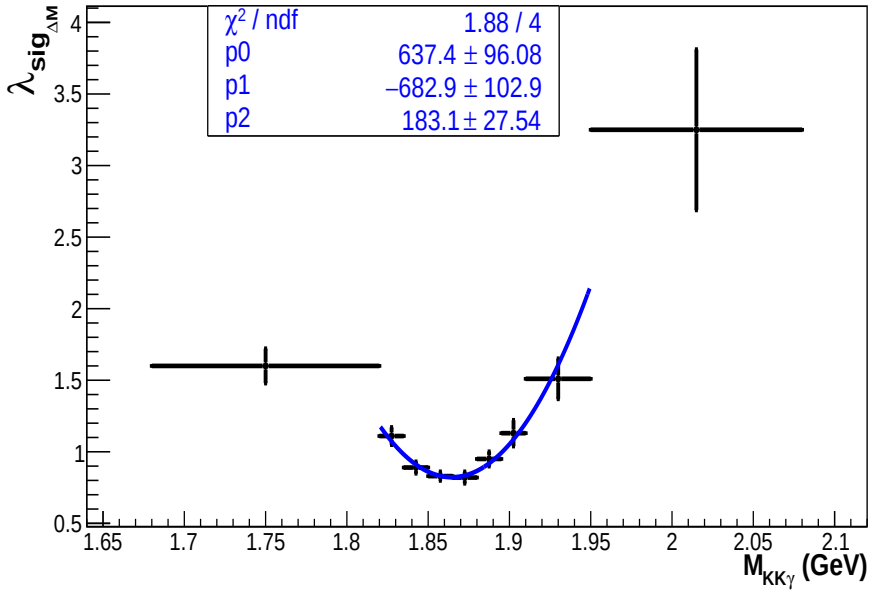

Figure **IV-32**: Correlation parameter λ for $D^0 \to \phi\gamma$ signal, obtained from ΔM fits in $M(D^0)$ bins, plotted against the corresponding $M(D^0)$ range. Result of χ^2 fit using 2^{nd} order polynomial is superimposed, and fit parameters are also given. The lowest- and highest-mass bins are excluded from the fit.

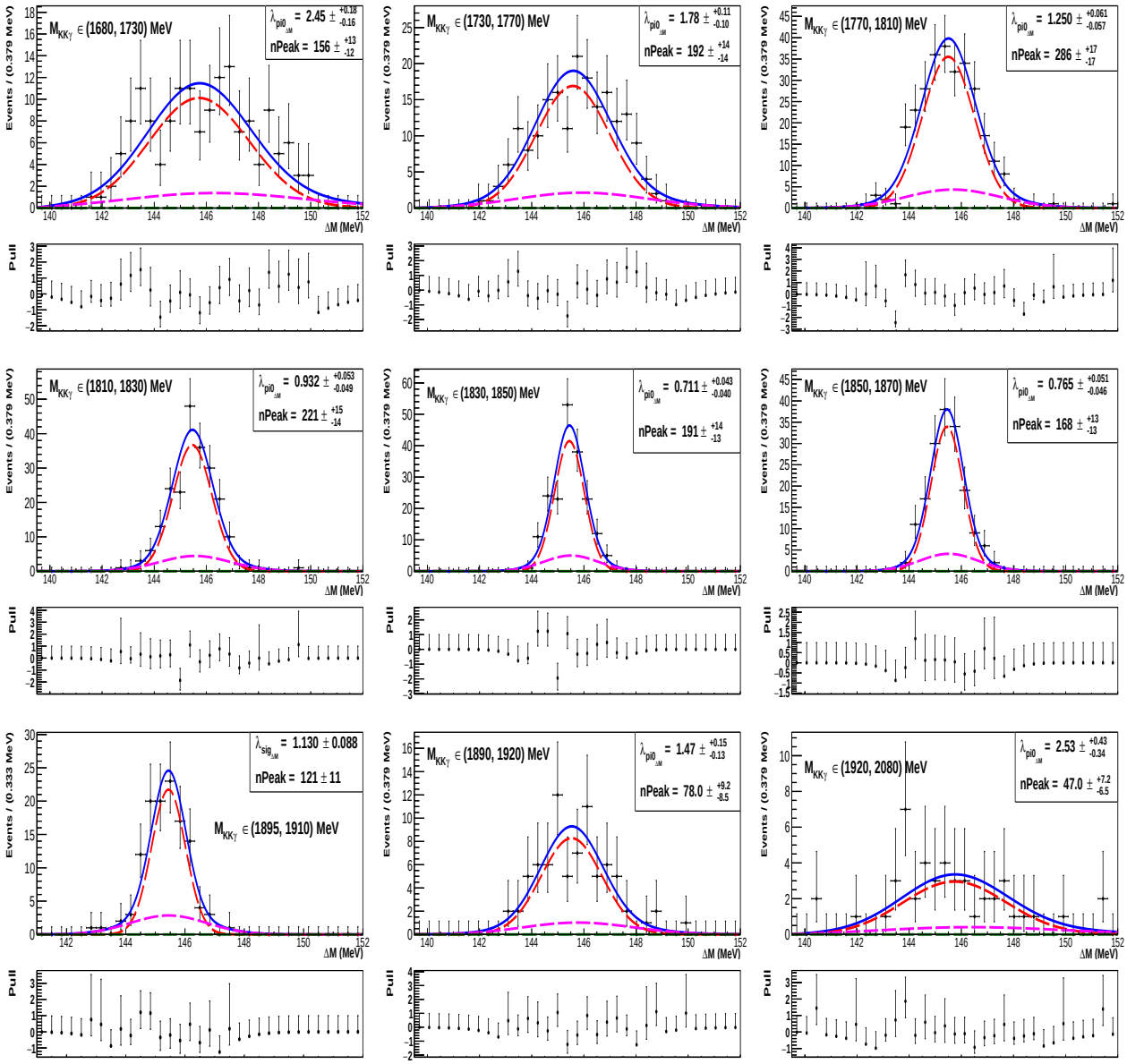

Figure **IV-33**: Results of ΔM fits in $M(D^0)$ bins performed using the $D^0 \to \phi\pi^0$ simulation sample. Considered $M(D^0)$ regions, as well as fitted λ values are indicated in individual figures.

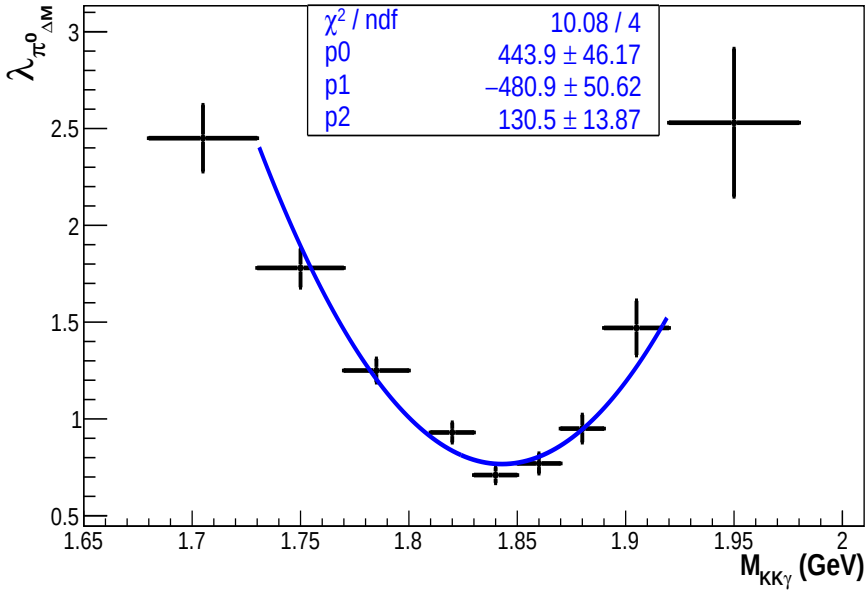

Figure **IV-34**: Correlation parameter λ for $D^0 \to \phi\pi^0$ signal, obtained from ΔM fits in $M(D^0)$ bins, plotted against the corresponding $M(D^0)$ range. Result of χ^2 fit using 2$^{\text{nd}}$ order polynomial is superimposed, and fit parameters are also given. The lowest- and highest-mass bins are excluded from the fit.

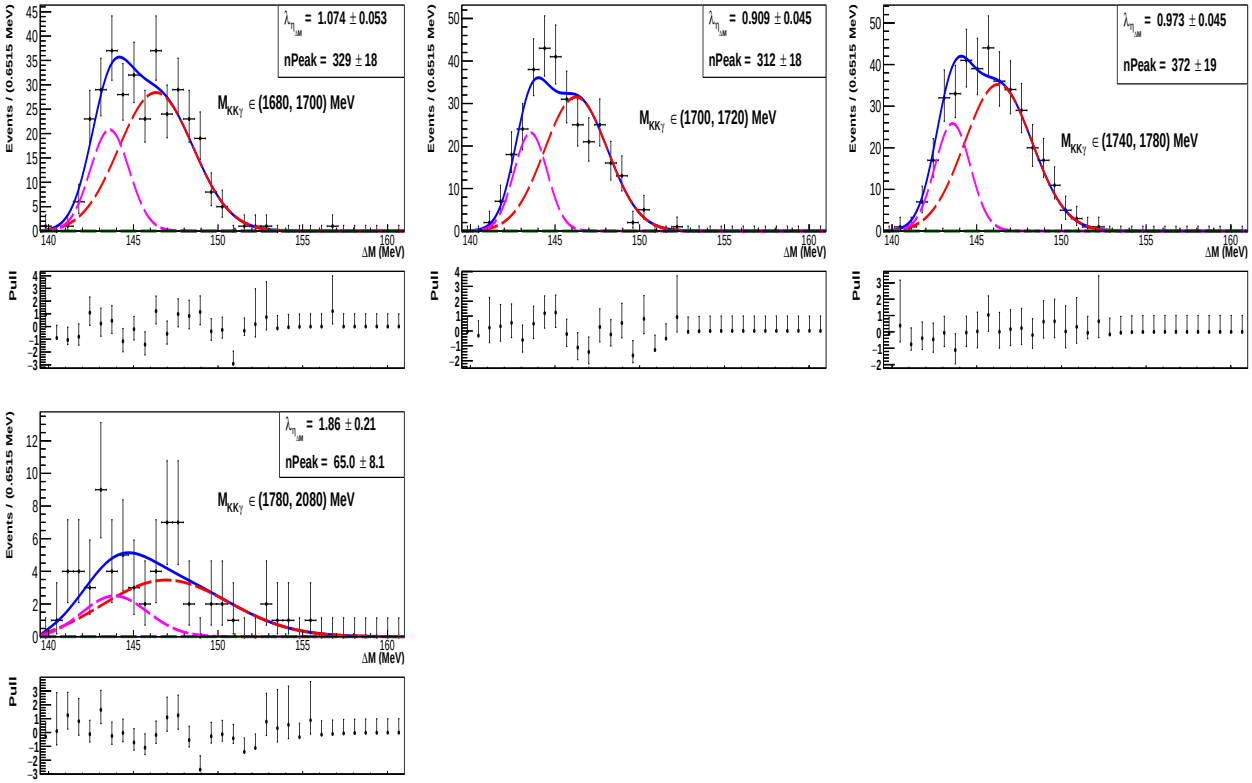

Figure **IV-35**: Results of ΔM fits in $M(D^0)$ bins performed using the $D^0 \to \phi\eta$ simulation sample. Considered $M(D^0)$ regions, as well as fitted λ values are indicated in individual figures.

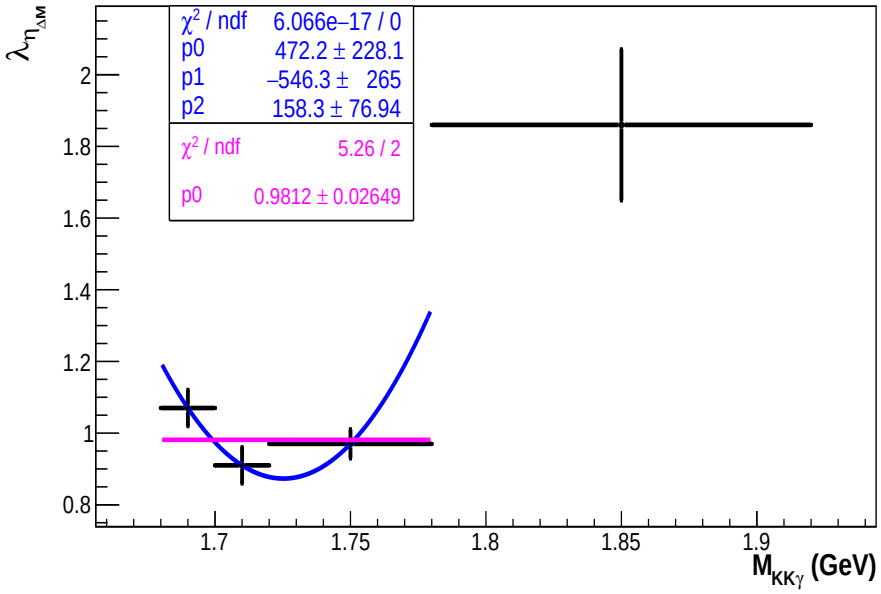

Figure **IV-36**: Correlation parameter λ for $D^0 \to \phi\eta$ signal, obtained from ΔM fits in $M(D^0)$ bins, plotted against the corresponding $M(D^0)$ bin. Results of χ^2 fit using 2^{nd} order polynomial (blue) and constant (magenta) are superimposed, and fit parameters are also given. The highest-mass bin is excluded from the fit.

IV.10 Validating $M(D^0)$–ΔM correlations in ϕ channels

Two-dimensional $M(D^0)$–ΔM fit for each considered ϕ channel, the $D^0 \to \phi\gamma$ signal, as well as $D^0 \to \phi\pi^0$ and $D^0 \to \phi\eta$ background, is performed with the corresponding $\lambda(M)$ correlation function fixed to that obtained in Section **IV.9**. PDFs for $M(D^0)$ variable are as introduced in Sections **IV.8.1**- **IV.8.3**, whereas PDFs for ΔM are conditional functions with correlations included according to Eq. **IV.4**. As in the fits for the K^* channels, some of the $M(D^0)$ and ΔM shape parameters are kept free, in particular $\sigma_1^{\Delta M}$, while the others are fixed to those from one-dimensional fits presented in Sections **IV.8.1**- **IV.8.3**. This is specified in Tables **IV-10**-**IV-12**, along with parameters obtained from these two-dimensional fits.

Results of the two-dimensional $M(D^0)$–ΔM fit performed for the $D^0 \to \phi\gamma$ simulation sample are presented in Fig. **IV-37** showing ΔM projections in $M(D^0)$ regions, and in Fig. **IV-38** showing $M(D^0)$ projections in ΔM regions. The corresponding fit projections for the $D^0 \to \phi\pi^0$ simulation sample are presented in Figs. **IV-39** and **IV-40**, while for the $D^0 \to \phi\eta$ simulation sample are presented in Figs. **IV-41** and **IV-42**.

Parameters obtained from these two-dimensional fits are used to model signal and peaking-background components in fits to the $D^0 \to \phi\gamma$ candidates from the experimental data Section **V.4**.

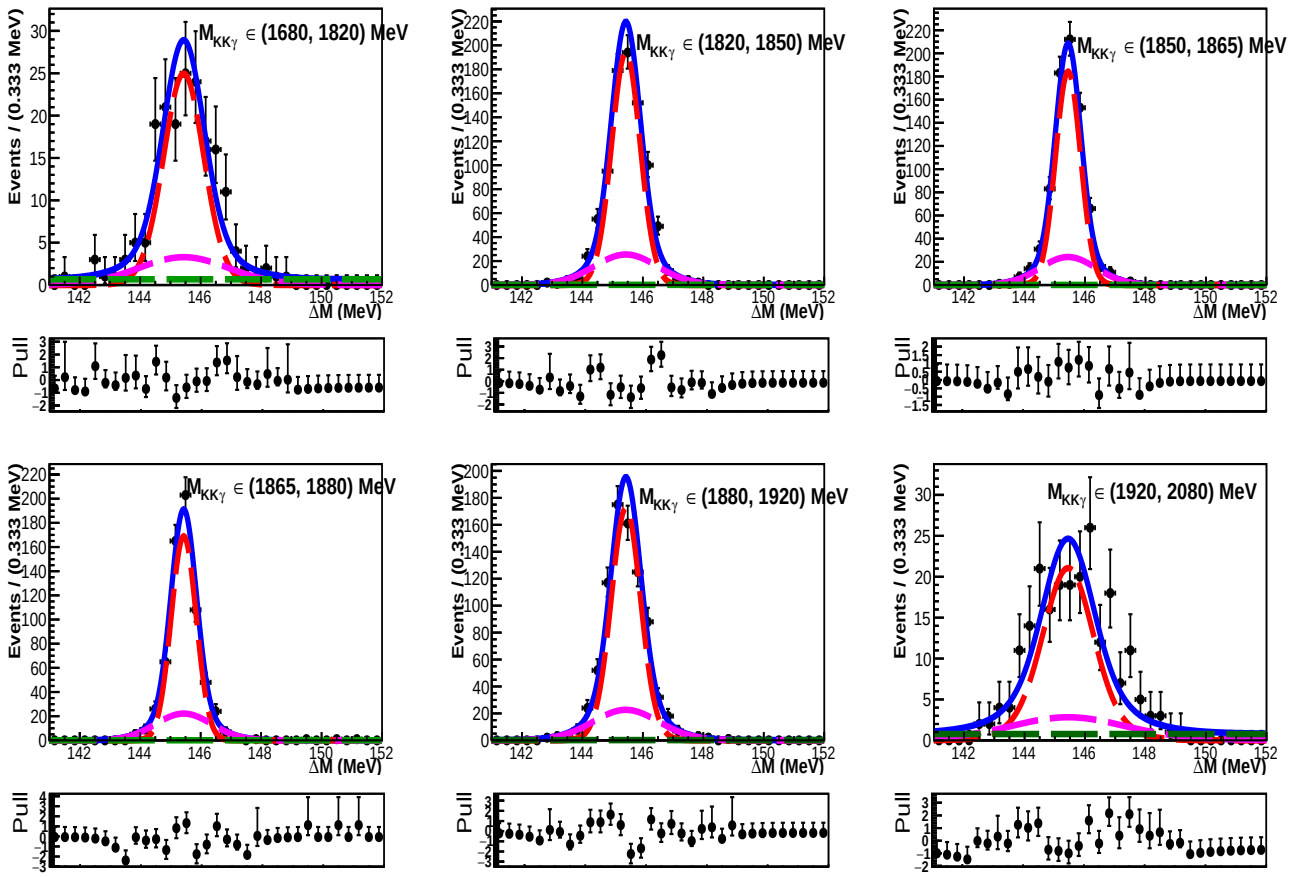

Figure **IV-37**: Results of two-dimensional $M(D^0)$–ΔM fit performed for $D^0 \to \phi\gamma$ simulation. ΔM projections are for $M(D^0)$ regions indicated in individual plots. Red and magenta lines describe G_1 and G_2 signal sub-components, green line is combinatorial background, blue line is total fit function.

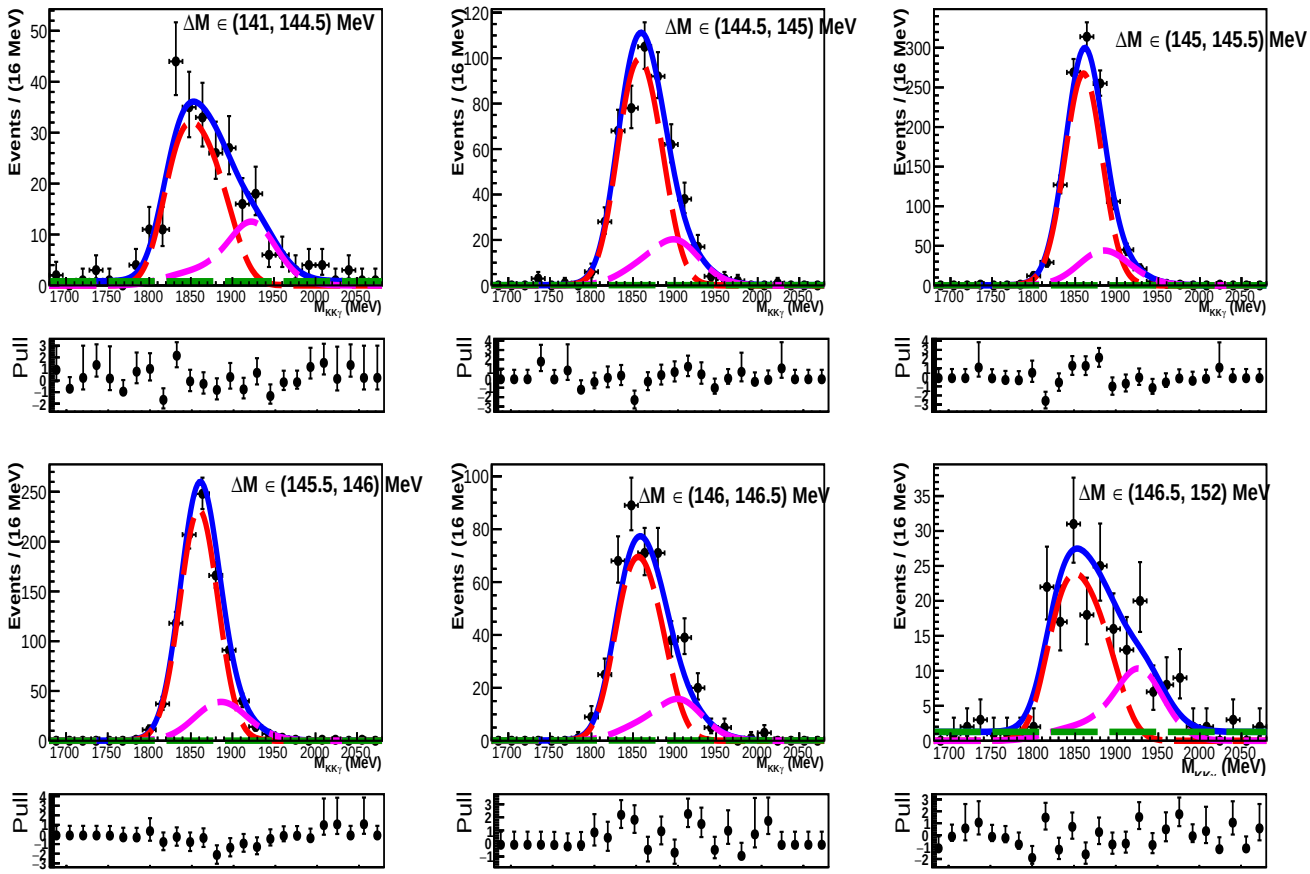

Figure **IV-38**: Results of two-dimensional $M(D^0)$–ΔM fit performed for $D^0 \to \phi\gamma$ simulation. $M(D^0)$ projections are for ΔM regions indicated in individual plots. Red and magenta lines describe G_1 and G_2 signal sub-components, green line is combinatorial background, blue line is total fit function.

Par/Obs	f_1 [%]	μ_1 [MeV/c^2]	σ_1 [MeV/c^2]	δ [MeV/c^2]	r
$M(D^0)$	$79.1^{+2.6}_{-2.8}$	$1859.2^{+0.9}_{-1.0}$	24.4 ± 0.6	33.8	1.47
ΔM	77.2	145.44 ± 0.01	$0.496^{+0.008}_{-0.007}$	0.0	2.25

Table **IV-10**: Parameter values obtained from two-dimensional $M(D^0)$–ΔM fit with correlations for the $D^0 \to \phi\gamma$ simulation sample. Parameters given without uncertainties are fixed to those from one-dimensional $M(D^0)$ and ΔM fits in Table **IV-7**.

Par/Obs	f_1 [%]	μ_1	σ_1	f_2/f_1	δ	r	μ_3	σ_L	σ_R
$M(D^0)$	47^{+4}_{-3}	1833 ± 3	$37.5^{+2.4}_{-2.3}$	0.277	33.8	1.47	1771.8	120^{+0}_{-33}	58.5
ΔM	82	145.42	0.73 ± 0.02	–	0.0	1.8	–	–	–

Table **IV-11**: Parameter values obtained from two-dimensional $M(D^0)$–ΔM fit with correlations for the $D^0 \to \phi\pi^0$ background sample. Parameters given without uncertainties are fixed to those from one-dimensional $M(D^0)$ and ΔM fits in Table **IV-8**. Means of Gaussian functions, μ_1 and μ_3, peak offset δ, and Gaussian widths σ_1, σ_L and σ_R, are given in MeV/c^2.

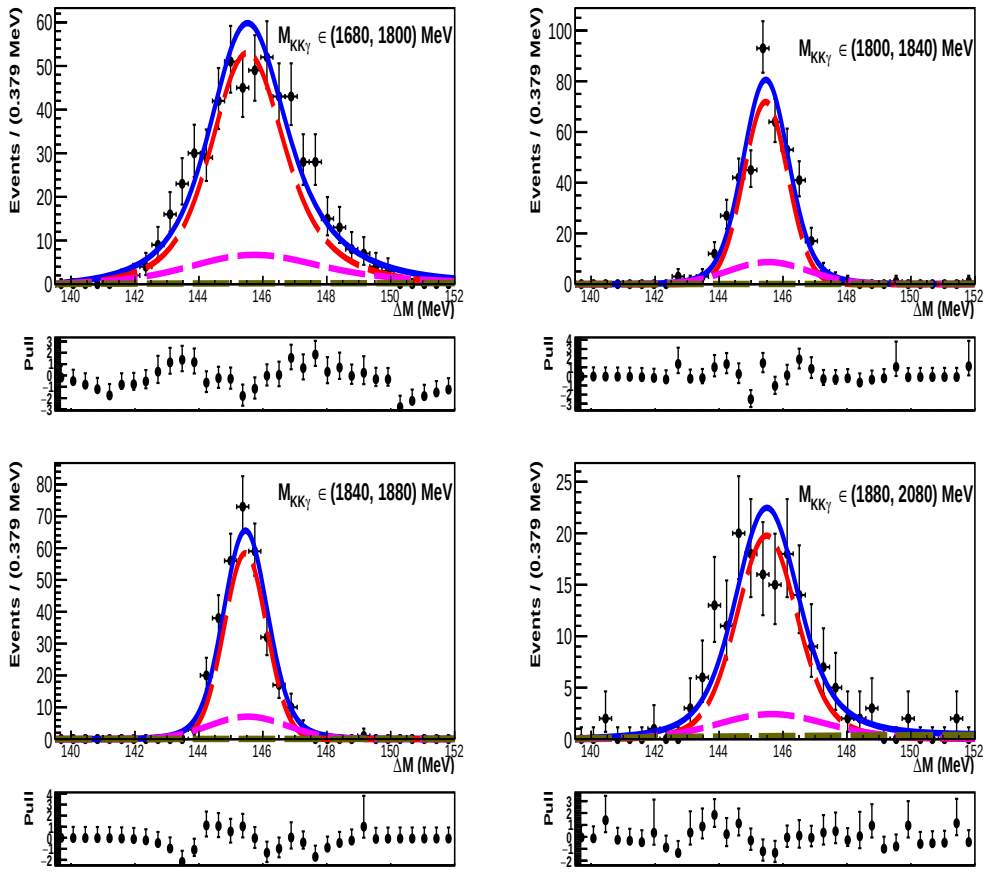

Figure **IV-39**: Results of two-dimensional $M(D^0)$–ΔM fit performed for $D^0 \to \phi\pi^0$ simulation. ΔM projections are for $M(D^0)$ regions indicated in individual plots. Red and magenta lines describe G_1 and G_2 π^0 sub-components, brown line is combinatorial background, blue line is total fit function.

Par/Obs	f_1 [%]	μ_1	σ_1	μ_2	σ_2	α	n
$M(D^0)$	–	1700.3 ± 2.9	32.0 ± 2.4	–	–	-1.6 ± 0.1	3.5
ΔM	72	145.98	2.10 ± 0.06	143.44	1.09	–	–

Table **IV-12**: Parameter values obtained from two-dimensional $M(D^0)$–ΔM fit with correlations for the $D^0 \to \phi\eta$ background sample. Parameters given without uncertainties are fixed to those from one-dimensional $M(D^0)$ and ΔM fits in Table **IV-9**. Means and widths of Gaussian and CB functions are given in MeV/c^2.

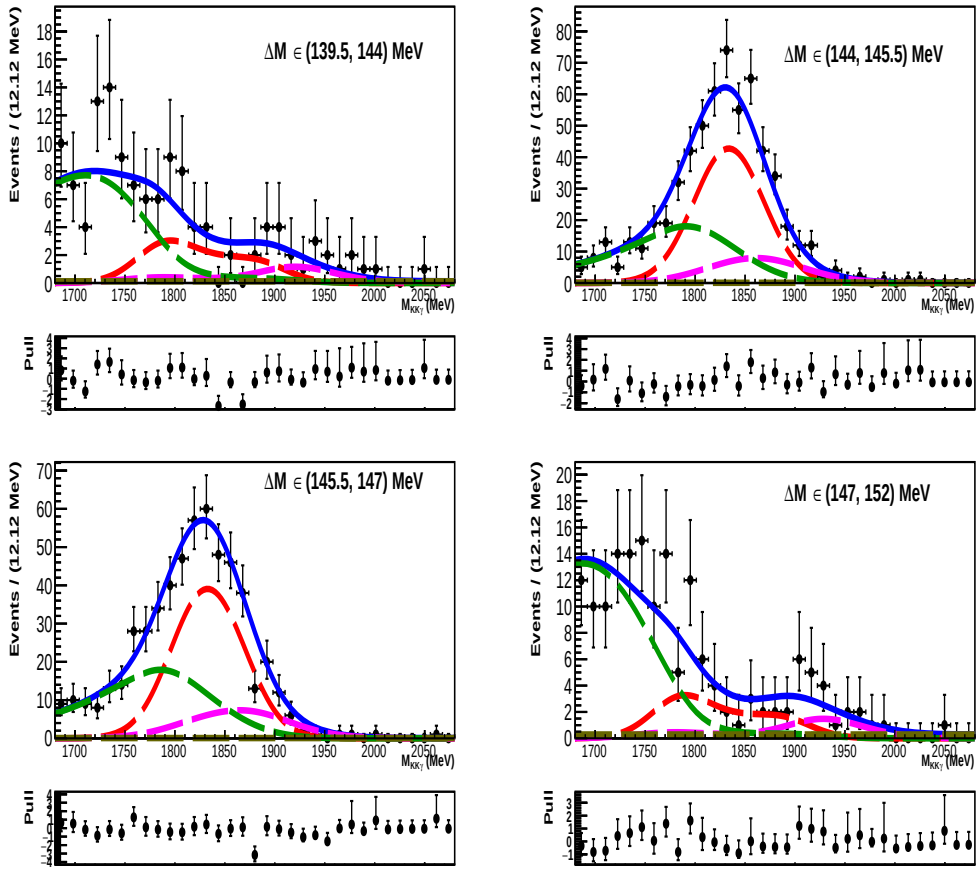

Figure **IV-40**: Results of two-dimensional $M(D^0)$–ΔM fit performed for $D^0 \to \phi\pi^0$ simulation. $M(D^0)$ projections are for ΔM regions indicated in individual plots. Red and magenta lines describe G_1 and G_2 π^0 sub-components, green line denotes threshold Gaussian, brown line is combinatorial background, blue line is total fit function.

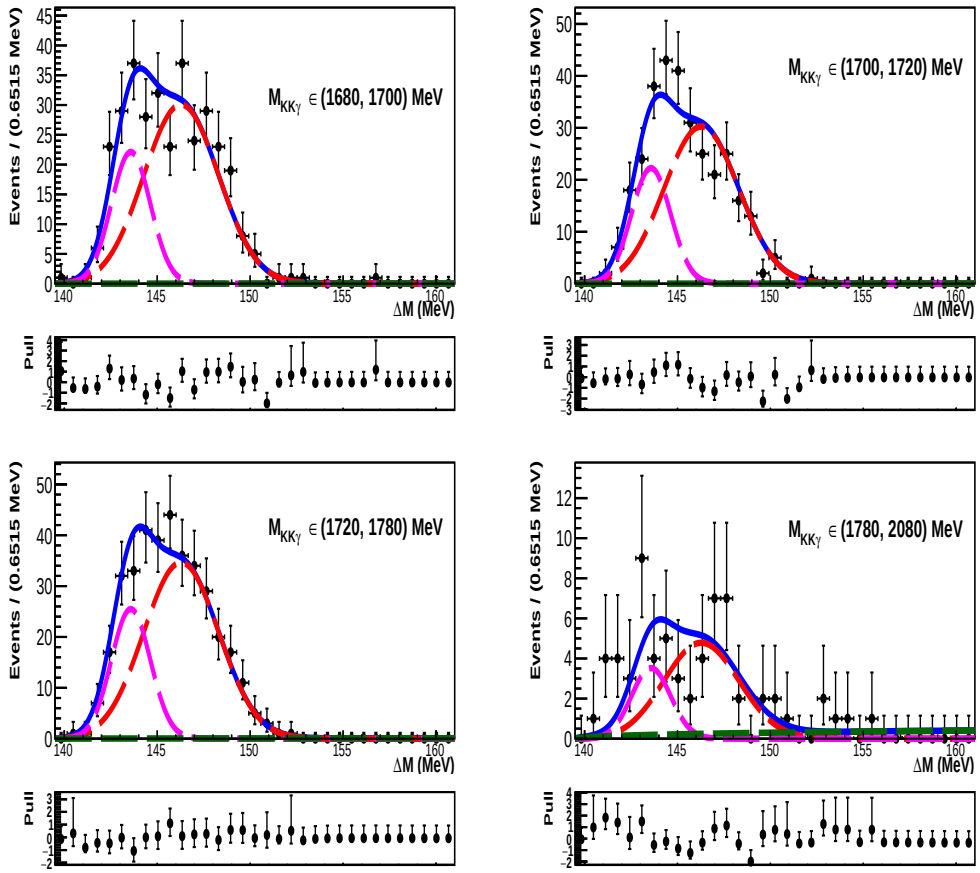

Figure **IV-41**: Results of two-dimensional $M(D^0)$–ΔM fit performed for $D^0 \to \phi\eta$ simulation. ΔM projections are for $M(D^0)$ regions indicated in individual plots. Red and magenta lines describe G_1 and G_2 sub-components, green line is combinatorial background, blue line is total fit function.

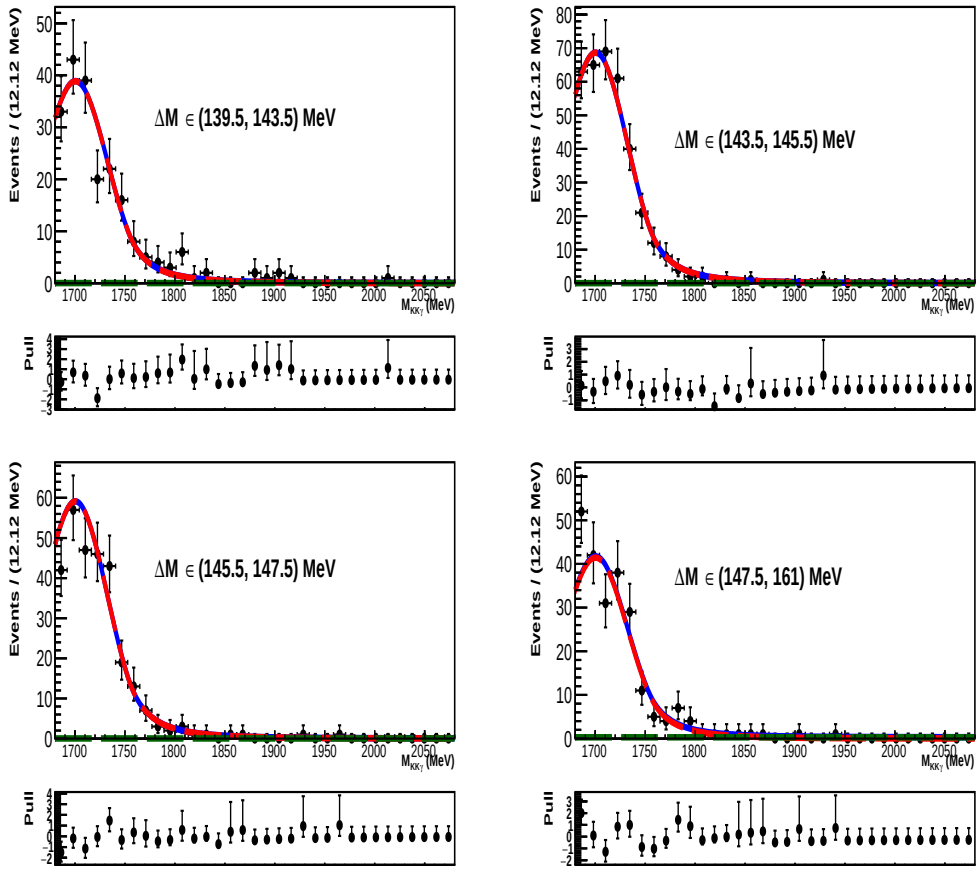

Figure **IV-42**: Results of two-dimensional $M(D^0)$–ΔM fit performed for $D^0 \to \phi\eta$ simulation. $M(D^0)$ projections are for ΔM regions indicated in individual plots. Red line describes η component, green line is combinatorial background, blue line is total fit function.

IV.11 Fits to $M(D^0)$, ΔM and $\cos\theta$ observables for ρ channels

IV.11.1 Fits for simulated $D^0 \to \rho^0\gamma$ decays

Distributions of discriminating variables for the $D^0 \to \rho^0\gamma$ simulation sample with fit results superimposed, are presented in Fig. **IV-43**; given variable is selected in the full ranges of the other two. The distributions are fitted using PDFs as for the $D^0 \to \bar{K}^{*0}\gamma$ signal in Eq. **IV.1**, with non-zero offset $\delta^{\Delta M}$ allowed between peak positions of G_1 and G_2 in the ΔM PDF. Parameter values obtained from one-dimensional fits to $M(D^0)$ and ΔM are summarised in Table **IV-13**. Overall, $M(D^0)$ and ΔM shapes are very similar between $D^0 \to \rho^0\gamma$ and $D^0 \to \bar{K}^{*0}\gamma$ signal channels, but resolutions are slightly worse in the former. In the $\cos\theta$ PDF, a_1 parameter is fixed to zero, while $a_2 = -0.41 \pm 0.04$ is measured.

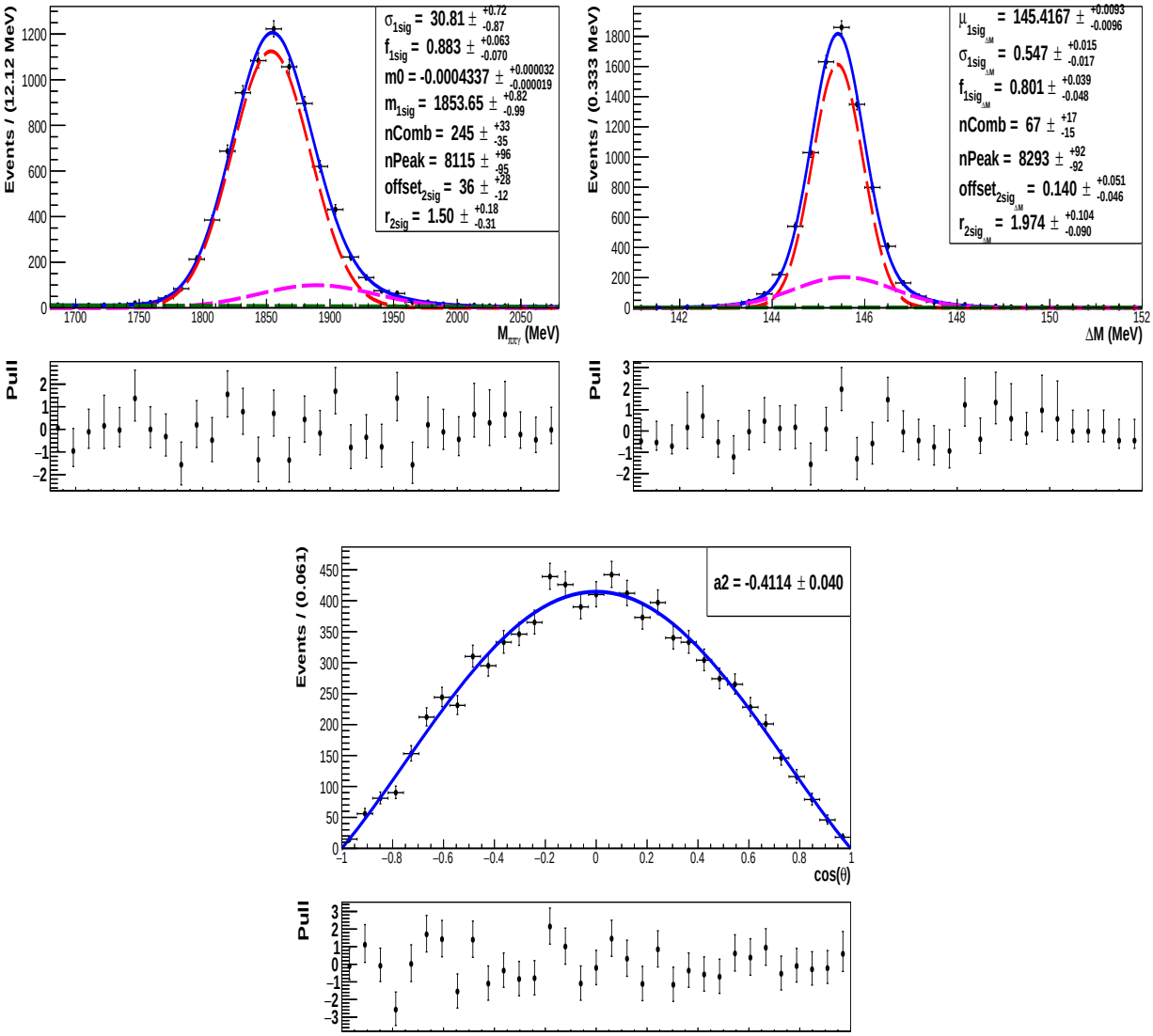

Figure **IV-43**: Distributions of (top left) $M(D^0)$, (top right) ΔM and (bottom) $\cos\theta$ for simulated $D^0 \to \rho^0\gamma$ decays. Results of one-dimensional fits are superimposed.

Par/Obs	f_1 [%]	μ_1 [MeV/c^2]	σ_1 [MeV/c^2]	δ [MeV/c^2]	r
$M(D^0)$	$88.3^{+6.3}_{-7.0}$	$1853.6^{+0.8}_{-1.0}$	$30.8^{+0.7}_{-0.9}$	36^{+28}_{-12}	$1.50^{+0.18}_{-0.31}$
ΔM	$80.1^{+3.9}_{-4.8}$	145.42 ± 0.01	$0.547^{+0.015}_{-0.017}$	0.14 ± 0.05	$1.97^{+0.10}_{-0.09}$

Table **IV-13**: Parameter values obtained from one-dimensional fits to $M(D^0)$ and ΔM observables in $D^0 \to \rho^0\gamma$ simulation sample.

IV.11.2 Fits for simulated $D^0 \to \rho^0\pi^0$ background

The $M(D^0)$ and ΔM distributions for the $D^0 \to \rho^0\pi^0$ simulation sample, passing the full signal selection, are shown in Fig. **IV-44**. $M(D^0)$ is selected in the full ΔM range, whereas ΔM in the restricted $M(D^0)$ range, $1800 < M(D^0) < 1890$ MeV/c^2, to facilitate modelling of $M(D^0)$–ΔM correlations. PDFs used for describing $M(D^0)$ and ΔM shapes are the same as for $D^0 \to \bar{K}^{*0}\pi^0$ background, given in Eq. **IV.2**. Parameters of the asymmetric *threshold* Gaussian in the mass PDF are constrained using the sample involving background from resolved π^0's. It is selected with the reversed `VetoPi0`, and shown in Fig. **IV-46** (bottom) together with results of the fit performed with an asymmetric Gaussian function. The parameters of G_2 in the $M(D^0)$ PDF, namely its fraction f_2 relative to f_1, as well as width ratio r and peak offset δ, are fixed to those of the $D^0 \to \rho^0\gamma$ signal. Parameter values obtained from one-dimensional fits to $M(D^0)$ and ΔM are summarised in Table **IV-14**.

The $\cos\theta$ distributions for the two helicity regions are shown in Fig. **IV-45**. They are fitted using a second-order polynomial in the helicity-edge region, and a third-order polynomial in the helicity-center region. This parameterization accounts for both, theoretical shape and acceptance effects, without disentangling them. The theoretical shape is driven by the $D^0 \to \pi^+\pi^-\pi^0$ decay model (Section **III.2.1**), thus is non-trivial. Results of the $\cos\theta$ fits, along with the obtained parameter values, are given in Fig. **IV-45**.

Par/Obs	f_1 [%]	μ_1	σ_1	f_2/f_1	δ	r	μ_3	σ_L	σ_R
$M(D^0)$	56 ± 2	1832 ± 2	43.1 ± 1.1	0.132	36.0	1.50	1759.8	130 ± 40	63.3
ΔM	69^{+11}_{-14}	$145.38^{+0.02}_{-0.03}$	$0.64^{+0.02}_{-0.03}$	–	0.11 ± 0.07	1.6 ± 0.1	–	–	–

Table **IV-14**: Parameter values obtained from one-dimensional fits to $M(D^0)$ and ΔM observables in $D^0 \to \rho^0\pi^0$ simulation sample passing the full signal selection. Means of Gaussian functions, μ_1 and μ_3, peak offset δ, and Gaussian widths σ_1, σ_L and σ_R, are given in MeV/c^2.

IV.11.3 Fits for simulated $D^0 \to \rho^0\eta$ background

The simulation sample of $D^0 \to \rho^0\eta$ background has been generated as an incoherent mixture of the two resonant decays, $D^0 \to \rho^0\eta$ and $D^0 \to a_0(980)^+\pi^-$, and non-resonant $D^0 \to \pi^+\pi^-\eta$ channel (Section **III.2.1**). As in the case of $D^0 \to \bar{K}^{*0}\eta$ background, these three sub-components of the η background are considered independently in fits to data. Their $M(D^0)$ and ΔM distributions have indistinguishable shapes, whereas their $\cos\theta$ distributions differ significantly.

$M(D^0)$ and ΔM distributions are shown in Fig. **IV-46** for the three decays of the η background combined; given variable is selected in the full range of the other. They are fitted with the same PDFs as used for $D^0 \to \bar{K}^{*0}\eta$ background, given in Eq. **IV.3**. Parameter values obtained from one-dimensional fits to $M(D^0)$ and ΔM are summarised in Table **IV-15**.

Distributions of $\cos\theta$ for the three decays of the η background are compared in Fig. **IV-47**. All these decays contribute to the both helicity regions, with dominant contribution expected from $D^0 \to \rho^0\eta$.

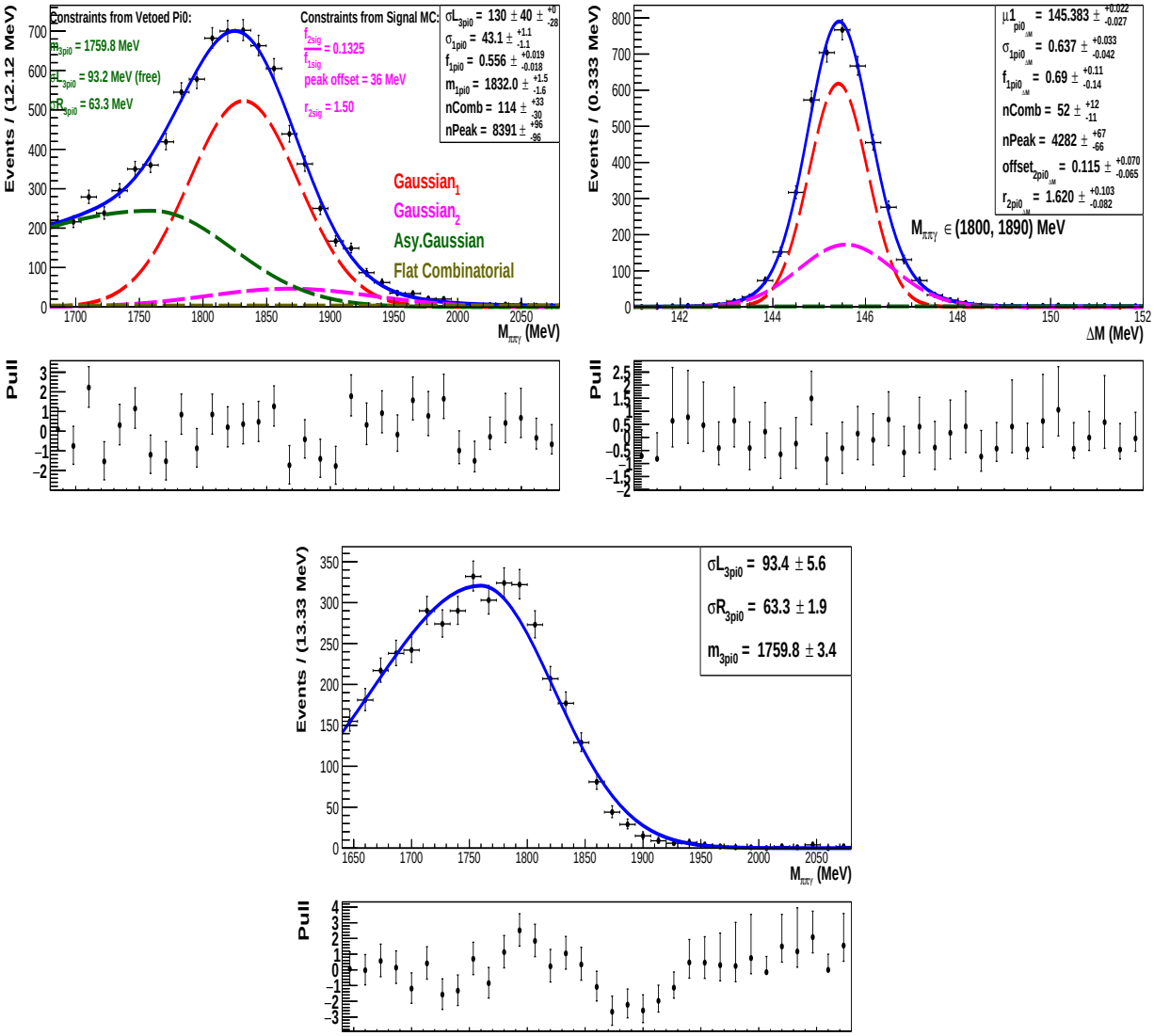

Figure **IV-44**: Distributions of (top left) $M(D^0)$, (top right) ΔM for simulated $D^0 \to \rho^0\pi^0$ sample passing the full signal selection. Results of one-dimensional fits are superimposed. The threshold asymmetric Gaussian in the $M(D^0)$ fit is constrained to the resolved-π^0 sample in the bottom figure. (Bottom) $M(D^0)$ distribution of the simulated $D^0 \to \rho^0\pi^0$ background involving resolved π^0 with one photon missing. Candidates pass the signal selection with `VetoPi0R` reversed. Result of the fit is superimposed.

Par/Obs	f_1 [%]	μ_1	σ_1	μ_2	σ_2	α	n
$M(D^0)$	–	1689.6 ± 3.8	49.4 ± 2.0	–	–	-2.44 ± 0.17	2.0 ± 0.6
ΔM	80 ± 5	146.0 ± 0.1	1.93 ± 0.05	143.9 ± 0.1	0.95 ± 0.12	–	–

Table **IV-15**: Parameter values obtained from one-dimensional fits to $M(D^0)$ and ΔM observables in $D^0 \to \rho^0\eta$ simulation sample. Means and widths of Gaussian and CB functions are given in MeV/c^2.

The $\cos\theta$ distributions in the helicity-edge region are shown in Fig. **IV-48** separately for each of the η background decays. The distributions for $D^0 \to \rho^0\eta$ and $D^0 \to \pi^+\pi^-\eta$ decays are consistent with

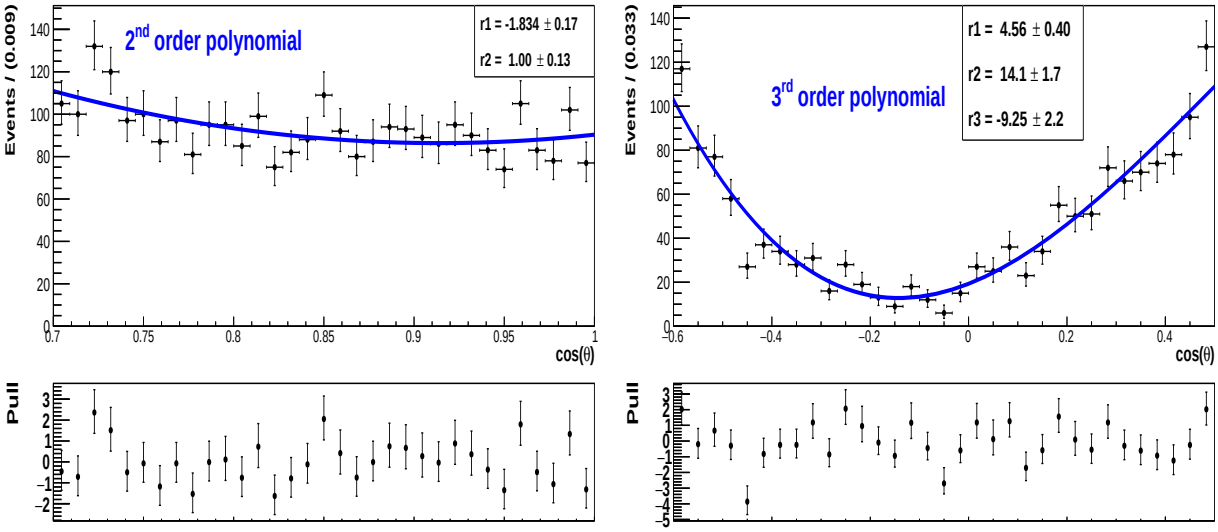

Figure **IV-45**: Distributions of $\cos\theta$ for $D^0 \to \rho^0\pi^0$ simulation sample in (left) helicity-edge and (right) helicity-center regions. Results of fits are superimposed.

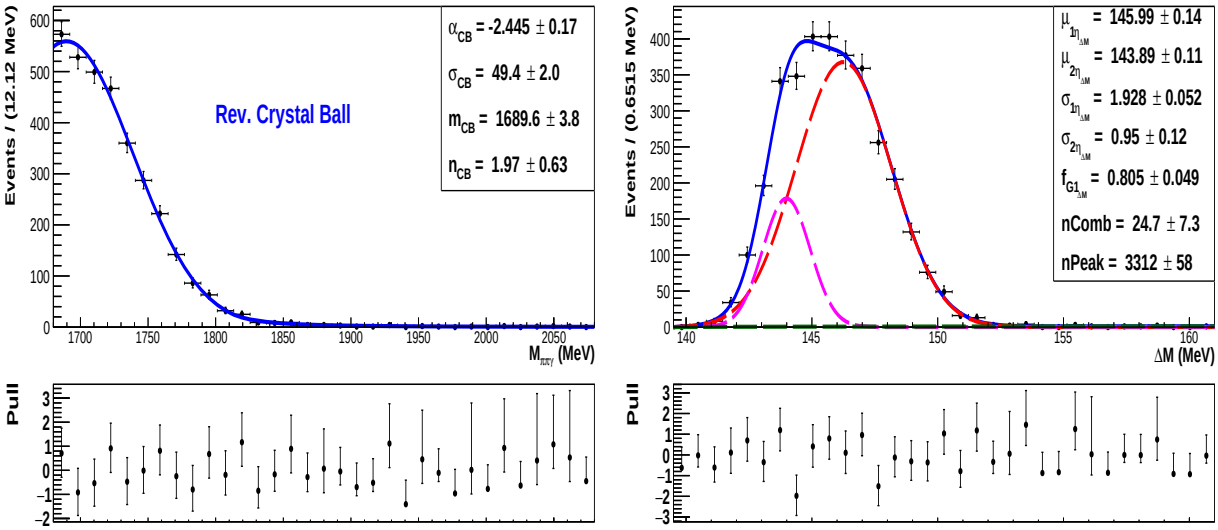

Figure **IV-46**: Distributions of (left) $M(D^0)$, (right) ΔM for simulated $D^0 \to \rho^0\eta$ background sample passing the full signal selection. Results of one-dimensional fits are superimposed.

their theoretical shapes, being $\cos^2\theta$ and constant, respectively. The distribution for $D^0 \to a_0(980)^+\pi^-$ channel is described with a second order polynomial. Results of these fits are presented in Fig. **IV-48**. The corresponding $\cos\theta$ distributions in the helicity-center region are shown in Fig. **IV-49**. The distributions for $D^0 \to \rho^0\eta$ decays is fitted the theoretical function multiplied by an acceptance function, $\cos^2\theta \times (1 + b_1\cos^2\theta)$, with the parameter $b_1 = -0.11 \pm 0.15$ showing non-significant acceptance correction. The distribution for $D^0 \to \pi^+\pi^-\eta$ is consistent with being flat, as expected for $\pi^+\pi^-$ system originating from non-resonant decays. The $\cos\theta$ distribution for $D^0 \to a_0(980)^+\pi^-$ channel is described with the sum of two exponential functions, with parameters given in Fig. **IV-49**.

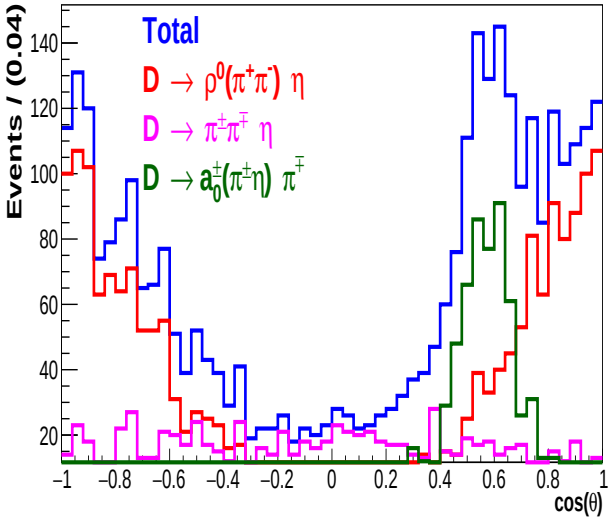

Figure **IV-47**: Distributions of $\cos\theta$ for three decays contributing to the simulated η background passing the full signal selection. Contributions from $D^0 \to \rho^0\eta$ decays are plotted in red, from $D^0 \to a_0(980)^+\pi^-$ in green, and from non-resonant $D^0 \to \pi^+\pi^-\eta$ in magenta.

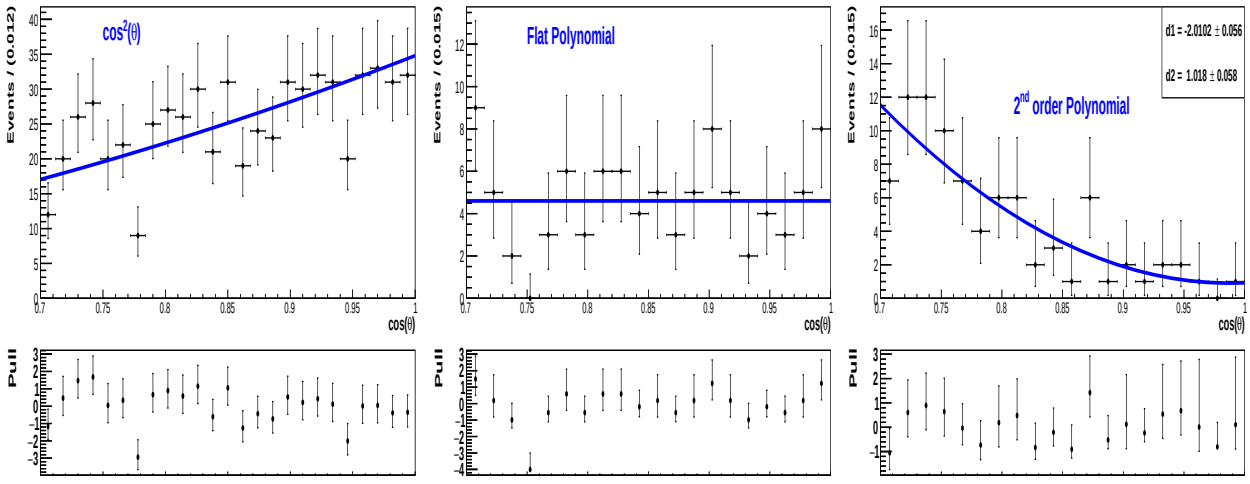

Figure **IV-48**: Distributions of $\cos\theta$ in the helicity-edge region for (left) $D^0 \to \rho^0\eta$ decays, (middle) $D^0 \to \pi^+\pi^-\eta$ decays, (right) $D^0 \to a_0(980)^+\pi^-$ decays. Fit results are superimposed.

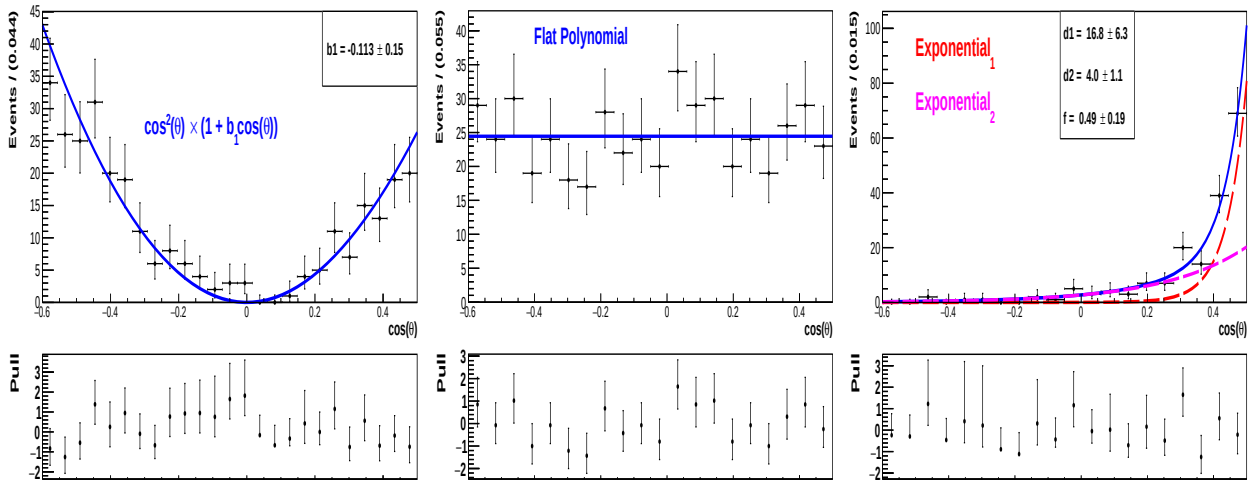

Figure **IV-49**: Distributions of $\cos\theta$ in the helicity-center region for (left) $D^0 \to \rho^0\eta$ decays, (middle) $D^0 \to \pi^+\pi^-\eta$ decays, (right) $D^0 \to a_0(980)^+\pi^-$ decays. Fit results are superimposed. Parameters quoted in the right figure are exponents d_1 and d_2 of two exponential functions, and fraction f of the first function.

IV.12 Describing $M(D^0)$–ΔM correlations in ρ channels

Dependence of the ΔM resolution on $M(D^0)$, described by $\lambda(M)$ function, is measured with the same method as for the K^* channels in Section **IV.6** and for the ϕ channels in Section **IV.9**. It starts from ΔM fits in $M(D^0)$ bins, performed for each signal and background ρ channel. A λ factor is applied to both Gaussian components of a ΔM PDF, as in Eq. **IV.4**. ΔM parameters are fixed to those from the one-dimensional ΔM fits in Section **IV.11**. The fitted values of the λ parameter as a function of $M(D^0)$ are then parameterised with a second-order polynomial function.

The above steps are illustrated for the $D^0 \to \rho^0\gamma$ signal in Figs. **IV-50** and **IV-51**, for the $D^0 \to \rho^0\pi^0$ background in Figs. **IV-52** and **IV-53**, and for the $D^0 \to \rho^0\eta$ background in Figs. **IV-54** and **IV-55**.

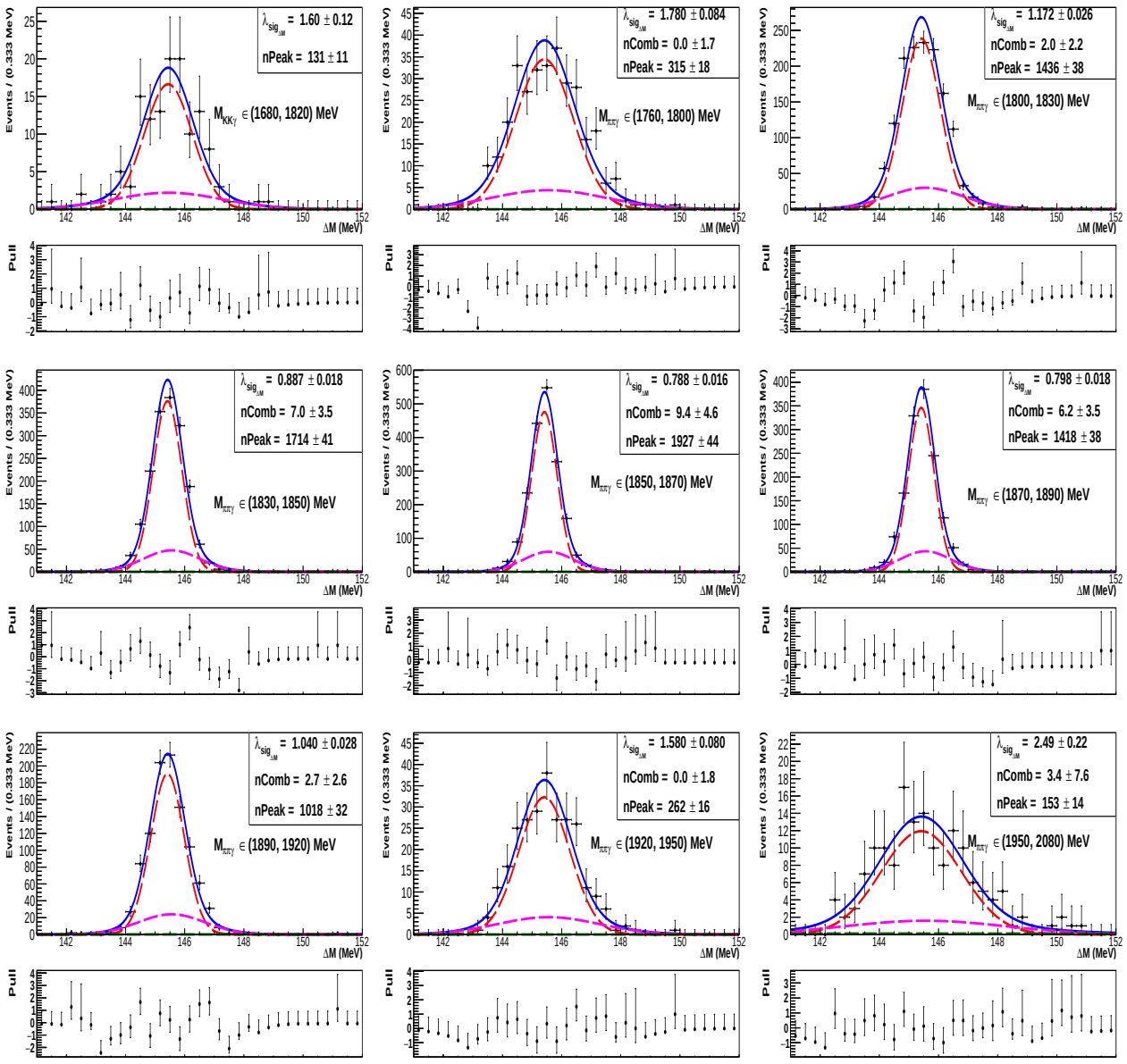

Figure **IV-50**: Results of ΔM fits in $M(D^0)$ bins performed using the $D^0 \to \rho^0\gamma$ simulation sample. Considered $M(D^0)$ regions, as well as fitted λ values are indicated in individual figures.

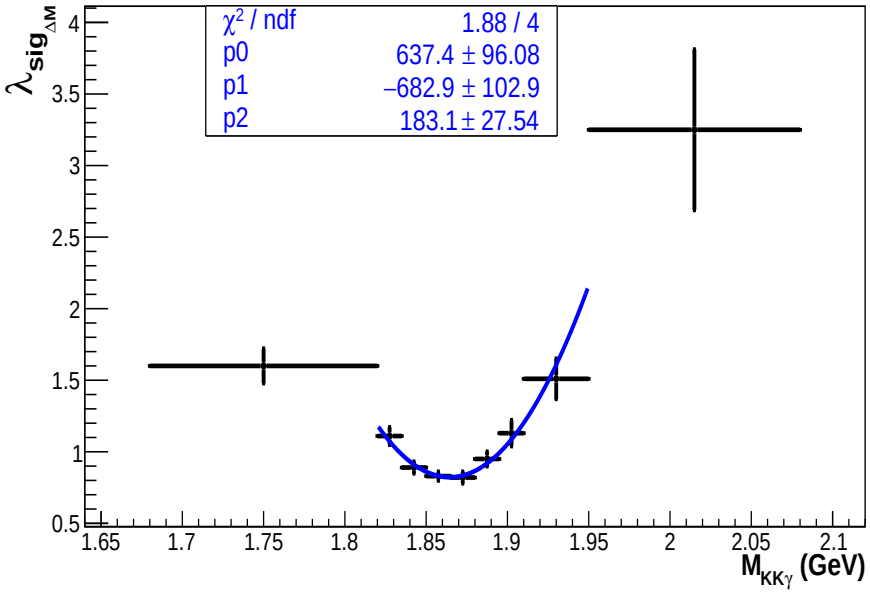

Figure **IV-51**: Correlation parameter λ for $D^0 \to \rho^0\gamma$ signal, obtained from ΔM fits in $M(D^0)$ bins, plotted against the corresponding $M(D^0)$ range. Result of χ^2 fit using 2^{nd} order polynomial is superimposed, and fit parameters are also given. The lowest- and highest-mass bins are excluded from the fit.

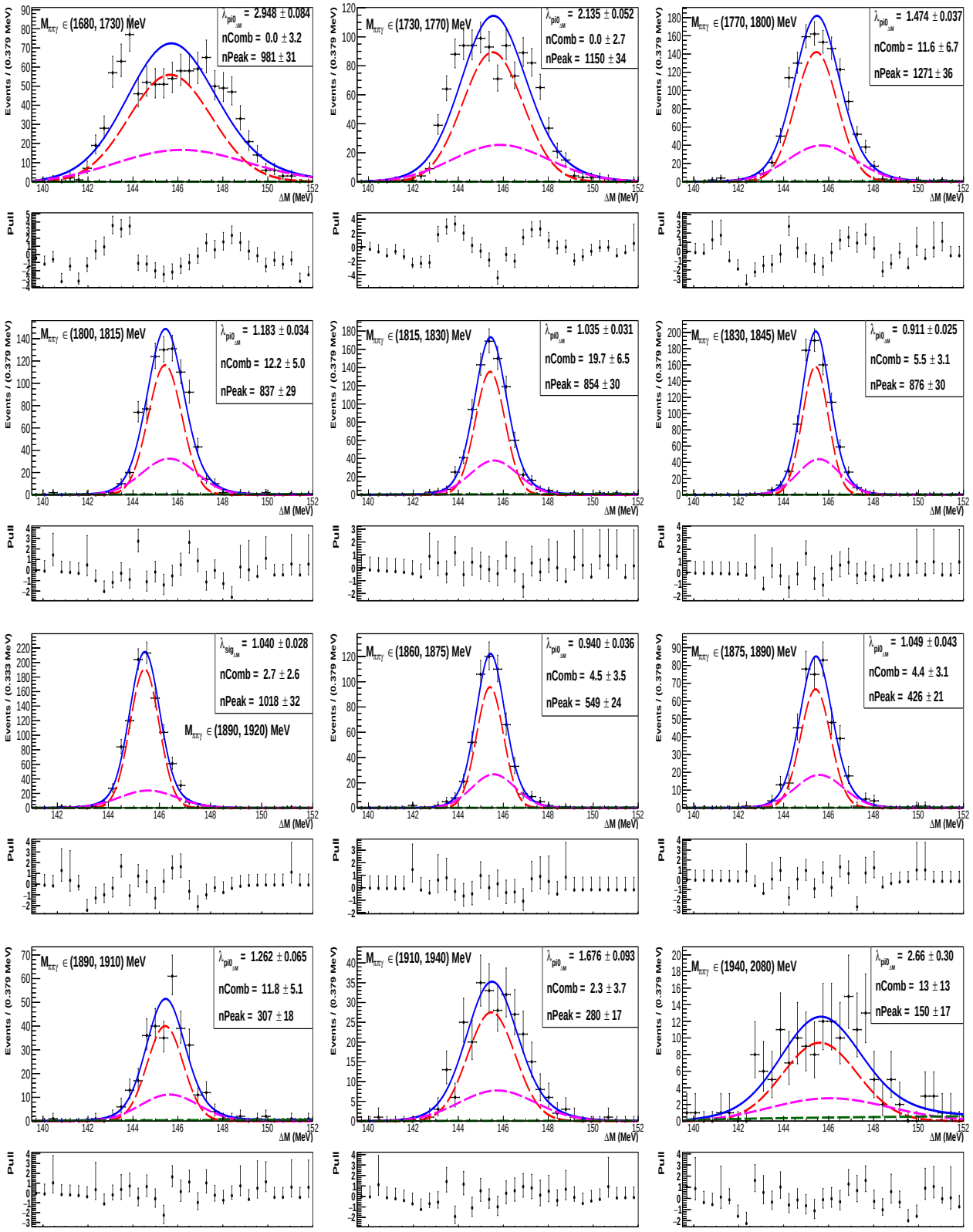

Figure **IV-52**: Results of ΔM fits in $M(D^0)$ bins performed using the $D^0 \to \rho^0\pi^0$ simulation sample. Considered $M(D^0)$ regions, as well as fitted λ values are indicated in individual figures.

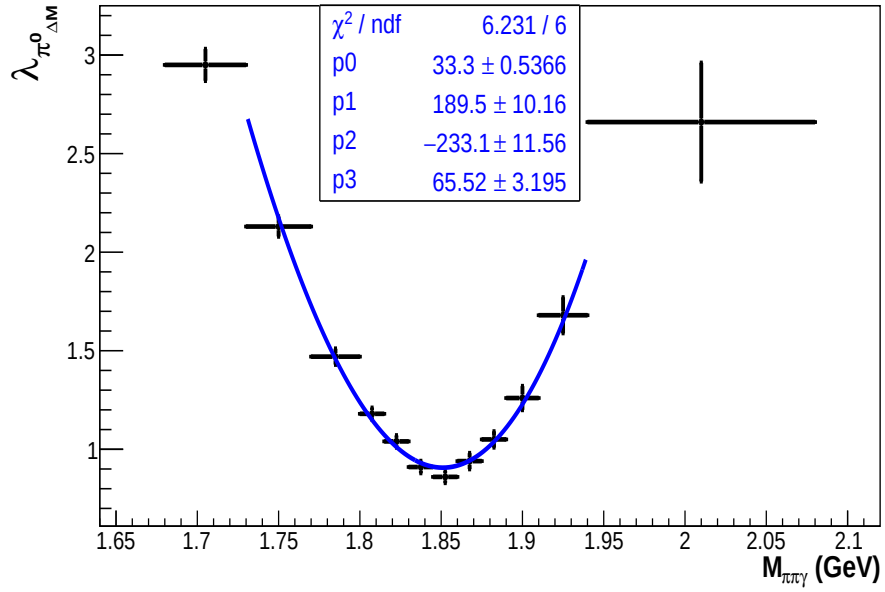

Figure **IV-53**: Correlation parameter λ for $D^0 \to \rho^0\pi^0$ signal, obtained from ΔM fits in $M(D^0)$ bins, plotted against the corresponding $M(D^0)$ range. Result of χ^2 fit using 2$^{\text{nd}}$ order polynomial is superimposed, and fit parameters are also given. The lowest- and highest-mass bins are excluded from the fit.

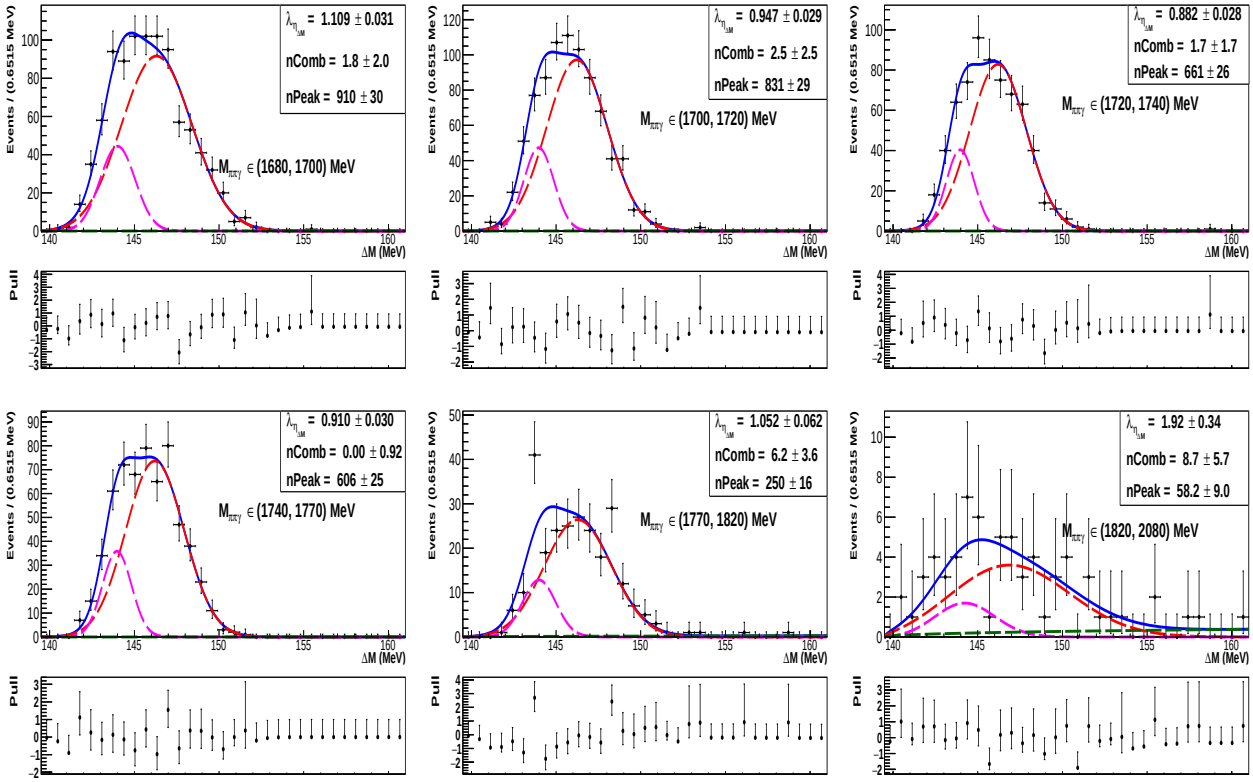

Figure **IV-54**: Results of ΔM fits in $M(D^0)$ bins performed using the $D^0 \to \rho^0\eta$ simulation sample. Considered $M(D^0)$ regions, as well as fitted λ values are indicated in individual figures.

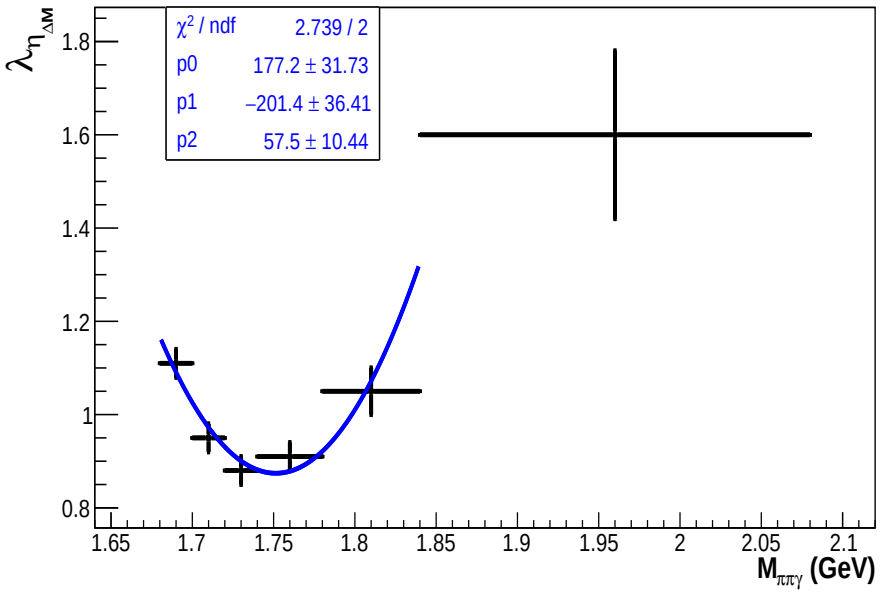

Figure **IV-55**: Correlation parameter λ for $D^0 \to \rho^0\eta$ signal, obtained from ΔM fits in $M(D^0)$ bins, plotted against the corresponding $M(D^0)$ range. Result of χ^2 fit using 2^{nd} order polynomial is superimposed, and fit parameters are also given. The highest-mass bin is excluded from the fit.

IV.13 Validating $M(D^0)$–ΔM correlations in ρ channels

Two-dimensional $M(D^0)$–ΔM fit for each considered ρ channel, the $D^0 \to \rho^0\gamma$ signal, as well as $D^0 \to \rho^0\pi^0$ and $D^0 \to \rho^0\eta$ background, is performed with the corresponding $\lambda(M)$ correlation function fixed to that obtained in Section **IV.12**. PDFs for $M(D^0)$ variable are as introduced in Sections **IV.11.1**-**IV.11.3**, whereas PDFs for ΔM are conditional functions with correlations included according to Eq. **IV.4**. As in the fits for the K^* and ϕ channels, some of the $M(D^0)$ and ΔM shape parameters are kept free, in particular $\sigma_1^{\Delta M}$, while the others are fixed to those from one-dimensional fits presented in Sections **IV.11.1**- **IV.11.3**. This is specified in Tables **IV-16**-**IV-18**, along with parameters obtained from these two-dimensional fits.

Results of the two-dimensional $M(D^0)$–ΔM fit performed for the $D^0 \to \rho^0\gamma$ simulation sample are presented in Fig. **IV-56** showing ΔM projections in $M(D^0)$ regions, and in Fig. **IV-57** showing $M(D^0)$ projections in ΔM regions. The corresponding fit projections for the $D^0 \to \rho^0\pi^0$ simulation sample are presented in Figs. **IV-58** and **IV-59**, while for the $D^0 \to \rho^0\eta$ simulation sample are presented in Figs. **IV-60** and **IV-61**.

Parameters obtained from these two-dimensional fits are used to model signal and peaking-background components in fits to the $D^0 \to \rho^0\gamma$ candidates from the experimental data in Section **V.5**.

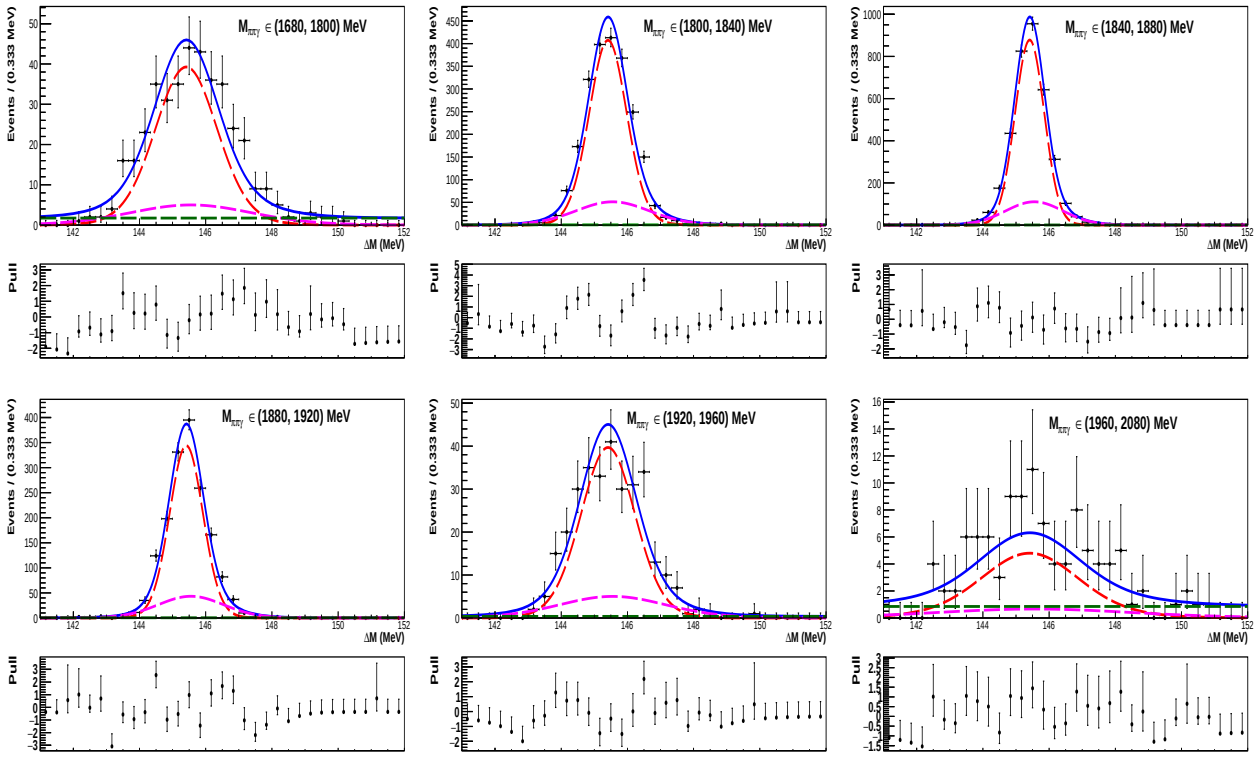

Figure **IV-56**: Results of two-dimensional $M(D^0)$–ΔM fit performed for $D^0 \to \rho^0\gamma$ simulation. ΔM projections are for $M(D^0)$ regions indicated in individual plots. Red and magenta lines describe G_1 and G_2 signal sub-components, green line is combinatorial background, blue line is total fit function.

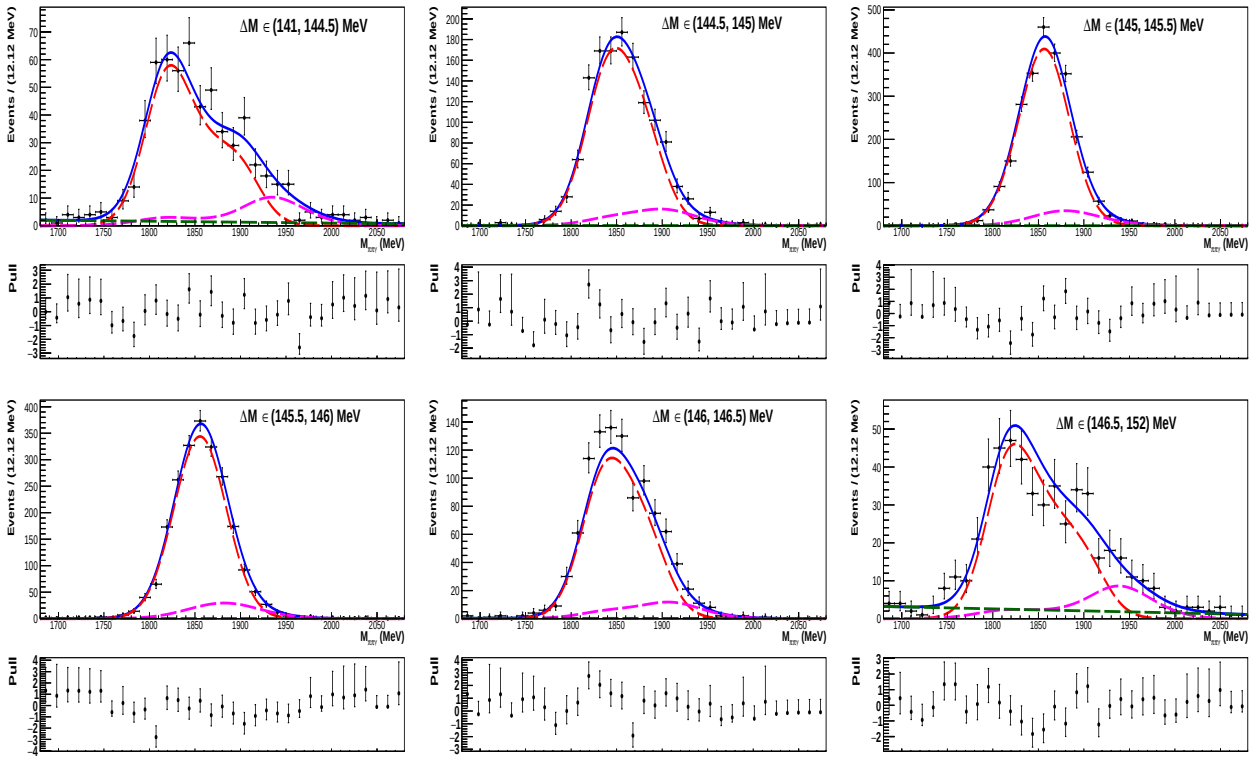

Figure **IV-57**: Results of two-dimensional $M(D^0)$–ΔM fit performed for $D^0 \to \rho^0\gamma$ simulation. $M(D^0)$ projections are for ΔM regions indicated in individual plots. Red and magenta lines describe G_1 and G_2 signal sub-components, green line is combinatorial background, blue line is total fit function.

Par/Obs	f_1 [%]	μ_1 [MeV/c^2]	σ_1 [MeV/c^2]	δ [MeV/c^2]	r
$M(D^0)$	88.3	1853.6 ± 0.4	31.6 ± 0.3	36.0	1.50
ΔM	80.1	145.413 ± 0.006	0.577 ± 0.005	0.14	1.97

Table **IV-16**: Parameter values obtained from two-dimensional $M(D^0)$–ΔM fit with correlations for the $D^0 \to \rho^0\gamma$ simulation sample. Parameters given without uncertainties are fixed to those from one-dimensional $M(D^0)$ and ΔM fits in Table **IV-13**.

Par/Obs	f_1 [%]	μ_1	σ_1	f_2/f_1	δ	r	μ_3	σ_L	σ_R
$M(D^0)$	56^{+0}_{-2}	1832 ± 2	$43.4^{+1.1}_{-1.0}$	0.132	36.0	1.50	1759.8	132^{+0}_{-29}	63.3
ΔM	69	145.38	0.615 ± 0.006	–	0.11	1.6	–	–	–

Table **IV-17**: Parameter values obtained from two-dimensional $M(D^0)$–ΔM fit with correlations for the $D^0 \to \rho^0\pi^0$ background sample. Parameters given without uncertainties are fixed to those from one-dimensional $M(D^0)$ and ΔM fits in Table **IV-14**. Means of Gaussian functions, μ_1 and μ_3, peak offset δ, and Gaussian widths σ_1, σ_L and σ_R, are given in MeV/c^2.

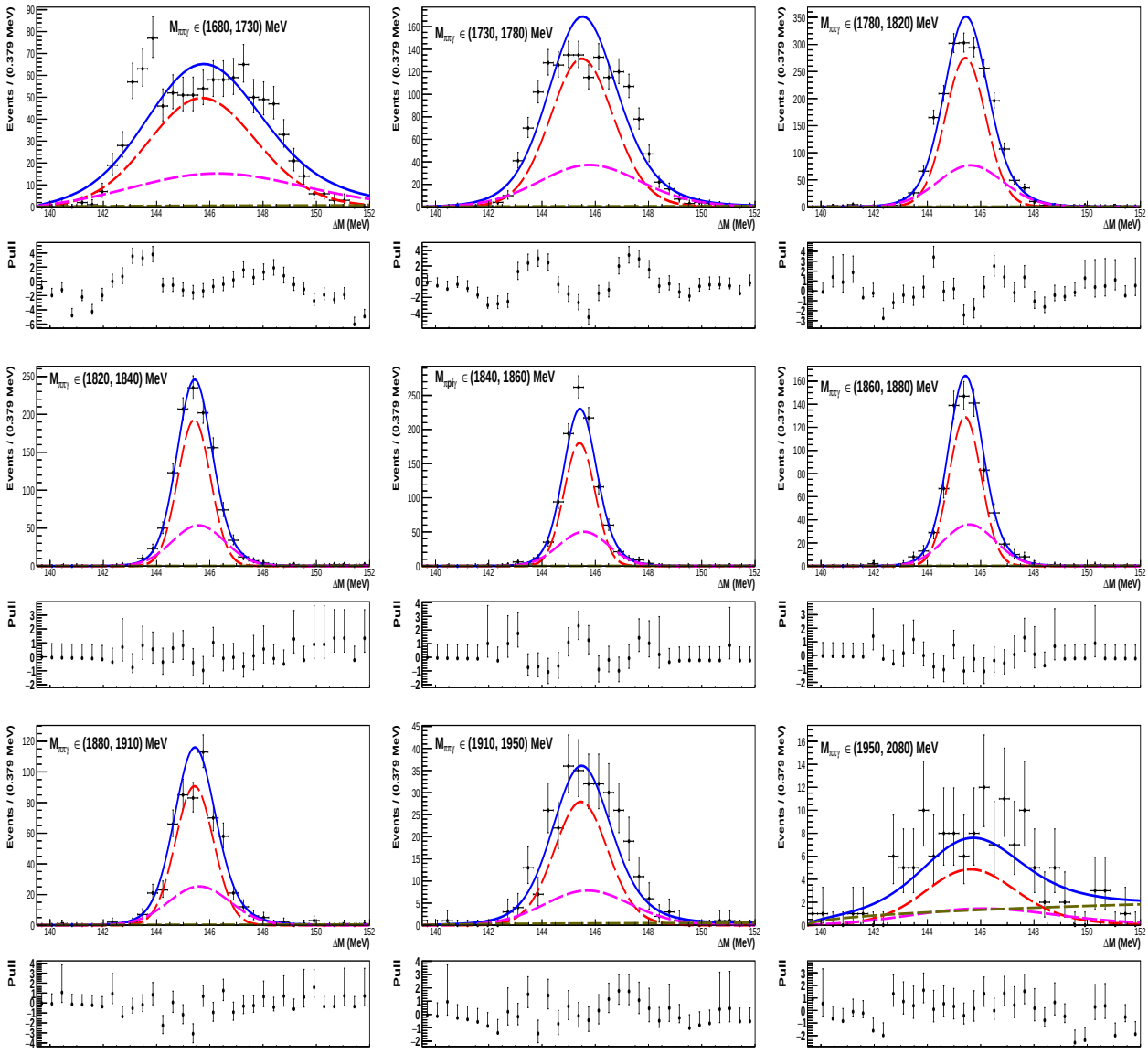

Figure **IV-58**: Results of two-dimensional $M(D^0)$–ΔM fit performed for $D^0 \to \rho^0\pi^0$ simulation. ΔM projections are for $M(D^0)$ regions indicated in individual plots. Red and magenta lines describe G_1 and G_2 π^0 sub-components, brown line is combinatorial background, blue line is total fit function.

Par/Obs	f_1 [%]	μ_1	σ_1	μ_2	σ_2	α	n
$M(D^0)$	–	1688.7 ± 4.0	49.9 ± 2.1	–	–	-2.66 ± 0.15	2.0
ΔM	80.0	146.0	2.10 ± 0.03	143.9	0.95	–	–

Table **IV-18**: Parameter values obtained from two-dimensional $M(D^0)$–ΔM fit with correlations for the $D^0 \to \rho^0\eta$ background sample. Parameters given without uncertainties are fixed to those from one-dimensional $M(D^0)$ and ΔM fits in Table **IV-15**. Means and widths of Gaussian and CB functions are given in MeV/c^2.

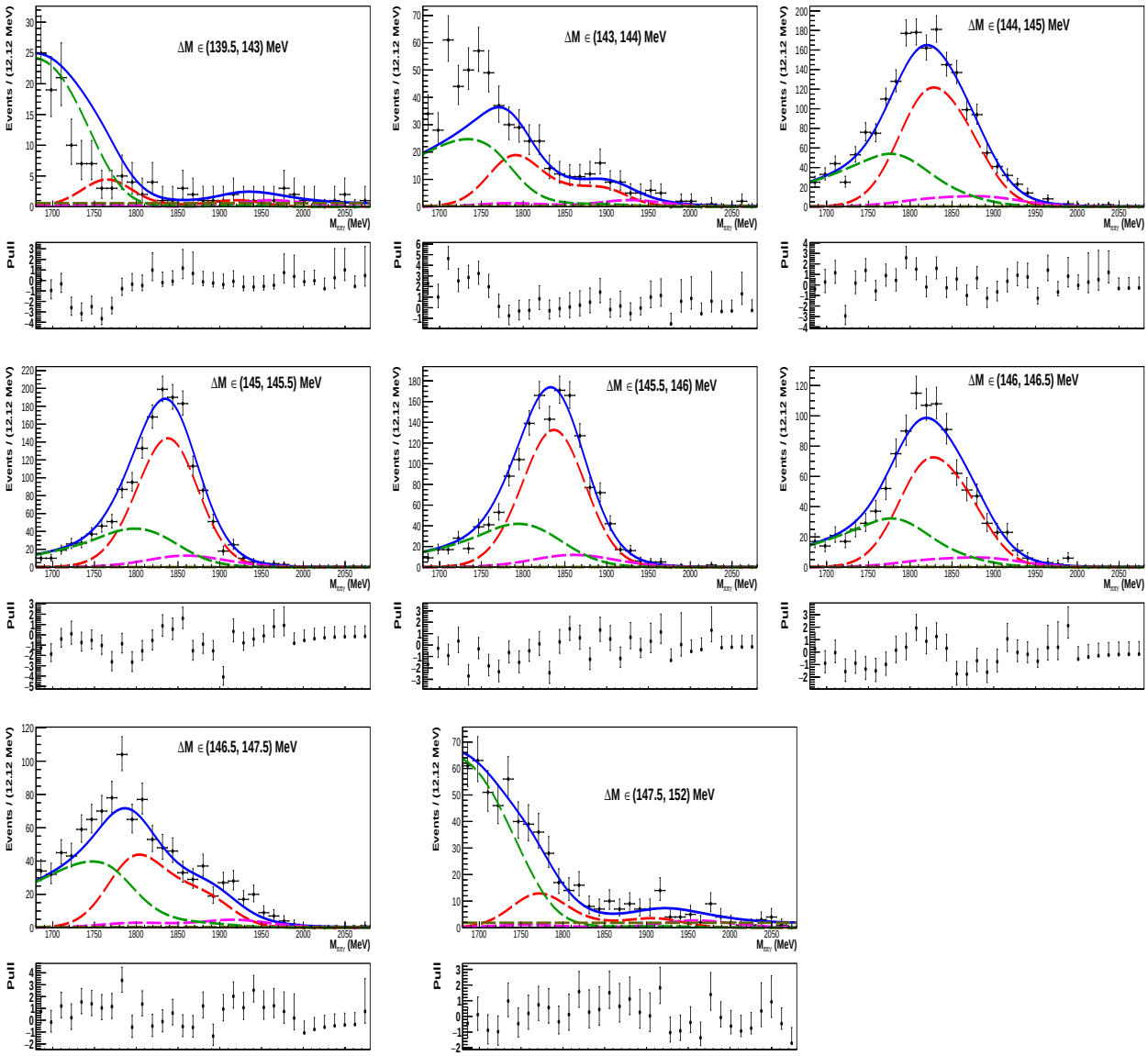

Figure **IV-59**: Results of two-dimensional $M(D^0)$–ΔM fit performed for $D^0 \to \rho^0\pi^0$ simulation. $M(D^0)$ projections are for ΔM regions indicated in individual plots. Red and magenta lines describe G_1 and G_2 π^0 sub-components, green line denotes threshold Gaussian, brown line is combinatorial background, blue line is total fit function.

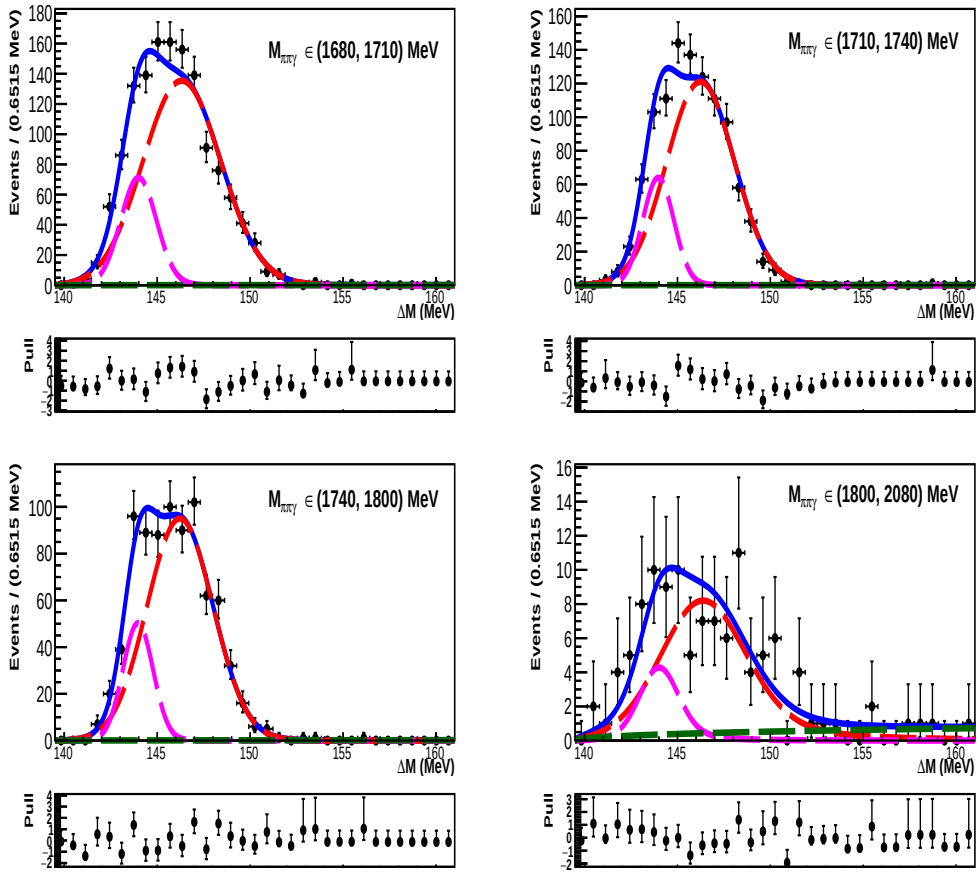

Figure **IV-60**: Results of two-dimensional $M(D^0)$–ΔM fit performed for $D^0 \to \rho^0\eta$ simulation. ΔM projections are for $M(D^0)$ regions indicated in individual plots. Red and magenta lines describe G_1 and G_2 η sub-components, green line is combinatorial background, blue line is total fit function.

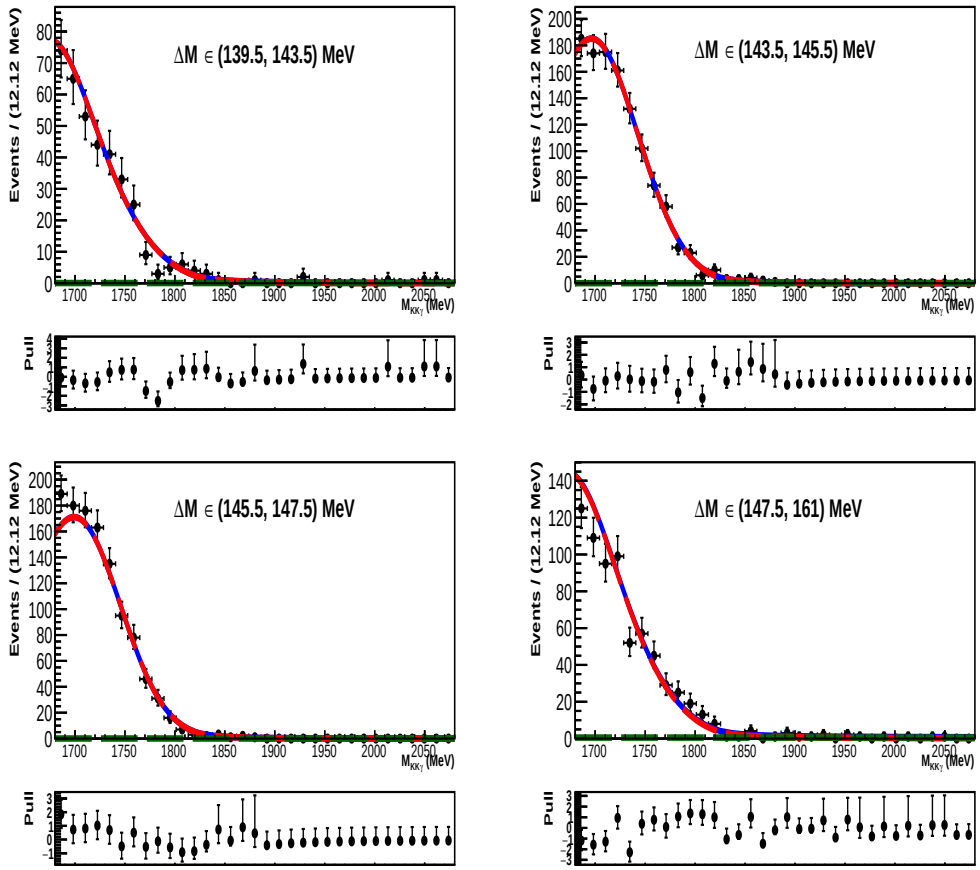

Figure **IV-61**: Results of two-dimensional $M(D^0)$–ΔM fit performed for $D^0 \to \rho^0\eta$ simulation. $M(D^0)$ projections are for ΔM regions indicated in individual plots. Red line describes η component, green line is combinatorial background, blue line is total fit function.

Chapter V

Fits to data for combined D^0 and $\bar{D}^0$

Three-dimensional fits in $M(D^0)$ vs. ΔM vs. $\cos\theta$ space are performed first to the data samples with combined candidates tagged as D^0 or $\bar{D}^0$. They are described in Sections **V.3**, **V.4** and **V.5** for $D^0 \to \bar{K}^{*0}\gamma$, $D^0 \to \phi\gamma$ and $D^0 \to \rho^0\gamma$ channels, respectively. A goal of these fits is to calibrate simulation-based shapes for signal and peaking-background components before D^0 and $\bar{D}^0$ samples are separated for measuring raw asymmetries. In addition to the three-dimensional fits, there is also the two-dimensional $M(D^0)$ vs. $\cos\theta$ fit performed (Section **V.2**) to $D^0 \to \bar{K}^{*0}\gamma$ candidates in order to estimate initial signal and π^0 background yields used in an optimisation of γ–π^0 separation. Before fitting the data samples, multiple candidates reconstructed in a single event are removed, as described in Section **V.1**.

V.1 Best-candidate selection

In the simulation samples (Chapter **IV**) there is only one D^{*+} candidate reconstructed in a single event. In the experimental data, in a small fraction of events there are more than one signal candidates reconstructed. Figure **V-1** (left) shows the multiplicity of the $D^0 \to \bar{K}^{*0}\gamma$ candidates after the full signal selection except for IsPhoton cut, and reconstructed in the full $\cos\theta$ range. In about 2% of events there are two candidates reconstructed. This multiplicity is very similar in the edge and central helicity regions, as well as for the $D^0 \to \rho^0\gamma$ and $D^0 \to \phi\gamma$ channels.

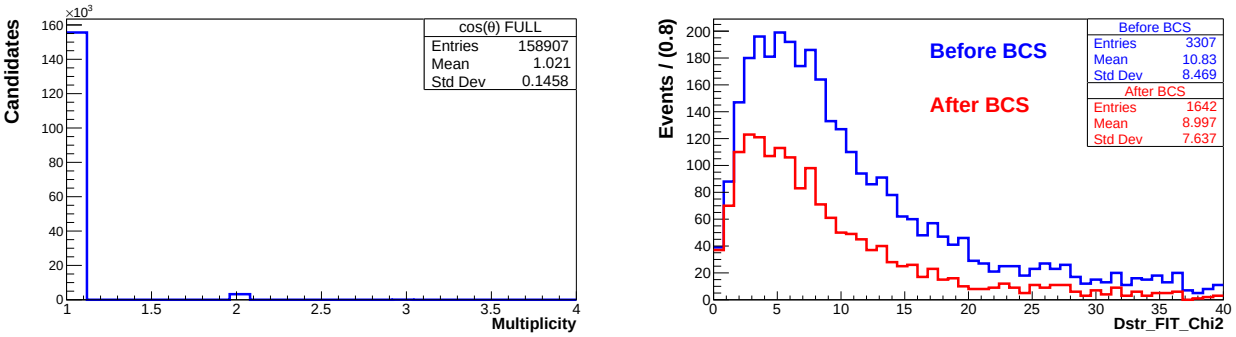

Figure **V-1**: (Left) Multiplicity of D^{*+} signal candidates in the $D^0 \to \bar{K}^{*0}\gamma$ channel reconstructed in the Run-1 data in the full $\cos\theta$ range. (Right) Comparison of DTF χ^2 for multiple D^{*+} candidates before (blue) and after (red) best-candidate selection.

Typically, multiple candidates share either the same photon candidate or the same charged track. Best-candidate selection (BCS) is based on the χ^2 of the DTF kinematic refit (Section **III.3.3**), as it considers the full decay chain. A D^{*+} candidate having smaller value of the DTF χ^2 is retained for

further analysis. Comparison of the DTF χ^2 for multiple candidates before and after BCS is shown in Fig. **V-1** (right).

V.2 Two-dimensional $M(D^0)$ vs. $\cos\theta$ fit to $D^0 \to \bar{K}^{*0}\gamma$ sample

Optimization of the γ–π^0 separation (Sections **IV.3** and **IV.4**) uses $D^0 \to \bar{K}^{*0}\gamma$ signal yield and $D^0 \to \bar{K}^{*0}\pi^0$ background yield, S_0 and B_0, estimated with no requirement on IsPhoton or γ–π^0 BDT classifier. They are measured using two-dimensional fit to the $M(D^0)$ and $\cos\theta$ distributions selected in the signal-enhanced ΔM region, $143.15 < \Delta M < 147.72$ MeV/c^2, to suppress random soft-pion background. The fit includes the signal component, π^0 and η backgrounds, and combinatorial background.

First, the two-dimensional fit is performed in the helicity-edge region in order to calibrate the $M(D^0)$ shape for the π^0 background. The fit projections are presented in Fig. **V-2**. Parameters of the π^0 component are fixed to those from one-dimensional fits of the $D^0 \to \bar{K}^{*0}\pi^0$ simulation (Section **IV.5.2**), except for the left width of the threshold Gaussian in the $M(D^0)$ PDF (Eq. **IV.2**). Its fitted value is $\sigma_L = 83.7 \pm 5.2$ MeV/c^2, whereas the π^0 background yield is 64858 ± 483 events. The $M(D^0)$ PDF of the η background is fixed from the simulation (Eq. **IV.3**), whereas the $\cos\theta$ shape is that of the $D^0 \to \bar{K}^{*0}\eta$ channel, which is expected to be dominant in the helicity edge (Fig. **IV-14**). The signal component, with all parameters fixed to those from the $D^0 \to \bar{K}^{*0}\gamma$ simulation (Section **IV.5.1**), has the yield of 0 ± 104 events. Combinatorial background is modelled with an exponential function for $M(D^0)$ and a second-order polynomial for $\cos\theta$, with all parameters kept free in the fit.

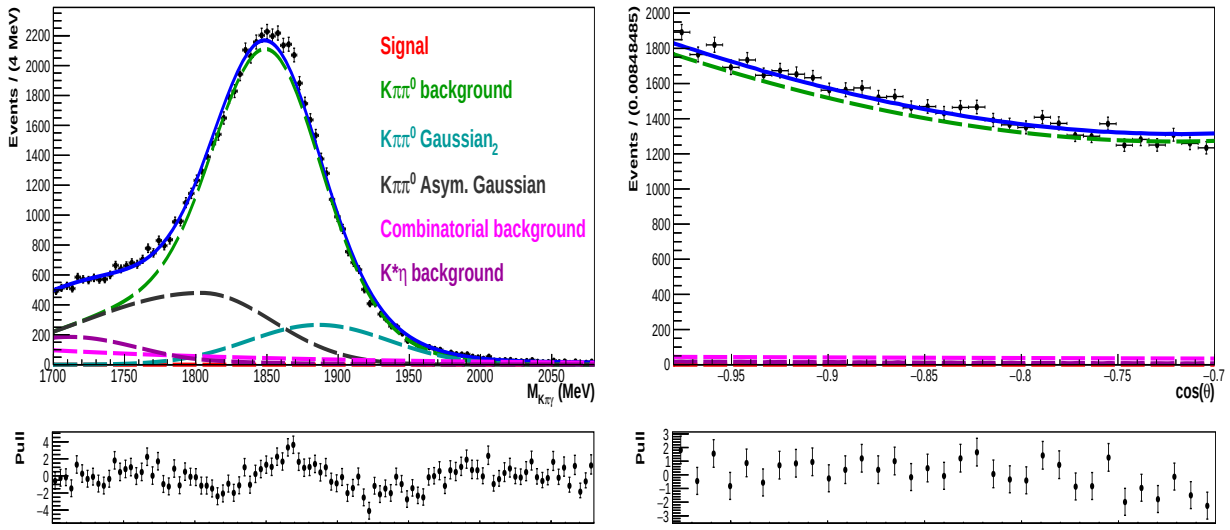

Figure **V-2**: (Left) $M(D^0)$ and (right) $\cos\theta$ projections of two-dimensional $M(D^0)$ vs. $\cos\theta$ fit to $D^0 \to \bar{K}^{*0}\gamma$ candidates reconstructed in the Run-1 data in the helicity edge. The $\cos\theta$ projection is for $1805 < M(D^0) < 1924$ MeV/c^2. No selection on IsPhoton or γ–π^0 BDT classifier is applied. Fit components are indicated in the legend.

Projections of the two-dimensional fit performed in the helicity center are presented in Fig. **V-3**. Here, the σ_L parameter of the π^0 background is fixed from the helicity-edge fit. Remaining parameters of the π^0 component, as well as the signal parameters are fixed to those from the corresponding simulations (Sections **IV.5.1** and **IV.5.2**). Within the η background, all three decays i.e. $D^0 \to \bar{K}^{*0}\eta$, $D^0 \to K^- a_0(980)^+$ and $D^0 \to \bar{K}_0(1430)^0\eta$, are considered with the common $M(D^0)$ shape (Eq. **IV.3**), independent $\cos\theta$ shapes, all fixed to the simulation (Section **IV.5.3**), and independent yields. Combinatorial background is modelled as in the helicity-edge fit, with all the parameters kept free. The measured yields of the signal and π^0 background are $S_0 = 5527 \pm 385$ and $B_0 = 101948 \pm 598$ events.

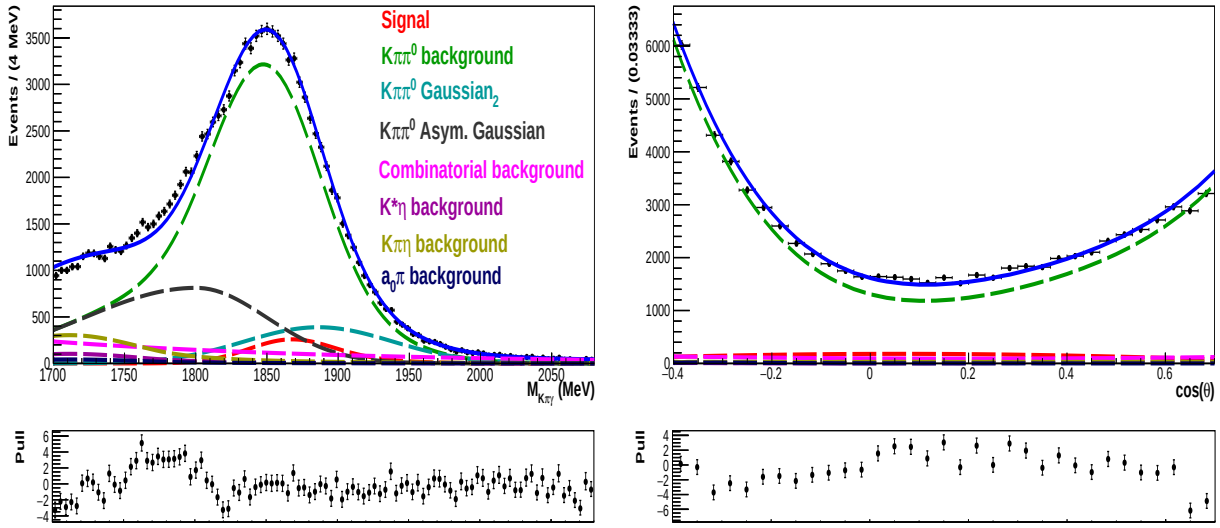

Figure **V-3**: (Left) $M(D^0)$ and (right) $\cos\theta$ projections of two-dimensional $M(D^0)$ vs. $\cos\theta$ fit to $D^0 \to \bar{K}^{*0}\gamma$ candidates reconstructed in the Run-1 data in the helicity center. The $\cos\theta$ projection is for $1805 < M(D^0) < 1924$ MeV/c^2. No selection on IsPhoton or γ–π^0 BDT classifier is applied. Fit components are indicated in the legend.

V.3 Three-dimensional fit to $D^0 \to \bar{K}^{*0}\gamma$ sample

Three-dimensional fit in the $M(D^0)$ vs. ΔM vs. $\cos\theta$ space is performed for the $D^0 \to \bar{K}^{*0}\gamma$ candidates, which have passed the full selection (Section **III.3**) including IsPhoton> 0.86. The fit incorporates three peaking components: signal, π^0 background, and η background, with PDFs based on the corresponding simulation samples, as described in Sections **IV.5.1**, **IV.5.2** and **IV.5.3**, respectively. Correlations between the $M(D^0)$ and ΔM observables are described with conditional functions PDF$(\Delta M|M)$ and taken from the simulations (Section **IV.6**), while the uncorrelated parameters of the $M(D^0)$ and ΔM PDFs are measured from the two-dimensional $M(D^0)$ vs. ΔM correlated fits to the simulations (Section **IV.7**). Overall, three-dimensional PDFs for the signal, π^0 background and η background become:

$$\begin{aligned}
&\mathrm{PDF}_\gamma(M,\Delta M,\cos\theta) = \mathrm{PDF}_\gamma(M)\times\mathrm{PDF}_\gamma(\Delta M|M)\times\mathrm{PDF}_\gamma(\cos\theta),\\
&\mathrm{PDF}_{\pi^0}(M,\Delta M,\cos\theta) = \mathrm{PDF}_{\pi^0}(M)\times\mathrm{PDF}_{\pi^0}(\Delta M|M)\times\mathrm{PDF}_{\pi^0}(\cos\theta),\\
&\mathrm{PDF}_\eta(M,\Delta M,\cos\theta) = \mathrm{PDF}_\eta(M)\times\mathrm{PDF}_\eta(\Delta M|M)\times\mathrm{PDF}_\eta(\cos\theta).
\end{aligned} \qquad \textbf{(V.1)}$$

The combinatorial-background component is modelled as the product:

$$\mathrm{PDF}_{\mathrm{cmb}}(M,\Delta M,\cos\theta) = \mathrm{PDF}_{\mathrm{cmb}}(M)\times\mathrm{PDF}_{\mathrm{cmb}}(\Delta M)\times\mathrm{PDF}_{\mathrm{cmb}}(\cos\theta) \qquad \textbf{(V.2)}$$

of the following PDFs:

$$\begin{aligned}
&\mathrm{PDF}_{\mathrm{cmb}}(M) = e^{-m\times M}\\
&\mathrm{PDF}_{\mathrm{cmb}}(\Delta M) = (\Delta M - m_\pi)^{1/\alpha}\times e^{-\beta(\Delta M - m_\pi)}\\
&\mathrm{PDF}_{\mathrm{cmb}}(\cos\theta) = p_2\cos^2\theta + p_1\cos\theta + 1,
\end{aligned} \qquad \textbf{(V.3)}$$

where m, α, β, p_1 and p_2 are free parameters in the fit.

In addition, for each of the three peaking components there is also a corresponding random soft-pion background included in the fit. Their $M(D^0)$ and $\cos\theta$ shapes are the same as for the peaking components, whereas their ΔM shapes are combinatorial-like, and described with PDF$_{\mathrm{cmb}}(\Delta M)$ in Eq. **V.3**.

Therefore, PDFs for the random soft-pion background associated with the signal, π^0 background, and η background, respectively, are:

$$\begin{aligned}
&\mathrm{PDF}_{\gamma\,\pi_s}(M,\Delta M,\cos\theta) = \mathrm{PDF}_{\gamma}(M)\times\mathrm{PDF}_{\mathrm{cmb}}(\Delta M)\times\mathrm{PDF}_{\gamma}(\cos\theta),\\
&\mathrm{PDF}_{\pi^0\,\pi_s}(M,\Delta M,\cos\theta) = \mathrm{PDF}_{\pi^0}(M)\times\mathrm{PDF}_{\mathrm{cmb}}(\Delta M)\times\mathrm{PDF}_{\pi^0}(\cos\theta),\\
&\mathrm{PDF}_{\eta\,\pi_s}(M,\Delta M,\cos\theta) = \mathrm{PDF}_{\eta}(M)\times\mathrm{PDF}_{\mathrm{cmb}}(\Delta M)\times\mathrm{PDF}_{\eta}(\cos\theta).
\end{aligned} \qquad \textbf{(V.4)}$$

$M(D^0)$ and ΔM observables in a random soft-pion background remain uncorrelated. Parameters of the mass- and $\cos\theta$-dependent PDF_{γ}, PDF_{π^0} and PDF_{η} in Eq. **V.4**, are shared with those in Eq. **V.1**. Parameters of the $\mathrm{PDF}_{\mathrm{cmb}}(\Delta M)$ are common for the purely combinatorial background (Eq. **V.3**) and the random soft-pion components (Eq. **V.4**). Overall, the total PDF is:

$$\begin{aligned}
\mathrm{PDF}_{\mathrm{tot}}(M,\Delta M,\cos\theta) = {} & S_{\gamma}\times\mathrm{PDF}_{\gamma}(M,\Delta M,\cos\theta) + B_{\pi^0}\times\mathrm{PDF}_{\pi^0}(M,\Delta M,\cos\theta)\\
& + B_{\eta}\times\mathrm{PDF}_{\eta}(M,\Delta M,\cos\theta) + B_{\gamma\,\pi_s}\times\mathrm{PDF}_{\gamma\,\pi_s}(M,\Delta M,\cos\theta)\\
& + B_{\pi^0\,\pi_s}\times\mathrm{PDF}_{\pi^0\,\pi_s}(M,\Delta M,\cos\theta) + B_{\eta\,\pi_s}\times\mathrm{PDF}_{\eta\,\pi_s}(M,\Delta M,\cos\theta)\\
& + B_{\mathrm{cmb}}\times\mathrm{PDF}_{\mathrm{cmb}}(M,\Delta M,\cos\theta),
\end{aligned} \qquad \textbf{(V.5)}$$

where S_{γ}, B_{π^0} and B_{η} denote yields of the signal, π^0 and η components, $S_{\gamma\,\pi_s}$, $B_{\pi^0\,\pi_s}$ and $B_{\eta\,\pi_s}$ are yields of the corresponding random π_s components, whereas B_{cmb} is combinatorial-background yield.

In the fits to the data, there are additional parameters included in the $M(D^0)$ PDFs and ΔM PDFs to account for possible data-MC differences due to imperfect simulations. For the signal these are:

– common scale factor, s_{γ}^{M}, multiplying the MC-based widths of the G_1 and G_2 sub-components in the $\mathrm{PDF}_{\gamma}(M)$,

– common offset, $\mathrm{off}_{\gamma}^{M}$, for the MC-based peak positions of the G_1 and G_2 sub-components in the $\mathrm{PDF}_{\gamma}(M)$,

– corresponding scale-factor and offset parameters, $s_{\gamma}^{\Delta M}$ and $\mathrm{off}_{\gamma}^{\Delta M}$, in the $\mathrm{PDF}_{\gamma}(\Delta M)$.

The same set of parameters is included for the π^0 component; they are denoted as $s_{\pi^0}^{M}$, $\mathrm{off}_{\pi^0}^{M}$, $s_{\pi^0}^{\Delta M}$ and $\mathrm{off}_{\pi^0}^{\Delta M}$. For the η component, there is a scale factor s_{η}^{M} multiplying the CB width introduced in the $\mathrm{PDF}_{\eta}(M)$. There are no additional parameters in the $\mathrm{PDF}_{\eta}(\Delta M)$; its resolution is too limited to be sensitive to any data-MC differences. These scale factors and offsets in the $M(D^0)$ PDFs are shared with the corresponding random-soft pion PDFs (Eq. **V.4**). No additional parameters are introduced for the helicity-dependent PDFs, as the $\cos\theta$ relies on momenta of the charged D^0 daughters, which are known to be well described in LHCb simulations.

V.3.1 Fit to $D^0 \to \bar{K}^{*0}\gamma$ in helicity-edge region

First, the three-dimensional fit is performed in the helicity-edge region, $-0.97 < \cos\theta < -0.7$, in order to calibrate the π^0 and η components using the experimental data. This is done by measuring the scale factors and offsets introduced to account for possible data-MC differences (Section **V.3**). As the signal contribution in the helicity edge is small, it is not sensitive to such differences. Therefore, $s_{\gamma}^{M}{=}s_{\gamma}^{\Delta M} = 1$ and $\mathrm{off}_{\gamma}^{M} = \mathrm{off}_{\gamma}^{\Delta M} = 0$ is assumed in this fit. All the remaining parameters of PDF_{γ}, PDF_{π^0} and PDF_{η} (Eqs. **V.1** and **V.4**) are fixed to their values from the corresponding simulation, except for the left width σ_L of the threshold Gaussian G_3 in the $\mathrm{PDF}_{\pi^0}(M)$ (Eq. **IV.2**), which is Gaussian-constrained to the simulation-based value. A reason for such a treatment of the σ_L is that this parameter is, to some extent, based on photons reconstructed in an underlying event (Section **IV.5.2**), which makes it more sensitive to any data-MC difference.

Within the η background, any contribution from $D^0 \to K^- a_0(980)^+$ decays is expected to be negligible in the helicity-edge region, and only $D^0 \to \bar{K}^{*0}\eta$ and $D^0 \to \bar{K}_0(1430)^0\eta$ channels are considered (Section **IV.5.3**). The $M(D^0)$ and ΔM shapes of these two contributions are shared in the fit, while their helicity shapes are independent. Their signal yields are also independent, and so are yields of their associated random soft-pion components.

As the overall fit is complicated, it is not feasible to measure simultaneously the mass scale factors $s^M_{\pi^0}$ and s^M_η for the π^0 and η background. It is done in two steps, first $s^M_{\pi^0}$ is measured assuming $s^M_\eta = 1$, second s^M_η is fixed to the measured $s^M_{\pi^0}$ value, and $s^M_{\pi^0}$ is refitted. The $s^M_{\pi^0}$ value from the second step is very close to that from the first step, showing that the η component does not have significant impact on the π^0 calibration. Approximating the s^M_η with the $s^M_{\pi^0}$ can be justified by the fact that both parameters describe similar reconstruction effects. These scale factors are close to unity, which demonstrates only small overestimation of the photon-energy resolution in simulations.

Projections of this three-dimensional fit on the $M(D^0)$, ΔM and $\cos\theta$ observables, performed to $D^0 \to \bar{K}^{*0}\gamma$ candidates with IsPhoton$>$ 0.86 and reconstructed in the helicity-edge region, $-0.97 < \cos\theta < -0.7$, are shown in Fig. **V-4** for the Run-1 data. These projections are made in the full fit region. Figure **V-5** shows $M(D^0)$ projections in ΔM regions, Fig. **V-6** presents ΔM projections in $M(D^0)$ regions, whereas Fig. **V-7** $\cos\theta$ projections in $M(D^0)$ regions.

$M(D^0)$ projections in ΔM regions (Figure **V-5**) show an impact of the $M(D^0)$–ΔM correlations on the $M(D^0)$ shape of the π^0 background, as expected from the simulation (Section **IV.7.2**). In the regions away from the ΔM peak, the threshold Gaussian dominates the $M(D^0)$ distribution of the π^0 background. In the $M(D^0)$ projections for the ΔM sidebands, $\Delta M > 149$ MeV/c^2, the $M(D^0)$ peak region at 1850 MeV/c^2 is dominated by the random π_s component of the π^0 background.

Overall, the fit shows a good quality. Somewhat worse quality for $M(D^0) < 1720$ MeV/c^2 and $\cos\theta < -0.95$ (Fig. **V-7**) can be due to a simplified (incoherent) model for the η background, which dominates this phase-space region. Nevertheless, limiting the fit range to $-0.95 < \cos\theta < -0.7$ does not affect the π^0 calibration parameters.

The fit parameters for the signal, π^0 and η components, and the corresponding random π_s components are summarised in Table **V-1**. The combinatorial-background yield is $B_{\rm cmb} = 600 \pm 104$ events. Yields of the random soft-pion background associated with the signal and the random soft-pion background associated with the η background from $D^0 \to \bar{K}_0(1430)^0\eta$ have been fixed to zero, as their contributions are found negligible.

Par/Comp	Yield	s^M	off^M	$s^{\Delta M}$	off$^{\Delta M}$	σ_L
γ signal	471 ± 89	1.0	0.0	1.0	0.0	–
γ; random π_s	0			–	–	
π^0 bkgd	24212 ± 243	0.98 ± 0.01	5.8 ± 0.4	1.089 ± 0.007	0.032 ± 0.005	80 ± 4
π^0; random π_s	2949 ± 97			–	–	
η bkgd: $D^0 \to \bar{K}^{*0}\eta$	3749 ± 122	0.98 ± 0.01	–	–	–	–
η: $D^0 \to \bar{K}^{*0}\eta$; rnd π_s	541 ± 67					
η bkgd: $D^0 \to \bar{K}^0_0\eta$	49 ± 54					
η: $D^0 \to \bar{K}^0_0\eta$; rnd π_s	0					

Table **V-1**: Parameter values measured for given component in three-dimensional fit to the combined $D^0 \to \bar{K}^{*0}\gamma$ and $\bar{D}^0 \to K^{*0}\gamma$ candidates from the helicity edge in the Run-1 data. Offsets off^M and off$^{\Delta M}$, and width σ_L are given in MeV/c^2. K^0_0 stands for the $K_0(1430)^0$ meson.

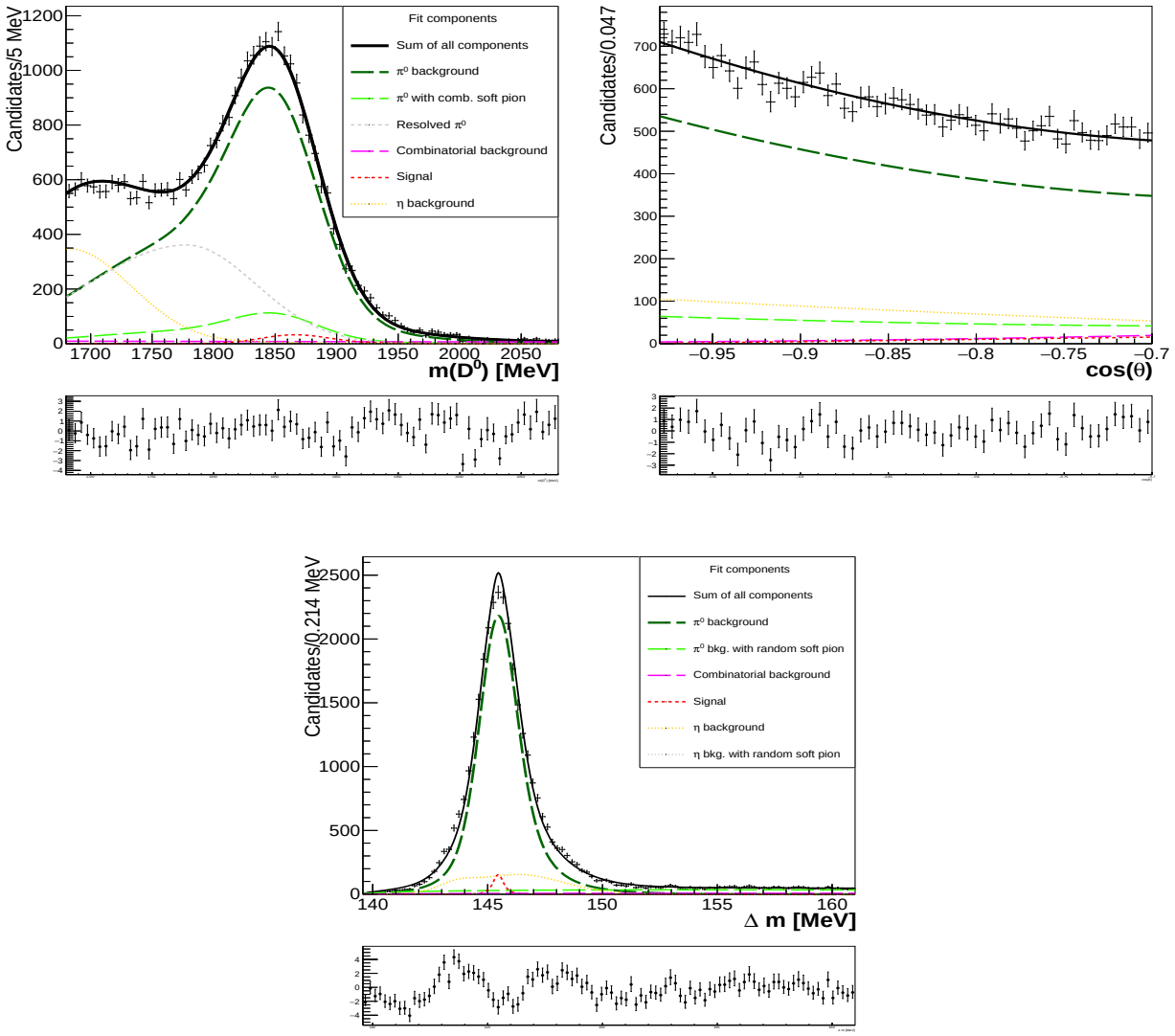

Figure **V-4**: (Top left) $M(D^0)$, (top right) $\cos\theta$ and (bottom) ΔM projections of three-dimensional fit to $D^0 \to \bar{K}^{*0}\gamma$ candidates, with IsPhoton> 0.86, reconstructed in the Run-1 data in the helicity-edge region $-0.97 < \cos\theta < -0.7$. These projections are in the full fit region. Fit components are indicated in the legend.

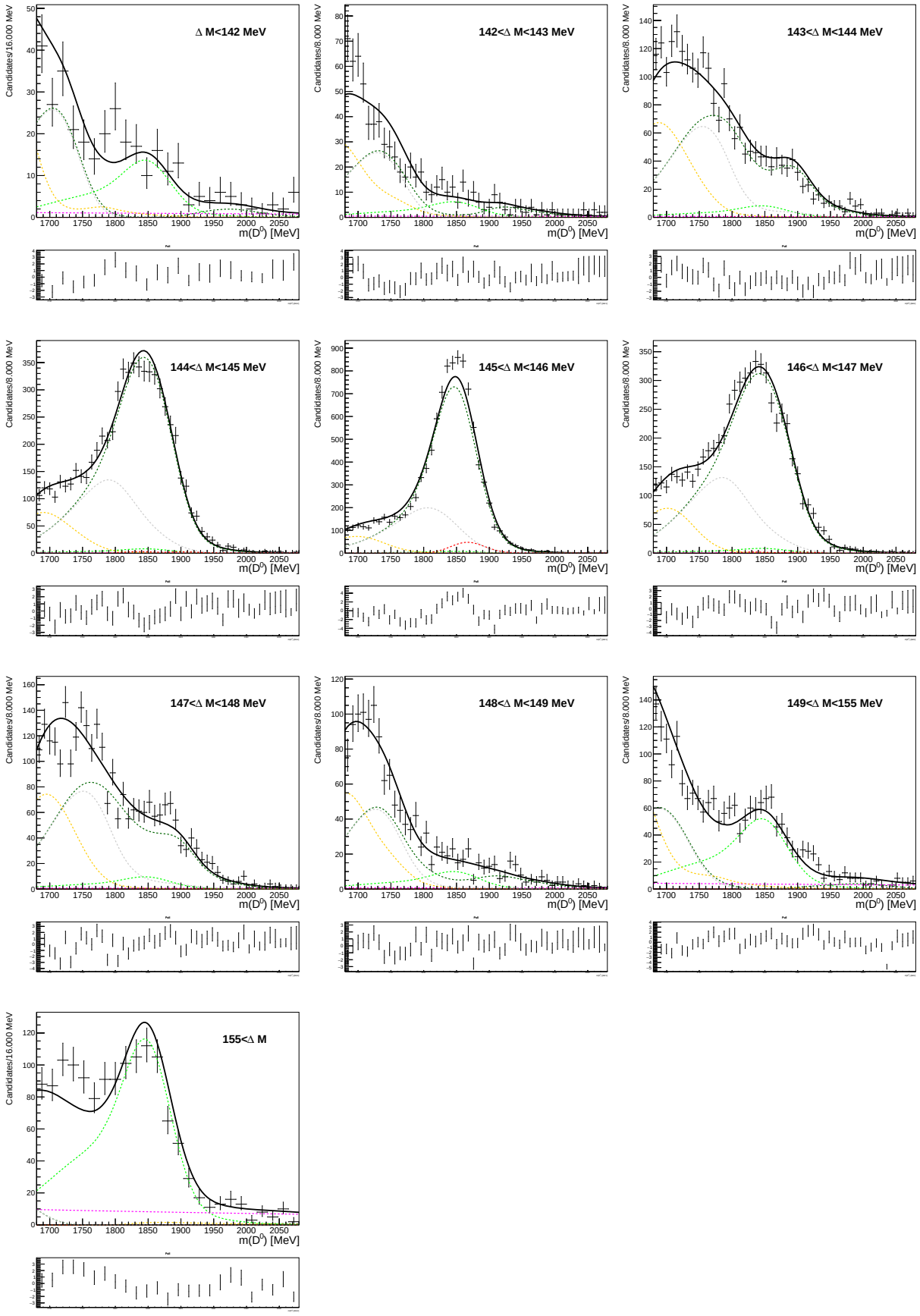

Figure **V-5**: $M(D^0)$ projections of three-dimensional fit to $D^0 \to \bar{K}^{*0}\gamma$ candidates in the Run-1 data in the helicity edge. $M(D^0)$ projections are for ΔM regions indicated in individual plots. Fit components are indicated with the same colours as in Fig. **V-4**.

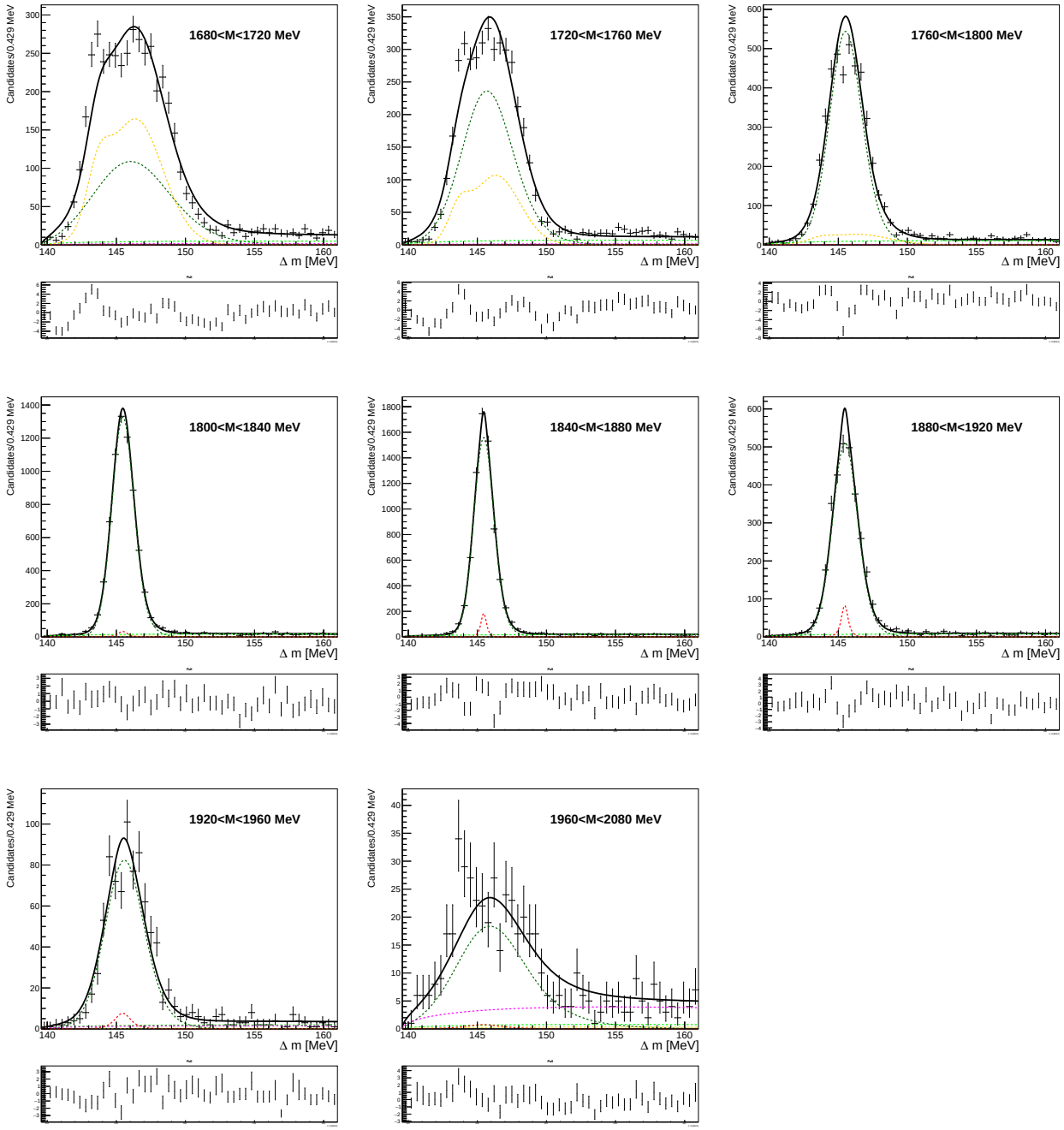

Figure **V-6**: ΔM projections of three-dimensional fit to $D^0 \to \bar{K}^{*0}\gamma$ candidates in the Run-1 data in the helicity edge. ΔM projections are for $M(D^0)$ regions indicated in individual plots. Fit components are indicated with the same colours as in Fig. **V-4**.

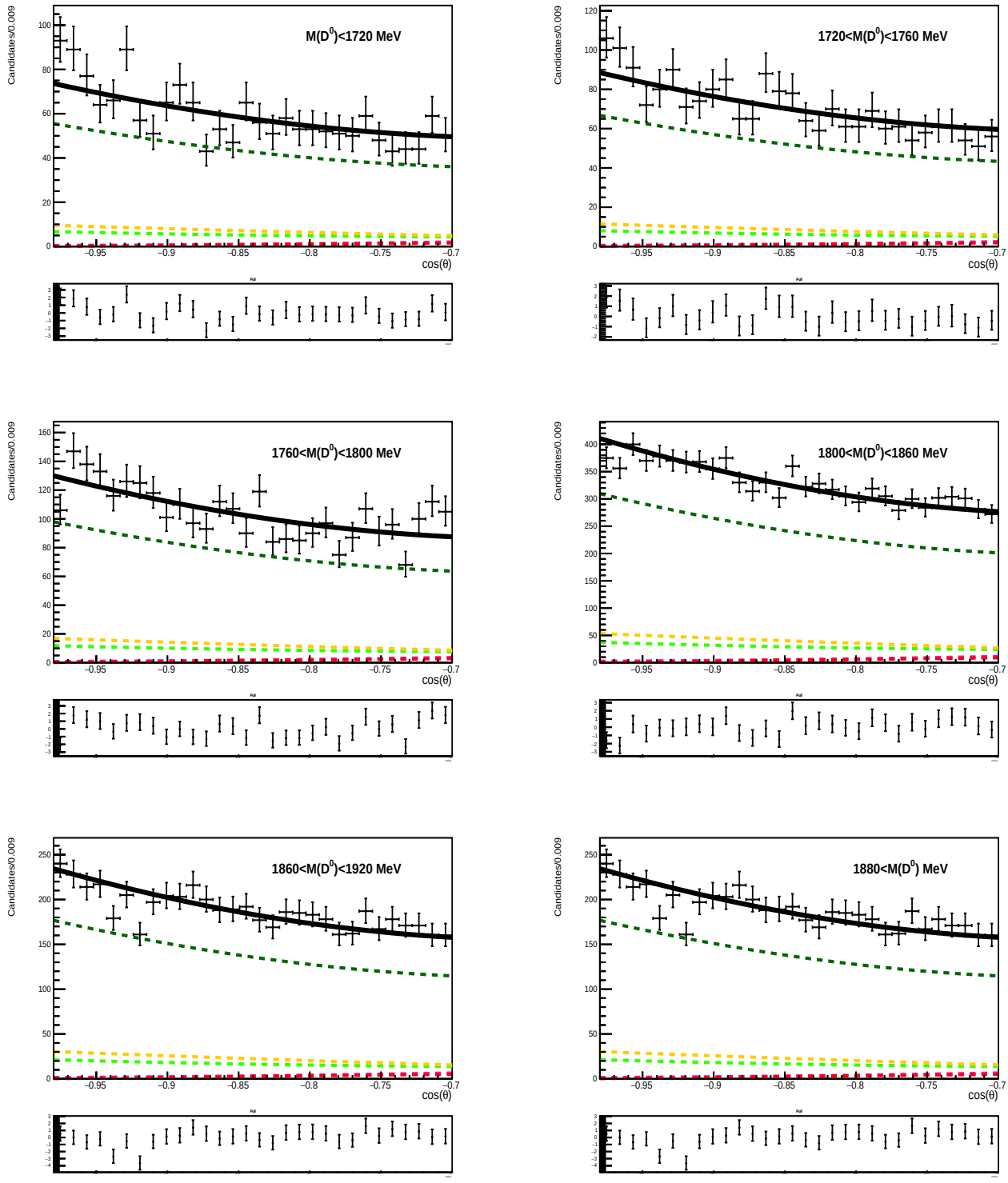

Figure **V-7**: $\cos\theta$ projections of three-dimensional fit to $D^0 \to \bar{K}^{*0}\gamma$ candidates in the Run-1 data in the helicity edge. Projections of $\cos\theta$ are for $M(D^0)$ regions indicated in individual plots, and in the full ΔM region. Fit components are indicated with the same colours as in Fig. **V-4**.

V.3.2 Fit to $D^0 \to \bar{K}^{*0}\gamma$ in helicity-center region

The three-dimensional fit is performed in the helicity-center region, $-0.4 < \cos\theta < 0.7$, in order to calibrate the signal component, and to measure the total signal yield for the combined D^0 and $\bar{D}^0$ samples. Similar to the fit performed in the helicity edge (Section **V.3.1**), the parameters of the PDF_γ, PDF_{π^0} and PDF_η (Eqs. **V.1** and **V.4**) are fixed to their values from the corresponding simulation. The σ_L width in the $\mathrm{PDF}_{\pi^0}(M)$ (Eq. **IV.2**) is either fixed or Gaussian-constrained to the value measured in the helicity-edge fit; its treatment has negligible impact on the fit result. Within the η background, contributions from all the three channels are included, $D^0 \to \bar{K}^{*0}\eta$ and $D^0 \to \bar{K}_0(1430)^0\eta$ and $D^0 \to K^- a_0(1430)^+$. They are treated similar to the helicity-edge fit, with shared $M(D^0)$ and ΔM shapes, and the independent helicity shapes and yields.

The offsets and scale factors, accounting for data-MC differences in the π^0 and η components, are fixed to their values from the helicity-edge fit (Table **V-1**). Instead, these parameters are released for the signal component.

Projections of this three-dimensional fit on the $M(D^0)$, ΔM and $\cos\theta$ observables, performed to $D^0 \to \bar{K}^{*0}\gamma$ candidates with IsPhoton>0.86 and reconstructed in the helicity-center region, $-0.4 < \cos\theta < 0.7$, are shown in Fig. **V-8** for the Run-1 data. The projections are made in the signal-enhanced region: the $M(D^0)$ distribution is shown for $144 < \Delta M < 147$ MeV/c^2, the ΔM for $1810 < M(D^0) < 1920$ MeV/c^2, whereas the $\cos\theta$ for both $M(D^0)$ and ΔM selected in above regions. Figure **V-9** shows $M(D^0)$ projections in ΔM regions, Fig. **V-10** presents ΔM projections in $M(D^0)$ regions, Fig. **V-11** shows $\cos\theta$ projections in $M(D^0)$ regions, whereas Fig. **V-12** shows $M(D^0)$ projections in $\cos\theta$ regions. An impact of the $M(D^0)$–ΔM correlations on the $M(D^0)$ shape of the signal (Figure **V-9**), is not as distorting as in the π^0 background; the $M(D^0)$ resolution of the signal becomes worse away from the ΔM peak. In the $M(D^0)$ projections for the ΔM sidebands, $\Delta M > 149$ MeV/c^2, the $M(D^0)$ peak region at 1850 MeV/c^2 is dominated by the random π_s background associated with the signal and π^0 components.

The fit parameters for the signal, π^0 and η components, and the related random soft-pion components are summarised in Table **V-2**. The combinatorial-background yield is $B_{comb} = 7113 \pm 193$. The $M(D^0)$ offset for the signal, off_γ^M is measured to be consistent with that for the π^0 background. It is understandable, given that neutral objects in both processes pass the same photon-like selection. Due to the relatively limited signal yield, the fit shows no sensitivity to the ΔM offset for the signal, $\mathrm{off}_\gamma^{\Delta M}$, thus it is fixed to zero. Both scale factors for the signal, s_γ^M and $s_\gamma^{\Delta M}$, are consistent with unity.

The default fit presented above shows a good quality. An alternative fit is also performed without calibrating the signal component, i.e. assuming $s_\gamma^M = s_\gamma^{\Delta M} = 1$ and $\mathrm{off}_\gamma^M = \mathrm{off}_\gamma^{\Delta M} = 0$. It gives the signal yield of $S_\gamma = 4616 \pm 201$, and the π^0 yield of $B_{\pi^0} = 41072 \pm 334$, consistent with those from the default. The observable projections and quality of this fit remain very similar to those in the default fit.

Par/Comp	Yield	s^M	off^M	$s^{\Delta M}$	off$^{\Delta M}$	σ_L
γ signal	4263 ± 193	0.992 ± 0.009	6.1 ± 0.4	0.996 ± 0.034	0.0	–
γ; random π_s	455 ± 112			–	–	–
π^0 bkgd	41527 ± 326	0.98	5.8	1.089	0.032	80
π^0; random π_s	3514 ± 211			–	–	
η bkgd: $D^0 \to \bar{K}^{*0}\eta$	2603 ± 135	0.98	–	–	–	–
η: $D^0 \to \bar{K}^{*0}\eta$; rnd π_s	224 ± 95		–	–	–	–
η bkgd: $D^0 \to \bar{K}^0_0\eta$	3471 ± 200		–	–	–	–
η: $D^0 \to \bar{K}^0_0\eta$; rnd π_s	0 ± 26		–	–	–	–
η bkgd: $D^0 \to K^- a_0^+$	423 ± 118		–	–	–	–
η: $D^0 \to K^- a_0^+$; rnd π_s	0 ± 9		–	–	–	–

Table **V-2**: Parameter values measured for given component in three-dimensional fit to the combined $D^0 \to \bar{K}^{*0}\gamma$ and $\bar{D}^0 \to K^{*0}\gamma$ candidates from the helicity center in the Run-1 data. Offsets off^M and off$^{\Delta M}$, and width σ_L are given in MeV/c^2. K^0_0 stands for the $K_0(1430)^0$ meson; a_0^+ stands for the $a_0(980)^+$ meson.

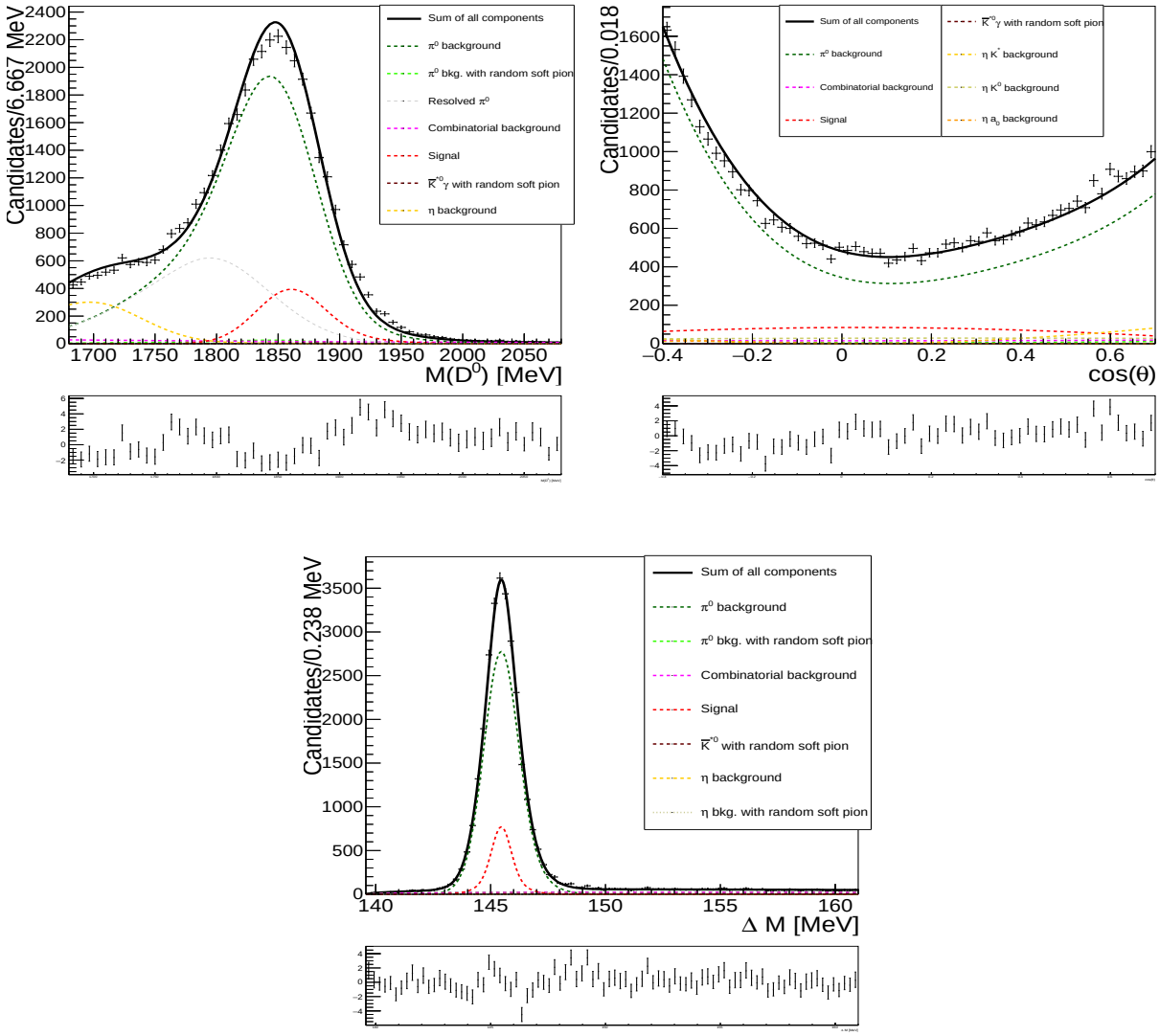

Figure **V-8**: (Top left) $M(D^0)$, (top right) $\cos\theta$ and (bottom) ΔM projections of three-dimensional fit to $D^0 \to \bar{K}^{*0}\gamma$ candidates, with IsPhoton>0.86, reconstructed in the Run-1 data in the helicity center $-0.4 < \cos\theta < 0.7$. These projections are in the signal-enhanced region. Fit components are indicated in the legend.

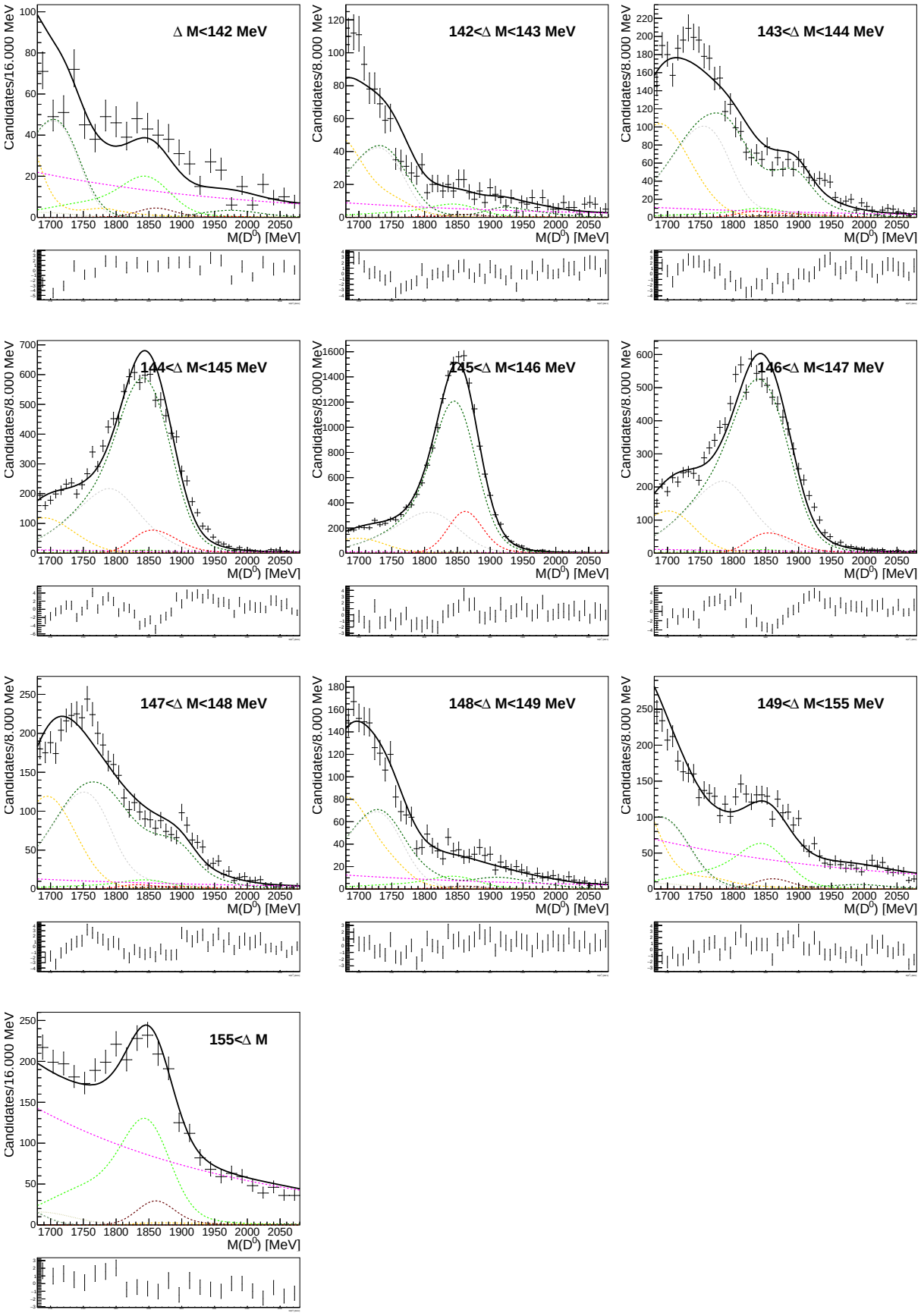

Figure **V-9**: $M(D^0)$ projections of three-dimensional fit to $D^0 \to \bar{K}^{*0}\gamma$ candidates in the Run-1 data in the helicity center. $M(D^0)$ projections are for ΔM regions indicated in individual plots. Fit components are indicated with the same colours as in Fig. **V-8**.

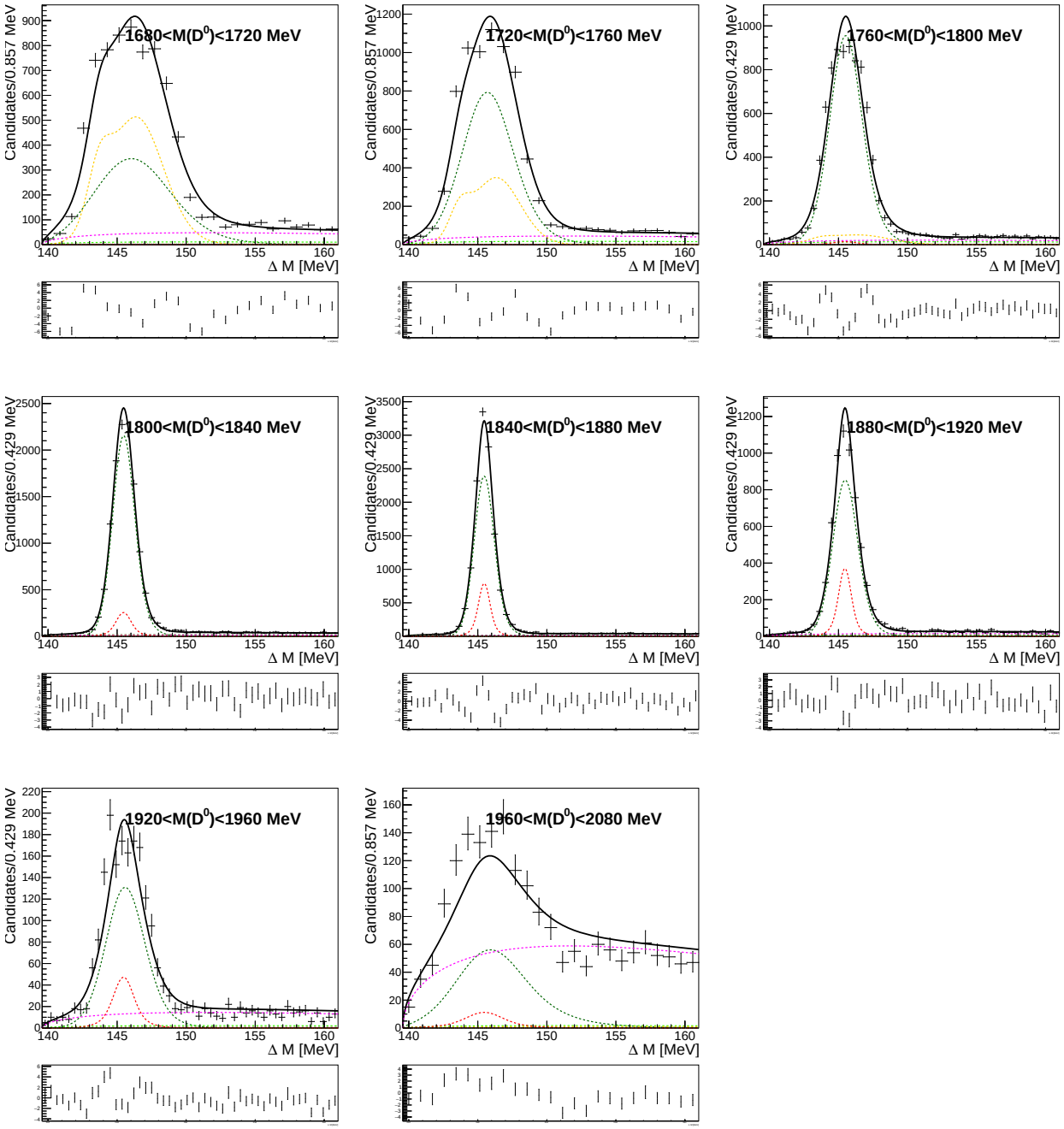

Figure **V-10**: ΔM projections of three-dimensional fit to $D^0 \to \bar{K}^{*0}\gamma$ candidates in the Run-1 data in the helicity center. ΔM projections are for $M(D^0)$ regions indicated in individual plots. Fit components are indicated with the same colours as in Fig. **V-8**.

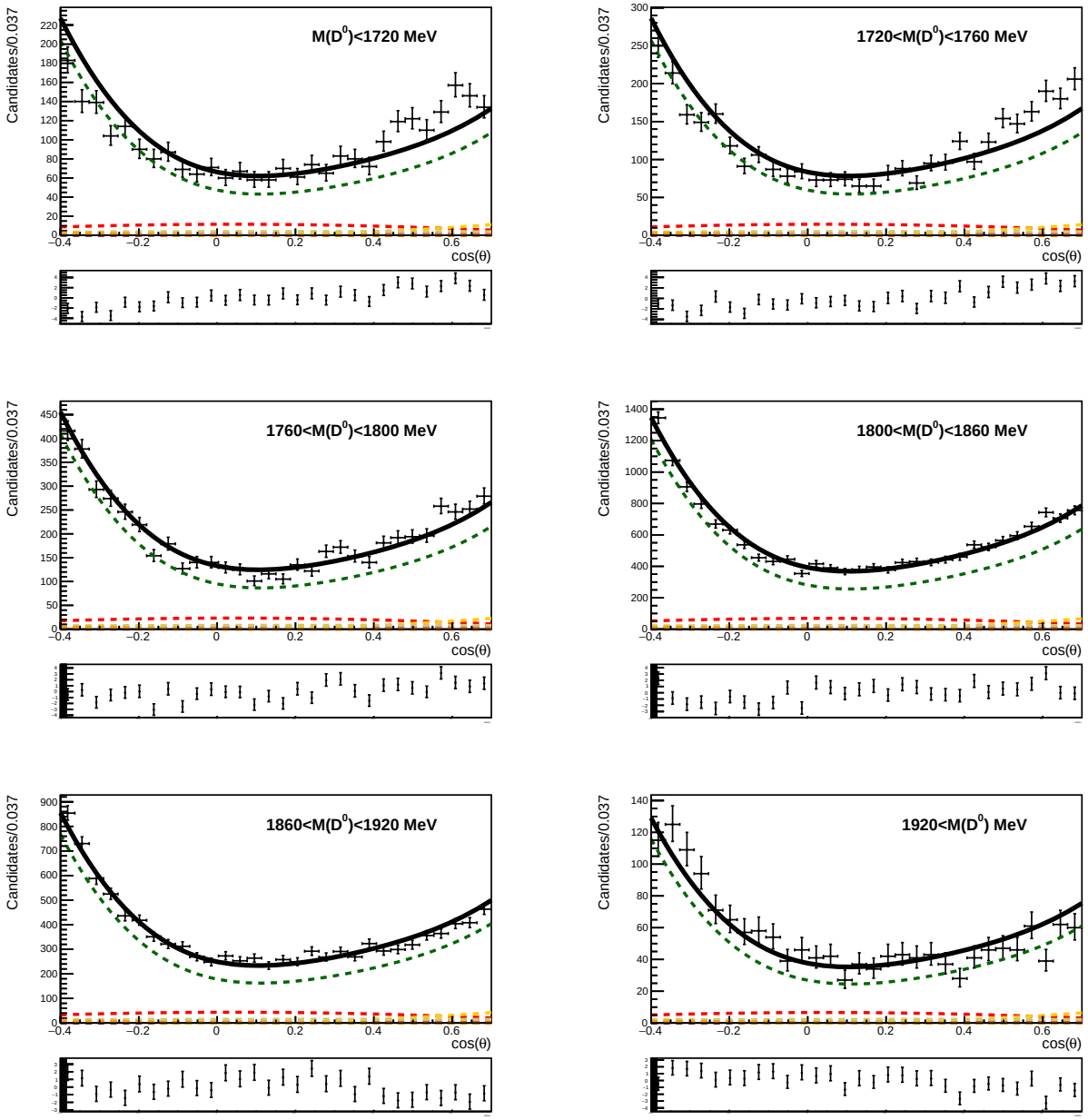

Figure **V-11**: $\cos\theta$ projections of three-dimensional fit to $D^0 \to \bar{K}^{*0}\gamma$ candidates in the Run-1 data in the helicity center. Projections of $\cos\theta$ are for $M(D^0)$ regions indicated in individual plots, and in the ΔM signal region. Fit components are indicated with the same colours as in Fig. **V-8**.

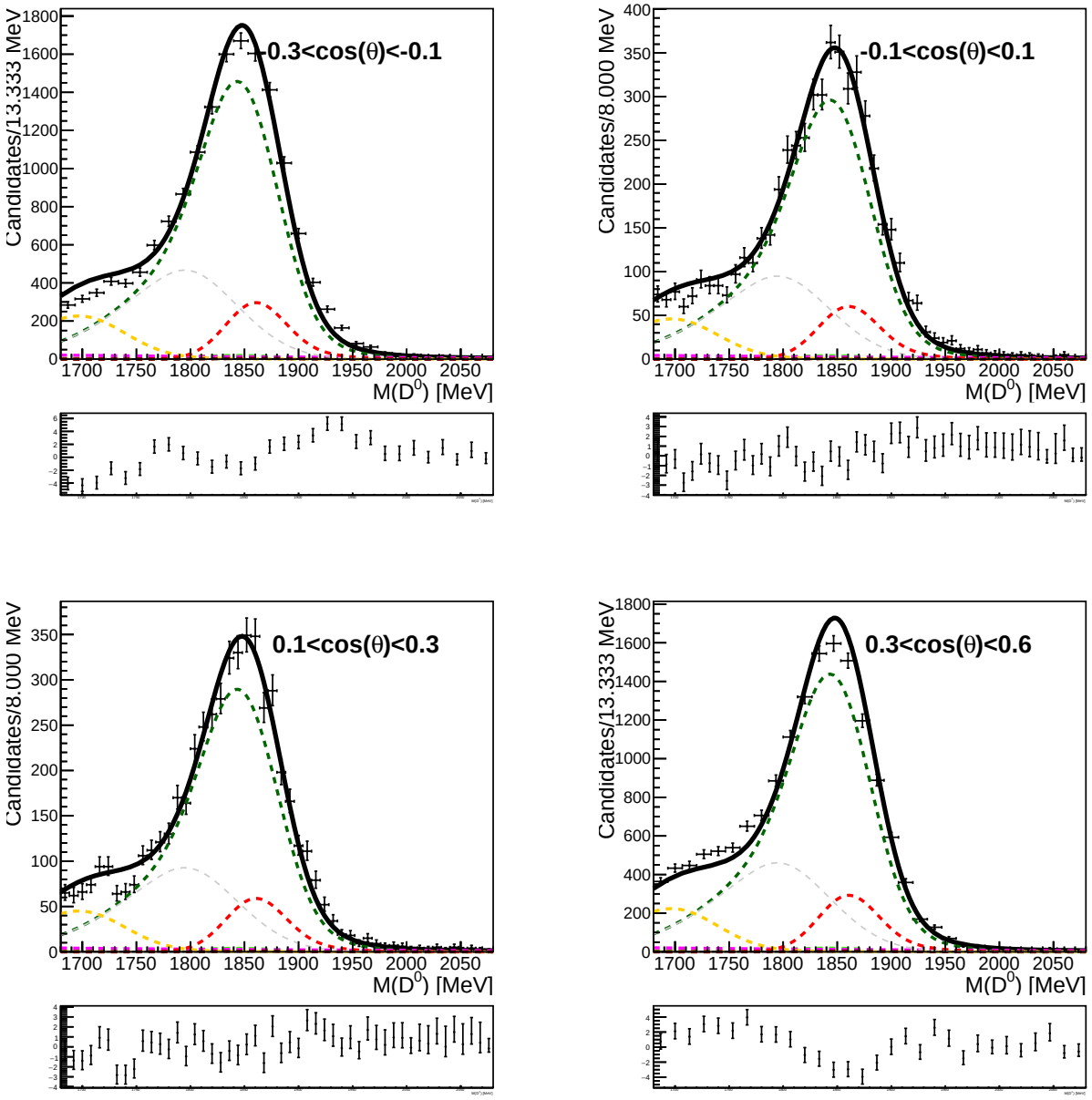

Figure **V-12**: $M(D^0)$ projections of three-dimensional fit to $D^0 \to \bar{K}^{*0}\gamma$ candidates in the Run-1 data in the helicity center. $M(D^0)$ projections are for $\cos\theta$ regions indicated in individual plots, and in the ΔM signal region. Fit components are indicated with the same colours as in Fig. **V-8**.

V.4 Three-dimensional fit to $D^0 \to \phi\gamma$ sample

In terms of the PDFs and strategy, the fit to $D^0 \to \phi\gamma$ sample is similar to that of the $D^0 \to \bar{K}^{*0}\gamma$ sample described in Section **V.3**. The η background is simpler for the ϕ channel, as it originates from a single decay, $D^0 \to \phi\eta$, in both helicity regions.

V.4.1 Fit to $D^0 \to \phi\gamma$ in helicity-edge region

The three-dimensional fit is performed to $D^0 \to \phi\gamma$ candidates with IsPhoton> 0.85 and reconstructed in the helicity-edge region, $|\cos\theta| > 0.8$.[32] Projections of this fit on the $M(D^0)$, ΔM and $\cos\theta$ observables are shown in Fig. **V-13** for the Run-1 data. These projections are made in the full fit region. Figure **V-14** shows $M(D^0)$ projections in ΔM regions, Fig. **V-15** presents ΔM projections in $M(D^0)$ regions, whereas Fig. **V-16** $\cos\theta$ projections in $M(D^0)$ regions.

Shape parameters of PDF_γ, PDF_{π^0} and PDF_η (Eqs. **V.1** and **V.4**) are fixed to their values from the corresponding simulation samples (Sections **IV.8**, **IV.9** and **IV.10**). An exception is the width σ_L in the $\text{PDF}_{\pi^0}(M)$ (Eq. **IV.2**), which is Gaussian-constrained to the simulation-based value.

The fit parameters for the signal, π^0 and η components, and the corresponding random π_s components are summarised in Table **V-3**. Yields of the signal component and the associated random soft-pion background have been fixed to zero, as their contributions are found negligible. As the mass scale factor $s^M_{\pi^0}$ of the π^0 component is consistent with unity, $s^M_\eta = 1$ is assumed for the η. Parameters of the combinatorial PDFs (Eq. **V.3**) are given in Table **V-4**. The parameter p_1 of the $\text{PDF}_{\text{cmb}}(\cos\theta)$ is fixed to zero, as it cannot be measured in the limited helicity range considered in the fit.

Par/Comp	Yield	s^M	off^M	$s^{\Delta M}$	$\text{off}^{\Delta M}$	σ_L
γ signal	0	1.0	0.0	1.0	0.0	–
γ; random π_s	0			–	–	
π^0 bkgd	1185 ± 47	1.005 ± 0.058	6.9 ± 2.2	1.064 ± 0.037	0.050 ± 0.035	117^{+33}_{-0}
π^0; random π_s	212 ± 47			–	–	
η bkgd: $D^0 \to \phi\eta$	172 ± 29	1.0	–	–	–	–
η: $D^0 \to \phi\eta$; rnd π_s	0 ± 22					

Table **V-3**: Parameter values measured for given component in three-dimensional fit to the combined $D^0 \to \phi\gamma$ and $\bar{D}^0 \to \phi\gamma$ candidates from the helicity edge in the Run-1 data. Offsets off^M and $\text{off}^{\Delta M}$, and width σ_L are given in MeV/c^2.

Par/Comp	Yield	m	α	β	p_1	p_2
Cmb	625 ± 63	-0.0048 ± 0.0005	0.75 ± 0.15	0.07 ± 0.02	0.0	1.3 ± 2.1

Table **V-4**: Parameter values measured for combinatorial component in three-dimensional fit to the combined $D^0 \to \phi\gamma$ and $\bar{D}^0 \to \phi\gamma$ candidates from the helicity edge in the Run-1 data.

[32] As $M(D^0)$ and ΔM shapes are consistent between the two helicity edges, $\cos\theta < -0.8$ and $\cos\theta > 0.8$, both regions are combined by considering $|\cos\theta|$ in fits to the data in the helicity-edge region.

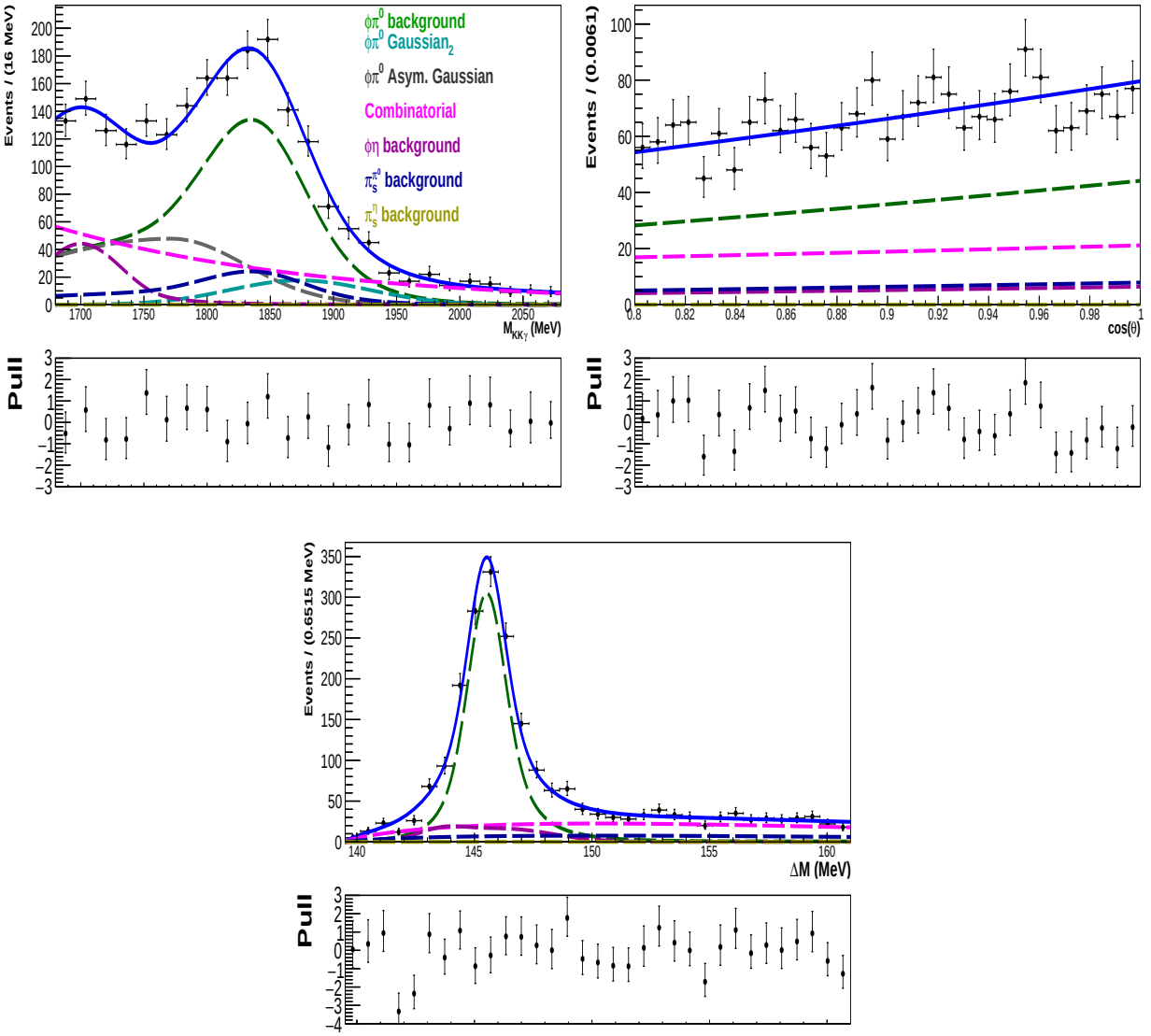

Figure **V-13**: (Top left) $M(D^0)$, (top right) $\cos\theta$ and (bottom) ΔM projections of three-dimensional fit to $D^0 \to \phi\gamma$ candidates, with IsPhoton>0.85, reconstructed in the Run-1 data in the helicity-edge region $|\cos\theta| > 0.8$. These projections are in the full fit region. Fit components are indicated in the legend.

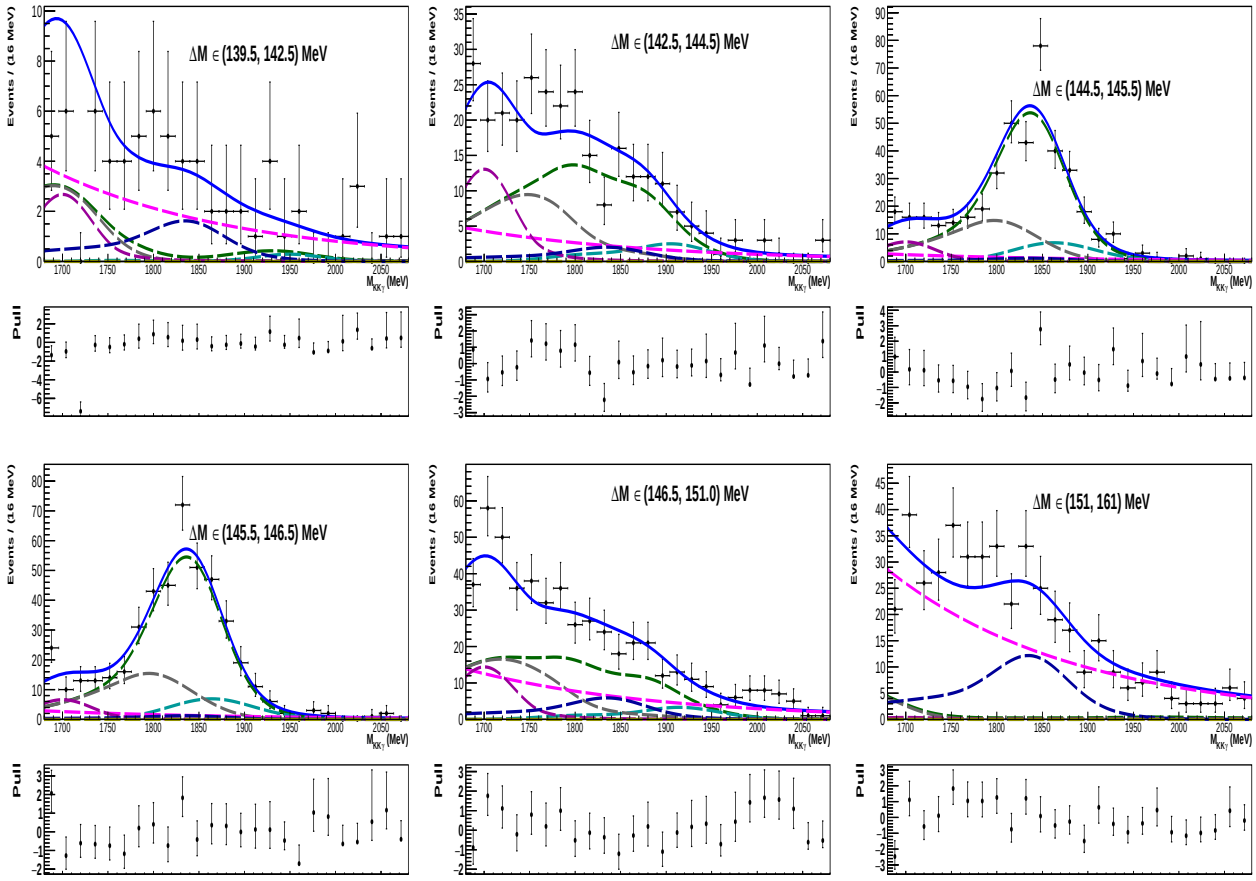

Figure **V-14**: $M(D^0)$ projections of three-dimensional fit to $D^0 \to \phi\gamma$ candidates in the Run-1 data in the helicity edge. $M(D^0)$ projections are for ΔM regions indicated in individual plots. Fit components are indicated with the same colours as in Fig. **V-13**.

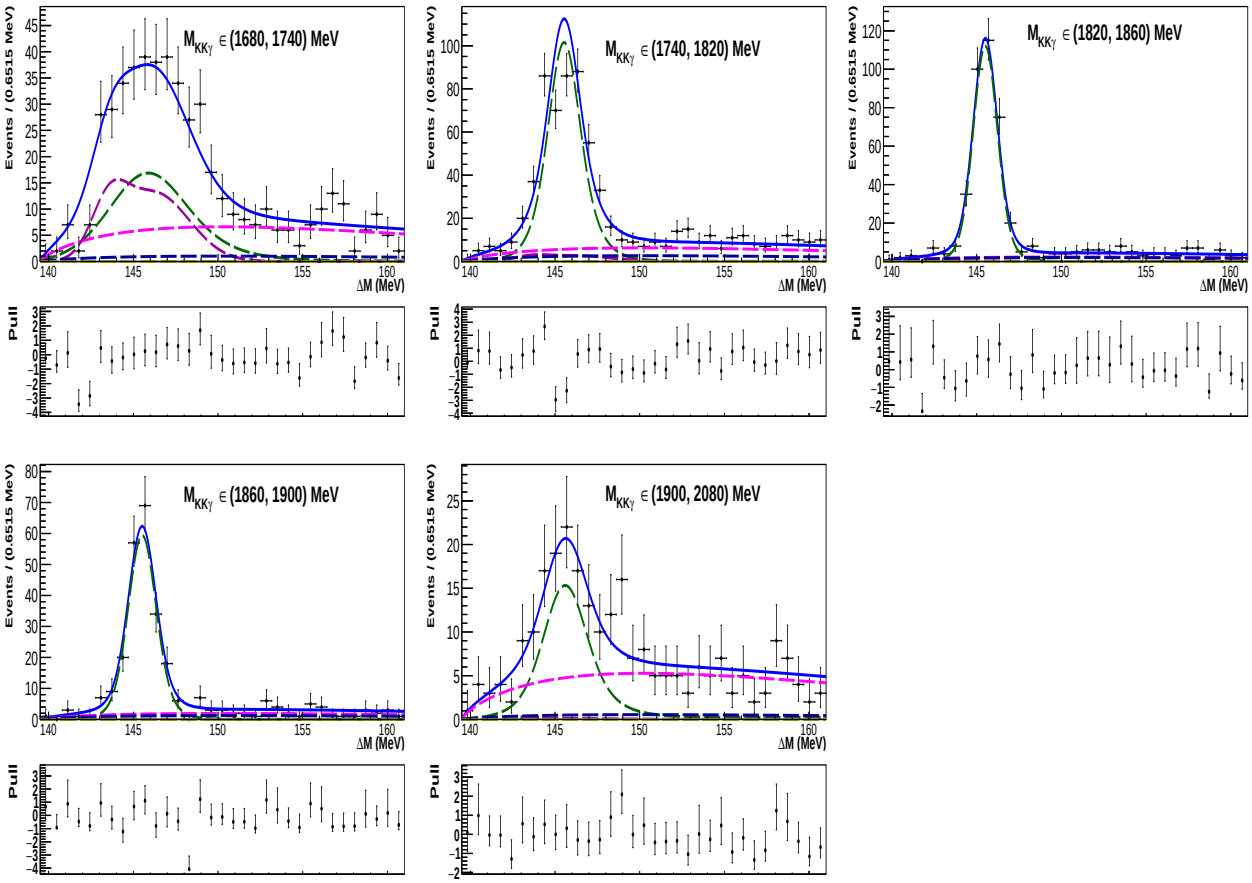

Figure **V-15**: ΔM projections of three-dimensional fit to $D^0 \to \phi\gamma$ candidates in the Run-1 data in the helicity edge. ΔM projections are for $M(D^0)$ regions indicated in individual plots. Fit components are indicated with the same colours as in Fig. **V-13**.

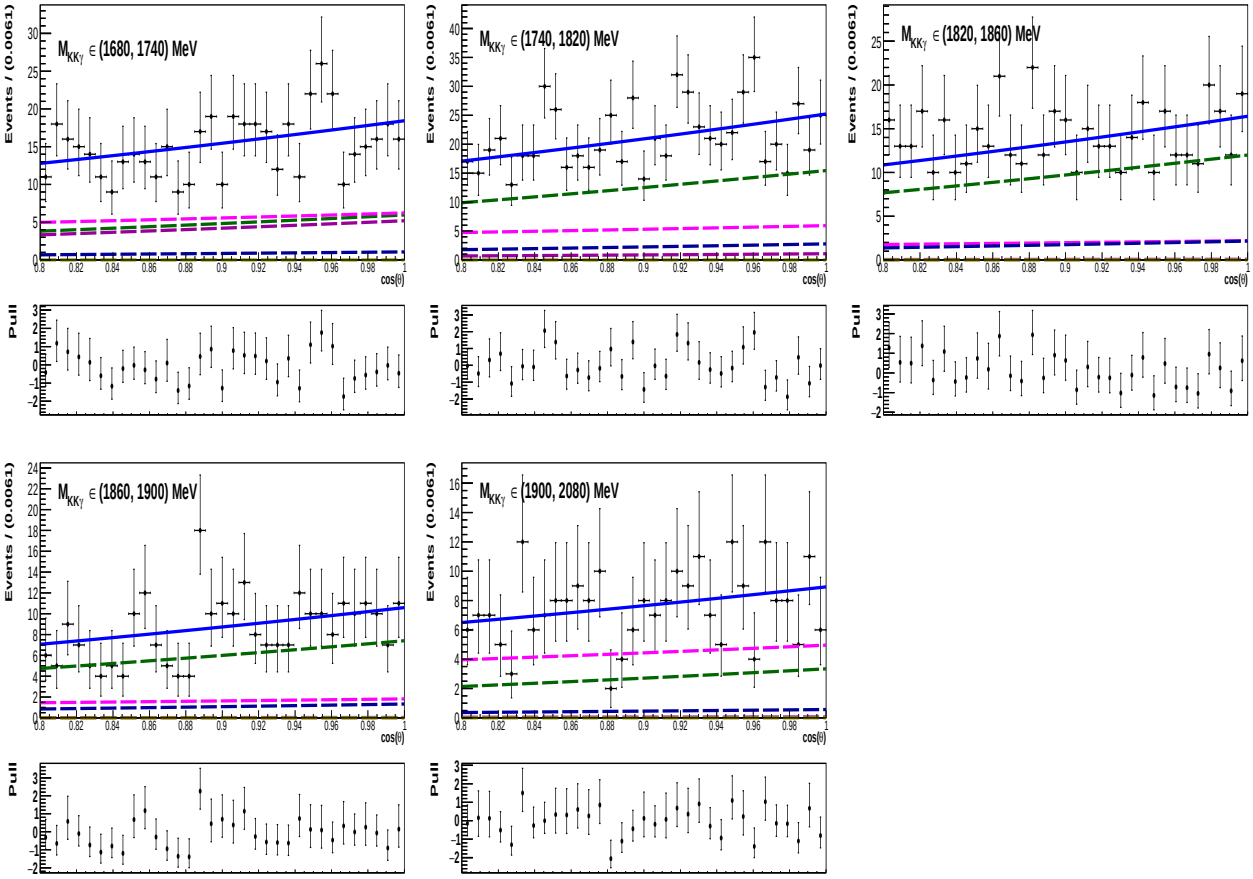

Figure **V-16**: $\cos\theta$ projections of three-dimensional fit to $D^0 \to \phi\gamma$ candidates in the Run-1 data in the helicity edge. Projections of $\cos\theta$ are for $M(D^0)$ regions indicated in individual plots, and in the full ΔM region. Fit components are indicated with the same colours as in Fig. **V-13**.

V.4.2 Fit to $D^0 \to \phi\gamma$ in central helicity region

The three-dimensional fit is performed to $D^0 \to \phi\gamma$ candidates with IsPhoton> 0.85 and reconstructed in the helicity-center region, $|\cos\theta| < 0.8$. Projections of this fit on the $M(D^0)$, ΔM and $\cos\theta$ observables are shown in Fig. **V-17** for the Run-1 data. The projections are made in the signal-enhanced region: the $M(D^0)$ distribution is shown for $144 < \Delta M < 147$ MeV/c^2, the ΔM for $1827 < M(D^0) < 1902$ MeV/c^2, whereas the $\cos\theta$ for both $M(D^0)$ and ΔM selected in above regions. Figure **V-18** shows $M(D^0)$ projections in ΔM regions, Fig. **V-19** presents ΔM projections in $M(D^0)$ regions, Fig. **V-20** $\cos\theta$ projections in $M(D^0)$ regions, whereas Fig. **V-21** $M(D^0)$ projections in $\cos\theta$ regions.

The fit parameters for the signal, π^0 and η components, and the corresponding random π_s components are summarised in Table **V-5**, whereas parameters of the combinatorial PDFs (Eq. **V.3**) are given in Table **V-6**. In this default fit, $\text{off}^M_{\pi^0}$, $s^M_{\pi^0}$, $\text{off}^{\Delta M}_{\pi^0}$ and σ_L for the π^0 background and s^M_η for the η background are fixed to the values measured in the helicity edge (Table **V-3**), whereas $s^{\Delta M}_{\pi^0}$ is Gaussian-constrained to the helicity-edge value. For the signal component, off^M_γ, s^M_γ, $\text{off}^{\Delta M}_\gamma$ and $s^{\Delta M}_\gamma$ are shared with the ones for the π^0 background. Other parameters of PDF_γ, PDF_{π^0} and PDF_η (Eqs. **V.1** and **V.4**) are fixed to their values from the corresponding simulation samples (Sections **IV.8**, **IV.9** and **IV.10**).

In the helicity shape of the π^0 component, the theoretical $\cos^2\theta$ function used for the $D^0 \to \phi\pi^0$ simulation (Section **IV.8.2**) is extended to:

$$\text{PDF}_{\pi^0}(\cos\theta) = \cos^2\theta + c_1\cos^2\theta + c_0, \qquad \textbf{(V.6)}$$

where c_0 and c_1 are free parameters. This is to account for a possible non-resonant K^+K^- contribution in the ϕ region. Its presence would introduce a constant term, whereas its interference with the ϕ resonance would make the helicity shape asymmetric with respect to $\cos\theta = 0$.[33] Such an asymmetry is clearly visible in Fig. **V-17**; similar effect is also seen by Belle [40]. These parameters are measured as: $c_1 = 0.156 \pm 0.020$ and $c_0 = 0.024 \pm 0.010$.

The treatment of the σ_L has negligible impact on the fit results; changing its value within its uncertainties from the helicity-edge fit, e.g. by ± 33 MeV/c^2, slightly affects only the very first bin in the $M(D^0)$ projection in Fig. **V-17**. The signal yield is too limited for calibrating the signal shape. Using the π^0 calibration parameters for the $D^0 \to \phi\gamma$ is encouraged by the calibration of the $D^0 \to \bar{K}^{*0}\gamma$. Alternative fits without calibrating the signal, i.e. assuming $s^M_\gamma = s^{\Delta M}_\gamma = 1$ and $\text{off}^M_\gamma = \text{off}^{\Delta M}_\gamma = 0$, or calibrating only the $M(D^0)$ offset by assuming $\text{off}^M_\gamma = \text{off}^M_{\pi^0}$, give results consistent with the default fit.

Par/Comp	Yield	s^M	off^M	$s^{\Delta M}$	$\text{off}^{\Delta M}$	σ_L
γ signal	216 ± 29	1.005	6.9	1.025 ± 0.026	0.050	–
γ; random π_s	0 ± 24			–	–	
π^0 bkgd	1309 ± 57	1.005	6.9	1.025 ± 0.026	0.050	117
π^0; random π_s	319 ± 66			–	–	
η bkgd: $D^0 \to \phi\eta$	188 ± 31	1.0	–	–	–	–
η: $D^0 \to \phi\eta$; rnd π_s	131 ± 47					

Table **V-5**: Parameter values measured for given component in three-dimensional fit to the combined $D^0 \to \phi\gamma$ and $\bar{D}^0 \to \phi\gamma$ candidates from the helicity center in the Run-1 data. Offsets off^M and $\text{off}^{\Delta M}$, and width σ_L are given in MeV/c^2.

[33] In the helicity edge this effect is visible through the different π^0 background yields for $\cos\theta < -0.8$ and $\cos\theta > 0.8$. After combining these regions, $\text{PDF}_{\pi^0}(\cos\theta)$ is not sensitive to this effect.

Par/Comp	Yield	m	α	β	p_1	p_2
Cmb	1307 ± 103	-0.0027 ± 0.0005	0.61 ± 0.09	0.06 ± 0.01	0.05 ± 0.11	0.81 ± 0.42

Table **V-6**: Parameter values measured for combinatorial component in three-dimensional fit to the combined $D^0 \to \phi\gamma$ and $\bar{D}^0 \to \phi\gamma$ candidates from the helicity center in the Run-1 data.

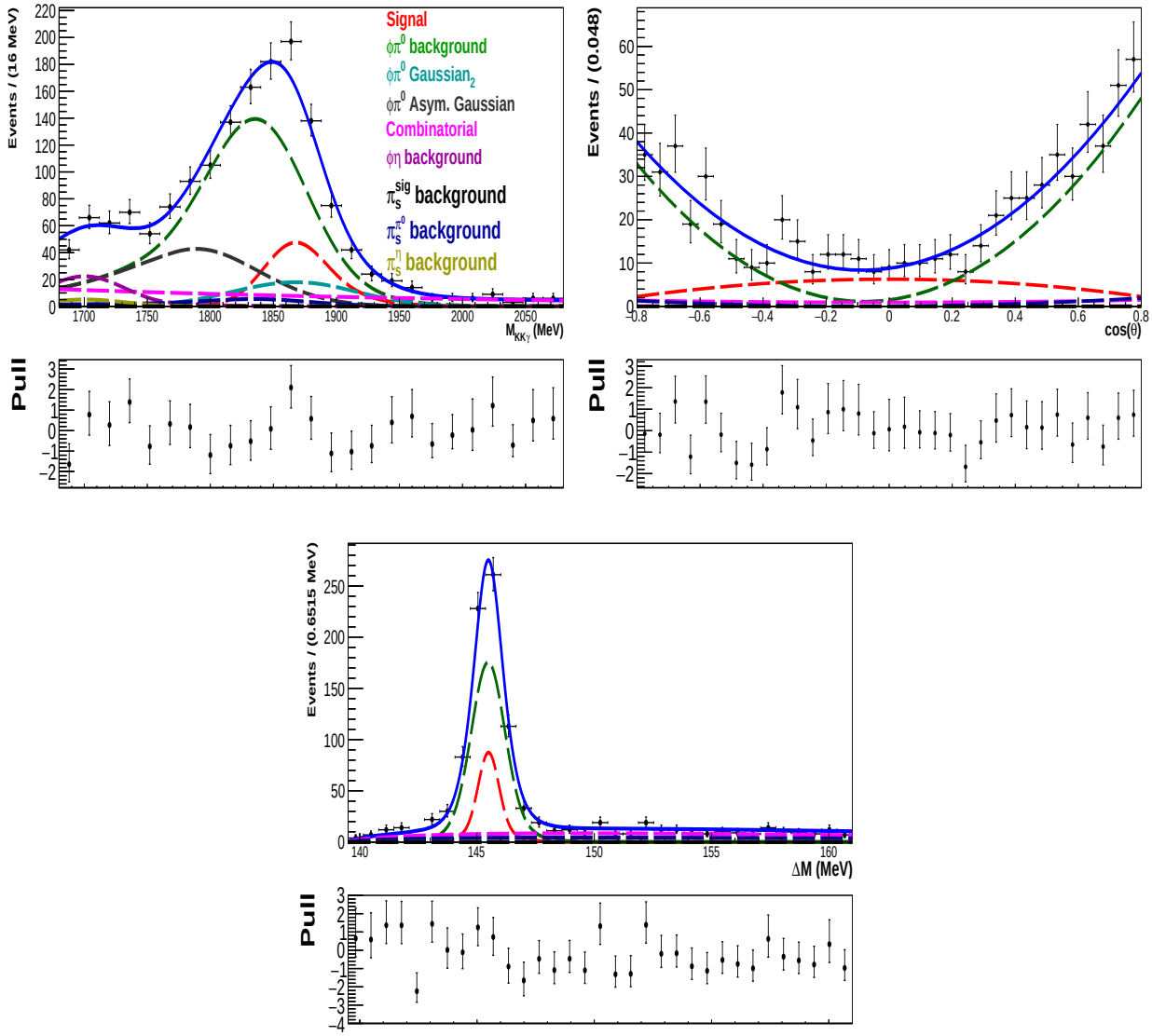

Figure **V-17**: (Top left) $M(D^0)$, (top right) $\cos\theta$ and (bottom) ΔM projections of three-dimensional fit to $D^0 \to \phi\gamma$ candidates, with IsPhoton>0.85, reconstructed in the Run-1 data in the helicity center $|\cos\theta| < 0.8$. These projections are in the signal-enhanced region. Fit components are indicated in the legend.

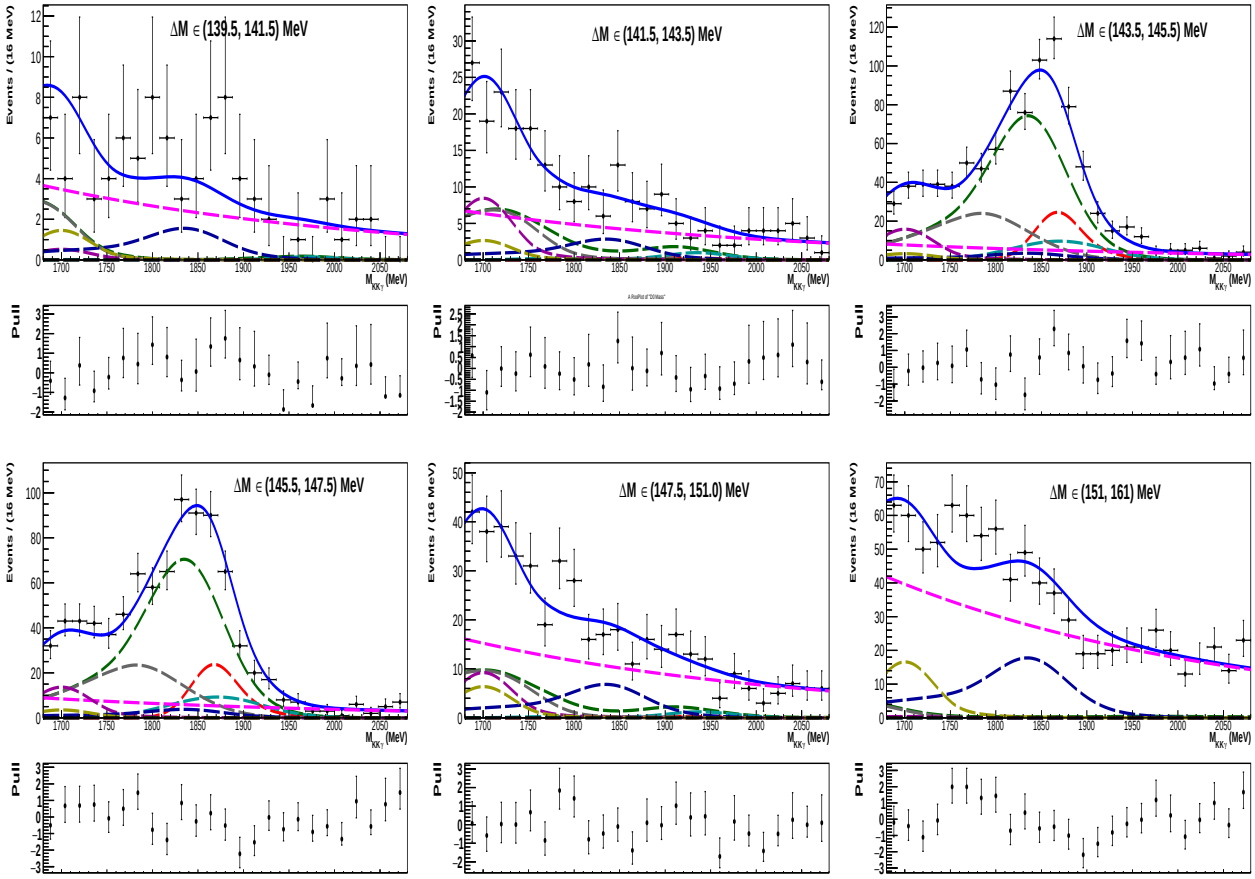

Figure **V-18**: $M(D^0)$ projections of three-dimensional fit to $D^0 \to \phi\gamma$ candidates in the Run-1 data in the helicity center. $M(D^0)$ projections are for ΔM regions indicated in individual plots. Fit components are indicated with the same colours as in Fig. **V-17**.

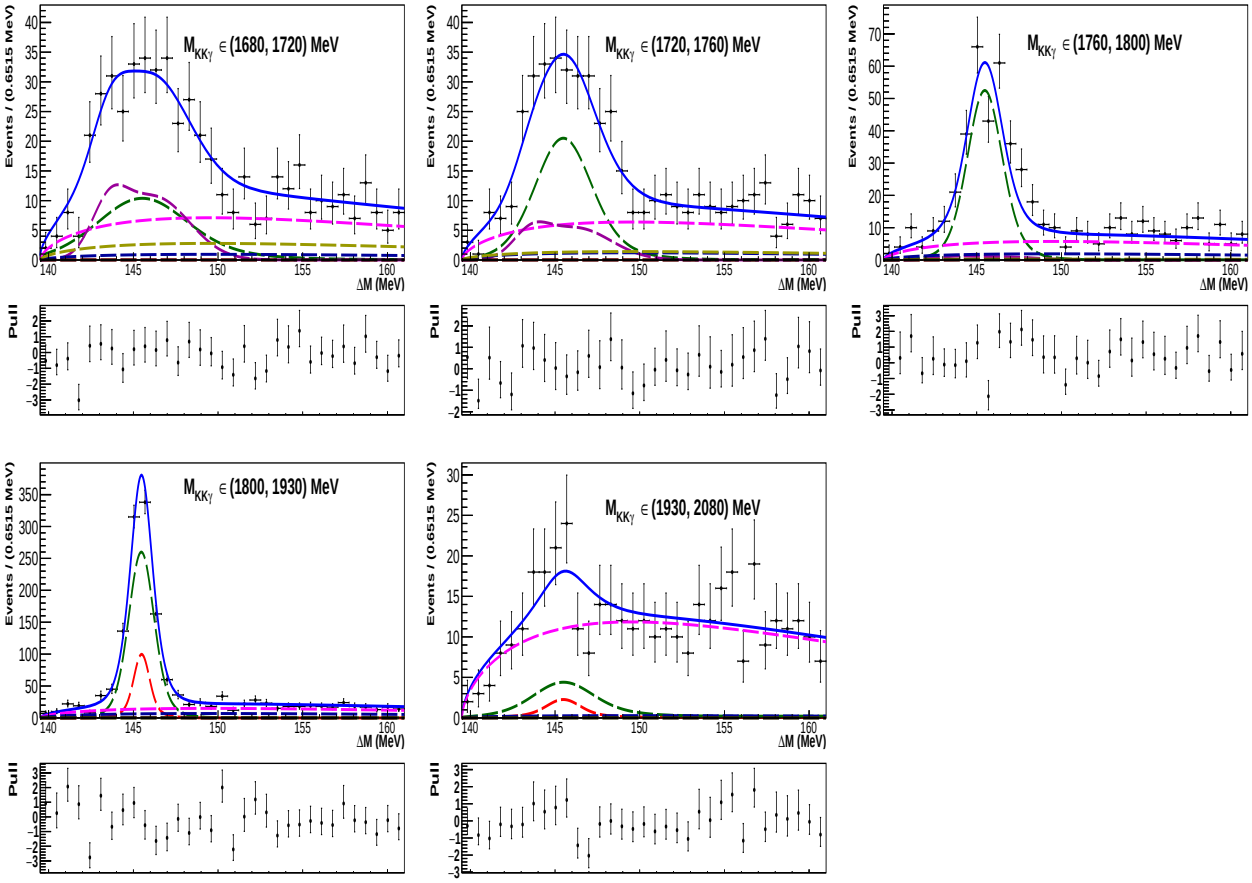

Figure **V-19**: ΔM projections of three-dimensional fit to $D^0 \to \phi\gamma$ candidates in the Run-1 data in the helicity center. ΔM projections are for $M(D^0)$ regions indicated in individual plots. Fit components are indicated with the same colours as in Fig. **V-17**.

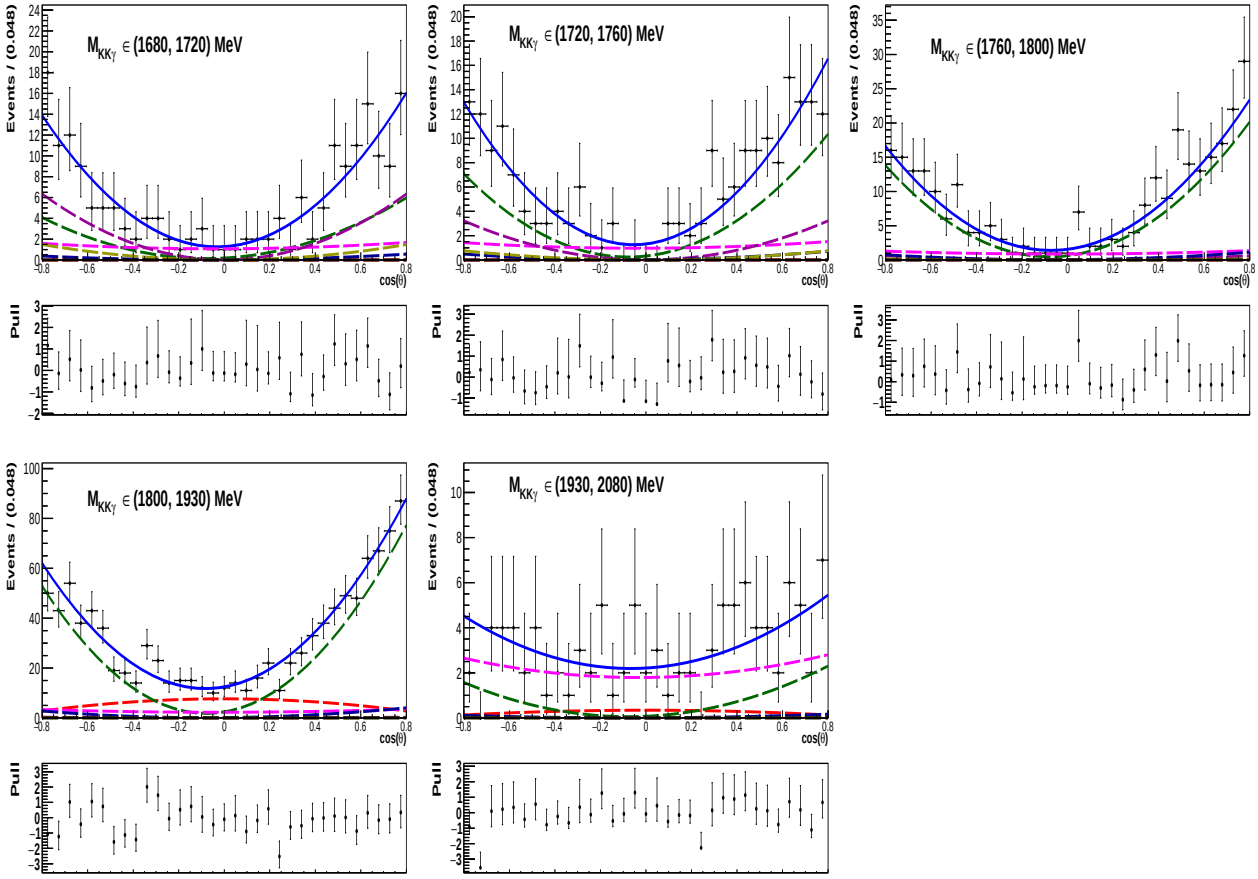

Figure **V-20**: $\cos\theta$ projections of three-dimensional fit to $D^0 \to \phi\gamma$ candidates in the Run-1 data in the helicity center. Projections of $\cos\theta$ are for $M(D^0)$ regions indicated in individual plots, and in the ΔM signal region. Fit components are indicated with the same colours as in Fig. **V-17**.

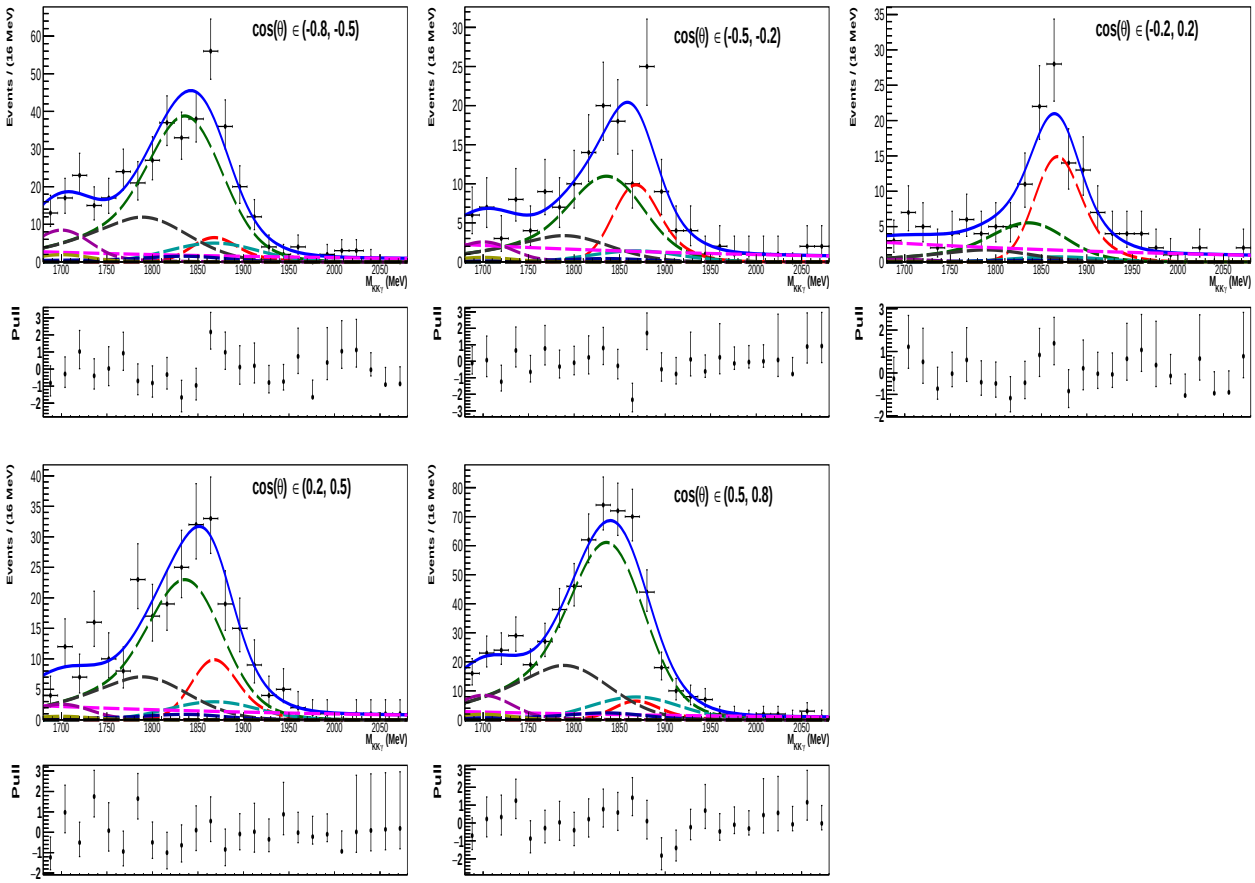

Figure **V-21**: $M(D^0)$ projections of three-dimensional fit to $D^0 \to \phi\gamma$ candidates in the Run-1 data in the helicity center. $M(D^0)$ projections are for $\cos\theta$ regions indicated in individual plots, and in the ΔM signal region. Fit components are indicated with the same colours as in Fig. **V-17**.

V.5 Three-dimensional fit to $D^0 \to \rho^0\gamma$ sample

The PDFs and strategy of the fit to $D^0 \to \rho^0\gamma$ sample are similar to these of the $D^0 \to \bar{K}^{*0}\gamma$ sample described in Section **V.3**. The η background considered in the helicity-edge region, $\cos\theta > 0.7$, originates from $D^0 \to \rho^0\eta$ decays, while in the helicity-center region, $-0.6 < \cos\theta < 0.5$, also contributions from $D^0 \to a_0(980)^+\pi^-$ and $D^0 \to \pi^+\pi^-\eta$ decays are included (Section **IV.11.3**).

V.5.1 Fit to $D^0 \to \rho^0\gamma$ in helicity-edge region

The three-dimensional fit is performed to $D^0 \to \rho^0\gamma$ candidates with IsPhoton>0.95 and reconstructed in the helicity-edge region, $\cos\theta > 0.7$. Projections of this fit on the $M(D^0)$, ΔM and $\cos\theta$ observables are shown in Fig. **V-22** for the Run-1 data. These projections are made in the full fit region. Figure **V-23** shows $M(D^0)$ projections in ΔM regions, Fig. **V-24** presents ΔM projections in $M(D^0)$ regions, whereas Fig. **V-25** $\cos\theta$ projections in $M(D^0)$ regions.

Shape parameters of PDF_γ, PDF_{π^0} and PDF_η (Eqs. **V.1** and **V.4**) are fixed to their values from the corresponding simulation samples (Sections **IV.11**, **IV.12** and **IV.13**). An exception is σ_L in the $\text{PDF}_{\pi^0}(M)$ (Eq. **IV.2**), which is Gaussian-constrained to the simulation-based value.

The fit parameters for the signal, π^0 and η components, and the corresponding random soft-pion components are summarised in Table **V-7**. Yields of the signal component and the associated random soft-pion background have been fixed to zero, as their contributions to the fit are found negligible. Parameters of the combinatorial PDFs (Eq. **V.3**) are given in Table **V-8**.

Par/Comp	Yield	s^M	off^M	$s^{\Delta M}$	$\text{off}^{\Delta M}$	σ_L
γ signal	0	1.0	0.0	1.0	0.0	–
γ; random π_s	0			–	–	
π^0 bkgd	3085 ± 79	0.976 ± 0.034	14.4 ± 1.5	1.072 ± 0.022	0.033 ± 0.019	108 ± 34
π^0; random π_s	510 ± 124			–	–	
η bkgd: $D^0 \to \rho^0\eta$	189 ± 47	0.976	–	–	–	–
η: $D^0 \to \rho^0\eta$; rnd π_s	56 ± 95					

Table **V-7**: Parameter values measured for given component in three-dimensional fit to the combined $D^0 \to \rho^0\gamma$ and $\bar{D}^0 \to \rho^0\gamma$ candidates from the helicity edge in the Run-1 data. Offsets off^M and $\text{off}^{\Delta M}$, and width σ_L are given in MeV/c^2.

Par/Comp	Yield	m	α	β	p_1	p_2
Cmb	1132 ± 222	-0.003 ± 0.001	0.77 ± 0.10	0.07 ± 0.01	-2.17 ± 0.08	1.26 ± 0.07

Table **V-8**: Parameter values measured for combinatorial component in three-dimensional fit to the combined $D^0 \to \rho^0\gamma$ and $\bar{D}^0 \to \rho^0\gamma$ candidates from the helicity edge in the Run-1 data.

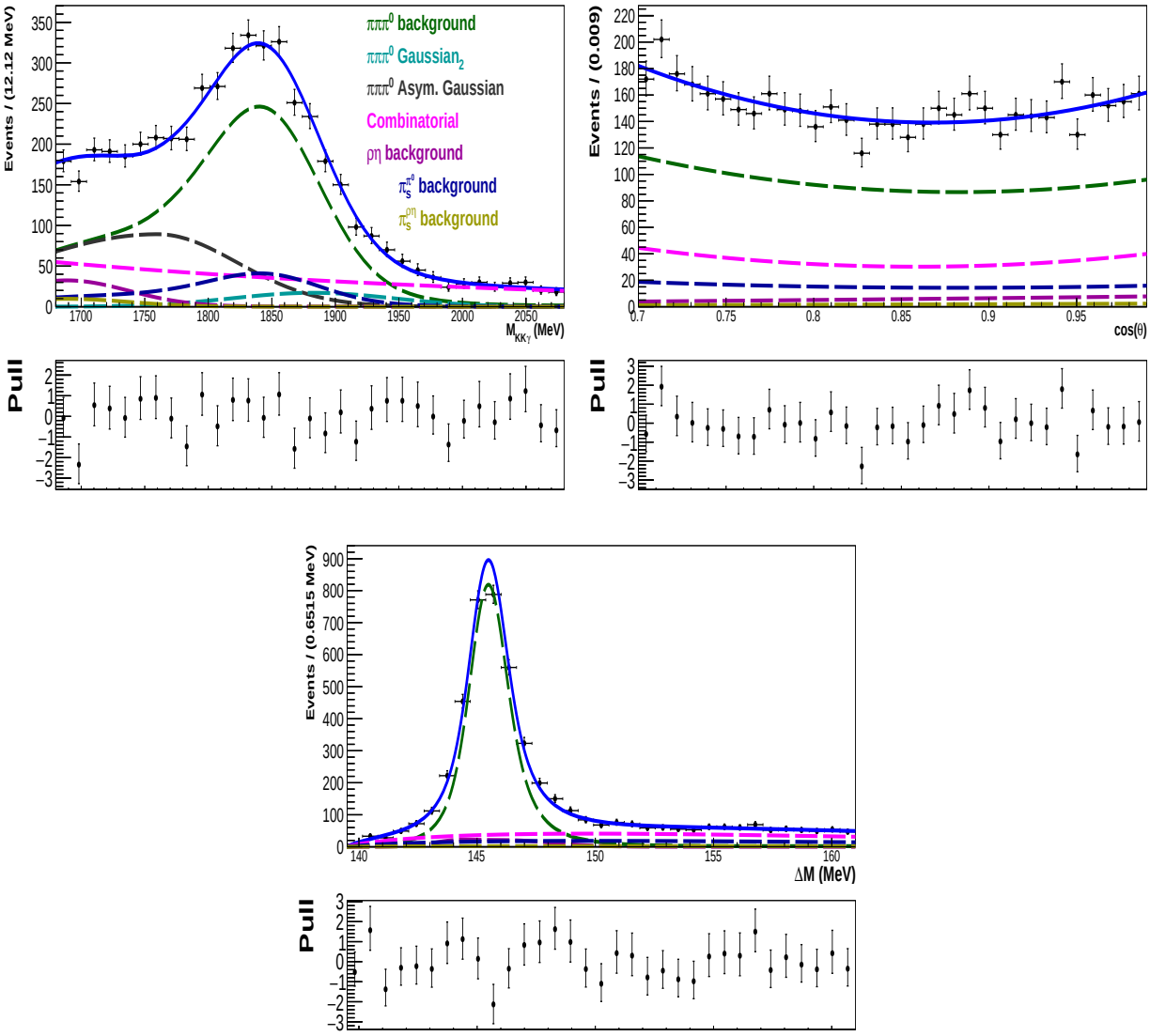

Figure **V-22**: (Top left) $M(D^0)$, (top right) $\cos\theta$ and (bottom) ΔM projections of three-dimensional fit to $D^0 \to \rho^0\gamma$ candidates, with IsPhoton>0.95, reconstructed in the Run-1 data in the helicity-edge region, $\cos\theta > 0.7$. These projections are in the full fit region. Fit components are indicated in the legend.

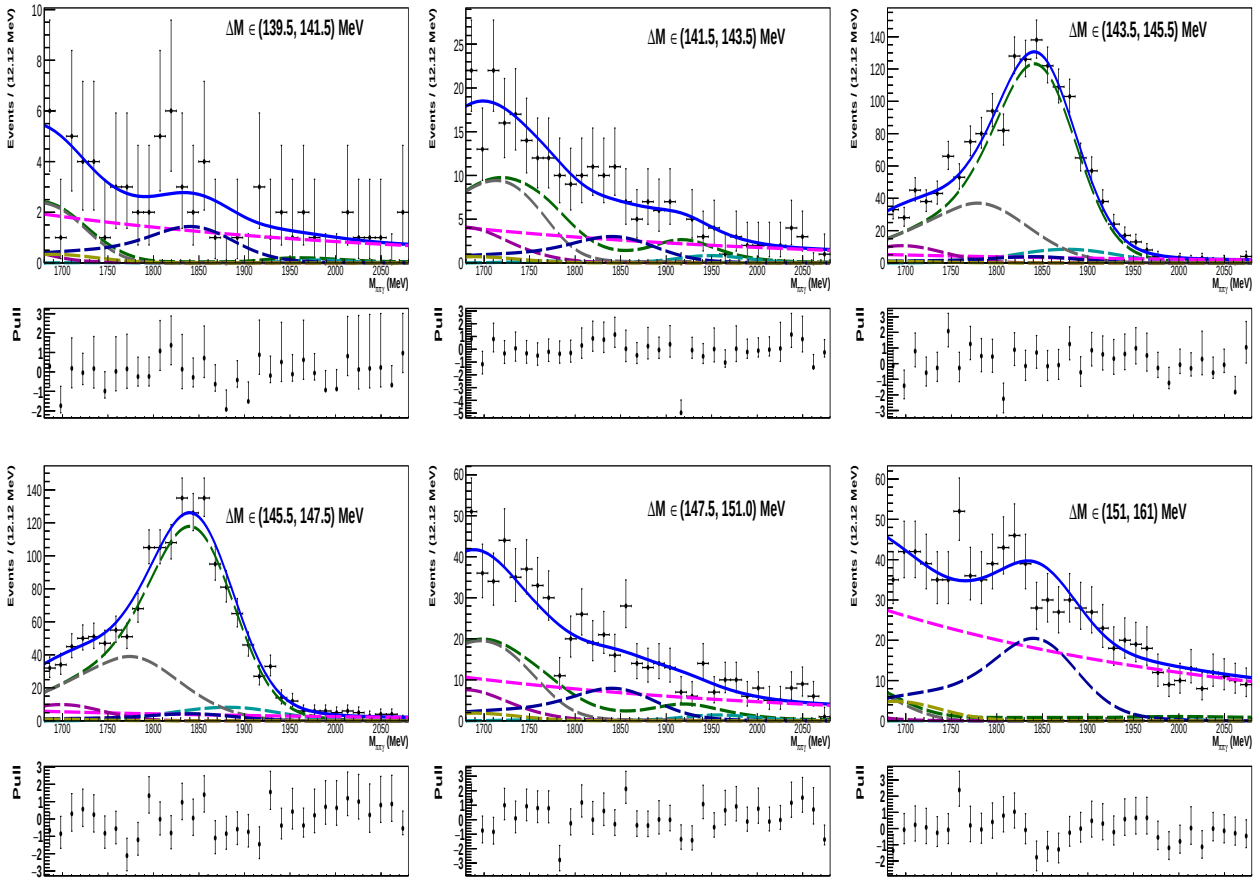

Figure **V-23**: $M(D^0)$ projections of three-dimensional fit to $D^0 \to \rho^0\gamma$ candidates in the Run-1 data in the helicity edge. $M(D^0)$ projections are for ΔM regions indicated in individual plots. Fit components are indicated with the same colours as in Fig. **V-13**.

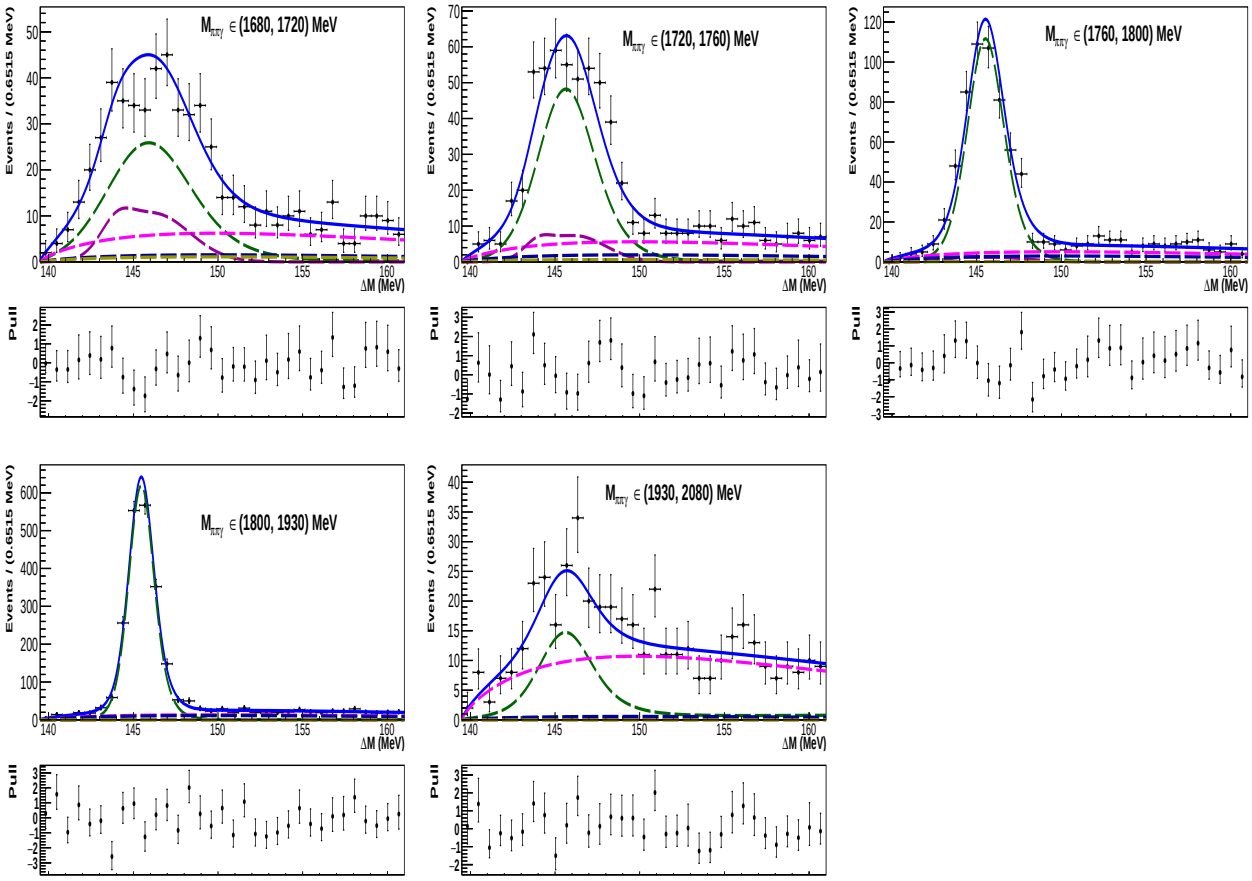

Figure **V-24**: ΔM projections of three-dimensional fit to $D^0 \to \rho^0\gamma$ candidates in the Run-1 data in the helicity edge. ΔM projections are for $M(D^0)$ regions indicated in individual plots. Fit components are indicated with the same colours as in Fig. **V-22**.

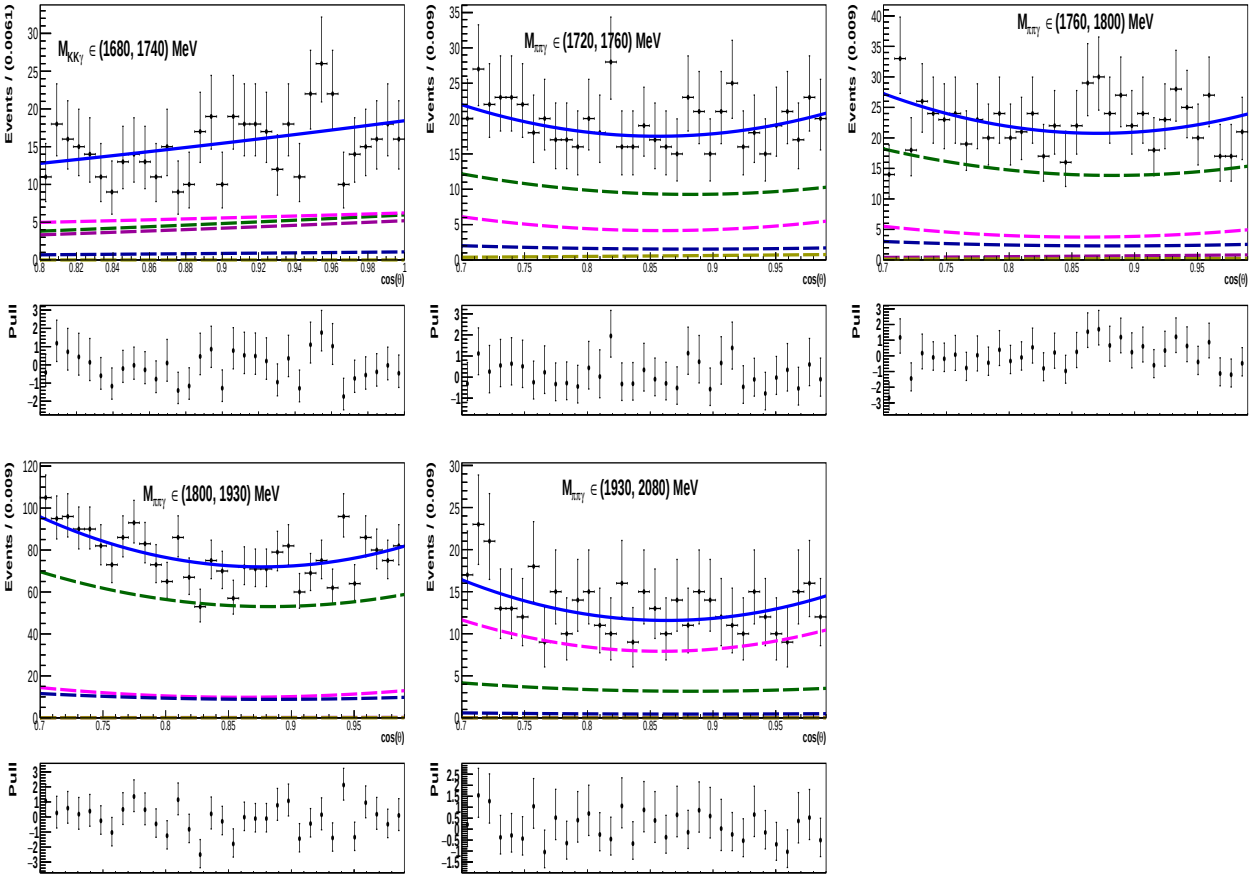

Figure **V-25**: $\cos\theta$ projections of three-dimensional fit to $D^0 \to \rho^0\gamma$ candidates in the Run-1 data in the helicity edge. Projections of $\cos\theta$ are for $M(D^0)$ regions indicated in individual plots, and in the full ΔM region. Fit components are indicated with the same colours as in Fig. **V-22**.

V.5.2 Fit to $D^0 \to \rho^0\gamma$ in central helicity region

The three-dimensional fit is performed to $D^0 \to \rho^0\gamma$ candidates with IsPhoton>0.95 and reconstructed in the helicity-center region, $-0.6 < \cos\theta < 0.5$. Projections of this fit on the $M(D^0)$, ΔM and $\cos\theta$ observables are shown in Fig. **V-26** for the Run-1 data. The projections are made in the signal-enhanced region: the $M(D^0)$ distribution is shown for $143.6 < \Delta M < 147.7$ MeV/c^2, the ΔM for $1802 < M(D^0) < 1921$ MeV/c^2, whereas the $\cos\theta$ for both $M(D^0)$ and ΔM selected in above regions. Figure **V-27** shows $M(D^0)$ projections in ΔM regions, Fig. **V-28** presents ΔM projections in $M(D^0)$ regions, Fig. **V-29** $\cos\theta$ projections in $M(D^0)$ regions, whereas Fig. **V-30** $M(D^0)$ projections in $\cos\theta$ regions.

The fit parameters for the signal, π^0 and η components, and the corresponding random soft-pion components are summarised in Table **V-9**, whereas parameters of the combinatorial PDFs (Eq. **V.3**) are given in Table **V-10**. In this fit, $\text{off}^M_{\pi^0}$, $s^M_{\pi^0}$, $\text{off}^{\Delta M}_{\pi^0}$ and σ_L for the π^0 background and s^M_η for the η background are fixed to the values measured in the helicity edge, whereas $s^{\Delta M}_{\pi^0}$ is Gaussian-constrained to the helicity-edge value. For the signal component, off^M_γ, s^M_γ, $\text{off}^{\Delta M}_\gamma$ and $s^{\Delta M}_\gamma$ are shared with the ones for the π^0 background. Other parameters of PDF_γ, PDF_{π^0} and PDF_η (Eqs. **V.1** and **V.4**) are fixed to their values from the corresponding simulation samples (Sections **IV.11**, **IV.12** and **IV.13**). No significant $D^0 \to \rho^0\gamma$ signal is found.

Par/Comp	Yield	s^M	off^M	$s^{\Delta M}$	$\text{off}^{\Delta M}$	σ_L
γ signal	0 ± 19	0.976	14.4	1.074 ± 0.015	0.033	–
γ; random π_s	0			–	–	–
π^0 bkgd	1392 ± 53	0.976	14.4	1.074 ± 0.015	0.033	108
π^0; random π_s	445 ± 85			–	–	
η bkgd: $D^0 \to \rho^0\eta$	109 ± 45	0.976	–	–	–	–
η: $D^0 \to \rho^0\eta$; rnd π_s	0 ± 7					
η bkgd: $D^0 \to \pi^+\pi^-\eta$	231 ± 53					
η: $D^0 \to \pi^+\pi^-\eta$; rnd π_s	0 ± 5					
η bkgd: $D^0 \to a_0(980)^+\pi^-$	15 ± 22					
η: $D^0 \to a_0(980)^+\pi^-$; rnd π_s	0					

Table **V-9**: Parameter values measured for given component in three-dimensional fit to the combined $D^0 \to \rho^0\gamma$ and $\bar{D}^0 \to \rho^0\gamma$ candidates from the helicity center in the Run-1 data. Offsets off^M and $\text{off}^{\Delta M}$, and width σ_L are given in MeV/c^2.

Par/Comp	Yield	m	α	β	p_1	p_2
Cmb	4156 ± 117	-0.0035 ± 0.0002	0.67 ± 0.06	0.06 ± 0.01	-0.30 ± 0.07	0.51 ± 0.26

Table **V-10**: Parameter values measured for combinatorial component in three-dimensional fit to the combined $D^0 \to \rho^0\gamma$ and $\bar{D}^0 \to \rho^0\gamma$ candidates from the helicity center in the Run-1 data.

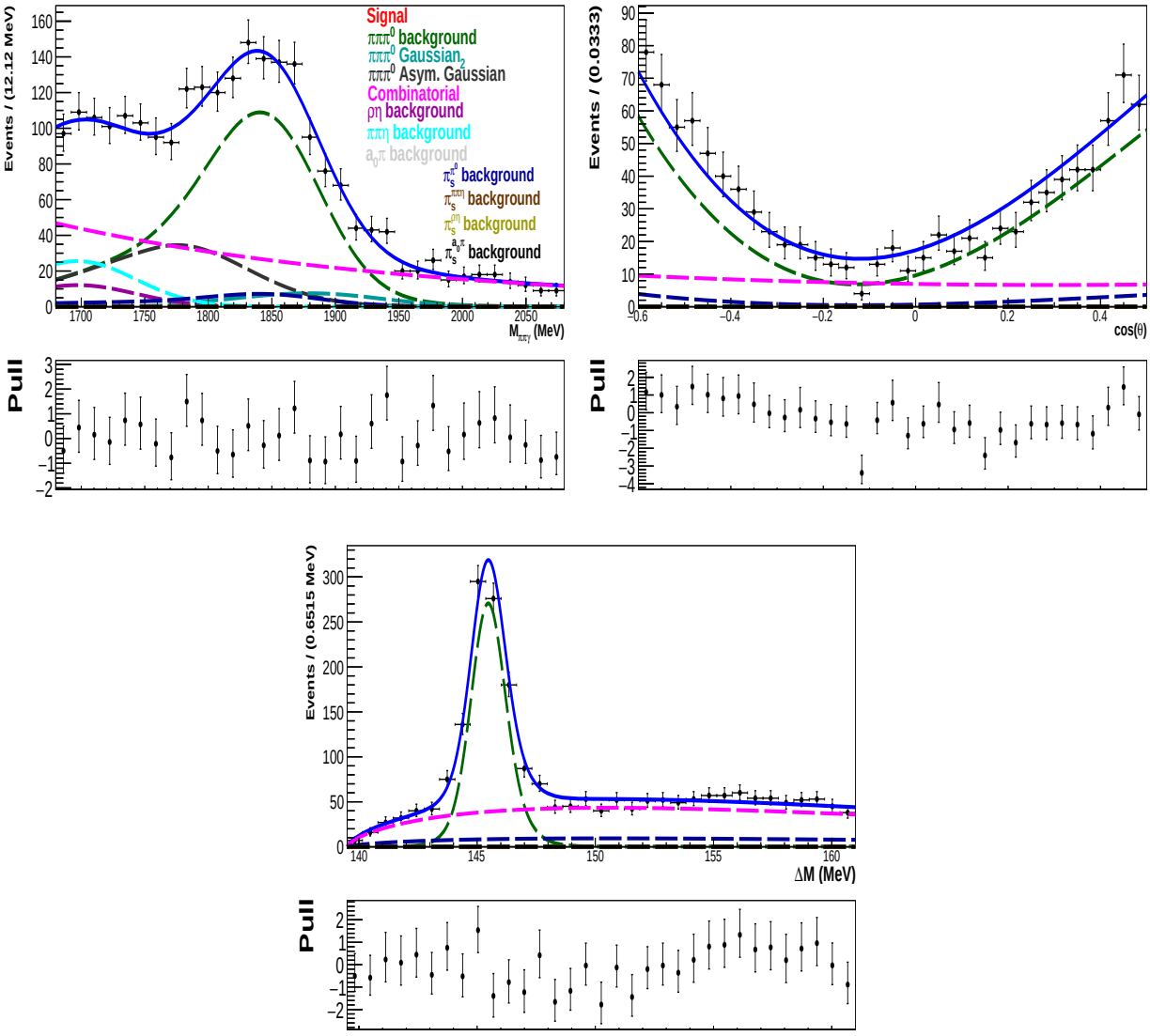

Figure **V-26**: (Top left) $M(D^0)$, (top right) $\cos\theta$ and (bottom) ΔM projections of three-dimensional fit to $D^0 \to \rho^0\gamma$ candidates, with IsPhoton> 0.95, reconstructed in the Run-1 data in the helicity center $-0.6 < \cos\theta < 0.5$. These projections are in the signal-enhanced region. Fit components are indicated in the legend.

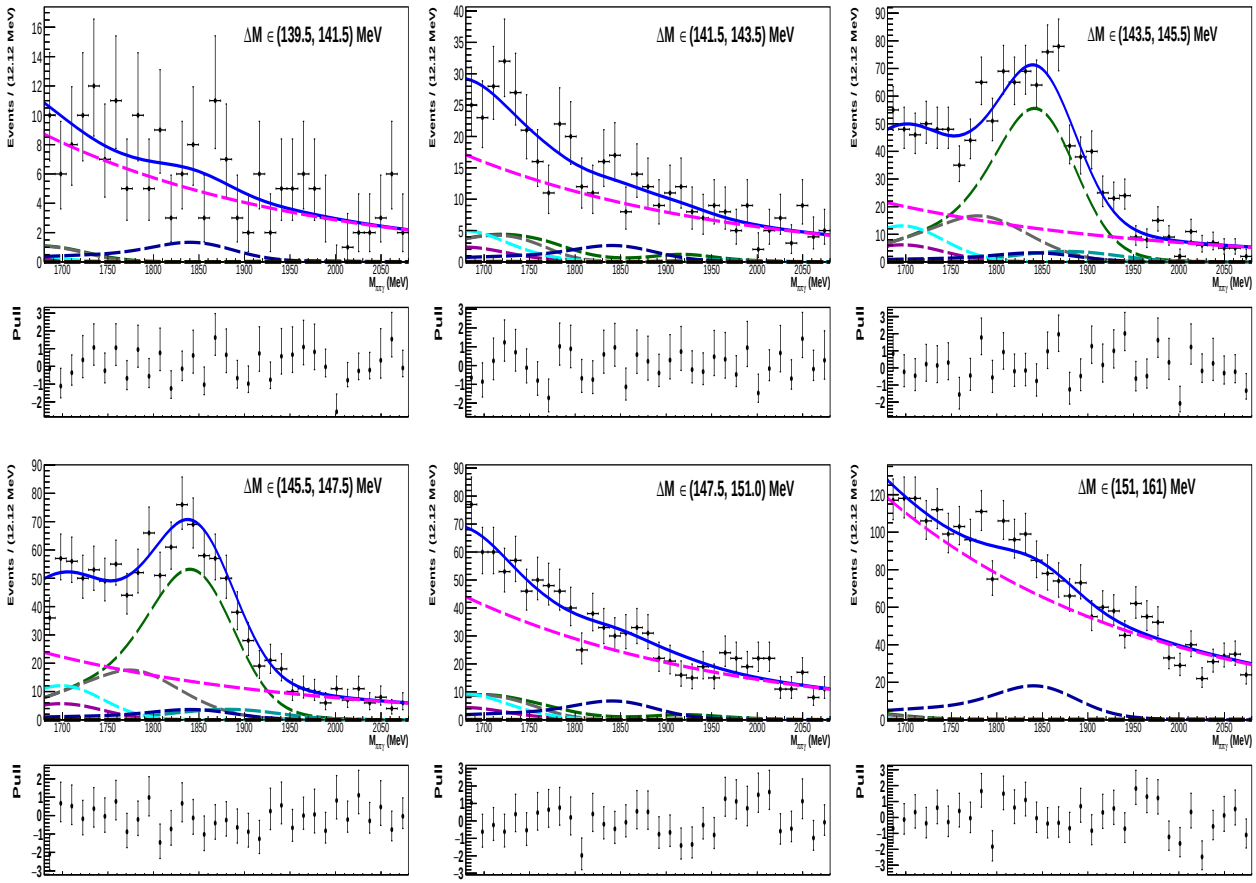

Figure **V-27**: $M(D^0)$ projections of three-dimensional fit to $D^0 \to \rho^0\gamma$ candidates in the Run-1 data in the helicity center. $M(D^0)$ projections are for ΔM regions indicated in individual plots. Fit components are indicated with the same colours as in Fig. **V-26**.

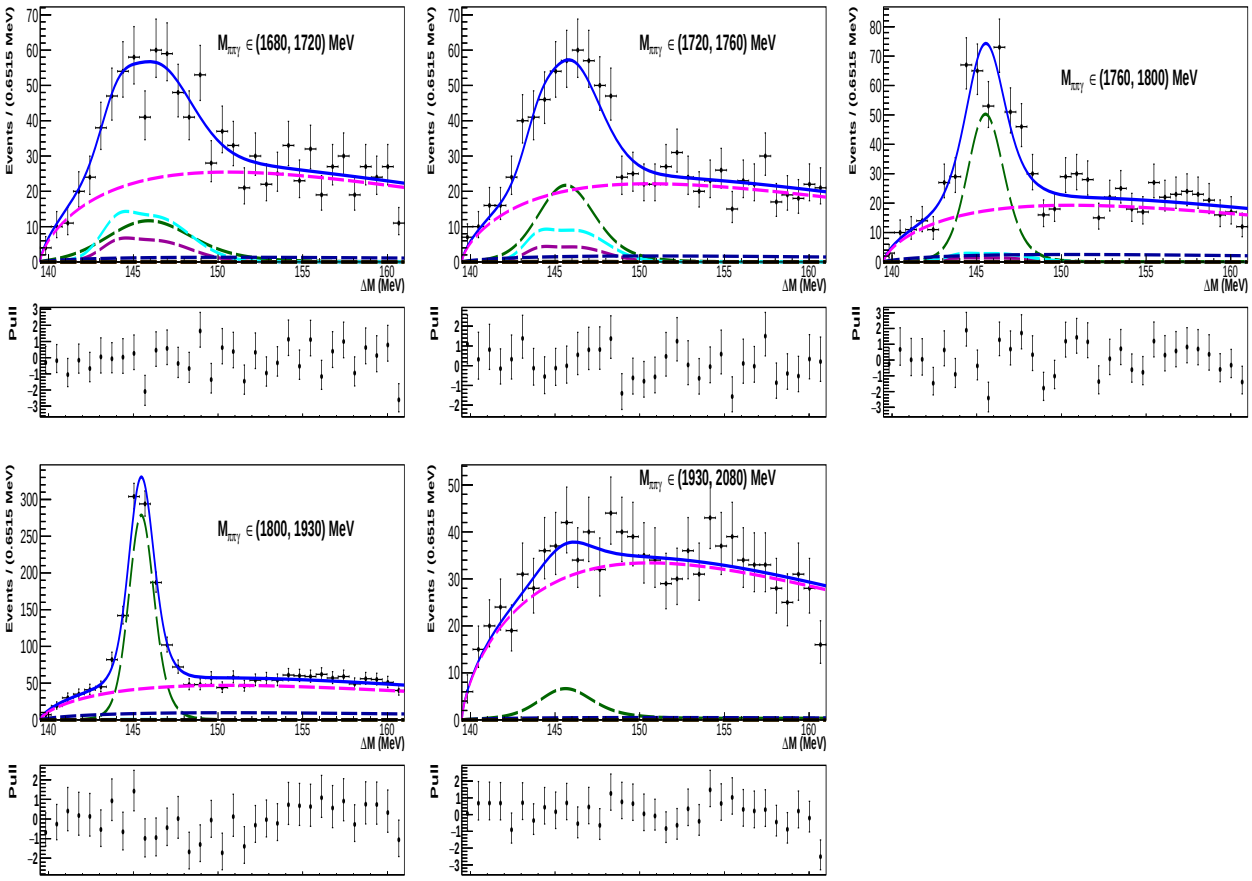

Figure **V-28**: ΔM projections of three-dimensional fit to $D^0 \to \rho^0\gamma$ candidates in the Run-1 data in the helicity center. ΔM projections are for $M(D^0)$ regions indicated in individual plots. Fit components are indicated with the same colours as in Fig. **V-26**.

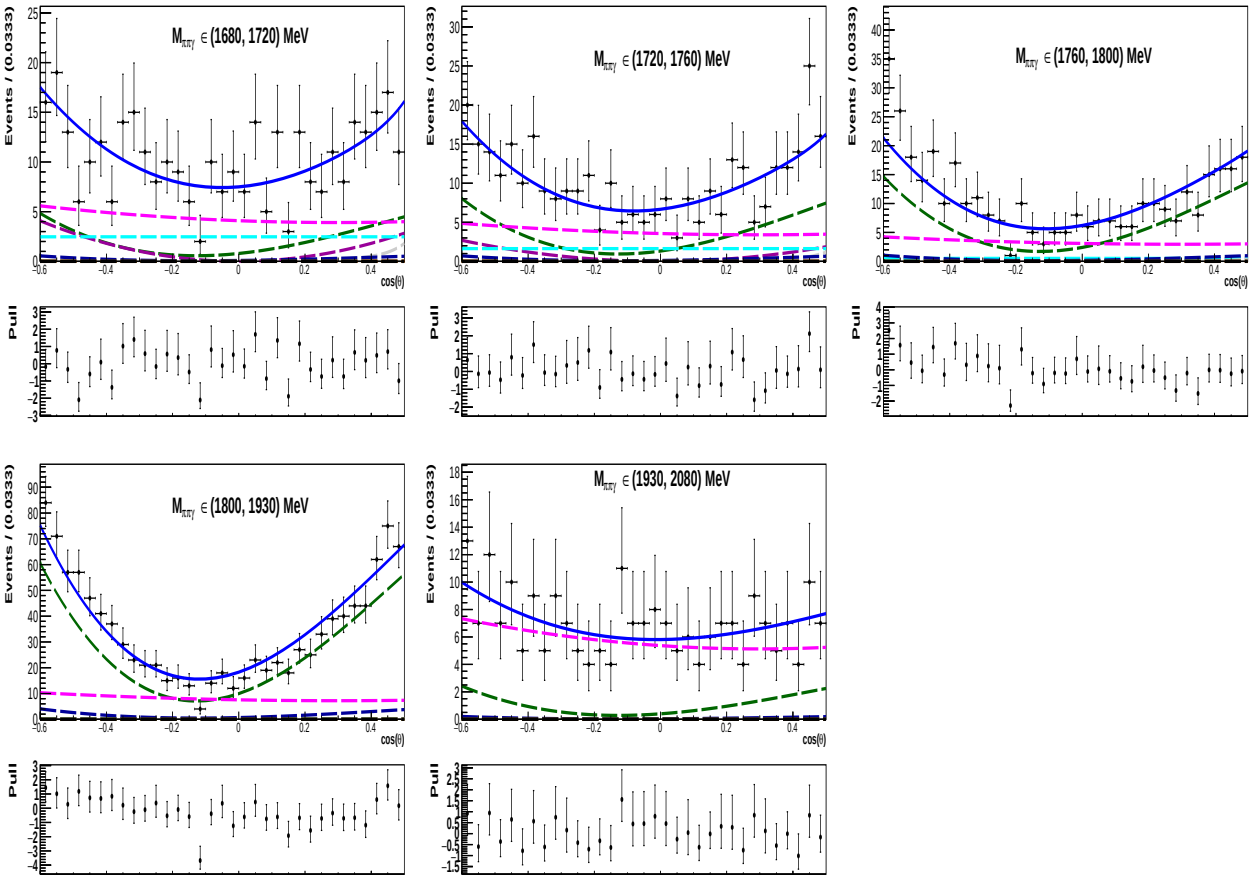

Figure **V-29**: $\cos\theta$ projections of three-dimensional fit to $D^0 \to \rho^0\gamma$ candidates in the Run-1 data in the helicity center. Projections of $\cos\theta$ are for $M(D^0)$ regions indicated in individual plots, and in the ΔM signal region. Fit components are indicated with the same colours as in Fig. **V-26**.

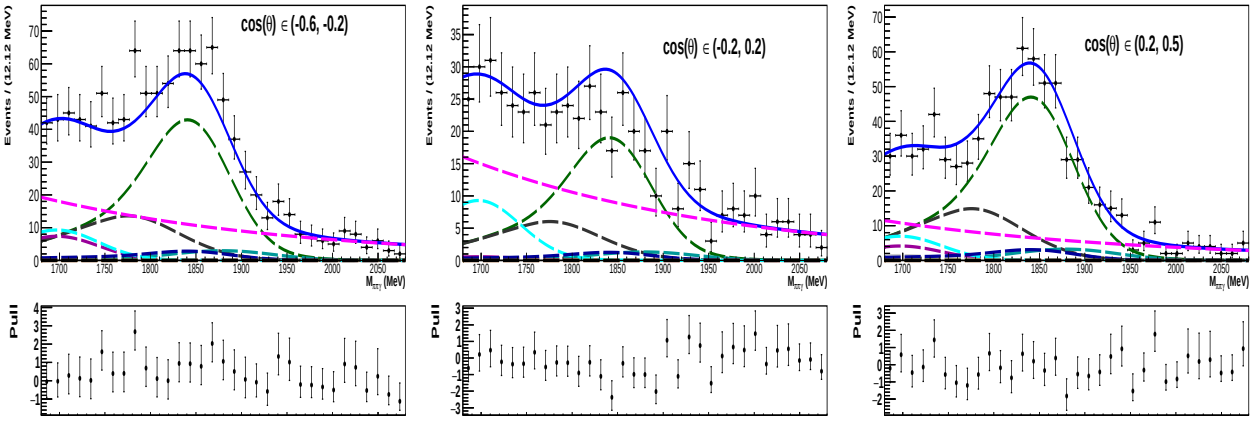

Figure **V-30**: $M(D^0)$ projections of three-dimensional fit to $D^0 \to \rho^0\gamma$ candidates in the Run-1 data in the helicity center. $M(D^0)$ projections are for $\cos\theta$ regions indicated in individual plots, and in the ΔM signal region. Fit components are indicated with the same colours as in Fig. **V-26**.

Chapter VI

Raw asymmetries for signal decays

VI.1 Method for measuring raw asymmetry

The goal of the analysis is measuring CP asymmetry through A_{CP} introduced in Eq. **I.9**. For a given decay of the neutral D meson, A_{CP} is the asymmetry between the decay widths of D^0 and $\bar{D}^0$. The first step is to measure *raw* asymmetry, A_{raw}, between yields of D^0 and $\bar{D}^0$ decays:

$$A_{raw} = \frac{N(D^0) - N(\bar{D}^0)}{N(D^0) + N(\bar{D}^0)}. \qquad \textbf{(VI.1)}$$

Here, $N(D^0)$ and $N(\bar{D}^0)$ denote number of given signal decays tagged with the soft-pion charge as D^0 and $\bar{D}^0$, respectively. These yields are measured through performing the three-dimensional fit in $M(D^0)$ vs. ΔM vs. $\cos\theta$ space (Sections **V.3**, **V.4** and **V.5**) to the signal samples split by the D meson flavour. To avoid possible biases related to the signal and background shapes, π_s^+-tagged sample and π_s^--tagged sample are fitted simultaneously rather than independently, with most of PDF parameters shared between the two samples. In this approach the fit becomes more stable, especially for the samples having signal and/or background components contributing with small yields. In addition, such a simultaneous method allows to incorporate A_{raw} as the fit parameter explicitly.

VI.2 Simultaneous fit to $D^0 \to \bar{K}^{*0}\gamma$ and $\bar{D}^0 \to K^{*0}\gamma$ samples

VI.2.1 Fit in helicity-edge region

The three-dimensional fit is performed simultaneously to $D^0 \to \bar{K}^{*0}\gamma$ and $\bar{D}^0 \to K^{*0}\gamma$ candidates with IsPhoton>0.86, and reconstructed in the helicity-edge region, $-0.97 < \cos\theta < -0.7$. The goal of this fit is to check for possible differences between the background shapes, in particular in the ΔM, for the two D flavours, as well as to measure A_{raw} for the background components. Projections of this fit on the $M(D^0)$, ΔM and $\cos\theta$ observables, separately for the two D flavours, are shown in Fig. **VI-1** for the Run-1 data. These projections are made in the full fit region.

Components included in this fit, as well as their PDFs are the same as in the fit performed for the combined D^0 and $\bar{D}^0$ samples (Section **V.3.1**). The calibration parameters: $\text{off}_{\pi^0}^M$, $s_{\pi^0}^M$ and σ_L for the π^0 background, and s_η^M for the η background, are fixed to those from the helicity-edge fit for the combined sample (Table **V-1**), whereas $\text{off}_{\pi^0}^{\Delta M}$ and $s_{\pi^0}^{\Delta M}$ are kept free and independent between the two D flavours. Remaining parameters of PDF_γ, PDF_{π^0} and PDF_η (Eqs. **V.1** and **V.4**) are fixed to their values from the corresponding simulation samples (Sections **IV.5**, **IV.6** and **IV.7**). Within combinatorial PDFs (Eq. **V.3**), parameters of the $\text{PDF}_{\text{cmb}}(M)$ and PDF_{cmb} are kept free and shared between the two samples, those in the $\text{PDF}_{\text{cmb}}(\Delta M)$ are free and independent for the two samples, to account for possible differences in background arising from random π_s^+ and π_s^-. Alternative fits, with

fully independent combinatorial PDFs give the corresponding parameters consistent in the two samples. In terms of shapes, the data distributions in Fig. **VI-1** are very similar between the two D flavours.

Raw asymmetries measured for the fit components are summarised in Table **VI-1**. Components with negligible yields observed in the combined sample (Section **V.3.1**) are not included in the simultaneous fit. These are: the random π_s component associated with the signal, as well as the η background from $D^0 \to \bar{K}_0(1430)^0\eta$ decays and the corresponding random π_s background. In order to assure blinding of the signal asymmetry, A_{raw} is injected for the signal component by assigning a number generated according to the Gaussian distribution with the mean at zero and the width of 5%.[34] As the signal yield is small, A_{raw} for the signal component is fixed in the fit. Instead, it is checked that the injected signal asymmetry does not affect fit results for the remaining fit components. This is done by running the fit multiple times with different A_{raw} values generated.

No component in Table **VI-1** exhibits significant asymmetry. A_{raw} for the π^0 background has the significance of 2.3σ, but this is not unexpected given that nuisance asymmetries are increased for this charge-asymmetric final state (Section **VII.1**). For the π^0 calibration, the fit gives $s_{\pi^0}^{\Delta M} = 1.069 \pm 0.012$ and $\mathrm{off}_{\pi^0}^{\Delta M} = 0.043 \pm 0.009$ for the D^0 sample, and $s_{\pi^0}^{\Delta M} = 1.076 \pm 0.011$ and $\mathrm{off}_{\pi^0}^{\Delta M} = 0.036 \pm 0.012$ for the $\bar{D}^0$ sample.

Par/Comp	A_{raw} [%]	$N(D^0) + N(\bar{D}^0)$
γ signal	+6.8 (injected)	320 ± 85
γ; random π_s	0	0
π^0 bkgd	-1.6 ± 0.7	25712 ± 210
π^0; random π_s	$+2.2 \pm 3.2$	3015 ± 99
η bkgd: $D^0 \to \bar{K}^{*0}\eta$	-2.1 ± 2.7	3978 ± 111
η: $D^0 \to \bar{K}^{*0}\eta$; random π_s	-10 ± 12	503 ± 58
η bkgd: $D^0 \to \bar{K}_0(1430)^0\eta$	0	0
η: $D^0 \to \bar{K}_0(1430)^0\eta$; random π_s	0	0
Combinatorial	-16 ± 10	570 ± 58

Table **VI-1**: Raw asymmetry and total D^0 and $\bar{D}^0$ yield measured for given component in three-dimensional fit performed simultaneously to $D^0 \to \bar{K}^{*0}\gamma$ and $\bar{D}^0 \to K^{*0}\gamma$ candidates from the helicity edge in the Run-1 data. A_{raw} for the signal is fixed to injected value.

VI.2.2 Fit in helicity-center region

The three-dimensional fit is performed simultaneously to $D^0 \to \bar{K}^{*0}\gamma$ and $\bar{D}^0 \to K^{*0}\gamma$ candidates with IsPhoton> 0.86, and reconstructed in the helicity-center region, $-0.4 < \cos\theta < 0.7$. Projections of this fit on the $M(D^0)$ and ΔM observables, separately for the two D flavours, are shown in Fig. **VI-2** for the Run-1 data. These projections are made in the signal-enhanced region: the $M(D^0)$ distribution is shown for $144 < \Delta M < 147$ MeV/c^2, the ΔM for $1810 < M(D^0) < 1920$ MeV/c^2. No $\cos\theta$ projection is presented, as the $M(D^0)$–ΔM signal window is currently blinded.[35] Pull distributions, revealed in the full $M(D^0)$ and ΔM ranges, show the good fit quality.

The fit strategy is the same as for the helicity-edge region (Section **VI.2.1**). Components included in this fit, as well as their PDFs are the same as in the fit performed for the combined D^0 and $\bar{D}^0$

[34] It is the expected statistical sensitivity of CP asymmetry for the $D^0 \to \bar{K}^{*0}\gamma$ signal in the helicity center.

[35] Unblinding will be done together with the Run-2 based measurement once it is finalised.

samples (Section **V.3.2**). The calibration parameters: $\text{off}^M_{\pi^0}$, $s^M_{\pi^0}$ and σ_L for the π^0 background, and s^M_η for the η background, are fixed to those from the helicity-center fit for the combined sample (Table **V-2**), whereas $\text{off}^{\Delta M}_{\pi^0}$ and $s^{\Delta M}_{\pi^0}$ are fixed to the values measured in the simultaneous helicity-edge fit (Section **VI.3.1**). The calibration parameters for the signal are fixed to those in the combined sample (Table **V-2**), except for $s^{\Delta M}_\gamma$ being Gaussian-constrained to the combined-fit value and independent for the two D flavours.[36] Remaining parameters of PDF_γ, PDF_{π^0} and PDF_η (Eqs. **V.1** and **V.4**) are fixed to their values from the corresponding simulation samples (Sections **IV.5**, **IV.6** and **IV.7**). Within combinatorial PDFs (Eq. **V.3**), parameters of the $\text{PDF}_{\text{cmb}}(M)$ and PDF_{cmb} are kept free and shared between the two samples, those in the $\text{PDF}_{\text{cmb}}(\Delta M)$ are free and independent for the two samples.

Raw asymmetries measured for the fit components are summarised in Table **VI-2**. For the components with negligible yields, A_{raw} is fixed to zero in the fit. The central value of the A_{raw} for the signal is blinded, whereas its uncertainty of 5.1% corresponds to the statistical sensitivity of for the CP asymmetry for the $D^0 \to \bar{K}^{*0}\gamma$ channel. No significant asymmetry is observed for the remaining components.

Par/Comp	A_{raw} [%]	$N(D^0) + N(\bar{D}^0)$
γ signal	$xx \pm 5.1$	3268 ± 183
γ; random π_s	-9 ± 27	170 ± 91
π^0 bkgd	-1.7 ± 0.7	43132 ± 320
π^0; random π_s	-0.3 ± 4.4	3924 ± 226
η bkgd: $D^0 \to \bar{K}^{*0}\eta$	-2 ± 5	2483 ± 140
η: $D^0 \to \bar{K}^{*0}\eta$; random π_s	-30 ± 40	171 ± 91
η bkgd: $D^0 \to \bar{K}_0(1430)^0\eta$	$+1 \pm 5$	3577 ± 192
η: $D^0 \to \bar{K}_0(1430)^0\eta$; random π_s	0	0
η bkgd: $D^0 \to K^- a_0(980)^+$	0	141 ± 95
η: $D^0 \to K^- a_0(980)^+$; random π_s	0	0
Combinatorial	-1.4 ± 2.6	6296 ± 245

Table **VI-2**: Raw asymmetry and total D^0 and $\bar{D}^0$ yield measured for given component in three-dimensional fit performed simultaneously to $D^0 \to \bar{K}^{*0}\gamma$ and $\bar{D}^0 \to K^{*0}\gamma$ candidates from the helicity center in the Run-1 data. Central value of A_{raw} for the signal is currently blinded.

[36] The fit gives $s^{\Delta M}_\gamma = 0.95 \pm 0.01$ for both D^0 and $\bar{D}^0$ samples.

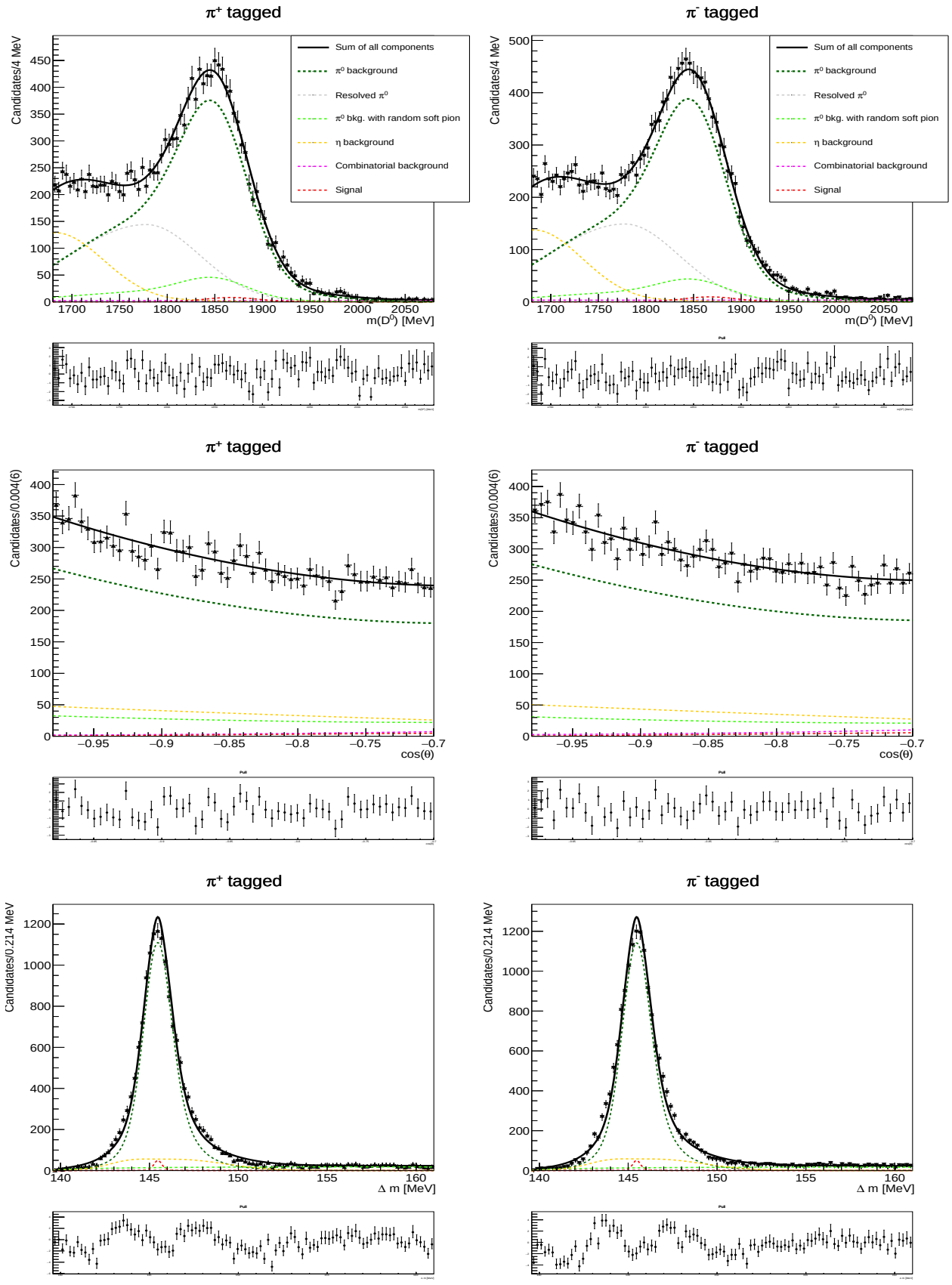

Figure **VI-1**: (Top) $M(D^0)$, (middle) $\cos\theta$ and (bottom) ΔM projections of three-dimensional fit performed simultaneously to (left) $D^0 \to \bar{K}^{*0}\gamma$ and (right) $\bar{D}^0 \to K^{*0}\gamma$ candidates reconstructed in the Run-1 data in the helicity-edge region. These projections are in the full fit region. Fit components are indicated in the legend.

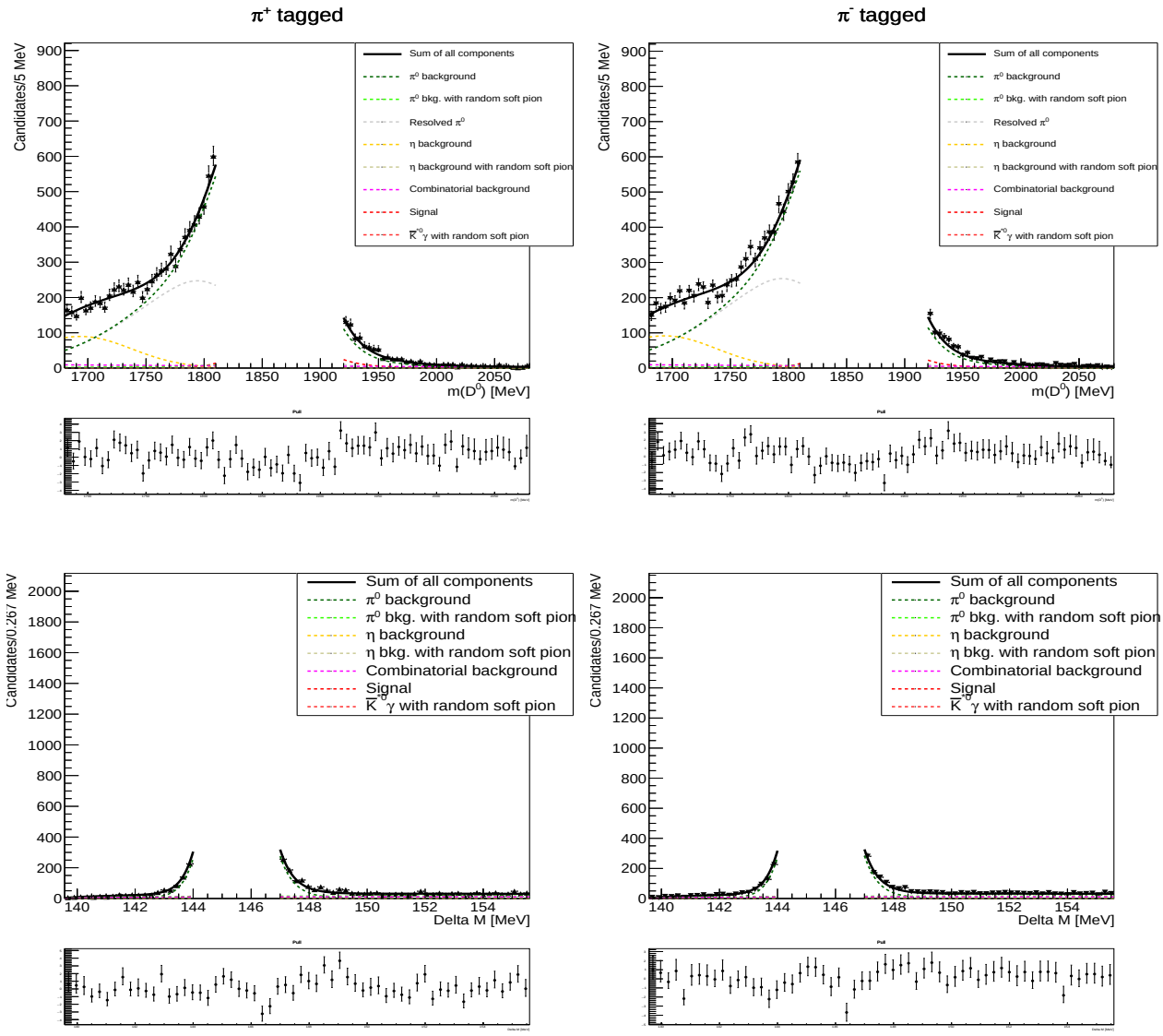

Figure **VI-2**: (Top) $M(D^0)$ and (bottom) ΔM projections of three-dimensional fit performed simultaneously to (left) $D^0 \to \bar{K}^{*0}\gamma$ and (right) $\bar{D}^0 \to K^{*0}\gamma$ candidates reconstructed in the Run-1 data in the helicity-center region. These projections are in the signal-enhanced region, and the signal region is currently blinded. Fit components are indicated in the legend.

VI.3 Simultaneous fit to $D^0 \to \phi\gamma$ and $\bar{D}^0 \to \phi\gamma$ samples

VI.3.1 Fit in helicity-edge region

The three-dimensional fit is performed simultaneously to $D^0 \to \phi\gamma$ and $\bar{D}^0 \to \phi\gamma$ candidates with IsPhoton>0.85, and reconstructed in the helicity-edge region, $|\cos\theta| > 0.8$. Projections of this fit on the $M(D^0)$, ΔM and $\cos\theta$ observables, separately for the two D flavours, are shown in Fig. **VI-3** for the Run-1 data. These projections are made in the full fit region.

Components included in this fit, as well as their PDFs are the same as in the fit performed for the combined D^0 and $\bar{D}^0$ samples (Section **V.4.1**). The calibration parameters: $\text{off}^M_{\pi^0}$, $s^M_{\pi^0}$, $\text{off}^{\Delta M}_{\pi^0}$ and σ_L for the π^0 background, and s^M_η for the η background, are fixed to those from the helicity-edge fit for the combined sample (Table **V-3**), whereas $s^{\Delta M}_{\pi^0}$ is Gaussian-constrained to the helicity-edge value and shared between the two D flavours.[37] Remaining parameters of PDF_{π^0} and PDF_η (Eqs. **V.1** and **V.4**) are fixed to their values from the corresponding simulation samples (Sections **IV.8**, **IV.9** and **IV.10**). As there is no signal observed in the combined sample (Section **V.4.1**), the signal component and the associated random π_s component are not included in the fit. Within combinatorial PDFs (Eq. **V.3**), parameters of the $\text{PDF}_{\text{cmb}}(M)$ and PDF_{cmb} are kept free and shared between the two samples, those in the $\text{PDF}_{\text{cmb}}(\Delta M)$ are free and independent for the two samples.

Alternative fits, with independent $s^{\Delta M}_{\pi^0}$ or fully independent combinatorial PDFs give the corresponding parameters being very similar for the two samples. Indeed, in terms of shapes, the data distributions in Fig. **VI-3** are very consistent between the two D flavours. Raw asymmetries measured for the fit components are summarised in Table **VI-3**. For the components with negligible yields, A_{raw} is fixed to zero in the fit. No component exhibits significant asymmetry.

Par/Comp	A_{raw} [%]	$N(D^0)$
γ signal	0	0
γ; random π_s	0	0
π^0 bkgd	-3.0 ± 3.6	572 ± 30
π^0; random π_s	-36 ± 22	67 ± 31
η bkgd: $D^0 \to \phi\eta$	-7 ± 15	79 ± 19
η: $D^0 \to \phi\eta$; random π_s	0	0 ± 13
Combinatorial	$+8.4 \pm 8.3$	343 ± 40

Table **VI-3**: Raw asymmetry and D^0 yield measured for given component in three-dimensional fit performed simultaneously to $D^0 \to \phi\gamma$ and $\bar{D}^0 \to \phi\gamma$ candidates from the helicity edge in the Run-1 data.

VI.3.2 Fit in helicity-center region

The three-dimensional fit is performed simultaneously to $D^0 \to \phi\gamma$ and $\bar{D}^0 \to \phi\gamma$ candidates with IsPhoton>0.85, and reconstructed in the helicity-center region, $|\cos\theta| < 0.8$. Projections of this fit on the $M(D^0)$ and ΔM observables, separately for the two D flavours, are shown in Fig. **VI-4** for the Run-1 data. These projections are made in the signal-enhanced region: the $M(D^0)$ distribution is shown for $144 < \Delta M < 147$ MeV/c^2, the ΔM for $1827 < M(D^0) < 1902$ MeV/c^2. No $\cos\theta$ projection

[37] The fit gives $s^{\Delta M}_{\pi^0} = 1.046 \pm 0.026$.

is presented, as the $M(D^0)$–ΔM signal window is currently blinded.[38] Pull distributions, revealed in the full $M(D^0)$ and ΔM ranges, show the good fit quality.

The fit strategy is the same as for the helicity-edge region (Section **VI.3.1**). Components included in this fit, as well as their PDFs are the same as in the fit performed for the combined D^0 and $\bar{D}^0$ samples (Section **V.4.2**). The calibration parameters: $\text{off}_{\pi^0}^{M}$, $s_{\pi^0}^{M}$, $\text{off}_{\pi^0}^{\Delta M}$ and σ_L for the π^0 background, and s_{η}^{M} for the η background, are fixed to those from the helicity-center fit for the combined sample (Table **V-5**), whereas $s_{\pi^0}^{\Delta M}$ is Gaussian-constrained to the helicity-center value and shared between the two D flavours.[39] The calibration parameters for the signal are shared with those for the π^0 background. Remaining parameters of PDF_{γ}, PDF_{π^0} and PDF_{η} (Eqs. **V.1** and **V.4**) are fixed to their values from the corresponding simulation samples (Sections **IV.8**, **IV.9** and **IV.10**). Within combinatorial PDFs (Eq. **V.3**), parameters of the $\text{PDF}_{\text{cmb}}(M)$ and PDF_{cmb} are kept free and shared between the two samples, those in the $\text{PDF}_{\text{cmb}}(\Delta M)$ are free and independent for the two samples.

Raw asymmetries measured for the fit components are summarised in Table **VI-4**. The central value of the A_{raw} for the signal is blinded, whereas its uncertainty of 12% corresponds to the statistical sensitivity of for the CP asymmetry for the $D^0 \to \phi\gamma$ channel. No significant asymmetry is observed for the remaining components.

Par/Comp	A_{raw} [%]	$N(D^0)$
γ signal	$xx \pm 12$	106 ± 18
γ; random π_s	0	11 ± 18
π^0 bkgd	$+1.6 \pm 3.9$	663 ± 37
π^0; random π_s	-1 ± 15	154 ± 42
η bkgd: $D^0 \to \phi\eta$	$+13 \pm 17$	105 ± 23
η: $D^0 \to \phi\eta$; random π_s	$+19 \pm 25$	77 ± 30
Combinatorial	$+4.3 \pm 4.5$	684 ± 59

Table **VI-4**: Raw asymmetry and D^0 yield measured for given component in three-dimensional fit performed simultaneously to $D^0 \to \phi\gamma$ and $\bar{D}^0 \to \phi\gamma$ candidates from the helicity center in the Run-1 data. Central value of A_{raw} for the signal is currently blinded.

[38] Unblinding will be done together with the Run-2 based measurement once it is finalised.
[39] The fit gives $s_{\pi^0}^{\Delta M} = s_{\gamma}^{\Delta M} = 1.012 \pm 0.021$.

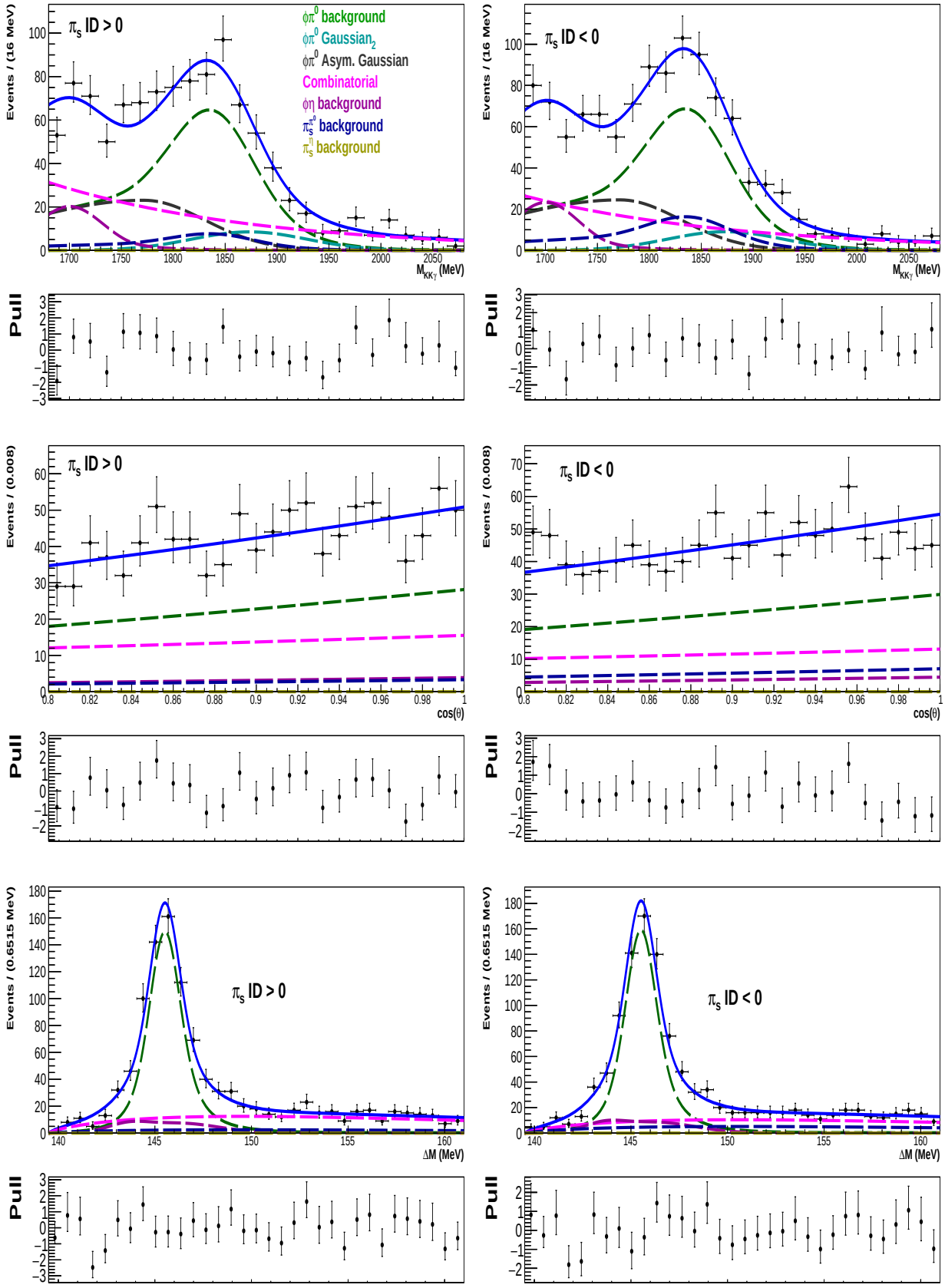

Figure **VI-3**: (Top) $M(D^0)$, (middle) $\cos\theta$ and (bottom) ΔM projections of three-dimensional fit performed simultaneously to (left) $D^0 \to \phi\gamma$ and (right) $\bar{D}^0 \to \phi\gamma$ candidates reconstructed in the Run-1 data in the helicity-edge region. These projections are in the full fit region. Fit components are indicated in the legend.

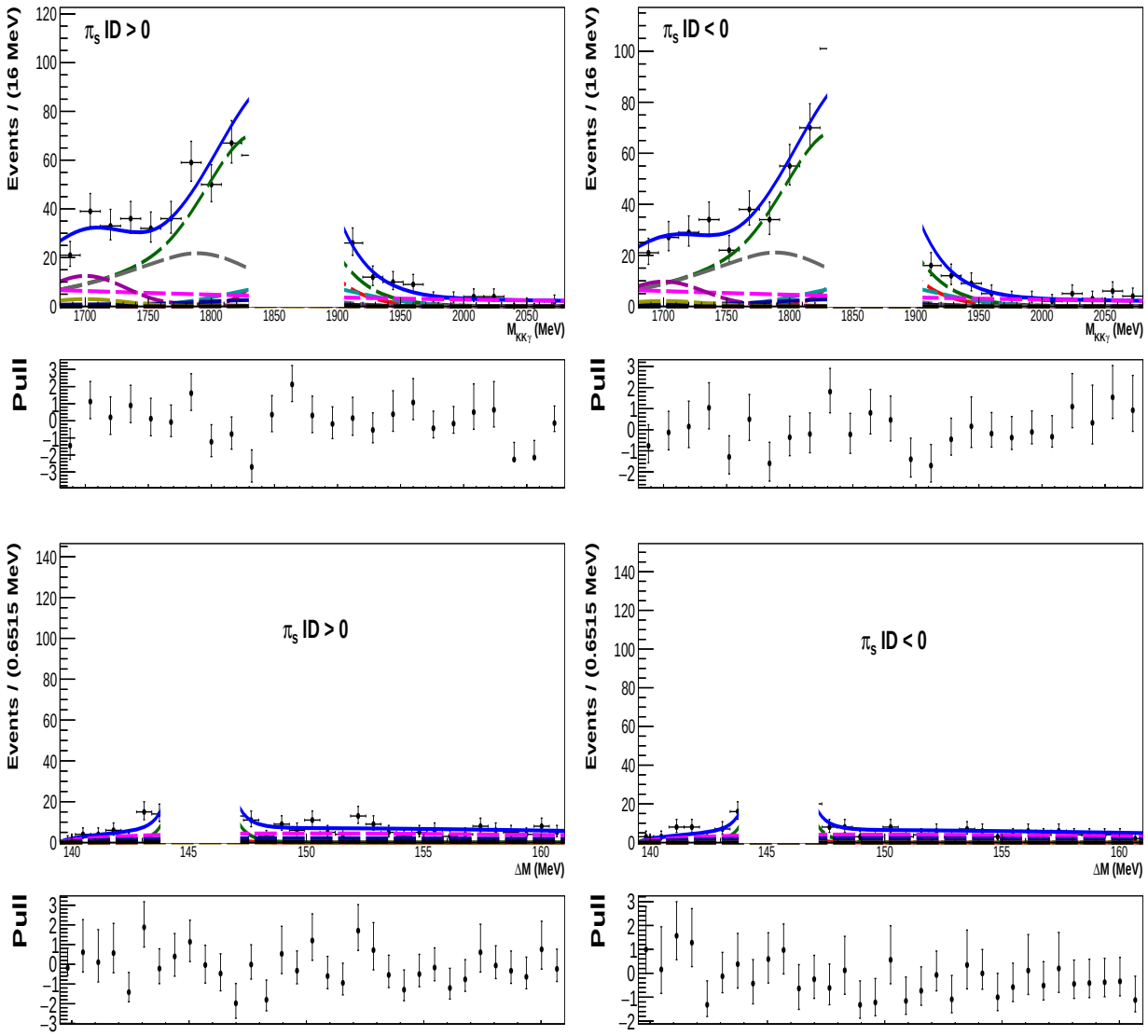

Figure **VI-4**: (Top) $M(D^0)$ and (bottom) ΔM projections of three-dimensional fit performed simultaneously to (left) $D^0 \to \phi\gamma$ and (right) $\bar{D}^0 \to \phi\gamma$ candidates reconstructed in the Run-1 data in the helicity-center region. These projections are in the signal-enhanced region, and the signal region is currently blinded. Fit components are indicated with the same colours as in Fig. **VI-3**.

VI.4 Simultaneous fit to $D^0 \to \rho^0\gamma$ and $\bar{D}^0 \to \rho^0\gamma$ samples

VI.4.1 Fit in helicity-edge region

The three-dimensional fit is performed simultaneously to $D^0 \to \rho^0\gamma$ and $\bar{D}^0 \to \rho^0\gamma$ candidates with IsPhoton> 0.95 and reconstructed in the helicity-edge region, $\cos\theta > 0.7$. Projections of this fit on the $M(D^0)$, ΔM and $\cos\theta$ observables, separately for the two D flavours, are shown in Fig. **VI-5** for the Run-1 data. These projections are made in the full fit region.

Components included in this fit, as well as their PDFs are the same as in the fit performed for the combined D^0 and $\bar{D}^0$ samples (Section **V.5.1**). The calibration parameters: $\text{off}^M_{\pi^0}$, $s^M_{\pi^0}$, $\text{off}^{\Delta M}_{\pi^0}$ and σ_L for the π^0 background, and s^M_η for the η background, are fixed to those from the helicity-edge fit for the combined sample (Table **V-7**), whereas $s^{\Delta M}_{\pi^0}$ is Gaussian-constrained to the helicity-edge value and shared between the two D flavours.[40] Remaining parameters of PDF_{π^0} and PDF_η (Eqs. **V.1** and **V.4**) are fixed to their values from the corresponding simulation samples (Sections **IV.11**, **IV.12** and **IV.13**). As there is no signal observed in the combined sample (Section **V.5.1**), the signal component and the associated random π_s component are not included in the fit. Within combinatorial PDFs (Eq. **V.3**), parameters of the $\text{PDF}_{\text{cmb}}(M)$ and PDF_{cmb} are kept free and shared between the two samples, those in the $\text{PDF}_{\text{cmb}}(\Delta M)$ are free and independent for the two samples.

Raw asymmetries measured for the fit components are summarised in Table **VI-5**. For the components with negligible yields, A_{raw} is fixed to zero in the fit. No component exhibits significant asymmetry.

Par/Comp	A_{raw} [%]	$N(D^0)$
γ signal	0	0
γ; random π_s	0	0
π^0 bkgd	-3.0 ± 2.2	1497 ± 47
π^0; random π_s	-10 ± 14	206 ± 45
η bkgd: $D^0 \to \rho^0\eta$	-11 ± 18	85 ± 25
η: $D^0 \to \rho^0\eta$; random π_s	0	0 ± 37
Combinatorial	$+5.0 \pm 6.5$	648 ± 57

Table **VI-5**: Raw asymmetry and D^0 yield measured for given component in three-dimensional fit performed simultaneously to $D^0 \to \rho^0\gamma$ and $\bar{D}^0 \to \rho^0\gamma$ candidates from the helicity edge in the Run-1 data.

VI.4.2 Fit in helicity-center region

The three-dimensional fit is performed simultaneously to $D^0 \to \rho^0\gamma$ and $\bar{D}^0 \to \rho^0\gamma$ candidates with IsPhoton> 0.95, and reconstructed in the helicity-center region, $-0.6 < \cos\theta < 0.5$. Projections of this fit on the $M(D^0)$, ΔM and $\cos\theta$ observables, separately for the two D flavours, are shown in Fig. **VI-6** for the Run-1 data. As no significant signal is observed, the signal region is unblinded and the $\cos\theta$ projection is also presented. These projections are made in the signal-enhanced region: the $M(D^0)$ distribution is shown for $143.6 < \Delta M < 147.7$ MeV/c^2, the ΔM for $1802 < M(D^0) < 1921$ MeV/c^2, whereas the $\cos\theta$ for both $M(D^0)$ and ΔM selected in above regions.

The fit strategy is the same as for the helicity-edge region (Section **VI.4.1**). Components included in this fit, as well as their PDFs are the same as in the fit performed for the combined D^0 and $\bar{D}^0$ samples

[40] The fit gives $s^{\Delta M}_{\pi^0} = 1.073 \pm 0.039$.

(Section **V.5.2**). The calibration parameters: $\text{off}^M_{\pi^0}$, $s^M_{\pi^0}$, $\text{off}^{\Delta M}_{\pi^0}$ and σ_L for the π^0 background, and s^M_η for the η background, are fixed to those from the helicity-center fit for the combined sample (Table **V-9**), whereas $s^{\Delta M}_{\pi^0}$ is Gaussian-constrained to the helicity-center value and shared between the two D flavours.[41] Remaining parameters of PDF_{π^0} and PDF_η (Eqs. **V.1** and **V.4**) are fixed to their values from the corresponding simulation samples (Sections **IV.8**, **IV.9** and **IV.10**). As there is no signal observed in the combined sample (Section **V.5.2**), the signal component and the associated random π_s component are not included in the fit. Within combinatorial PDFs (Eq. **V.3**), parameters of the $\text{PDF}_{\text{cmb}}(M)$ and PDF_{cmb} are kept free and shared between the two samples, those in the $\text{PDF}_{\text{cmb}}(\Delta M)$ are free and independent for the two samples.

Raw asymmetries measured for the fit components are summarised in Table **VI-6**. No component exhibits significant asymmetry.

Par/Comp	A_{raw} [%]	$N(D^0)$
γ signal	0	0
γ; random π_s	0	0
π^0 bkgd	$+1.7 \pm 3.7$	713 ± 38
π^0; random π_s	$+16 \pm 20$	232 ± 61
η bkgd: $D^0 \to \rho^0\eta$	-44 ± 46	25 ± 29
η: $D^0 \to \rho^0\eta$; random π_s	0	7 ± 69
η bkgd: $D^0 \to \pi^+\pi^-\eta$	-48 ± 23	60 ± 34
η: $D^0 \to \pi^+\pi^-\eta$; random π_s	0	0 ± 20
η bkgd: $D^0 \to a_0(980)^+\pi^-$	0	20 ± 19
η: $D^0 \to a_0(980)^+\pi^-$; random π_s	0	12 ± 15
Combinatorial	$+1.4 \pm 3.1$	2115 ± 99

Table **VI-6**: Raw asymmetry and D^0 yield measured for given component in three-dimensional fit performed simultaneously to $D^0 \to \rho^0\gamma$ and $\bar{D}^0 \to \rho^0\gamma$ candidates from the helicity center in the Run-1 data.

[41] The fit gives $s^{\Delta M}_{\pi^0} = 1.075 \pm 0.017$.

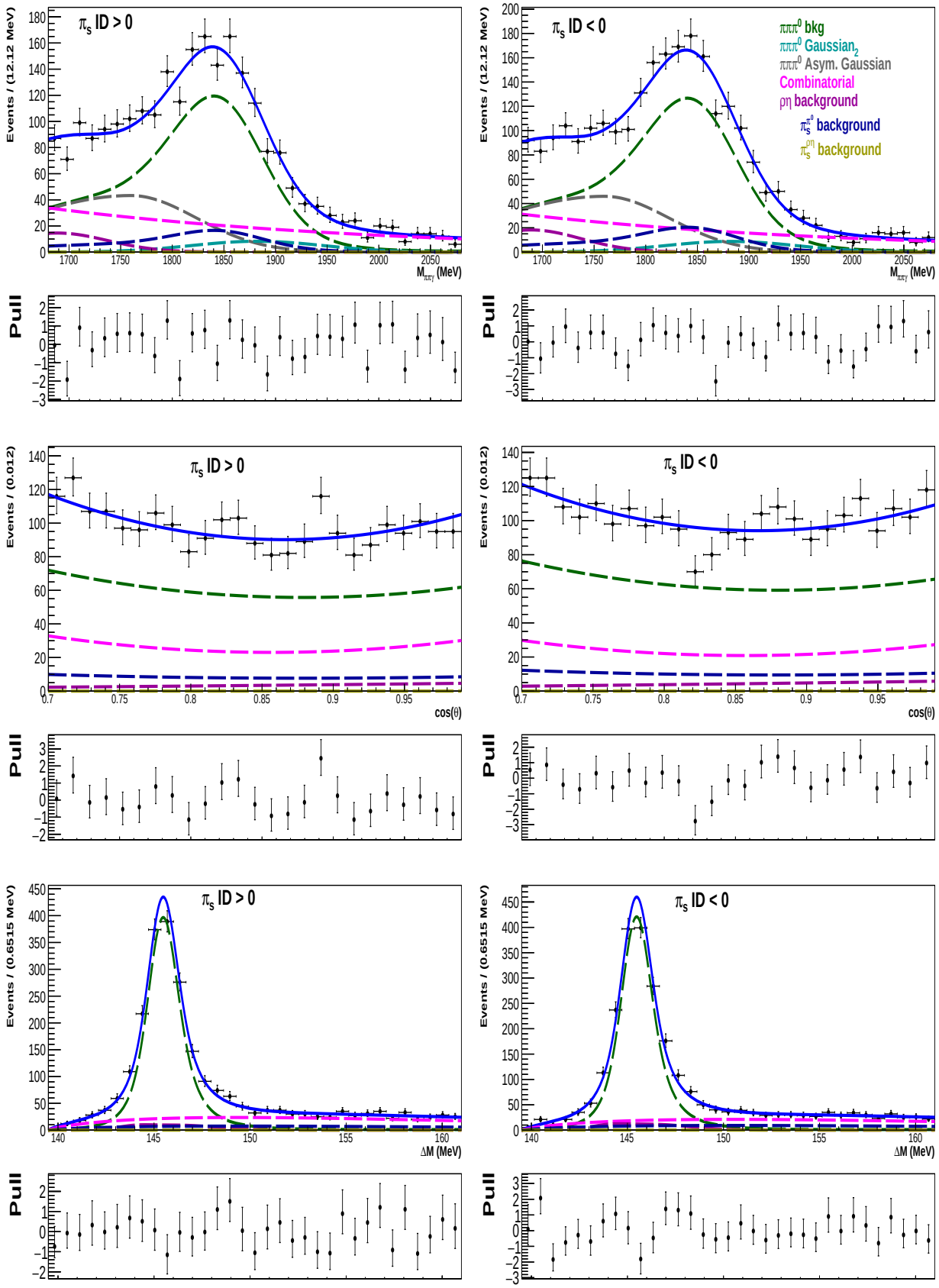

Figure **VI-5**: (Top) $M(D^0)$, (middle) $\cos\theta$ and (bottom) ΔM projections of three-dimensional fit performed simultaneously to (left) $D^0 \to \rho^0\gamma$ and (right) $\bar{D}^0 \to \rho^0\gamma$ candidates reconstructed in the Run-1 data in the helicity-edge region. These projections are in the full fit region. Fit components are indicated in the legend.

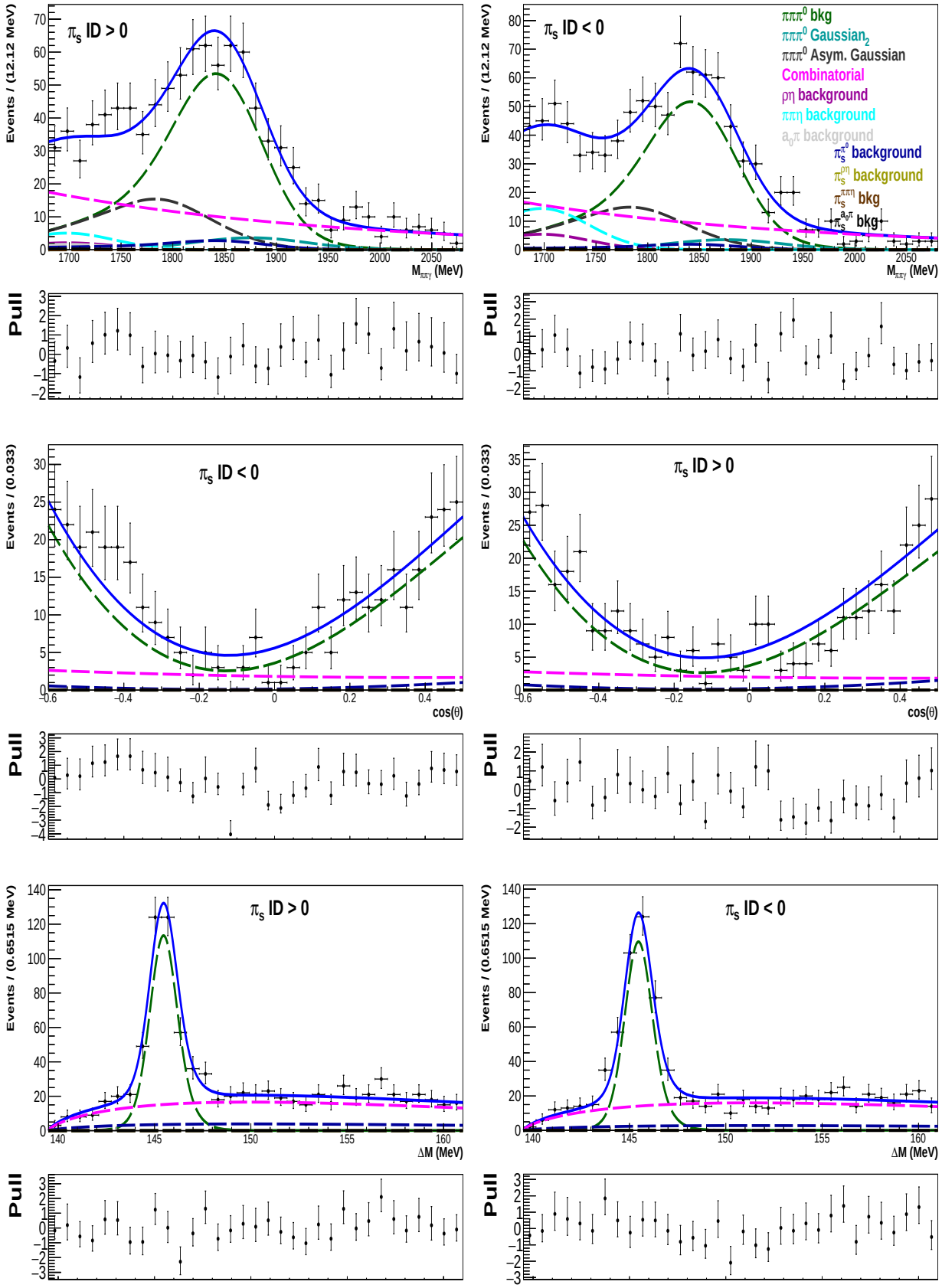

Figure **VI-6**: Top) $M(D^0)$, (middle) $\cos\theta$ and (bottom) ΔM projections of three-dimensional fit performed simultaneously to (left) $D^0 \to \rho^0\gamma$ and (right) $\bar{D}^0 \to \rho^0\gamma$ candidates reconstructed in the Run-1 data in the helicity-center region. These projections are in the signal-enhanced region, and, since no significant signal is observed, the signal region is unblinded. Fit components are indicated in the legend.

Chapter VII

Analysis of reference channels

VII.1 Method to correct for nuisance asymmetries

As mentioned in Section **II.4**, there are other sources than CP violation contributing to the raw asymmetry (Eq. **VI.1**) between π_s^+-tagged D^0 yields and π_s^--tagged $\bar{D}^0$ yields. Main ones are production and detection asymmetries, discussed in Sections **II.4.1** and **II.4.2**, respectively. Those effects can reach the percent level and are known to be kinematics-dependent, stronger for soft particles and becoming smaller for highly boosted ones. In general, the consensus is that precise calculation of detection and production asymmetries from the first principles is implausible. Therefore, any analysis attempting to measure A_{CP} needs to find a reference channel that has same production and detection asymmetries (referred to as nuisance asymmetries), but negligible or precisely measured CP asymmetry. In this measurement, pion-tagged $D^0 \to K^+K^-$ and $D^0 \to \pi^+\pi^-$ decays are chosen as reference channels for $D^0 \to \phi\gamma$ and $D^0 \to \rho^0\gamma$ signal decays, respectively, whereas $D^0 \to K^-\pi^+\pi^0$ is used as a reference channel for $D^0 \to \bar{K}^{*0}\gamma$.

VII.1.1 Nuisance asymmetries in $D^0 \to \phi\gamma$ and $D^0 \to \rho^0\gamma$

The raw asymmetry between measured yields of $D^{*+} \to D^0\pi_s^+$, $D^0 \to \phi\gamma$, $\phi \to K^+K^-$ decay chain and of the charge-conjugate process can be expressed as:

$$A_{raw}(D^0 \to \phi\gamma) = A_{CP}(D^0 \to \phi\gamma) + A_{prod}(D^{*+}) + A_{det}(\pi_s^+) + A_{det}(K^+K^-), \qquad \textbf{(VII.1)}$$

where $A_{prod}(D^{*+})$ is the production asymmetry between D^{*+} and D^{*-} mesons, $A_{det}(\pi_s^+)$ is the detection asymmetry related to the soft tagging pion, whereas $A_{det}(K^+K^-)$ is the detection asymmetry of the K^+K^- system. As kinematics of K^+ and K^- mesons originating from the $\phi \to K^+K^-$ decays are equal, one gets $A_{det}(K^+K^-) = 0$.[42] The presence of the neutral object, such as photon, does not introduce any nuisance asymmetry. Similarly, A_{raw} for the corresponding reference channel, $D^{*+} \to D^0\pi_s^+$, $D^0 \to K^+K^-$, is:

$$A_{raw}(D^0 \to K^+K^-) = A_{CP}(D^0 \to K^+K^-) + A_{prod}(D^{*+}) + A_{det}(\pi_s^+) + A_{det}(K^+K^-), \qquad \textbf{(VII.2)}$$

and, again, as $D^0 \to K^+K^-$ is charge-symmetric final state, one gets $A_{det}(K^+K^-) = 0$. If the kinematics of the soft pion and D^{*+} mesons are the same between the signal and the reference channels, then $A_{prod}(D^{*+})$ and $A_{det}(\pi_s^+)$ cancel out in the difference between Eqs. **VII.1** and **VII.2**:

$$A_{raw}(D^0 \to \phi\gamma) - A_{raw}(D^0 \to K^+K^-) = A_{CP}(D^0 \to \phi\gamma) - A_{CP}(D^0 \to K^+K^-). \qquad \textbf{(VII.3)}$$

[42] Detection asymmetry of the K^+K^- system in the D^0 decays is equal to that of the K^-K^+ in the $\bar{D}^0$ decays, and thus cancels out in A_{raw}.

Therefore CP asymmetry for the $D^0 \to \phi\gamma$ decay is measured as:

$$A_{CP}(D^0 \to \phi\gamma) = A_{raw}(D^0 \to \phi\gamma) - A_{raw}(D^0 \to K^+K^-) + A_{CP}(D^0 \to K^+K^-), \qquad \textbf{(VII.4)}$$

where $A_{raw}(D^0 \to \phi\gamma)$ is measured as described in Chapter **VI**, $A_{raw}(D^0 \to K^+K^-)$ is the measured raw asymmetry of the $D^0 \to K^+K^-$ decay after reweighing of the D^{*+} and π_s^+ kinematics to match those in the $D^0 \to \phi\gamma$ signal decay. $A_{CP}(D^0 \to K^+K^-) = (0.44 \pm 0.54) \times 10^{-3}$ [21] is considered as an external input. The reference-channel A_{CP} uncertainty will be considered as a systematic uncertainty of $A_{CP}(D^0 \to \phi\gamma)$. Anyhow, it is well below the sensitivity expected for the signal channel.

Similar considerations apply for the $D^0 \to \rho^0\gamma$ decay and the corresponding reference channel $D^0 \to \pi^+\pi^-$, for which one gets:

$$A_{CP}(D^0 \to \rho^0\gamma) = A_{raw}(D^0 \to \rho^0\gamma) - A_{raw}(D^0 \to \pi^+\pi^-) + A_{CP}(D^0 \to \pi^+\pi^-), \qquad \textbf{(VII.5)}$$

with $A_{CP}(D^0 \to \pi^+\pi^-) = (2.30 \pm 0.59) \times 10^{-3}$ [21].

VII.1.2 Nuisance asymmetries in $D^0 \to \bar{K}^{*0}\gamma$

The raw asymmetry for $D^{*+} \to D^0\pi_s^+$, $D^0 \to \bar{K}^{*0}\gamma$, $\bar{K}^{*0} \to K^-\pi^+$ process is:

$$A_{raw}(D^0 \to \bar{K}^{*0}\gamma) = A_{CP}(D^0 \to \bar{K}^{*0}\gamma) + A_{prod}(D^{*+}) + A_{det}(\pi_s^+) + A_{det}(K^-\pi^+). \qquad \textbf{(VII.6)}$$

Here, the D^0 final state is not charge-symmetric and the detection asymmetry of the $K^-\pi^+$ system, $A_{det}(K^-\pi^+)$, does not cancel out.

For the pion-tagged reference channel, $D^0 \to K^-\pi^+\pi^0$, the raw asymmetry is:

$$A_{raw}(D^0 \to K^-\pi^+\pi^0) = A_{prod}(D^{*+}) + A_{det}(\pi_s^+) + A_{det}(K^-\pi^+). \qquad \textbf{(VII.7)}$$

As the $D^0 \to K^-\pi^+\pi^0$ decay is primarily a CF decay, it is expected to be CP-symmetric, thus $A_{CP}(D^0 \to K^-\pi^+\pi^0) = 0$. Any mixing-induced CP asymmetry is expected to below the 10^{-5} level [66], and can be neglected. In order to remove all the nuisance asymmetries in Eq. **VII.6**, it is necessary to equalize the kinematics of the D^{*+}, π_s^+, as well as K^- and π^+ between the signal and the reference decays. The $D^0 \to K^-\pi^+\pi^0$ decay is chosen as the reference channel, instead of $D^0 \to K^-\pi^+$, because it is easier to equalize kinematics of D^0 decay products originating from three-body decays than between three-body and two-body processes.

From the difference between Eqs. **VII.6** and **VII.7**, one gets the CP asymmetry for the $D^0 \to \bar{K}^{*0}\gamma$ decay measured as:

$$A_{CP}(D^0 \to \bar{K}^{*0}\gamma) = A_{raw}(D^0 \to \bar{K}^{*0}\gamma) - A_{raw}(D^0 \to K^-\pi^+\pi^0), \qquad \textbf{(VII.8)}$$

where $A_{raw}(D^0 \to \bar{K}^{*0}\gamma)$ is measured as described in Chapter **VI**, $A_{raw}(D^0 \to K^-\pi^+\pi^0)$ is the measured raw asymmetry of the $D^0 \to K^-\pi^+\pi^0$ decay after reweighing of the D^{*+}, π_s^+, K^- and π^+ kinematics to match those in the $D^0 \to \bar{K}^{*0}\gamma$ signal decay.

Reweighing of kinematics in the reference channels is discussed in Section **VII.4**. Measurement of the raw asymmetries for the reference channels is described in Section **VII.5**.

VII.2 Selection of reference channels

Selection of the reference channels is aligned to the signal selection as much as possible, in order to facilitate their kinematic matching. However, decays are obviously different - $D^0 \to K^+K^-$ and $D^0 \to \pi^+\pi^-$ lack a neutral object, which means that there are no variables related to photon reconstruction, and Hlt2 lines are different. In the selection of the $D^0 \to K^-\pi^+\pi^0$ channel, a neutral object is selected to be π^0-like, while Hlt2 line is the same as for the signal channel.

VII.2.1 Stripping preselection

In order to assure large statistics, each of the reference channels has its dedicated stripping line, as listed in Table **VII-1**. $D^0 \to K^-\pi^+\pi^0$ uses two stripping lines, one for resolved π^0 category and other for merged π^0 category (Section **II.2.4**). The data for $D^0 \to K^+K^-$ and $D^0 \to \pi^+\pi^-$ decays are taken from the `CharmToBeSwum` stream, while for $D^0 \to K^-\pi^+\pi^0$ from the `Charm` stream. The stripping version used is `Stripping21`. Table **VII-2** summarizes requirements for $D^0 \to K^+K^-$ and $D^0 \to \pi^+\pi^-$ channels, and Table **VII-3** for the $D^0 \to K^-\pi^+\pi^0$ channel.

Reference channel	Stripping line
$D^0 \to K^+K^-$	`D2hhPromptDst2D2KKLine`
$D^0 \to \pi^+\pi^-$	`D2hhPromptDst2D2PiPiLine`
$D^0 \to K^-\pi^+\pi^0$	`StrippingDstarToHHPi0_Kpipi0_R_Line`
	`StrippingDstarToHHPi0_Kpipi0_M_Line`

Table **VII-1**: Stripping lines used for the reference channels. For the $D^0 \to K^-\pi^+\pi^0$ decay, `R_Line` uses resolved π^0 mesons and `M_Line` uses merged π^0 mesons.

VII.2.2 Trigger selection

The L0 and Hlt1 selections are aligned with the signal selection (Section **III.3.2**), which is possible as they do not rely on a signal photon. Hlt2 lines used for the reference channels are summarised in Table **VII-4**. Dedicated lines are employed for $D^0 \to K^+K^-$ and $D^0 \to \pi^+\pi^-$ channels, whereas the $D^0 \to K^-\pi^+\pi^0$ decay is triggered with the same *inclusive* D^* line as used for the signal decays (Section **III.3.2**). The selection requirements in the Hlt2 lines for $D^0 \to K^+K^-$ and $D^0 \to \pi^+\pi^-$ decays are given in Table **VII-5**.

VII.2.3 Offline selection

After stripping and trigger selections, additional offline selection is imposed, in order to align requirements, in particular related to decay kinematics and topology, with those applied for signal candidates. In the offline analysis, $D^0 \to K^+K^-$ and $D^0 \to \pi^+\pi^+$ candidates selected at the stripping stage (Section **VII.2.1**) are combined with π_s^+ tracks to form $D^{*+} \to D^0\pi_s^+$ candidates. In addition, DTF is applied to all the reference decays with the same constraint as employed for the signal decays i.e. requiring that D^{*+} candidates originate from the associated PV. Offline selection also includes the fiducial volume cuts applied for soft pions, defined in Section **II.4.2**.

Selections common for all channels are described in Table **VII-6**. D^0 invariant mass is selected to be in the signal region around the known D^0 mass; requirement for $D^0 \to K^+K^-$ and $D^0 \to \pi^+\pi^-$ decays is different from that for $D^0 \to K^-\pi^+\pi^0$ to account for different mass resolutions.

Additional requirements, given in Table **VII-7**, are imposed for the $D^0 \to K^-\pi^+\pi^0$ channel as the addition of a neutral object changes topology of the decay, significantly worsens mass resolution and results in higher combinatorial background. A neutral object is selected to be π^0-like using the π^0 confidence level, π^0_{CL}. For resolved π^0 candidates it is defined as the product of the γ_{CL} for two daughter photons (Section **III.3.3**), whereas for merged π^0 candidates $\pi^0_{CL} = 1 - \text{IsPhoton}$.

Variable	Cut	Variable description
	Global event cuts	
Trigger	`D_Hlt1TrackAllL0`	Track firing Hlt1
	Charged track $h^{\pm}$	
p_T	> 800 MeV/c	Transverse momentum
p	> 5 GeV/c	Momentum
$PID_K(K)$	> 0	Kaon-like PID applied for kaons
$PID_K(\pi)$	< 0	Kaon-like PID applied for pions
IsMuon	False	Remove muon-like tracks
χ^2_{track}	< 3	Track quality
χ^2_{IP}	< 9	Significance of IP
max $[PID_K(K^+),\ PID_K(K^-)]$	> 5	Best kaon PID
min $[PID_K(\pi^+),\ PID_K(\pi^-)]$	< -5	Best pion PID
max $[p_T(h^+),\ p_T(h^-)]$	> 1500 MeV/c	Largest p_T
$DOCA$	< 0.7 mm	DOCA between h^+ and h^- tracks
	$D^0 \to h^+h^-$	
p_T	> 2 GeV/c	Transverse momentum
p	> 5 GeV/c	Momentum
$M(K^+K^-)$	(1765, 2065) MeV/c^2	Invariant mass
$M(\pi^+\pi^-)$	(1790, 2065) MeV/c^2	Invariant mass
$DIRA$	> 0.9999	Cosine of direction angle
χ^2_{VD}	> 40	Significance of vertex displacement
χ^2_{VTX}	< 10	Vertex quality

Table **VII-2**: Stripping selection for reference channels $D^0 \to K^+K^-$ and $D^0 \to \pi^+\pi^-$.

Variable	Cut	Variable description
	Global event cuts	
Trigger	`Dst_Hlt2CharmHadD02HHXDsthhX`	D^* firing Hlt2
	Charged tracks $h^\pm$	
p_T	> 500 MeV/c	Transverse momentum
$GhostProb$	< 0.35	Probability that track is a ghost
$PID_K(K)$	> 7	Kaon-like PID applied for kaons
$PID_K(\pi)$	< 0	Kaon-like PID applied for pions
max $[p_T(h^+),\ p_T(h^-)]$	> 1.7 GeV/c	Largest p_T
max $[\chi^2_{IP}(h^+),\ \chi^2_{IP}(h^-)]$	> 36	Largest χ^2_{IP}
	Resolved π^0	
p_T	> 500 MeV/c	Transverse momentum
$M(\pi^0)$	(120, 150) MeV/c^2	Invariant mass
	Merged π^0	
p_T	> 500 MeV/c	Transverse momentum
	$D^0 \to K^-\pi^+\pi^0$	
χ^2_{VD}	> 100	Significance of vertex displacement
χ^2_{VTX}	< 3	Vertex quality
$M(D^0)$	(1724.83, 2064.83) MeV/c^2	Invariant mass
p_T	> 1400 MeV/c	Transverse momentum
	Soft pion	
p_T	> 300 MeV/c	Transverse momentum
$GhostProb$	< 0.35	Probability that track is a ghost
PID_e	< 5	Electron-like PID for pions
χ^2_{IP}	< 9	Significance of IP
	$D^{*+} \to D^0\pi^+_s$	
ΔM	< 180 MeV/c^2	$M(D^{*+}) - M(D^0)$
χ^2_{VTX}	< 9	Vertex quality

Table **VII-3**: Stripping selection for $D^0 \to K^-\pi^+\pi^0$ reference channel.

Decay mode	Hlt2 selection
$D^0 \to K^+K^-$	`D_Hlt2CharmHadD02HH_D02KKDecision_TOS==1`
$D^0 \to \pi^+\pi^-$	`D_Hlt2CharmHadD02HH_D02PiPiDecision_TOS==1`
$D^0 \to K^-\pi^+\pi^0$	`Dst_Hlt2CharmHadD02HHXDst_hhXDecision_TOS==1`

Table **VII-4**: Hlt2 selection used for reference channels.

Variable	Cut	Variable description
	Charged tracks $h^\pm$	
χ^2_{track}	< 3	Track quality
p_T	> 800 MeV/c	Transverse momentum
p	> 5 GeV/c	Momentum
χ^2_{IP}	> 9	Significance of IP
	h^+h^- combination	
p_T	> 2 GeV/c	Transverse momentum
$DOCA$	< 0.1 mm	DOCA between h^+ and h^-
max $[p_T(h^+), p_T(h^-)]$	> 1.5 GeV/c	Largest p_T
$M(h^+h^-)$	(1715, 2065) MeV/c^2	Invariant mass
	$D^0 \to h^+h^-$	
χ^2_{VTX}	< 10	Vertex quality
χ^2_{VD}	> 40	Vertex displacement
$DIRA$	> 0.99985	Cosine of direction angle
$M(D^0)$	(1815, 1915) MeV/c^2	Invariant mass
Trigger	`D_Hlt1TrackAllL0_TOS==1`	D^0 daughter firing Hlt1

Table **VII-5**: Selection requirements in Hlt2 lines dedicated for $D^0 \to K^+K^-$ and $D^0 \to \pi^+\pi^-$ decays.

Variable	Cut
$PID_K(K)$	≥ 10
$PID_K(\pi)$	≤ -10
$p_T(K)$	> 800 MeV/c
$p_T(\pi)$	> 800 MeV/c
$GhostProb(\pi_s^+)$	< 0.8
$p_T(\pi_s^+)$	> 300 MeV/c
$\arccos[DIRA(D^0)]$	≤ 0.02 rad
$\ln \chi^2_{IP}(D^0)$	≤ 3
$M(h^+h^-)$	(1844, 1878) MeV/c^2
$M(K^-\pi^+\pi^0)$	(1833, 1900) MeV/c^2
$p_T(D^{*+})$	> 5 GeV/c

Table **VII-6**: Summary of offline selection applied for all reference channels.

Variable	Cut
$\ln \pi^0_{CL}$	≥ -3
$t(D^0)$	≤ 0.1 ns
χ^2_{DTF}	< 50

Table **VII-7**: Additional selection imposed on $D^0 \to K^-\pi^+\pi^0$ channel.

VII.3 ΔM fits to unweighted reference decays

After selection described in Section **VII.2**, separation of reference signal from residual background is done by the means of unbinned maximum-likelihood fit to the ΔM observable, performed simultaneously to the π_s^+-tagged and π_s^--tagged samples. Candidates are selected to have $M(D^0)$ in the signal region (Table **VII-6**) and $139.5 < \Delta M < 157.5$ MeV/c^2. Reference signals are measured with one-dimensional ΔM fit, rather than two-dimensional $M(D^0)$ vs. ΔM fit, because selected samples are very clean, $M(D^0)$ resolutions are good, and any background peaking in the chosen signal regions of $M(D^0)$ is negligible.

Figures **VII-1** and **VII-2** show ΔM distributions for $D^0 \to K^+K^-$ and $D^0 \to \pi^+\pi^-$ samples, respectively, Figure **VII-3** presents ΔM for $D^0 \to K^-\pi^+\pi^0$ sample. One can clearly see how addition of a neutral cluster to the final state degrades the resolution even in the ΔM observable. In these distributions the signal peak is described by a triple Gaussian function with common means, whereas combinatorial background is described by a product of a decaying exponential multiplied by a phase-space factor $\sqrt{1-\frac{m_\pi}{\Delta M}}$. Some shape parameters, in particular the signal-peak position, are allowed to differ between the D^0 and $\bar{D}^0$ samples. Total signal yield and background yield, as well as raw asymmetry (Eq. **VI.1**) of the signal and background contributions are fit parameters for each reference channel. They are summarised in Table **VII-8**. The largest A_{raw} is measured for the $D^0 \to K^-\pi^+\pi^0$ decay, which is due to a contribution from $A_{det}(K^-\pi^+)$ (Eq. **VII.7**), not present for charge-symmetric decays $D^0 \to K^+K^-$ and $D^0 \to \pi^+\pi^-$.

As reference-decay kinematics have not been reweighted yet, the fits presented in this Section, only serve to test PDFs, purity and yields of the selected reference samples.

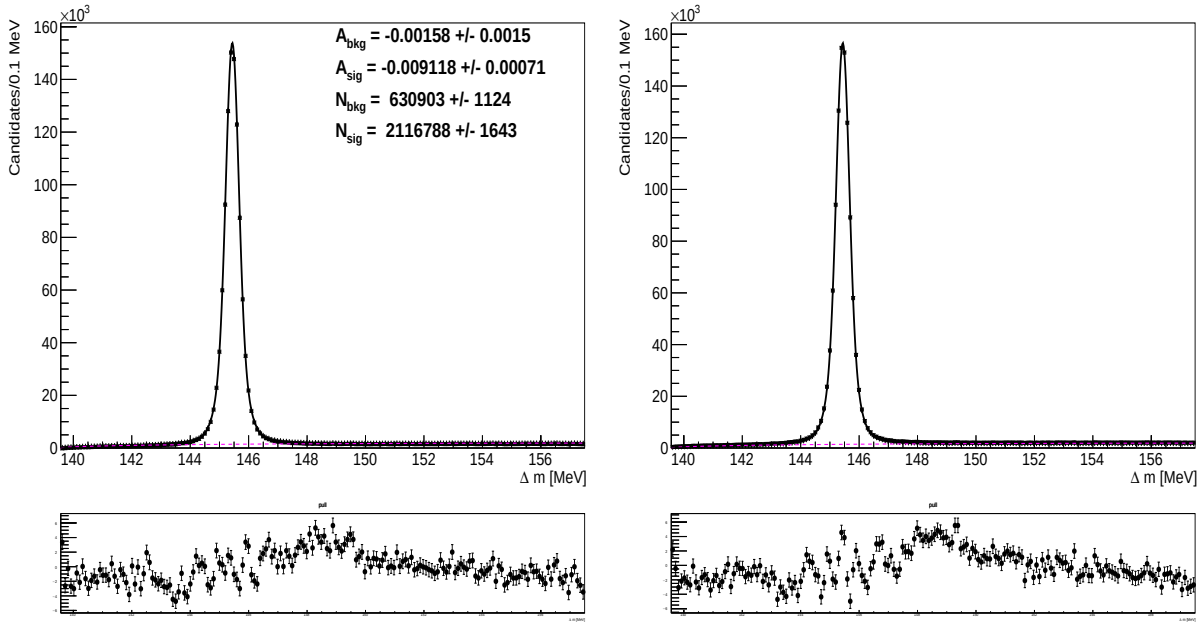

Figure **VII-1**: ΔM distribution for (left) π_s^+-tagged $D^0 \to K^+K^-$ and (right) π_s^--tagged $\bar{D}^0 \to K^-K^+$ candidates in the Run-1 data before kinematic reweighing. Results of the simultaneous fit are superimposed; black line shows the total fit, dashed magenta line shows combinatorial background.

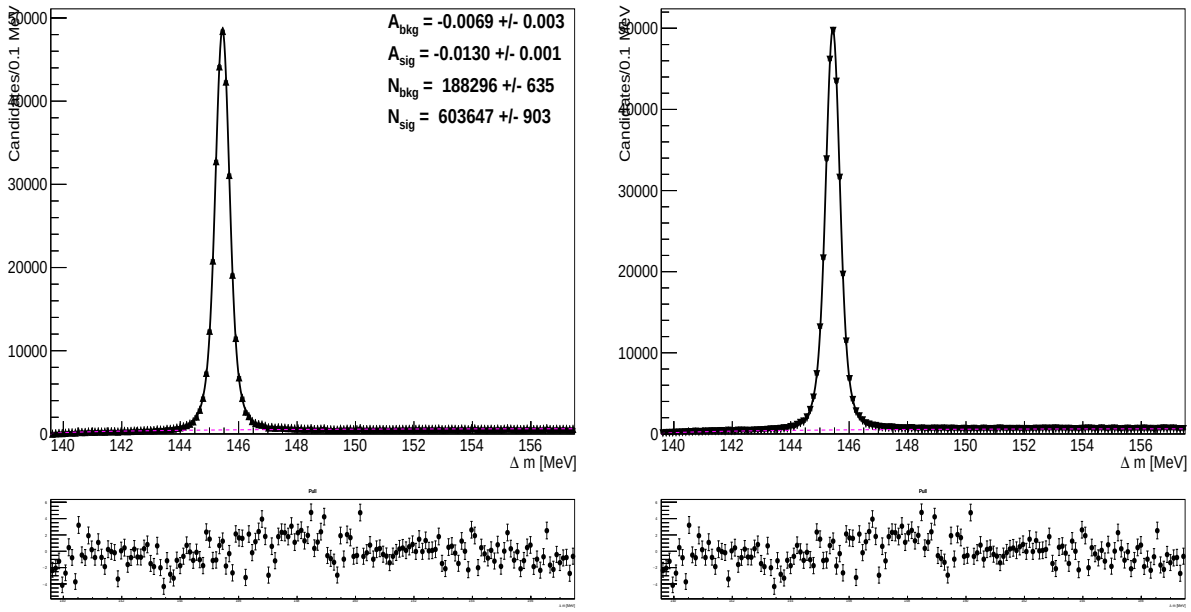

Figure **VII-2**: ΔM distribution for (left) π_s^+-tagged $D^0 \to \pi^+\pi^-$ and (right) π_s^--tagged $\bar{D}^0 \to \pi^-\pi^+$ candidates in the Run-1 data before kinematic reweighing. Results of the simultaneous fit are superimposed; black line shows the total fit, dashed magenta line shows combinatorial background.

Channel	Signal yield [10^3]	Signal A_{raw} [%]	Bkg yield [10^3]	Bkg A_{raw} [%]
$D^0 \to K^+K^-$	2116.8 ± 1.6	-0.91 ± 0.07	630.9 ± 1.1	-0.16 ± 0.15
$D^0 \to \pi^+\pi^-$	603.6 ± 0.9	-1.30 ± 0.10	188.3 ± 0.6	-0.69 ± 0.30
$D^0 \to K^-\pi^+\pi^0$	1304.1 ± 1.7	-1.54 ± 0.10	426.3 ± 1.4	-0.96 ± 0.20

Table **VII-8**: Yields and raw asymmetries of reference channels in the Run-1 data before kinematic reweighing.

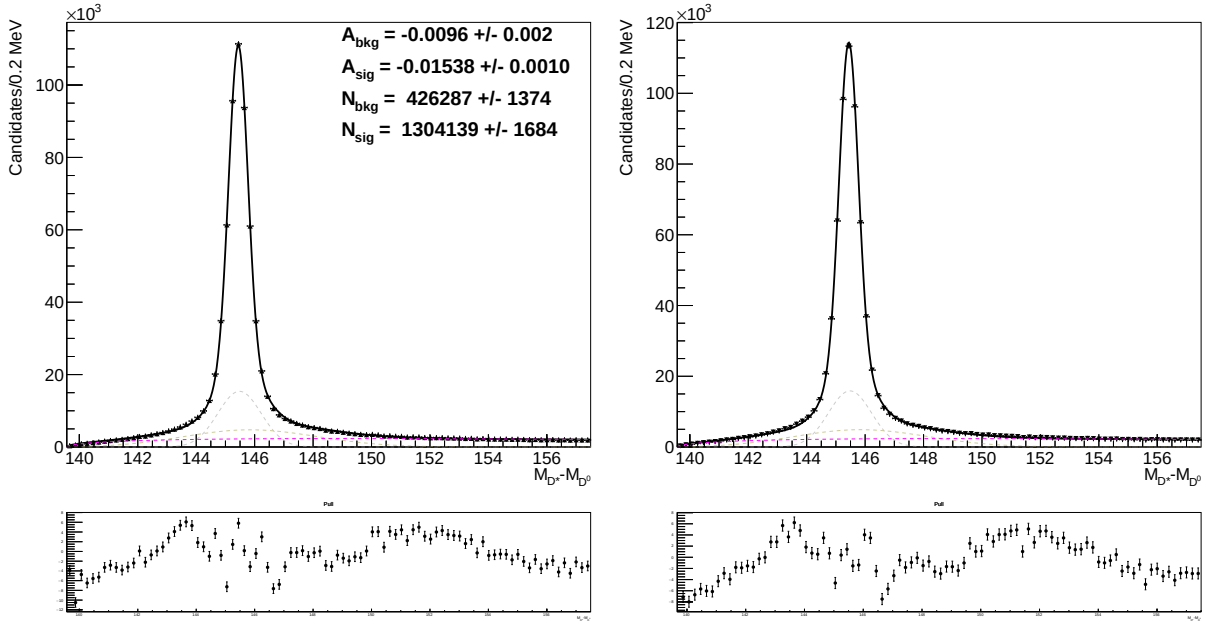

Figure **VII-3**: ΔM distribution for (left) π_s^+-tagged $D^0 \to K^-\pi^+\pi^0$ and (right) π_s^--tagged $\bar{D}^0 \to K^+\pi^-\pi^0$ candidates in the Run-1 data before kinematic reweighing. Results of the simultaneous fit are superimposed; black line shows the total fit, grey dashed lines show two broader Gaussian contributions to the signal, dashed magenta line shows combinatorial background.

VII.4 Kinematic reweighing of reference decays

Due to aforementioned kinematics differences, production and detection asymmetries (Section **VII.1**) may differ between signal and reference channels. The reference decay data are modified by applying a reweighing procedure, which assigns a weight on per-event basis. In our approach, a BDT classifier is trained to match the reference decay data to simulated signal events, using *k-folding* technique to avoid putting aside a separate data set for training. Technical tool for training the classifier is *hep-ml* software package [67].

For the $D^0 \to K^+K^-$ decays a set of *active* variables that are matched to those in the $D^0 \to \phi\gamma$ simulation are pseudorapidities and transverse momenta of D^{*+} and π_s^+ mesons. Their initial (i.e. unweighted) distributions for the reference and signal decays are compared in Fig. **VII-4**. A program takes these initial datasets and attempts to find an optimal set of per-event real positive weights for the dataset being reweighed (green) such as it becomes as close as possible to the target set (blue). The distributions after reweighing are presented in Fig. **VII-5**. What is displayed here is only projections of a four-dimensional feature space - one advantage of using the machine learning approach is the ability to handle spaces of many dimensions. For matching of $D^0 \to \pi^+\pi^-$ data to $D^0 \to \rho^0\gamma$ simulation, the procedure is the same and results are very similar to those for $D^0 \to K^+K^-$. For matching of $D^0 \to K^-\pi^+\pi^0$ data to $D^0 \to \bar{K}^{*0}\gamma$ simulation a feature space is extended to match also kinematics of D^0 daughters, $p_T(K^-)$ and $p_T(\pi^+)$. Initial distributions of active variables are shown in Fig. **VII-6**. The distributions after reweighing are presented in Fig. **VII-7**.

Since weights are applied to each event, they change the other variables that are not part of the feature set. As a control measure, some of those are also shown. Distributions of control variables for $D^0 \to K^+K^-$ compared to those for $D^0 \to \phi\gamma$ simulation before reweighing are shown in Fig. **VII-8** and after reweighing in Fig. **VII-9**. Figures **VII-10** and **VII-11** present control variables for $D^0 \to K^-\pi^+\pi^0$ compared to those for $D^0 \to \bar{K}^{*0}\gamma$ before and after reweighing, respectively. A few important observations regarding those plots are:

– Although weights slightly change the kinematics of K^- and K^+ in $D^0 \to K^+K^-$ decays, the matching algorithm does not break the charge-symmetry of the final state.

– $\eta(K^-)$ and $\eta(\pi^+)$ for $D^0 \to K^-\pi^+\pi^0$ decays are not treated as active variables as their matching is assured by reweighing the other variables.

– Distributions of the $\ln\chi^2_{IP}(D^0)$ are identical for signal and reference channels, meaning that one should expect very similar contamination from charm produced in B-meson decays (Section **II.4.1**). Thus, any production asymmetry arising from such a secondary-charm contribution will also be removed.

– ΔM distributions remain largely unchanged after the reweighing, thus PDFs used for unweighted reference data (Section **VII.3**) can also be employed in the ΔM fits to weighted data.

Overall, the matching of the kinematics achieved in Figs. **VII-5** and **VII-7** is very good. Any residual differences in the kinematic distributions will have negligible impact on A_{raw} for reference channels. The matching set for reference data includes the background; while it would be more accurate to match background-subtracted (*sWeighted* [76]) reference data to simulation signal events, interpretation of per-event weights, which end up being a product of *sWeights* and kinematics weights becomes difficult. However, as the selected reference data show high purity, a presence of background is not expected to worsen the matching. On the other hand, matching the reference-channel data to the background-subtracted signal measured in data would introduce large uncertainties due to limited statistics of the signal decays. Simulations of the signal decays describe their kinematics well enough for this purpose.

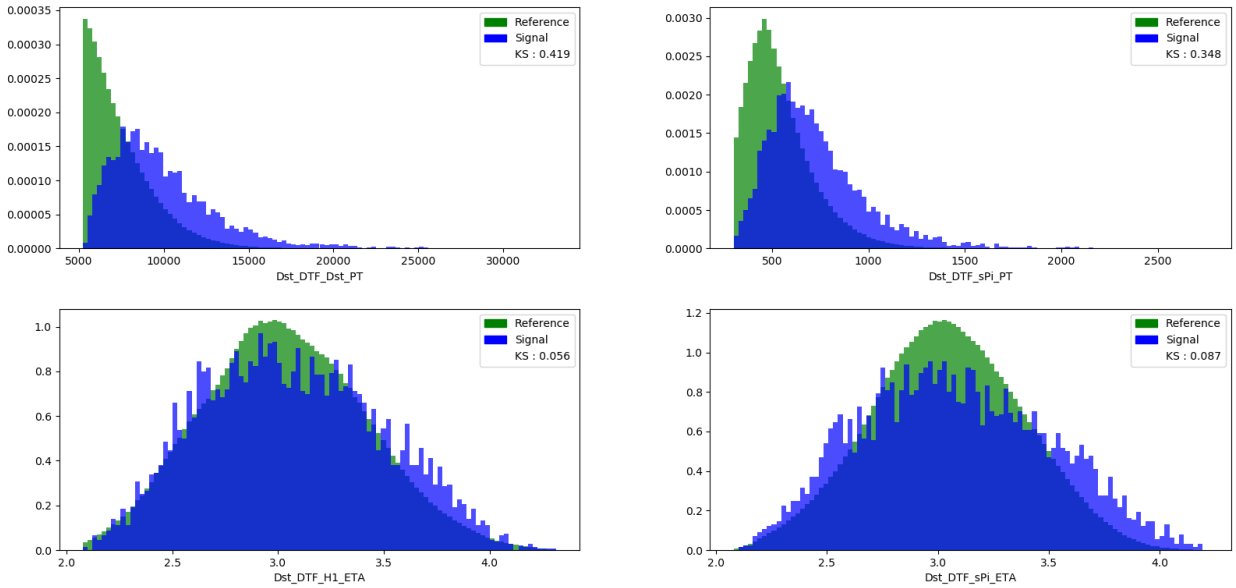

Figure **VII-4**: Initial distributions of kinematic variables used in training of the BDT classifier. Green histograms show $D^0 \to K^+K^-$ reference data, while blue histograms show $D^0 \to \phi\gamma$ simulation. The variables are: (top left) $p_T(D^{*+})$, (top right) $p_T(\pi_s^+)$, (bottom left) $\eta(D^{*+})$, (bottom right) $\eta(\pi_s^+)$.

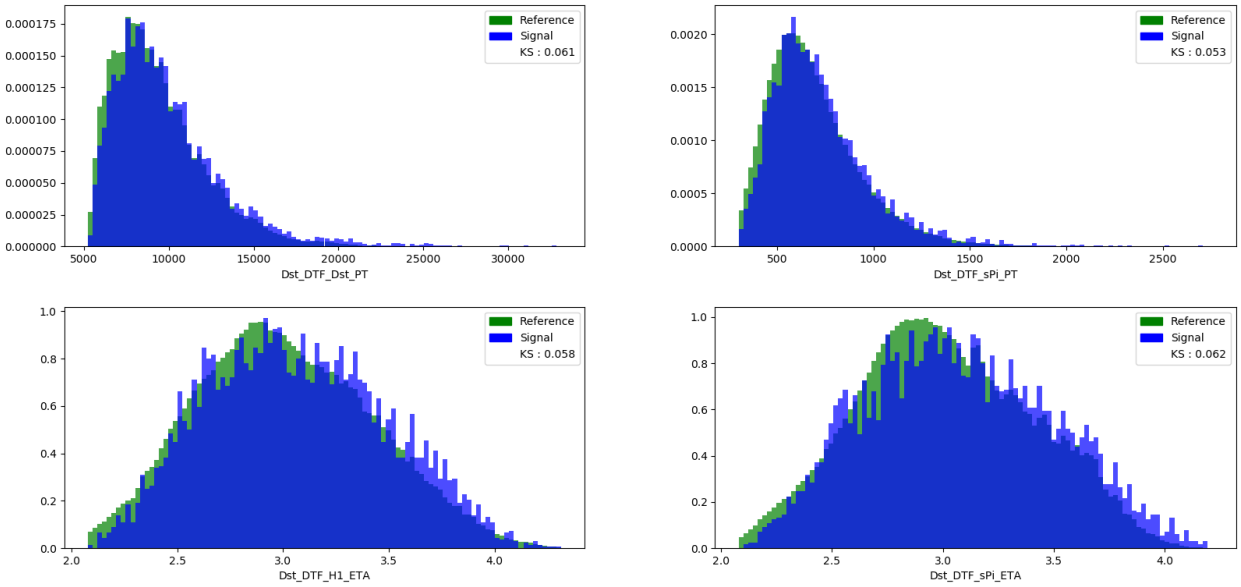

Figure **VII-5**: Weighted distributions of kinematic variables used in training of the BDT classifier. Green histograms show $D^0 \to K^+K^-$ reference data, while blue histograms show $D^0 \to \phi\gamma$ simulation. The variables are: (top left) $p_T(D^{*+})$, (top right) $p_T(\pi_s^+)$, (bottom left) $\eta(D^{*+})$, (bottom right) $\eta(\pi_s^+)$.

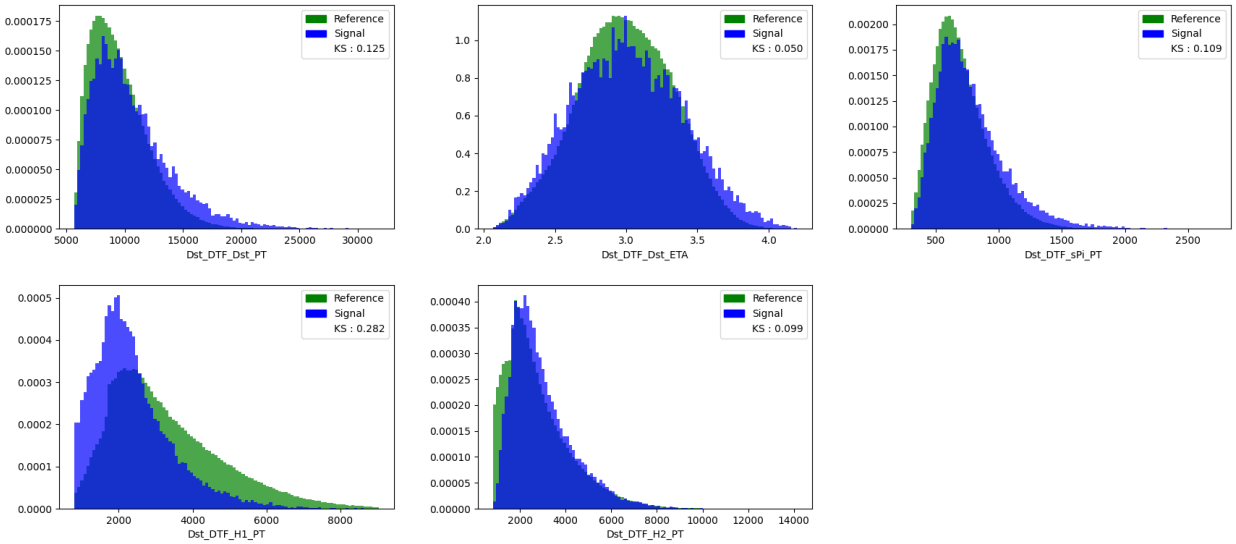

Figure **VII-6**: Initial distributions of kinematic variables used in training of the BDT classifier. Green histograms show $D^0 \to K^-\pi^+\pi^0$ reference data, while blue histograms show $D^0 \to \bar{K}^{*0}\gamma$ simulation. The variables are: (top left) $p_T(D^{*+})$, (top middle) $\eta(D^{*+})$, (top right) $p_T(\pi_s^+)$, (bottom left) $p_T(K^-)$, (bottom middle) $p_T(\pi^+)$.

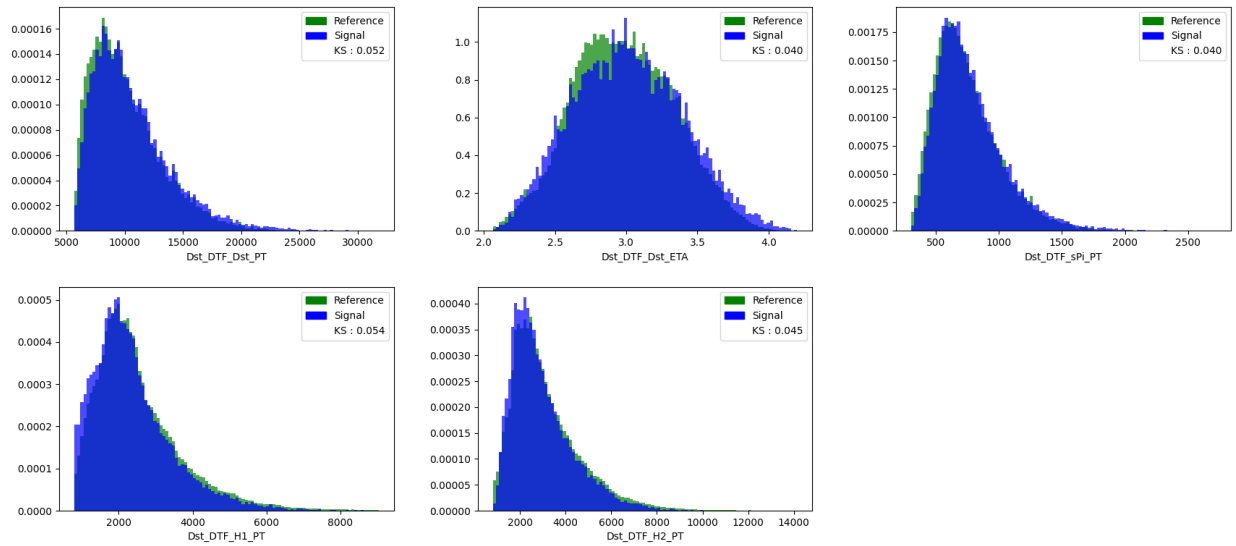

Figure **VII-7**: Weighted distributions of kinematic variables used in training of the BDT classifier. Green histograms show $D^0 \to K^-\pi^+\pi^0$ reference data, while blue histograms show $D^0 \to \bar{K}^{*0}\gamma$ simulation. The variables are: (top left) $p_T(D^{*+})$, (top middle) $\eta(D^{*+})$, (top right) $p_T(\pi_s^+)$, (bottom left) $p_T(K^-)$, (bottom middle) $p_T(\pi^+)$.

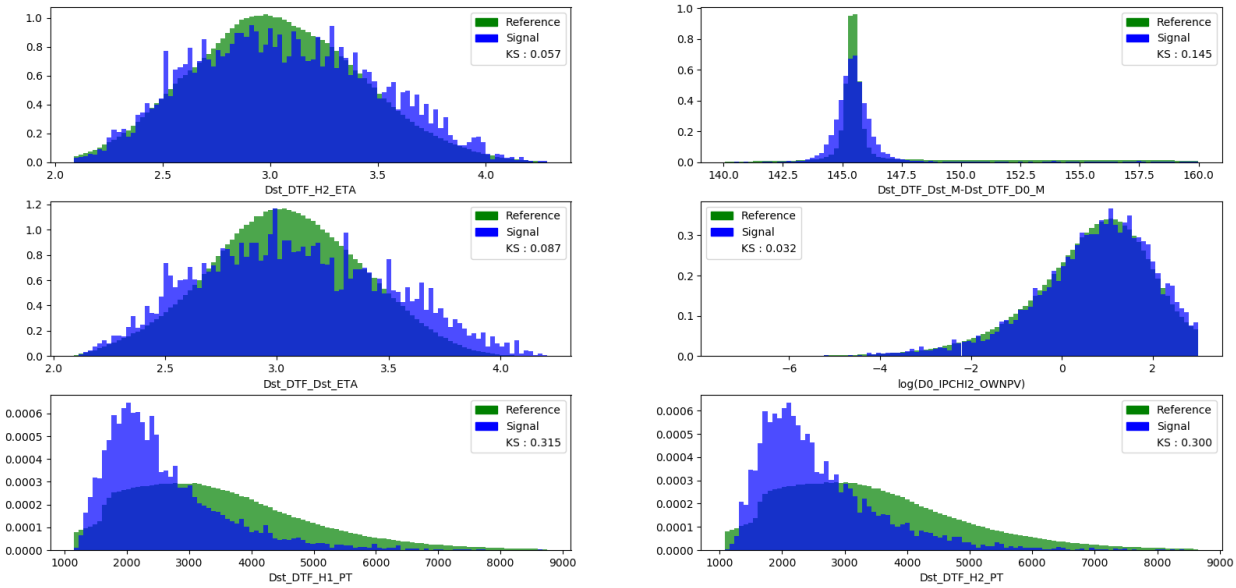

Figure **VII-8**: Distributions of control variables before multivariate regression. Green histograms show $D^0 \to K^+K^-$ reference data, while blue histograms show $D^0 \to \phi\gamma$ simulation. The variables are: (top left) $\eta(K^+)$, (top right) ΔM, (middle left) $\eta(D^{*+})$, (middle right) $\ln \chi^2_{IP}(D^0)$, (bottom left) $p_T(K^-)$, (bottom right) $p_T(K^+)$.

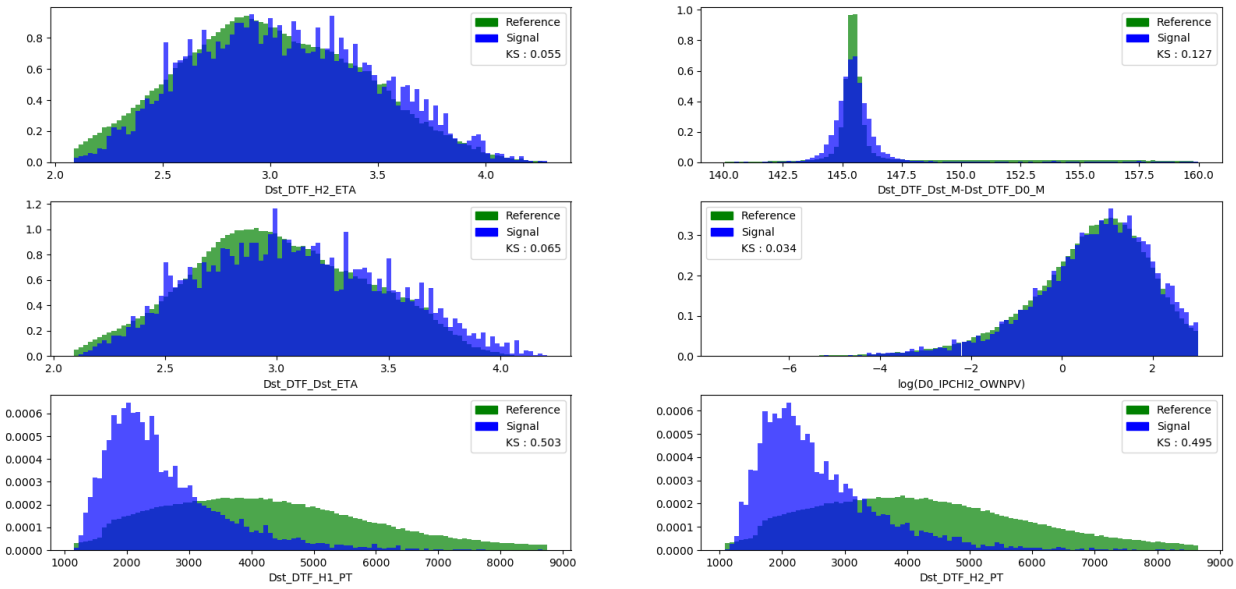

Figure **VII-9**: Distributions of control variables after multivariate regression. Green histograms show $D^0 \to K^+K^-$ reference data, while blue histograms show $D^0 \to \phi\gamma$ simulation. The variables are: (top left) $\eta(K^+)$, (top right) ΔM, (middle left) $\eta(D^{*+})$, (middle right) $\ln \chi^2_{IP}(D^0)$, (bottom left) $p_T(K^-)$, (bottom right) $p_T(K^+)$.

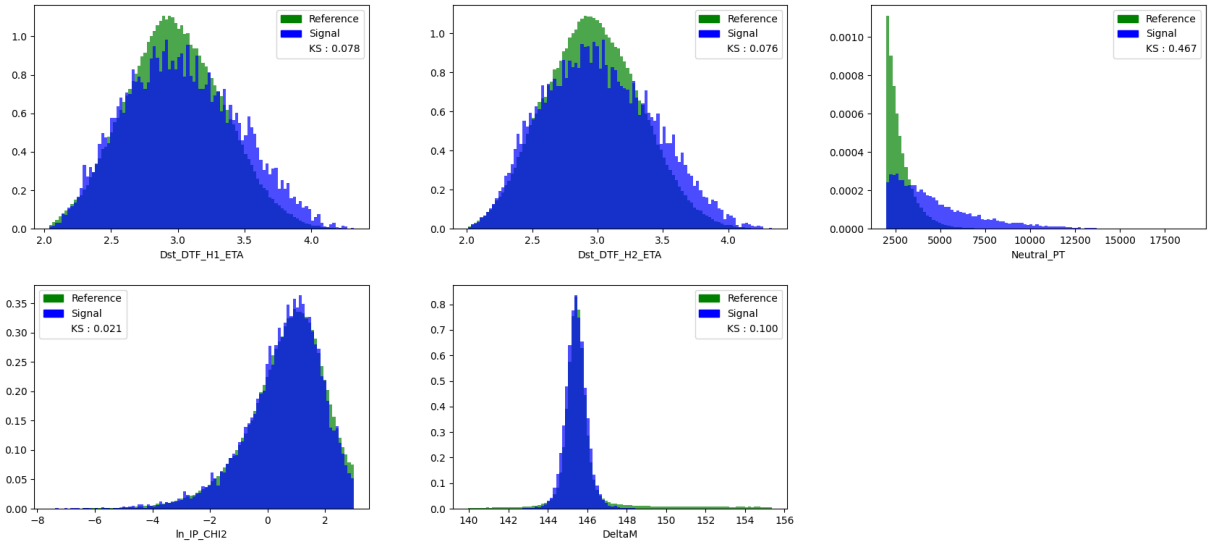

Figure **VII-10**: Distributions of control variables before multivariate regression. Green histograms show $D^0 \to K^-\pi^+\pi^0$ reference data, while blue histograms show $D^0 \to \bar{K}^{*0}\gamma$ simulation. The variables are: (top left) $\eta(K^-)$, (top middle) $\eta(\pi^+)$, (top right) $p_T(\pi^0)$, (bottom left) $\ln \chi^2_{IP}(D^0)$, (bottom middle) ΔM.

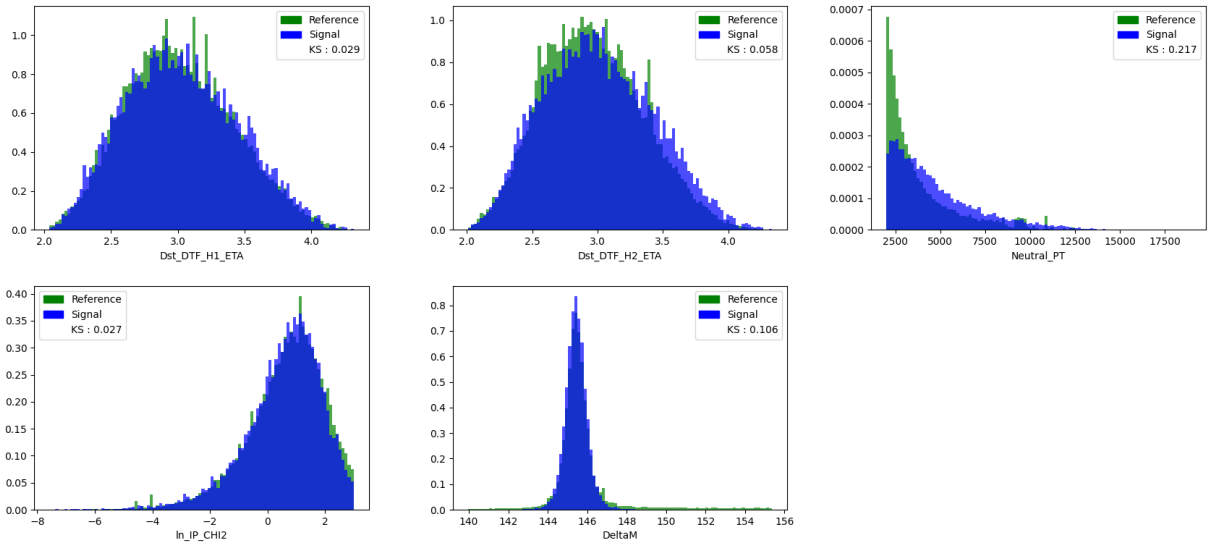

Figure **VII-11**: Distributions of control variables after multivariate regression. Green histograms show $D^0 \to K^-\pi^+\pi^0$ reference data, while blue histograms show $D^0 \to \bar{K}^{*0}\gamma$ simulation. The variables are: (top left) $\eta(K^-)$, (top middle) $\eta(\pi^+)$, (top right) $p_T(\pi^0)$, (bottom left) $\ln \chi^2_{IP}(D^0)$, (bottom middle) ΔM.

VII.5 A_{raw} from ΔM fits to reference decays after weighting

After kinematics matching, we repeat the ΔM fits shown in Figs. **VII-1**, **VII-2** and **VII-3**, but this time applying the weights obtained by multivariate regression and using the asymptotic error approach to calculate parameter uncertainties [68]. An explicit requirement limiting the weights to be less than 100 is applied in order to avoid single events with very large weights, typically arising as a consequence of attempting to match regions of feature space with little overlap between signal and reference channels.

Figures **VII-12**, **VII-13** and **VII-14** show ΔM distributions for weighted $D^0 \to K^+K^-$, $D^0 \to \pi^+\pi^-$ and $D^0 \to K^-\pi^+\pi^0$ reference samples, respectively, split according to the charge of tagging pion. For each reference decay, both flavours are fitted simultaneously with the same PDFs as used for unweighted samples (Section **VII.3**). While in the charge-symmetric channels, the effects of the matching on the ΔM shape are subtle, the ΔM resolution is improved for the $D^0 \to K^-\pi^+\pi^0$ decay. This is primarily due to the increased $p_T(\pi^0)$ after matching of the $K^-\pi^+$ system (Figs. **VII-10** and **VII-11**). Total yields and raw asymmetries for reference signals and combinatorial background are summarised in Table **VII-9**.

A penalty that comes with the weighting is loss of effective yields: as yield moves from a simple number of events in a given decay to an integral of weight variable over fit space. The yield reduction is by about 40% in $D^0 \to K^+K^-$ and $D^0 \to \pi^+\pi^-$ channels, and more than 50% in $D^0 \to K^-\pi^+\pi^0$. Measured A_{raw} for reference decays only slightly changed with respect to those in the unweighted samples (Tables **VII-9**).

The A_{raw} for the reference decays given in Table **VII-9** will be used to extract A_{CP} for the radiative decays, according to Eqs. **VII.4**, **VII.5** and **VII.8**. Quoted statistical uncertainties of the reference A_{raw} will contribute to systematic uncertainties of the A_{CP}.

Channel	Signal yield [10^3]	Signal A_{raw} [%]	Bkg yield [10^3]	Bkg A_{raw} [%]
$D^0 \to K^+K^-$	1301.9 ± 1.0	-0.93 ± 0.16	294.7 ± 1.1	-0.20 ± 0.38
$D^0 \to \pi^+\pi^-$	262.3 ± 0.3	-1.10 ± 0.16	65.6 ± 0.3	-0.12 ± 0.40
$D^0 \to K^-\pi^+\pi^0$	529.3 ± 1.3	-1.70 ± 0.30	104.4 ± 1.3	-0.58 ± 0.68

Table **VII-9**: Effective yields and raw asymmetries of reference channels in the Run-1 data after kinematic reweighing.

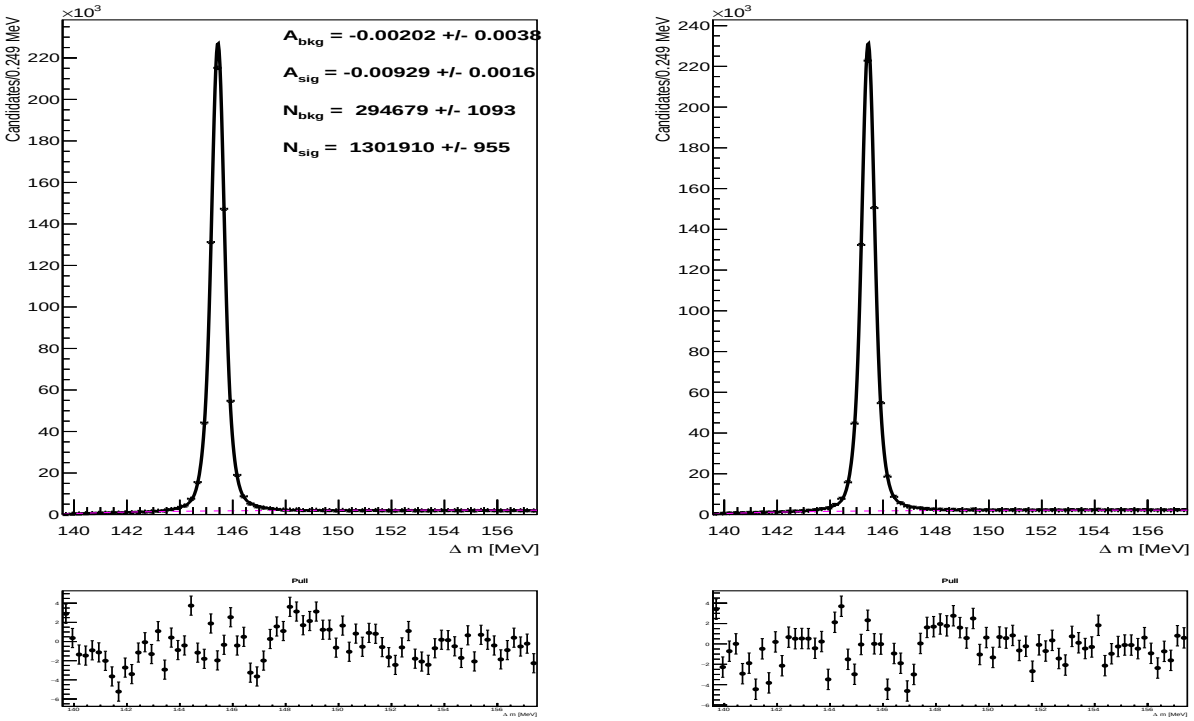

Figure **VII-12**: ΔM distribution for (left) π_s^+-tagged $D^0 \to K^+K^-$ and (right) π_s^--tagged $\bar{D}^0 \to K^-K^+$ candidates in the Run-1 data after kinematic reweighing. Results of the simultaneous fit are superimposed; black line shows the total fit, grey dashed lines show two broader Gaussian contributions to the signal, dashed magenta line shows combinatorial background.

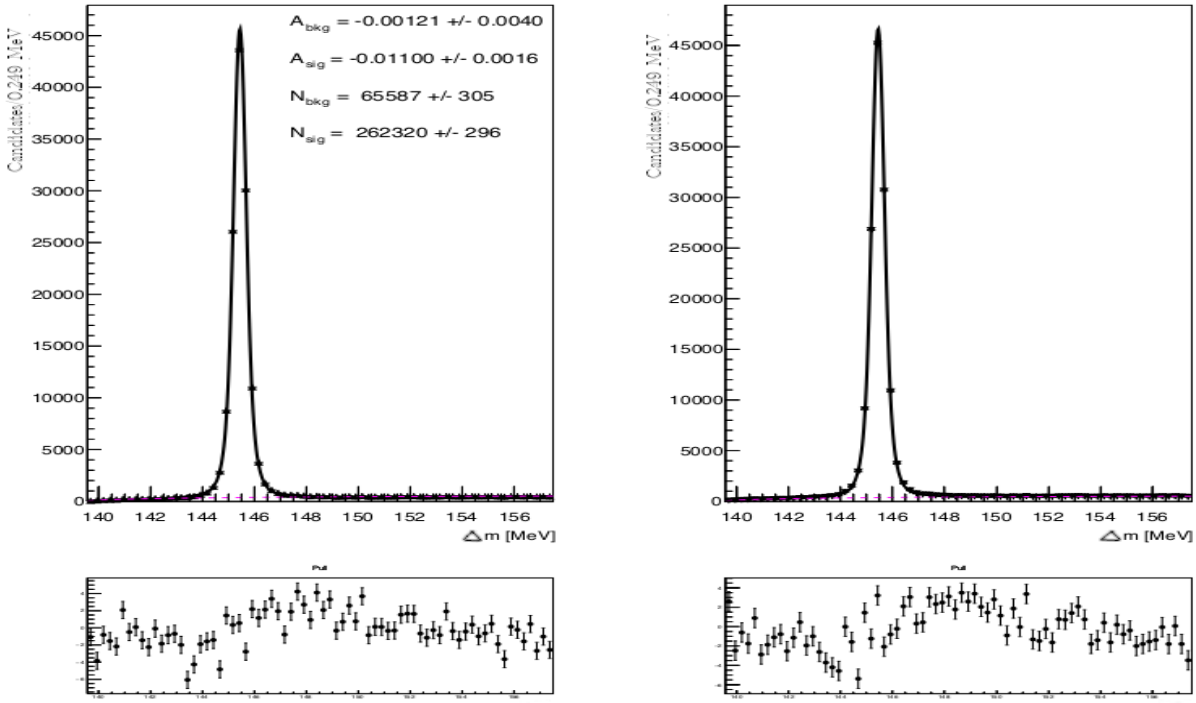

Figure **VII-13**: ΔM distribution for (left) π_s^+-tagged $D^0 \to \pi^+\pi^-$ and (right) π_s^--tagged $\bar{D}^0 \to \pi^-\pi^+$ candidates in the Run-1 data after kinematic reweighing. Results of the simultaneous fit are superimposed; black line shows the total fit, grey dashed lines show two broader Gaussian contributions to the signal, dashed magenta line shows combinatorial background.

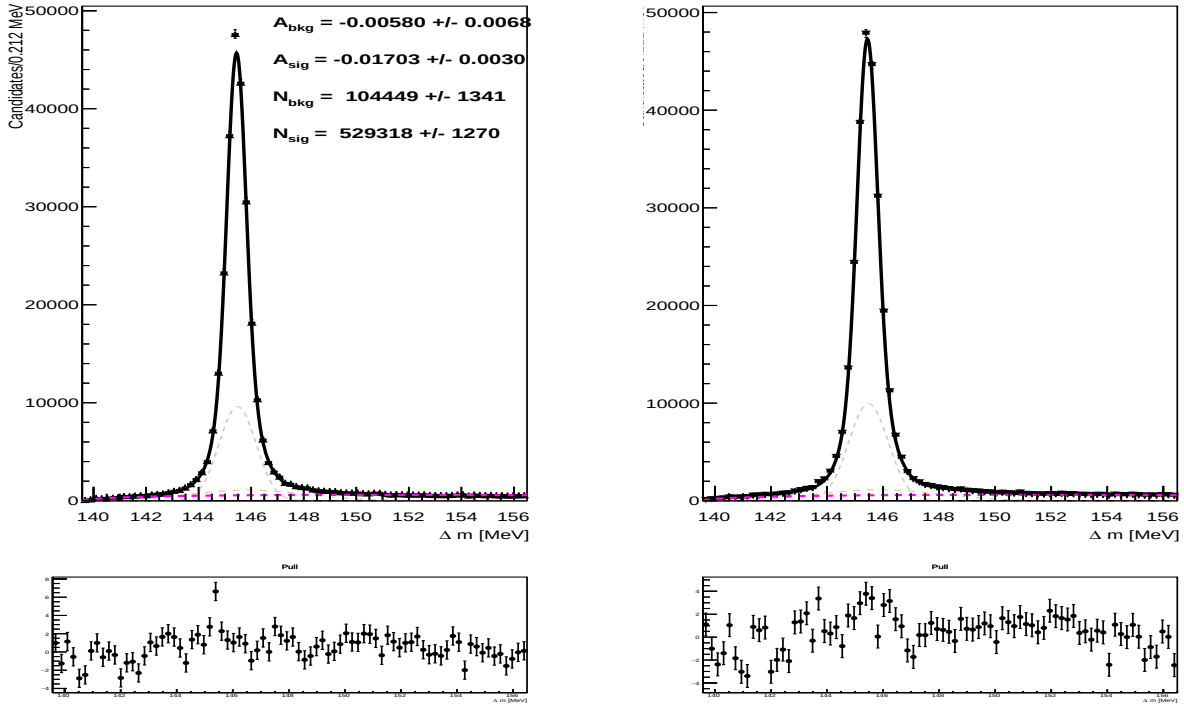

Figure **VII-14**: ΔM distribution for (left) π_s^+-tagged $D^0 \to K^-\pi^+\pi^0$ and (right) π_s^--tagged $\bar{D}^0 \to K^+\pi^-\pi^0$ candidates in the Run-1 data after kinematic reweighing. Results of the simultaneous fit are superimposed; black line shows the total fit, grey dashed lines show two broader Gaussian contributions to the signal, dashed magenta line shows combinatorial background.

Chapter VIII

Systematic uncertainties

A_{CP} for the $D^0 \to \bar{K}^{*0}\gamma$ decay is extracted as defined in Eq. **VII.8**, whereas for $D^0 \to \phi\gamma$ and $D^0 \to \rho^0\gamma$ according to Eq. **VII.4** and Eq. **VII.5**, respectively. Therefore, systematic uncertainties for all the three channels include contributions from A_{raw} measured for the signal (Chapter **VI**) and from A_{raw} for the corresponding reference decays (Chapter **VII**). For the charge-symmetric channels, uncertainties of the external input, $A_{CP}(D^0 \to K^+K^-)$ and $A_{CP}(D^0 \to \pi^+\pi^-)$ need to be also included; they amount to $\pm 0.5 \times 10^{-3}$ (Table **I-1**).

However, it is important to stress that the presented measurement is statistically limited. With the Run-1 data, the statistical uncertainty of the signal A_{CP}, corresponding to the statistical uncertainty of the signal A_{raw}, is 5% for $D^0 \to \bar{K}^{*0}\gamma$ and 12% for $D^0 \to \phi\gamma$; the analysis is not sensitive to the $A_{CP}(D^0 \to \rho^0\gamma)$, as no significant signal is observed for this channel.

For the systematics related to the reference channels, the dominant one comes from the statistical uncertainty on the reference A_{raw} (Table **VII-9**). Its contribution is $\pm 0.30\%$ for $D^0 \to \bar{K}^{*0}\gamma$, and $\pm 0.16\%$ for $D^0 \to \phi\gamma$. Other contributions may arise in relation with individual steps in the analysis of reference channels: kinematical reweighing and fits to the reweighted ΔM distributions. The kinematic reweighing in its default version (Section **VII.4**) does not change significantly the central values of the reference A_{raw}'s. Alternative reweighing versions, such as performed in a limited feature space (e.g. with excluded pseudorapidity distributions) or with different settings in the classifier training have negligible impact on the reference A_{raw}'s. Similar conclusion applies to fitting the ΔM distributions using alternative PDFs. The fitted ΔM spectra (Figs. **VII-12**, **VII-13** and **VII-14**) have very large purities, and changing the fit PDFs only slightly affects the reference decay yields. These changes largely cancel in the A_{raw} asymmetry between D^0 and $\bar{D}^0$ yields. These reference systematic contributions are the level of 10^{-4} at most, and can be neglected.

For the systematic related to the signal channels, one needs to consider contributions related to the signal selection and three-dimensional fits in $M(D^0)$ vs. ΔM vs. $\cos\theta$ space used for extracting the signal yields and the corresponding signal A_{raw}'s. For the former, the IsPhoton selection is slightly changed with respect to the default values. This affects an ability for distinguishing between the signal and the π^0 background. As expected, the signal yields change while changing the IsPhoton selection[43]. However, as the signal and background shapes are consistent between the D^0 and $\bar{D}^0$ samples (Sections **VI.2**, **VI.3** and **VI.4**), these difference will largely cancel in the A_{raw} asymmetry. An exact impact of the IsPhoton selection on the signal A_{raw}'s will be estimated after unblinding.

Regarding the fitting, an assessment of related systematic effects depends on how individual fit parameters are treated in the data fits. Some PDF parameters are fixed to the their simulation values, namely the ones behind the $M(D^0)$–ΔM correlations and those describing $\cos\theta$ distributions. When performing the fits to the combined D^0 and $\bar{D}^0$ data (Sections **V.3**, **V.4** and **V.5**) these parameters' values are changed within their simulation-based uncertainties. The changes in the $\cos\theta$ parameters are

[43] No significant $D^0 \to \rho^0\gamma$ signal is observed for alternative IsPhoton cuts.

done in such a way that distinguishing power between the signal and the π^0 background is degraded. No significant effects on the total signal yields is found, thus no impact is expected on the A_{raw}'s either. On the other hand, the $M(D^0)$ and ΔM shapes for the signal and peaking backgrounds are calibrated using the helicity-edge data rather than fixed to the simulations. Here, some systematic effects can arise from different treating of the the data-MC calibration parameters, the offsets and scale factors. As already discussed in Sections **V.3**, **V.4** and **V.5**, alternative treatment of these parameters does not affect the signal yields significantly. In the simultaneous fits performed to the separated D^0 and $\bar{D}^0$ samples (Sections **VI.2**, **VI.3** and **VI.2**) these parameters are, as much as possible, *re-calibrated* by allowing for different values between the two D flavours; consistent yields are obtained for the signal yields. The final impact of this calibration on the signal A_{raw}'s will be estimated after unblinding.

The above mentioned systematic contributions are considered to be uncorrelated and, thus, can be added in quadrature. The total systematic uncertainties on the signal A_{CP}'s are expected to be below 1%, and dominated by statistical uncertainties of the reference A_{raw} asymmetries.

Chapter IX

Summary and outlook

This thesis presents the analysis of radiative decays of charm mesons, $D^0 \to \bar{K}^{*0}\gamma$, $D^0 \to \phi\gamma$ and $D^0 \to \rho\gamma$, collectively denoted as $D^0 \to V\gamma$, and their charge conjugates. The study is based on the pp collision data collected at a centre-of-mass energy of $\sqrt{s} = 8$ TeV by the LHCb experiment in 2012, during Run-1 of the LHC. This data sample corresponds to an integrated luminosity of 2 fb^{-1}. The reconstructed neutral D mesons originate from strong decays of the $D^{*\pm}$ states, $D^{*+} \to D^0\pi_s^+$ and $D^{*-} \to \bar{D}^0\pi_s^-$, with the π_s charge used for tagging of a D flavour at the production. This is important, as the study aims at measuring CP asymmetry, A_{CP}, between D^0 and $\bar{D}^0$ decays. It was previously measured for $D^0 \to V\gamma$ channels by the Belle collaboration.

The presented analysis is the first study of radiative charm decays performed at LHCb. While LHCb has successfully measured radiative decays of b-hadrons, their charm counterparts are more challenging, as they involve photons with lower p_T, and suffer from much higher and irreducible peaking background from decays involving π^0 mesons, $D^0 \to V\pi^0$. This background is suppressed using a multivariate classifier based on distinguished shapes of energy clusters produced by photons and π^0 mesons in the LHCb calorimeter system. The signal decays are separated from residual background with the three-dimensional fit to D^0 invariant mass $M(D^0)$, the difference between invariant masses of D^{*+} and D^0, $\Delta M = M(D^{*+}) - M(D^0)$, and V-meson helicity angle $\cos\theta$, as observables. In this fit, the correlations observed between $M(D^0)$ and ΔM observables for both signal and background channels, are modelled based on the corresponding simulation samples. The fits performed in the π^0-enhanced $\cos\theta$ regions, with small or negligible signal contribution, allow for data-based calibration of the $M(D^0)$ and ΔM shapes of the main background components.

The signal yields are measured from the fits to the combined D^0 and $\bar{D}^0$ samples, and performed in the signal-enhanced $\cos\theta$ regions. The total D^0 and $\bar{D}^0$ signal yields are measured to be: 4263 ± 193 events for $D^0 \to \bar{K}^{*0}\gamma$ decay, and 216 ± 29 events for the $D^0 \to \phi\gamma$ decay; no significant signal is observed for the $D^0 \to \rho\gamma$ decay. For comparison, the corresponding yields measured by Belle, using their sample collected during about 10 years of data taking, are: 9104 ± 396, 524 ± 35 and 500 ± 85 [40]. However, the π^0 background is much smaller at Belle, and their $M(D^0)$ resolution is better, owing to the better calorimeter system.

The A_{raw} asymmetries are measured by performing the three-dimensional fits simultaneously to the separated D^0 and $\bar{D}^0$ samples. While the central values are still blinded, the statistical uncertainties are 5% for $D^0 \to \bar{K}^{*0}\gamma$ and 12% for $D^0 \to \phi\gamma$; the Run-1 analysis is not sensitive to the asymmetry in the $D^0 \to \rho^0\gamma$ decay. These uncertainties correspond to the statistical uncertainties of the A_{CP}'s. For comparison, the statistical sensitivities of the Belle measurement are 2% for $D^0 \to \bar{K}^{*0}\gamma$, 7% for $D^0 \to \phi\gamma$ and 15% for $D^0 \to \rho^0\gamma$ [40].

There are also other sources than CP violation contributing to the measured A_{raw} asymmetries, with main ones being due to asymmetric charm production and asymmetric detection of positively and negatively charged hadrons. These nuisance asymmetries are measured as A_{raw} asymmetries in high-

statistics and high-purity reference channels, and subtracted from the signal A_{raw}'s. The pion-tagged $D^0 \to K^+K^-$ and $D^0 \to \pi^+\pi^-$ decays are chosen as reference channels for $D^0 \to \phi\gamma$ and $D^0 \to \rho^0\gamma$ signal decays, respectively, whereas $D^0 \to K^-\pi^+\pi^0$ is used as a reference channel for $D^0 \to \bar{K}^{*0}\gamma$. As nuisance asymmetries are known to be kinematic-dependent, it is necessary to equalize the kinematics of the reference channels with that of the corresponding signal channel. This multidimensional kinematic reweighing is performed using a multivariate classier. The nuisance asymmetries are measured to be about $(-1.0 \pm 0.2)\%$ in $D^0 \to K^+K^-$ and $D^0 \to \pi^+\pi^-$ channels, and $(-1.7 \pm 0.3)\%$ in $D^0 \to K^-\pi^+\pi^0$. They are subtracted from the A_{raw} asymmetries measured for the signal channels in order to access A_{CP}.

The presented measurement is statistically limited. The total systematic uncertainties on the signal A_{CP}'s are expected to be below 1%, and dominated by statistical uncertainties on the asymmetries measured in the reference channels.

As mentioned, the central values of the signal asymmetries are still blinded. Unblinding is planned together with the Run-2 measurement, which is currently ongoing. The Run-2 analysis benefits from the dedicated exclusive Hlt2 trigger line, implemented during 2017. The analysis method employed is the same as developed for the Run-1 study, and presented in this thesis. $D^0 \to \bar{K}^{*0}\gamma$ signal yield expected in the Run-2 measurement, based on 3.5 fb^{-1} data sample from 2017-2018, is about three times larger than the one measured with the Run-1 data. For the $D^0 \to \rho^0\gamma$ decay, an optimization of the selection against both π^0 background and combinatorial background is employed in order to increase the signal significance.

The Run-3 of the data-taking at the LHC is ongoing, and Hlt2 trigger selection for radiative charm decays had been finalized. The LHCb calorimeter system remained largely unchanged, but the hardware-level trigger had been removed, and the instantaneous luminosity has been increased by a factor of 5, to $\mathcal{L} \simeq 2 \times 10^{33}$ cm^{-2}s^{-1}. This means that analyzing Run-3 data will present other challenges to overcome compared to Run-1 and Run-2. However, with 50 fb^{-1} data sample planned to be collected by 2027, studying radiative charm decays with converted photons, $\gamma \to e^+e^-$, seems feasible.

Bibliography

[1] G. Aad et al. (ATLAS Collab.), *Observation of a new particle in the search for the Standard Model Higgs boson with the ATLAS detector at the LHC*, Phys. Lett. B716, 1 (2012).

[2] S. Chatrchyan et al. (CMS Collab.), *Observation of a new boson at a mass of 125 GeV with the CMS experiment at the LHC*, Phys. Lett. B716, 30 (2012).

[3] A. D. Sakharov, *Violation of CP Invariance, C asymmetry, and baryon asymmetry of the universe*, Pisma Z. Eksp. Teor. Fiz. 5, 32 (1967); English translation: JETP Lett. 5, 24 (1967).

[4] K. G. Wilson, W. Zimmerman, *Operator Product Expansions and Composite Field Operators in the General Framework of the Quantum Field Theory*, Commun. Math. Phys 24, 87-106 (1972).

[5] M. Kobayashi and T. Maskawa, *CP-Violation in the Renormalizable Theory of Weak Interaction*, Prog. Theor. Phys. 49, 652 (1973).

[6] R.L. Workman et al. (Particle Data Group), *The Review of Particle Physics*, Prog. Theor. Exp. Phys. 2022, 083 C01 (2022), and 2023 update.

[7] J. Charles et al. (CKMfitter Group), *CP Violation and the CKM Matrix: Assessing the Impact of the Asymmetric B Factories*, Eur. Phys. J. C41, 1 (2005). Updated results and plots available at: http://ckmfitter.in2p3.fr

[8] S. L. Glashow, J. Iliopoulos and L. Maiani, *Weak Interactions with Lepton-Hadron Symmetry*, Phys. Rev. D2, 1285 (1970).

[9] Y. Grossman, A. L. Kagan et al., *Testing for new physics in singly Cabibbo suppressed D decays*, Phys. Rev. D85, 114036 (2012).

[10] T. Feldmann, S. Nand et al., *Repercussions of Flavour Symmetry Breaking on CP Violation in D-Meson Decays*, J. High Energy Phys. 06, 007 (2012).

[11] S. Müller, U. Nierste et al., *Topological amplitudes in D decays to two pseudoscalars: a global analysis with linear $SU(3)_F$ breaking*, Phys. Rev. D92, 014004 (2015).

[12] D. Atwood and A. Soni, *Searching for the origin of CP violation in Cabibbo-suppressed D-meson decays*, PTEP 2013, 093B05 (2013).

[13] A. L. Kagan and L. Silvestrini, *Dispersive and absorptive CP violation in D^0-$\bar{D}^0$ mixing*, Phys. Rev. D103, 053008 (2021).

[14] M. Bobrowski, A. Lenz et al., *How large can the SM contribution to CP violation in $D^0 - \bar{D}^0$ mixing be?*, J. High Energy Phys. 03, 009 (2010).

[15] R. Aaij et al. (LHCb Collab.), *Observation of CP Violation in Charm Decays* Phys. Rev. Lett. 122, 211803 (2019).

[16] A. Dery and Y. Nir, *Implications of the LHCb discovery of CP violation in charm decays*, J. High Energy Phys. 12, 104 (2019).

[17] M. Chala, A. Lenz et al., *ΔA_{CP} within the Standard Model and beyond*, J. High Energy Phys. 1907, 161 (2019).

[18] Y. Amhis et al. (HFLAV Group), *Averages of b-hadron, c-hadron, and τ-lepton properties as of 2021*, Phys. Rev. D107, 052008 (2023).

[19] R. Aaij et al. (LHCb Collab.), *Measurement of the time-integrated CP asymmetry in $D^0 \to K^-K^+$ decays*, Phys. Rev. Lett. 131, 091802 (2023).

[20] R. Aaij et al. (LHCb Collab.), *Search for time-dependent CP violation in $D^0 \to K^+K^-$ and $D^0 \to \pi^+\pi^-$ decays*, Phys. Rev. D104, 072010 (2021).

[21] Charm Heavy Flavour Averaging (HFLAV) Group, https://hflav.web.cern.ch/content/charm-cpv-and-oscillations

[22] G. Buchalla, A. J. Buras et al., *Weak decays beyond leading logarithms*, Rev. Mod. Phys. 68, 1125 (1996).

[23] S. de Boer, B. Müller et al., *Higher-order Wilson coefficients for $c \to u$ transitions in the Standard Model*, J. High Energy Phys. 08, 091 (2016).

[24] S. de Boer, *Two loop virtual corrections to $b \to (d,s)l^+l^-$ and $c \to l^+l^-$ for arbitrary momentum transfer*, Eur. Phys. J. C77, 801 (2017).

[25] A. Lenz and T. Rauh, *D-meson lifetimes within the heavy quark expansion*, Phys. Rev. D88, 034004 (2013).

[26] G. Burdman, E. Golowich et al., *Radiative Weak Decays of Charm Mesons*, Phys. Rev. D52, 6383 (1995).

[27] C. Greub, T. Hurth et al., *The $c \to u\gamma$ contribution to weak radiative charm decay*, Phys. Lett. B382, 415 (1996).

[28] S. Fajfer, S. Prelovsek et al., *Long distance contributions in $D \to V\gamma$ decays*, Eur. Phys. J. C6, 471 (1999).

[29] S. de Boer and G. Hiller *Rare radiative charm decays in the standard model and beyond*, J. High Energy Phys. 08, 091 (2017).

[30] G. Isidori and J. F. Kamenik *Shedding Light on CP Violation in the Charm System via $D^0 \to V\gamma$ Decays*, Phys. Rev. Lett. 109, 171801 (2012).

[31] H.-Y. Cheng and C.-W. Chiang, *$SU(3)$ symmetry breaking and CP violation in $D \to PP$ decays*, Phys. Rev. D86, 014014 (2012).

[32] H.-Y. Cheng and C.-W. Chiang, *Revisiting CP violation in $D \to PP$ and $D \to VP$ decays*, Phys. Rev. D 100, 093002 (2019).

[33] G. F. Giudice, G. Isidori et al., Direct CP violation in charm and flavor mixing beyond the SM J. High Energy Phys. 04, 060 (2012).

[34] J. Lyon and R. Zwicky, *$A_{CP}(D^{0,+}_{(s)} \to V\gamma)$ from Large O_8*, arXiv:1210.6546 [hep-ph].

[35] A. Soni, *Resonance enhancement of Charm CP*, arXiv:1905.00907 [hep-ph].

[36] S. de Boer and G. Hiller *The photon polarization in radiative D decays, phenomenologically*, Eur. Phys. J. C78, 188 (2018).

[37] N. Adolph, G. Hiller et al., *Testing the standard model with* $D_{(s)} \to K_1(\to K\pi\pi)\gamma$ *decays*, Phys. Rev. D99, 075023 (2019).

[38] O. Tajima et al. (Belle Collab.), *Observation of the Radiative Decay* $D^0 \to \phi\gamma$, Phys. Rev. Lett. 92, 101803 (2004).

[39] B. Aubert et al. (BaBar Collab.), *Measurement of the Branching Fractions of the Radiative Charm Decays* $D^0 \to \bar{K}^{*0}\gamma$ *and* $D^0 \to \phi\gamma$, Phys. Rev. D78, 071101 (2008).

[40] T. Nanut et al. (Belle Collab.), *Observation of* $D^0 \to \rho\gamma$ *and Search for CP Violation in Radiative Charm Decays*, Phys. Rev. Lett. 118, 051801 (2017).

[41] Y.Li et al. (Belle Collab.), *First search for the weak radiative decays* $\Lambda_c^+ \to \Sigma^+\gamma$ *and* $\Xi_c^0 \to \Xi^0\gamma$, Phys. Rev. D107, 032001 (2023).

[42] R. Aaij et al. (LHCb Collab.), *Measurement of the b-Quark Production Cross Section in 7 and 13 TeV pp Collisions*, Phys. Rev. Lett. 118, 052002 (2017).

[43] R. Aaij et al. (LHCb Collab.), *Prompt charm production in pp collisions at* $\sqrt{s} = 7$ *TeV*, Nucl. Phys. B871, 1 (2013).

[44] R. Aaij et al. (LHCb Collab.), *Measurements of prompt charm production cross-sections in pp collisions at* $\sqrt{s} = 13$ *TeV*, J. High Energy Phys. 03, 159 (2016).

[45] R. Aaij et al. (LHCb Collab.), *LHCb detector performance*, Int. J. Mod. Phys. A 30, 1530022 (2015).

[46] P. Billoir, M. De Cian et al., *A parametrized Kalman filter for fast track fitting at LHCb*, Comput. Phys. Commun. 265, 108026 (2021).

[47] R. Aaij et al. (LHCb Collab.), *Measurement of the track reconstruction efficiency at LHCb*, JINST 10, P02007 (2015).

[48] M. Adinolfi et al. (LHCb RICH Collab.), *Performance of the LHCb RICH detector at the LHC*, Eur. Phys. J. C73, 2431 (2013).

[49] E. P. Olloqui, *LHCb Preshower (PS) and Scintillating Pad Detector (SPD): Commissioning, calibration, and monitoring*, Phys.: Conf. Ser. 160 012046 (2009).

[50] C. Abellán Beteta et al. (LHCb Calorimeter Group), *Calibration and performance of the LHCb calorimeters in Run 1 and 2 at the LHC*, arXiv:2008.11556 [physics.ins-det].

[51] O. Deschamps, F. P. Machefert et al., *Photon and neutral pion reconstruction*, CERN-LHCb-2003-091.

[52] F. Archilli, W. Baldini et al., *Performance of the Muon Identification at LHCb*, JINST 8, P10020 (2013).

[53] R. Aaij et al. (LHCb Collab.), *Measurement of the* $D^{\pm}$ *production asymmetry in 7 TeV pp collisions*, Phys. Lett. B718, 902 (2013).

[54] R. Aaij et al. (LHCb Collab.), *Measurement of* $D_s^{\pm}$ *production asymmetry in pp collisions at* $\sqrt{s} = 7$ *and 8 TeV*, J. High Energy Phys. 08, 008 (2018).

[55] E. Norrbin and T. Sjöstrand, *Production and Hadronization of Heavy Quarks*, Eur. Phys. J. C17, 137 (2000).

[56] A. Davis, L. Dufour et al., *Measurement of the instrumental asymmetry for $K^-\pi^+$ at LHCb in Run 2*, CERN-LHCb-PUB-2018-004.

[57] R. Aaij et al. (LHCb Collab.), *Measurement of the ratio of branching fractions $\frac{\mathcal{BF}(B^0\to K^{*0}\gamma)}{\mathcal{BF}(B_s^0\to\phi\gamma)}$ and the direct CP asymmetry in $B^0 \to K^{*0}\gamma$*, Nucl. Phys. B867, 1 (2013).

[58] R. Aaij et al. (LHCb Collab.), *First experimental study of photon polarisation in radiative B_s^0 decays*, Phys. Rev. Lett. 118, 021801 (2017).

[59] M. Calvo Gomez, E. Cogneras et al. *A tool for γ/π^0 separation at high energies*, CERN-LHCb-PUB-2015-016.

[60] A. Hoecker, P. Speckmayer et al., TMVA, the Toolkit for Multivariate Data Analysis with ROOT, arXiv:physics/0703039 [physics.data-an].

[61] T. Sjöstrand, S. Mrenna et al., A Brief Introduction to PYTHIA 8.1, Comput. Phys. Commun. 178, 852 (2008).

[62] I. Belyaev, T. Brambach et al., *Handling of the generation of primary events in Gauss, the LHCb simulation framework*, J. Phys. Conf. Ser. 331, 032047 (2011).

[63] D. Lange, *The EvtGen particle decay simulation package*, Nucl. Instrum. Meth. A462, 152 (2001).

[64] P. Golonka and Z. Was, *PHOTOS Monte Carlo: a precision tool for QED corrections in Z and W decays*, Eur. Phys. J. C45, 97 (2006).

[65] S. Agostinelli et al. (GEANT4 Collab), *GEANT4 – a simulation toolkit*, Nucl. Instrum. Meth. A506, 250 (2003).

[66] R. Aaij et al. (LHCb Collab.), *Search for time-dependent CP violation in $D^0 \to \pi^+\pi^-\pi^0$ decays*, arXiv:2405.06556 [hep-ex] (submitted to Phys. Rev. Lett.).

[67] A. Rogozhnikov, Machine Learning for High Energy Physics (HEP ML) Project, https://pypi.org/project/hep-ml/

[68] C. Langenbruch, *Parameter uncertainties in weighted unbinned maximum likelihood fits*, Eur. Phys. J. C82, 393 (2022).

[69] S. Kopp et al. (CLEO Collab.), *Dalitz Analysis of the Decay $D^0 \to K^-\pi^+\pi^0$*, Phys. Rev. D63, 092001 (2001).

[70] D. Cronin-Hennessy et al. (CLEO Collab.), *Searches for CP Violation and $\pi\pi$ S-Wave in the Dalitz-Plot Analysis of $D^0 \to \pi^+\pi^-\pi^0$*, Phys. Rev. D72, 031102 (2005).

[71] Y. Q. Chen et al. (Belle Collab.), *Dalitz analysis of $D^0 \to K^-\pi^+\eta$ decays at Belle*, Phys. Rev. D102, 012002 (2020).

[72] L. K. Li et al. Belle Collab., *Measurement of branching fractions and search for CP violation in $D^0 \to \pi^+\pi^-\eta$, $D^0 \to K^+K^-\eta$, and $D^0 \to \phi\eta$ at Belle*, J. High Energy Phys. 09, 075 (2021).

[73] B. Aubert et al. (BaBar Collab.), *Measurement of $D^0-\bar{D}^0$ mixing from a time-dependent amplitude analysis of $D^0 \to K^+\pi^-\pi^0$ decays*, Phys. Rev. Lett. 103, 211801 (2009); M. Pelliccioni, PhD thesis, Universitá degli Studi di Torino, SLAC-R-1017.

[74] W. D. Hulsbergen, *Decay Chain Fitting with a Kalman Filter*, Nucl. Instrum. Meth. A552, 566 (2005).

[75] L. Anderlini, A. Contu et al., *The PIDCalib package*, CERN-LHCb-PUB-2016-021.

[76] M. Pivk and F. R. Le Diberder, *sPlot: a statistical tool to unfold data distributions*, Nucl. Instrum. Meth. A555, 356 (2005).